Vibronic Coupling Density Analysis and Its Applications(Dissertation_全文)

AUTHOR(S):

Shizu, Katsuyuki

Vibronic Coupling Density Analysis and Its Applications

Katsuyuki Shizu

2011

Preface

Vibronic couplings, or electron-molecular vibration couplings are ubiquitous in material science. Vibronic couplings play an important role in charge transport, superconductivity, chemical reaction, luminescence, etc. For example, in a charge-transport process, vibronic couplings inhibit the carrier transport and cause a power loss. Therefore molecules exhibiting weak vibronic couplings are preferable as a charge-transporting molecule. Recent development of nanoscience has enabled us to measure the current through a single molecule. Inelastic electron tunneling (IET) spectroscopy has provided a direct observation of the vibronic couplings in a single molecule electron transport. IET spectra are characteristic for molecules and IET spectroscopy can be a direct identification method for molecular species adsorbed on an electrode. Thus, precise understanding of vibronic couplings at the molecular scale is needed in science and engineering.

Vibronic coupling density (VCD) analysis provides a local picture of vibronic couplings in a molecule. Employing the analysis, the vibronic couplings of various molecules have been investigated, and the reason for the size of the vibronic coupling constants (VCCs) have been elucidated. The fundamental understanding of vibronic couplings at the molecular scale leads to molecular design through controlling vibronic couplings: *vibronics*.

The aim of this thesis is to analyze vibronic couplings in a charge-transport process, derive the guiding principles for designing effective charge-transporting molecules, and theoretically design novel charge-transporting molecules by controlling their vibronic couplings. In Part I of this thesis, through analyzing existing charge-transporting molecules, guiding principles for designing effective charge-transporting molecules are derived, and novel charge-transporting molecules are theoretically designed. In Part II, vibronic couplings in the charge-transport of metal-molecule-metal junctions are investigated employing the VCD analysis. In Part III, miscellaneous applications of the VCD analysis are discussed.

The author hopes that findings in this thesis could give effective guiding principles for designing charge-transporting molecules and molecular wires, and form the basis for the *vibronics*.

Acknowledgments

The present thesis is a summary of the author's studies from 2005 to 2010 at the Department of Molecular Engineering, Graduate School of Engineering, Kyoto University.

The author would like to express his gratitude to Professor Kazuyoshi Tanaka for his valuable suggestions, stimulating discussions, and continuous encouragement throughout this work. The author is sincerely grateful to Associate Professor Tohru Sato for his precise guidance, stimulating suggestions, informative discussion, and constant encouragement to complete this study.

The author is thankful to Professor Sei-ichi Nishimoto for his kind guidance and the undergraduate education. The author would like to thank Professor Hironori Kaji (Kyoto University) for his instructive discussions and suggestions in molecular design of charge-transporting materials for organic light-emitting diodes. The author would like to show his gratitude to Associate Professor Yoshihiro Matano (Kyoto University) for his kind advices and helpful discussions in molecular design of boron-containing electron-transporting molecules. The author wishes to thank Associate Professor Masateru Taniguchi (Osaka University) for helpful discussions in inelastic electron tunneling spectra.

The author is grateful to Associate Professor Akihiro Ito and Dr. Hiroyuki Fueno for their kind advices. The author wishes to thank the members of Associate Professor Sato's research group, Dr. Ken Tokunaga (Kogakuin University), Dr. Guo Wang, Mr. Motoyuki Uejima, Mr. Kazuaki Kamiya, Mr. Sho Shimauchi, Mr. Naoya Iwahara, Mr. Daisuke Sakamaki, Mr. Keisuke Uegaito, Mr. Tomoharu Arai, Mr. Naoki Haruta, and Mr. Kota Usui for their kindness and valuable supports. The author is also thankful for other members of Tanaka Laboratory, and the secretaries, Ms. Yuko Otsuki, Ms. Ayako Tanaka, and Ms. Miya Kitao.

Finally, the author wishes to express his sincere gratitude to his parents Yoshitaka Shizu and Kiyomi Shizu, his brother Motoki Shizu, and his grandparents Kazuyoshi Tokuda and Tsuyuko Tokuda for their support, understanding, and encouragement.

Kyoto, December 2010

Katsuyuki Shizu

List of Publications

Part I

Chapter 1

(1) "Electron-vibration interactions in carrier-transport material:
Vibronic coupling density analysis in TPD",
T. Sato, K. Shizu, T. Kuga, K. Tanaka, and H. Kaji, Chem. Phys. Lett. **458**, 152 (2008).

Chapter 2

(2) "Electron-vibration interactions in triphenylamine cation:
Why are triphenylamine-based molecules good hole-transport materials?",
K. Shizu, T. Sato, K. Tanaka, and H. Kaji, Chem. Phys. Lett. **486**, 130 (2010).

Chapter 3

(3) "Vibronic coupling density analysis of hole-transporting materials:
Electron-density difference in DFT and HF methods",
K. Shizu, T. Sato, K. Tanaka, and H. Kaji, Org. Electron. **11**, 1277 (2010).

Chapter 4

(4) "Inverse proportionality between vibronic coupling constant and electron-density difference distribution",
K. Shizu, T. Sato, and K. Tanaka, submitted.

Chapter 5

(5) "Theoretical design of a hole-transporting material: Hexaaza[1_6]parabiphenylophane",
K. Shizu, T. Sato, A. Ito, K. Tanaka, and H. Kaji, submitted.

Chapter 6

(6) "A boron-containing molecule as an efficient electron-transporting material
with low-power consumption",
K. Shizu, T. Sato, K. Tanaka, and H. Kaji, Appl. Phys. Lett. **97**, 142111 (2010).

Chapter 7

(7) "Vibronic interactions in hole-transporting molecules:
An interplay with electron-hole interactions",
T. Sato, K. Shizu, K. Uegaito, N. Iwahara, K. Tanaka, and H. Kaji, submitted.

Part II

Chapter 1

(8) "Vibronic coupling density analysis for α-oligothiophene cations:
A new insight for polaronic defects",
K. Shizu, T. Sato, and K. Tanaka, Chem. Phys. **368**, 108 (2010).

Chapter 2

(9) "Inelastic electron tunneling spectra and vibronic coupling density analysis of
2,5-dimercapto-1,3,4-thiadiazole and tetrathiafulvalene dithiol",
K. Shizu, T. Sato, and K. Tanaka, Nanoscale **2**, 2186 (2010).

Part III

Chapter 1

(10) "Reduced vibronic coupling density and its application to
bis(ethylenedithio)tetrathiafulvalene (BEDT-TTF)",
K. Shizu, T. Sato, and K. Tanaka, Chem. Phys. Lett. **491**, 65 (2010).

Chapter 2

(11) "Vibronic coupling density analysis for free-base porphin cation",
K. Shizu, T. Sato, and K. Tanaka, submitted.

The following publications are not included in this thesis.

(12) "Preparation and characterization of *N*-anisyl-substituted hexaaza[1_6]paracyclophane", A. Ito, Y. Yokoyama, R. Aihara, K. Fukui, S. Eguchi, K. Shizu, T. Sato, and K. Tanaka, Angew. Chem., Int. Ed. **49**, 8205 (2010).

(13) "Vibronic coupling constant and vibronic coupling density",
T. Sato, K. Tokunaga, N. Iwahara, K. Shizu, K. Tanaka,
in: H. Köppel, D.R. Yarkony, and H. Barentzen (Eds.), The Jahn–Teller-Effect–Fundamentals and Implications for Physics and Chemistry, Springer-Verlag, Berlin and Heidelberg, 2009.

(14) "Origin of the Jahn–Teller distortions:
Vibronic coupling density analysis for Jahn–Teller molecules",
T. Sato, K. Shizu, N. Iwahara, N. Haruta, and K. Tanaka, submitted.

Contents

General Introduction

0.1 Molecular Design of Charge-Transporting Materials

Organic light-emitting diodes (OLEDs) and organic field-effect transistors (OFETs) have received considerable attention because of their potential applications in low-cost, large area, light-weight, and flexible electronic devices.[1–13] Since OLEDs and OFETs involve charge transport process, efficient charge-transporting materials are needed for the development of high-performance OLEDs and OFETs. One of the most important progress in engineering in recent years has been the development of molecular electronics.[14–22] Molecular electronics aims to use a single molecule as a fundamental unit for electronics. Metal-molecule-metal junctions have been studied extensively towards future applications for molecular electronics. To realize molecular electronics it is necessary to understand the charge transport at the nanoscale.

Vibronic couplings, or electron-molecular vibration couplings are ubiquitous in material science. Vibronic coupling plays an important role in charge transport, superconductivity, chemical reaction, luminescence, etc. For example, in a charge-transport process, vibronic couplings inhibit the carrier transport and cause a power loss, and molecules exhibiting weak vibronic couplings are preferable as charge-transporting molecules. In the last two decades, intramolecular vibronic couplings of organic molecules have been studied extensively.[23–50] However, little attention has been paid to designing charge-transporting materials by controlling vibronic couplings. The aim of this thesis is to analyze vibronic couplings in the charge-transport process, derive the guiding principles for designing effective charge-transporting molecules, and theoretically design novel charge-transporting molecules by controlling their vibronic couplings.

0.1.1 Hole-Transporting Materials for OLEDs

A typical multi-layer OLED consists of an anode (for example, indium-tin-oxide (ITO)), a hole-transport layer, an emitting layer, an electron-transport layer, and a cathode. Amorphous molecular materials or molecular glasses are attractive candidates for materials in OLEDs.[51–59] The advantage of amorphous materials is the capability of large-area thin-film fabrication at low temperatures.

The hole-transport layers in OLEDs play a role of the assisting hole injection from the anode, preventing electrons from escaping from the emitting layer (blocking electrons), and transporting holes to the emitting layer (Fig. 1). Hence, the hole-transporting molecules should have a highest occupied molecular orbital (HOMO) energy close to the Fermi level of the anode $E_{F,\mathrm{A}}$ and a lowest unoccupied molecular orbital (LUMO) energy higher than that of the emitting molecule, and exhibit a high-hole mobility. Since hole-transporting materials in OLEDs are used in their amorphous state, they should also exhibit a high glass-transition temperature T_g to keep a device durability.

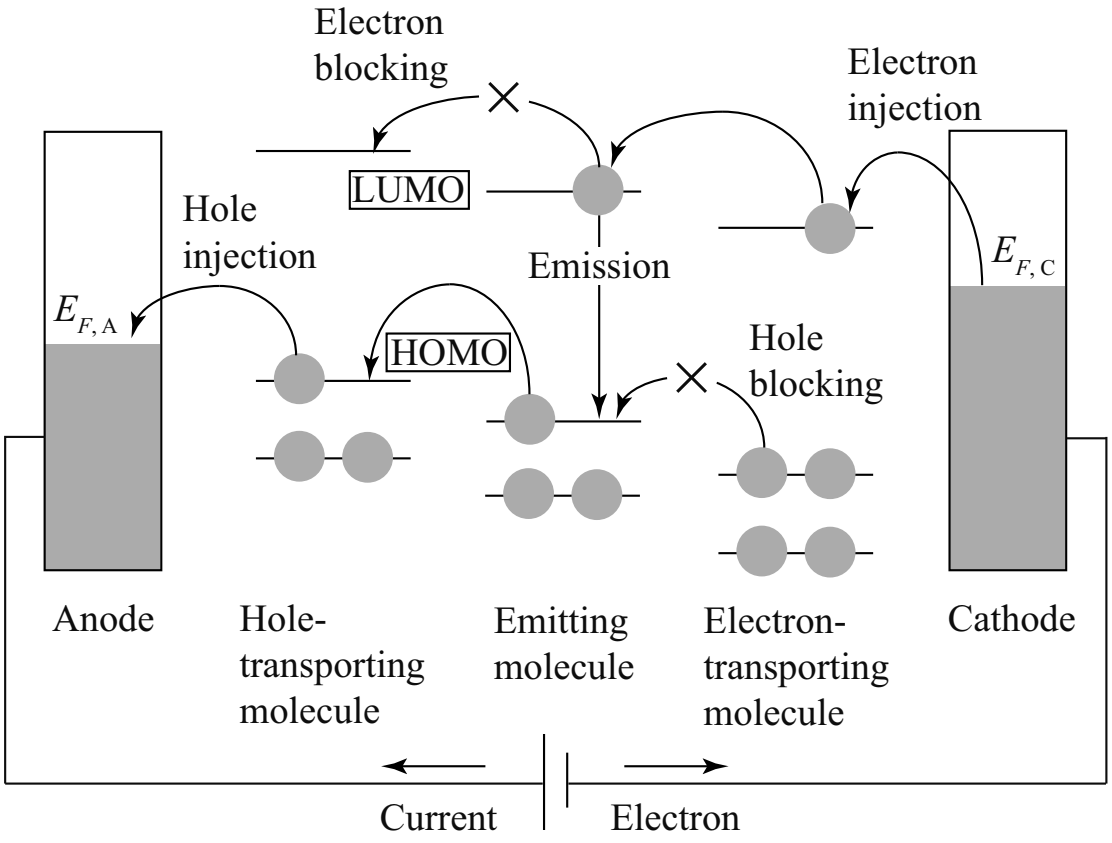

Figure 1: Energy level diagram of a multi-layer OLED.

A number of compounds have been synthesized and used as the hole-transporting materials for OLEDs.[51–56,58,59] Most of the hole-transporting molecules consist of triarylamine moieties. Among them, N,N'-bis(3-methylphenyl)-N,N'-diphenyl-[1,1′-biphenyl]-4,4′-diamine (TPD, Fig. 2) has been one of the most widely used hole-transporting material because of its high-hole mobility (1.0×10^{-3} cm^{2}V^{-1}s^{-1} at an electric field 1.5×10^5 Vcm^{-1} obtained using the time-of-flight (TOF) technique) and the electron-blocking property.[60,61] However, since TPD exhibits a low glass transition temperature T_g (= 62°C), it lacks thermal stability.[56,62] N,N,N',N'-tetraphenylbenzidine (TAD), which has a chemical structure similar to that of TPD, exhibits a hole-transporting property, but easily crystallized because of its low T_g (= 70°C).[56] N,N'-di(1-naphthyl)-N,N'-diphenyl-[1,1′-biphenyl]-4,4′-diamine (α-NPD), which exhibits higher T_g (= 95°C) and better thermal stability than TPD, has been also used as a hole-transporting material in OLEDs.[62,63]

Saragi *et al.* have shown that T_g of TPD/TAD/α-NPD raises by joining two TPD/TAD/α-NPD molecules through a spiro carbon center (Fig. 2).[56,57] In general, introduction of bulky or heavy substituents and structurally rigid moieties, and enlargement of the molecular size have the effect of raising T_g and enhancing the thermal stability of amorphous materials.[58]

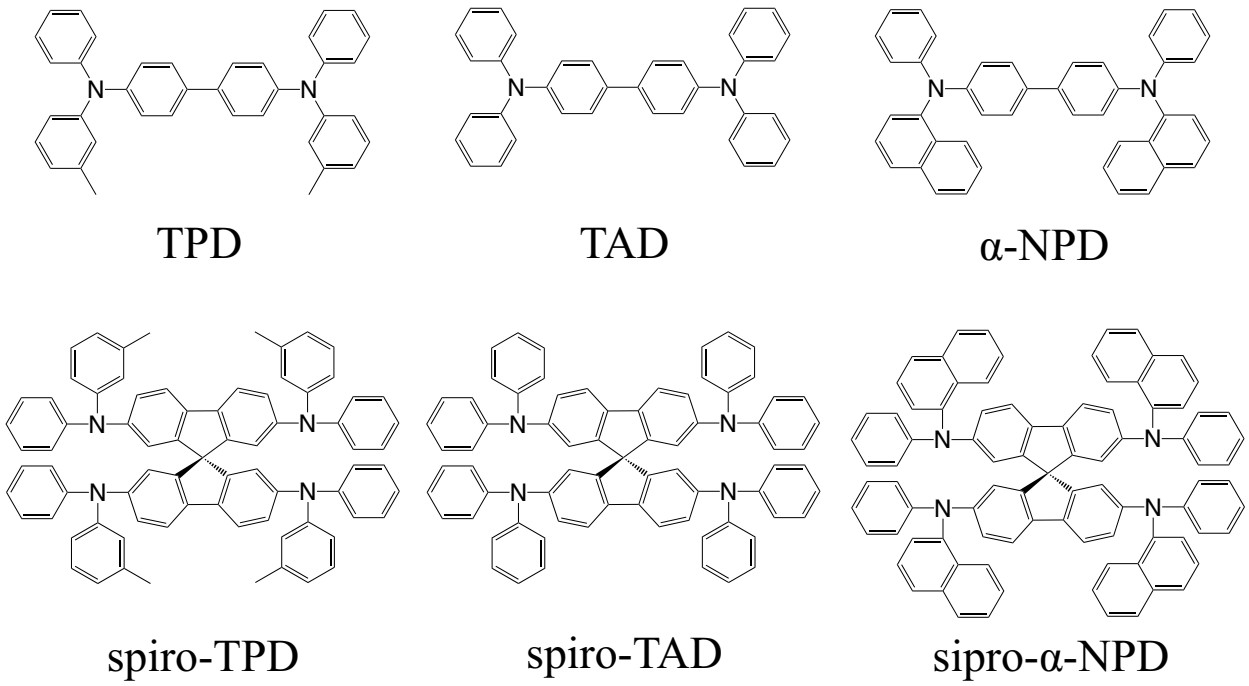

Figure 2: Hole-transporting materials for OLEDs.

0.1.2 Electron-Transporting Materials for OLEDs

The electron-transport layers have a role of assisting the electron injection from the cathode, preventing holes from escaping from the emitting layer (blocking holes), and transporting electrons to the emitting layer (Fig. 1). Hence, the electron-transporting molecules should have a LUMO energy close to the Fermi level of the cathode $E_{F,\mathrm{C}}$ and a HOMO energy lower than that of the emitting molecule, and exhibit high-electron mobility. The electron-transporting molecules should also exhibit a high T_g.

While most of the hole-transporting molecules consist of triarylamine moieties, electron-transporting molecules consisting different structural units have been developed. The best-known electron-transporting molecule for OLEDs is tris-(8-hydroxyquinoline) aluminum(III) (Alq_3, Fig. 3), which has also been employed as a green emitter.[1,64] The electron mobility of Alq_3 is about 10^{-6}–10^{-5} $cm^2V^{-1}s^{-1}$.[65] Silole derivatives such as 2,5-bis-(2′,2″-bipyridin-6-yl)-1,1-dimethyl-3,4-diphenylsilacyclopentadiene (PyPySPyPy), have been used as an electron-transporting material.[66–71] PyPySPyPy exhibits a mobility of 2×10^{-4} $cm^2V^{-1}s^{-1}$,[67] which is about ten times of that of Alq_3. 4,7-Diphenyl-1,10-phenanthroline (bathophenanthroline or BPhen) also exhibits electron-transporting properties.[72–75] 2,9-Dimethyl-4,7-diphenyl-1,10-phenanthroline (bathocuproine or BCP) functions as an electron transporting and hole-blocking material.[76,77] Electron mobilities of BPhen and BCP are comparable to those of hole-transporting materials such as TPD.[78]

1,2,4-Triazole and 1,3,4-oxadiazole derivatives have been widely employed as electron-transporting materials for OLEDs.[61,78–88] Chemical structures of various triazole- and oxadiazole-based electron-transporting molecules are shown in Fig. 3. Although 3-(4-biphenylyl)-4-phenyl-5-(4-tert-butylphenyl)-1,2,4-triazole (TAZ)[61] and 2-(4-tert-butylphenyl)-5-(4-biphenylyl)-1,3,4-oxadiazole (PBD)[61,78–83,85,88] exhibit lower-electron mobilities than Alq_3, they display good hole-blocking properties. Kido *et al.* have shown that TAZ exhibits a better hole-blocking property than PBD.[61] 1,3-Bis(*N*,*N*-dimethylaminophenyl)-1,3,4-oxadiazole (OXD-8) has an ambipolar character: it displays a hole-transporting property as well as an electron-transporting property.[84] OXD-8 has also been known as a blue emitter.

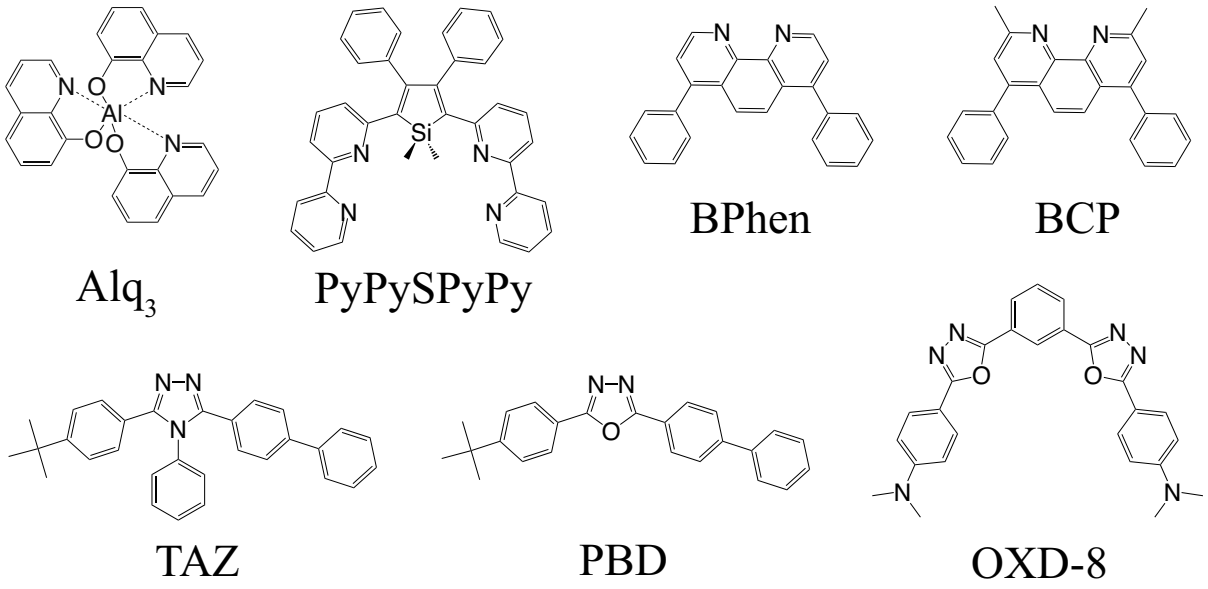

Figure 3: Electron-transporting materials for OLEDs.

Organoboron compounds have electron-transporting characters,[89–94] suggesting that boron atom plays a key role in electron-transporting process. 5,5′-Bis(dimesitylboryl)-2,2′-bithiophene (BMB-2T) and 5,5″-bis(dimesitylboryl)-2,2′:5′,2″-terthiophene (BMB-3T) have been used as electron-transport layers for OLEDs (Fig. 4).[89] Amorphous states of BMB-2T and BMB-3T are thermally stable because T_g of BMB-2T and BMB-3T are 107 and 115°C, respectively, which are sufficiently high for use in OLEDs.[89]

Compounds containing triarylborane central core, tris(2,3,5,6-tetramethylphenyl)borane (TPhB), tris(2,3,5,6-tetramethylbiphenyl-4-yl)borane (TBPhB), tris(2,3,5,6-tetramethyl-1,1′:4′,1″-terphenyl-4-yl)borane (TTPhB), and tris[2,3,5,6-tetramethyl-4-(1,1′:3′,1″-terphenyl-5′-yl)phenyl]borane (TTPhPhB) function as effective hole-blocking materials.[93] T_g of TPhB, TBPhB, TTPhB, and TTPhPhB are 63, 127, 163, and 183°C, respectively.[93] This result clearly shows that the introduction of the bulky or heavy substituents raises T_g and enhances the thermal stability of these amorphous materials. Recently, Tanaka *et al.* have reported that tris[3-(3-pyridyl)mesityl]borane (3TPYMB) exhibits electron mobility about ten times higher than that of Alq_3 and has hole-blocking property.[94] Thus, triarylborane-based compounds are attractive candidates for electron-transporting and hole-blocking materials.

Charge balance of holes and electrons in emitting layers is a major factor that influences the device efficiency of OLEDs.[95] Good charge balance lowers drive voltage and

the device efficiency of OLEDs. However, the electron mobilities of most of the electron-transporting materials are lower than the hole mobilities of hole-transporting materials such as TPD. Hence, to enhance the device efficiency it is necessary to develop electron-transporting materials with a high-electron mobility and improve the charge balance in OLEDs.

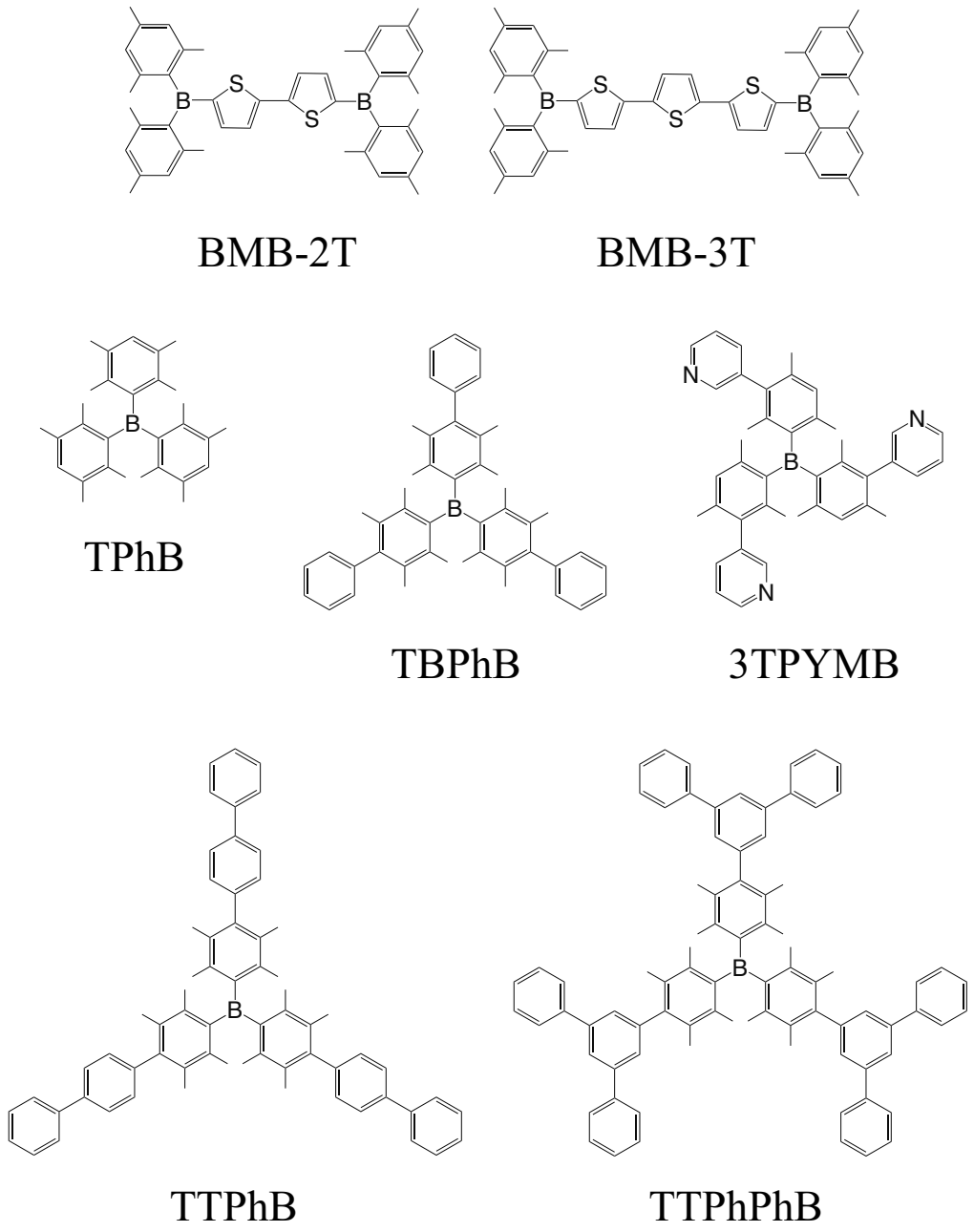

Figure 4: Boron-containing electron-transporting materials.

0.1.3 Organic Semiconductors for OFETs

Phthalocyanine and porphyrin derivatives have been widely investigated as p-type semiconductors for OFETs.[96–118] Copper phthalocyanine (CuPc) is one of the most studied organic semiconductors (Fig. 5). The hole mobility of CuPc reaches 10^{-2} $cm^2V^{-1}s^{-1}$.[97] The hole mobilities of porphyrin derivatives range between 10^{-6}–10^{-1} $cm^2V^{-1}s^{-1}$. Pt(OX) exhibits a hole mobility of 3.1×10^{-1} $cm^2V^{-1}s^{-1}$, which is comparable to those of organic semiconductors, such as oligothiophenes.[117]

Oligothiophenes and polythiophenes are promising materials for electronic devices. α,α'-oligothiophenes (denoted α-nT, where n is the number of thiophene rings) have been attracting much attention because of their good charge-transport properties, high chemical stability, and synthetic flexibility.[119] α-nT (n=3, 4, 5, 6, 8) thin films have been used as semiconductors in OFETs and organic thin-film transistors (OTFTs).[98,120–133] Halik *et al.* investigated that the effect of α-6T alkyl side-chain length on mobility and reported that the measured carrier mobility to be 1.1 $cm^2V^{-1}s^{-1}$ for α,α'-diethylsexithiophene, which has the highest hole mobility other than pentacene.[134]

OFETs using highly ordered pentacene and rubrene single crystals as semiconductors exhibit high hole mobilities of about 30 $cm^2V^{-1}s^{-1}$ at room temperature.[134,135] Pentacene and rubrene satisfy the requirement for practical application: field-effect mobilities should be greater than 1 $cm^2V^{-1}s^{-1}$.[58]

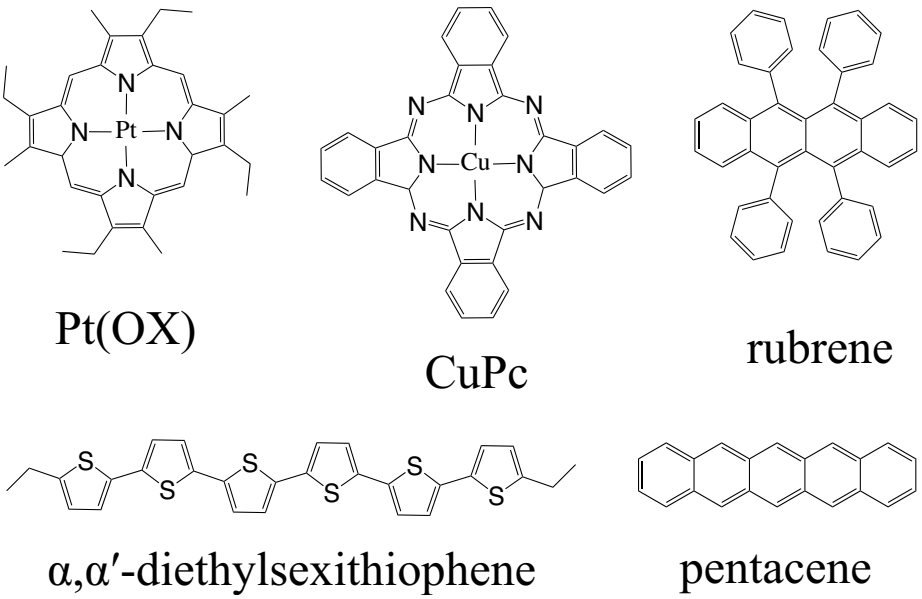

Figure 5: Semiconductors for OFETs.

0.1.4 Effects of Vibronic Coupling on Charge Transport

In a charge-transport process, intramolecular vibronic couplings cause inelastic scatterings of charge carriers, inhibit the charge transport, decrease the mobility, and generate a Joule heat. The vibronic couplings in a charge transport have been often discussed in terms of the Marcus' theory.[136–141] In the Marcus' theory, the vibronic couplings are related to a reorganization energy. The reorganization energy quantitatively represents the strength of the vibronic couplings of a molecule as well as vibrational frequencies. Molecules with small reorganization energies are preferable for charge-transporting molecules.

In this thesis, we study effects of the vibronic couplings on a charge transport employing the non-equilibrium Green's function (NEGF) method.[142] The NEGF method has been widely used to simulate electronic transports in nanoscale systems such as metal-single molecule-metal junctions. In the NEGF theory, the strength of the inelastic scatterings due to the vibronic couplings are defined by the square of the corresponding electron-phonon coupling constants as described in the following section. In the NEGF theory, molecules with small electron-phonon coupling constants are preferable for charge-transporting molecules.

Recently, studies of the vibronic couplings have been extended to intermolecular transfer integrals. Coropceanu *et al.* have investigated effects of the vibronic couplings on the transfer integrals for a naphthalene crystal[49] employing the Su-Schrieffer-Heeger (SSH) model,[30,143–145] and pointed out the possibility that the intermolecular vibronic couplings assist charge transport, and enhance mobility. In this thesis, we focus on the effects of the intramolecular vibronic couplings on the charge transport.

0.1.5 Vibronic Coupling of Molecular Wire Conduction: Inelastic Electron Tunneling Spectra

Recent development of nanoscience has enabled us to measure a current through a single molecule and self-assembled monolayer (SAM). Our knowledge of the vibronic couplings in a charge-transport process has greatly increased in recent years, driven by improvements of inelastic electron tunneling (IET) spectroscopy.[146,147] IET spectroscopy has provided a direct observation of the vibronic couplings in a charge transport process. IET spectra for metal-molecule-metal junctions or metal-SAM-metal junctions have been studied exten-

sively.[17,148–165] The peak positions of an IET spectrum correspond to vibrational energies of a molecule that interacts with a carrier, and the peak heights reflect relative strength of the vibronic couplings.[22] Thus, the IET spectra contain information about the vibronic couplings between the carrier and the molecular vibrations. The IET spectra are characteristic for molecules and the IET spectroscopy can serve as an identification method for molecular species adsorbed on an electrode. IET spectra are also useful for choosing a molecule when we construct a molecular wire junction, and therefore, a fundamental understanding of the IET spectra is needed for development of future nanoelectronics. IET spectra have been a subject of interest from the standpoints of both fundamental science and technology.

The selection rule for an IET spectrum is yet controversial. For oligo (phenylene ethynylene) (OPE), the ring mode and C≡C stretching mode show intense peaks; for oligo (vinylene ethynylene) (OPV), the ring mode and C=C stretching mode show intense peaks.[154] This result shows that the carriers are scattered by the IR and Raman active modes. In contrast, the systematic experimental observation of the IET spectra for semifluorinated alkanethiol junctions has made it clear that the relative intensity of the spectra is not necessarily proportional to the calculated IR nor Raman intensities of the isolated semifluorinated alkanethiols.[162] Using a scanning tunneling microscope (STM), Okabayashi *et al.* have measured high-resolution STM-IET spectra of alkanethiol SAMs[166,167] and reported that the inelastic intermolecular scatterings are important in the electron tunneling in the SAMs. Troisi *et al.* have estimated peak intensities in IET spectra by calculating the first derivative of the Green's function with respect to the normal mode coordinates, and concluded that only the totally symmetric modes show peak when a single tunneling channel is available.[160]

One of the purpose of this thesis is to provide an understanding of the relative intensities in IET spectra.

0.2 Theory

In this section, the method of analyzing vibronic couplings and calculating IET spectra are described.

0.2.1 Vibronic Coupling Constant and Vibronic Coupling Density

The molecular Hamiltonian is given by

$$\mathcal{H}\left(\mathbf{r},\mathbf{R}\right)=\mathcal{H}_{\mathrm{e}}\left(\mathbf{r},\mathbf{R}\right)+\mathcal{T}_{\mathrm{n}}\left(\mathbf{R}\right), \tag{1}$$

where $\mathcal{H}_{\mathrm{e}}\left(\mathbf{r},\mathbf{R}\right)$ is an electronic Hamiltonian, $\mathcal{T}_{\mathrm{n}}\left(\mathbf{R}\right)$ is the nuclear kinetic operator, and $\mathbf{r}$ and $\mathbf{R}$ are sets of electronic and nuclear coordinates, respectively. The electronic Hamiltonian $\mathcal{H}_{\mathrm{e}}\left(\mathbf{r},\mathbf{R}\right)$ is the sum of the electronic kinetic, the electronic-electronic, the electronic–nuclear, and the nuclear–nuclear operators. Employing the Herzberg–Teller expansion, $\mathcal{H}_{\mathrm{e}}\left(\mathbf{r},\mathbf{R}\right)$ is expressed as

$$\mathcal{H}_{\mathrm{e}}\left(\mathbf{r},\mathbf{R}\right)=\mathcal{H}_{\mathrm{e}}\left(\mathbf{r},\mathbf{R_0}\right)+\sum_{\alpha}\left(\frac{\partial\mathcal{H}_{\mathrm{e}}\left(\mathbf{r},\mathbf{R}\right)}{\partial Q_{\alpha}}\right)_{\mathbf{R_0}}Q_{\alpha}+\cdots, \tag{2}$$

where $\{Q_{\alpha}\}$ is a set of mass-weighted normal coordinates for the α^{th} vibrational mode and $\mathbf{R_0}$ is the nuclear configuration of the equilibrium geometry for the reference system.

Once an equilibrium nuclear configuration $\mathbf{R}_0$ and vibrational frequencies of the molecule are obtained, we can calculate the VCC V_{ij}^{α} for the α^{th} mode:

$$V_{ij}^{\alpha}=\left\langle \Psi_i\left(\mathbf{r},\mathbf{R_0}\right)\left|\left(\frac{\partial\mathcal{H}_{\mathrm{e}}\left(\mathbf{r},\mathbf{R}\right)}{\partial Q_{\alpha}}\right)_{\mathbf{R}=\mathbf{R}_0}\right|\Psi_j\left(\mathbf{r},\mathbf{R_0}\right)\right\rangle, \tag{3}$$

where $|\Psi_i\rangle$ is the state in which an electron or a hole is generated in the i^{th} molecular orbital of the molecule.

$\partial/\partial Q_{\alpha}$ can be written as

$$\frac{\partial}{\partial Q_{\alpha}}=\sum_{A}\frac{\mathbf{e}_A^{(\alpha)}}{\sqrt{M_A}}\cdot\frac{\partial}{\partial\mathbf{R}}, \tag{4}$$

where M_A is the mass of nucleus A, and $\mathbf{e}_A^{(\alpha)}$ is the A^{th} component of a vibrational vector of the α^{th} vibrational mode in the mass-weighted coordinates Q_{α}. $\mathbf{e}_A^{(\alpha)}$ is a 3D vector and represents the relative displacement of nucleus A for the α^{th} mode. The three components

of $\mathbf{e}_A^{(\alpha)}$ represent displacements of nucleus A along the x, y, and z axes, and are denoted as

$$\mathbf{e}_A^{(\alpha)} = \left(e_{A,1}^{(\alpha)}, e_{A,2}^{(\alpha)}, e_{A,3}^{(\alpha)} \right). \tag{5}$$

Substituting Eq. (4) into Eq. (3), we obtain

$$\begin{aligned} V_{ij}^{\alpha} &= \sum_A \frac{1}{\sqrt{M_A}} \mathbf{e}_A^{(\alpha)} \cdot \left\langle \Psi_i(\mathbf{r}, \mathbf{R_0}) \left| \left(\frac{\partial \mathcal{H}_{\mathrm{e}}(\mathbf{r}, \mathbf{R})}{\partial \mathbf{R}} \right)_{\mathbf{R_0}} \right| \Psi_j(\mathbf{r}, \mathbf{R_0}) \right\rangle \\ &= \sum_A V_{ij,A}^{\alpha}, \end{aligned} \tag{6}$$

where $V_{ij,A}^{\alpha}$ is the atomic vibronic coupling constant (AVCC) for atom A, and represents the contribution to the VCC V_{ij}^{α} from atom A.

For $i = j$, V_i^{α} ($\equiv V_{ii}^{\alpha}$) can be written in terms of the electron-density difference $\Delta\rho_i$ and the one-electron part of the derivative of the nuclear–electronic potential v_{α}:[168–171]

$$V_i^{\alpha} = \int \Delta\rho_i(\mathbf{x}) \times v_{\alpha}(\mathbf{x})\, d\mathbf{x}, \tag{7}$$

where

$$\Delta\rho_i(\mathbf{x}) = \rho_i(\mathbf{x}) - \rho_0(\mathbf{x}), \tag{8}$$

$$v_{\alpha}(\mathbf{x}) = \frac{\partial}{\partial Q_{\alpha}} \frac{Z_A}{|\mathbf{x} - \mathbf{R}_A|} = -\sum_A \frac{Z_A}{\sqrt{M_A}} \mathbf{e}_A^{(\alpha)} \cdot \frac{\mathbf{x} - \mathbf{R}_A}{|\mathbf{x} - \mathbf{R}_A|^3}, \tag{9}$$

and $\rho_i(\mathbf{x})$ and $\rho_0(\mathbf{x})$ represent the electron densities for the state $|\Psi_i\rangle$ and reference system, respectively. $\mathbf{x}$ denotes a position of electron in three-dimensional space, and Z_A is the atomic number of nucleus A. The product $\Delta\rho_i(\mathbf{x}) \times v_{\alpha}(\mathbf{x})$ is called the VCD[168–171] and is expressed as

$$\eta_i^{\alpha}(\mathbf{x}) = \Delta\rho_i(\mathbf{x}) \times v_{\alpha}(\mathbf{x}). \tag{10}$$

The VCD provides a local picture of vibronic coupling in a molecule.

The contribution from atom A to $\eta_i^{\alpha}(\mathbf{x})$ is described by the atomic vibronic coupling density (AVCD) $\eta_{i,A}^{\alpha}(\mathbf{x})$, which is given by

$$\begin{aligned} \eta_{i,A}^{\alpha}(\mathbf{x}) &= \Delta\rho_i(\mathbf{x}) \times \left(-\frac{Z_A}{\sqrt{M_A}} \mathbf{e}_A^{(\alpha)} \cdot \frac{\mathbf{x} - \mathbf{R}_A}{|\mathbf{x} - \mathbf{R}_A|^3} \right) \\ &= \Delta\rho_i(\mathbf{x}) \times v_{\alpha,A}(\mathbf{x}). \end{aligned} \tag{11}$$

Integration over space of the AVCD yields the AVCC $V_{i,A}^{\alpha}$:

$$V_{i,A}^{\alpha} = \int \eta_{i,A}^{\alpha}(\mathbf{x})\, d\mathbf{x}. \tag{12}$$

η_i^{α} gives a local picture of the vibronic coupling in a molecule. Since $\Delta\rho_i$ represents change in the electronic structure, while v_{α} represents the vibrational structure, we can relate V_i^{α} to the electronic and vibrational structures by analyzing η_i^{α}.

$\Delta\rho_i$ has a great influence on the strength of vibronic couplings. In general, V_i^{α} is small when $\Delta\rho_i$ is strongly localized on atoms. By contrast, V_i^{α} is large when $\Delta\rho_i$ is largely delocalized on bonds. Figure 6 illustrates this trend. We consider here the vibronic coupling around the atom A. $v_{\alpha,A}$ is almost antisymmetric around the atom A per Eq. (11). In the case where $\Delta\rho_i$ is strongly localized on the atom A (Fig. 6(a)), $\Delta\rho_i$ overlaps with the negative and positive regions of $v_{\alpha,A}$. Consequently, $\eta_{i,A}^{\alpha}$ is antisymmetric around the atom A. The cancellation of $\eta_{i,A}^{\alpha}$ leads to small $V_{i,A}^{\alpha}$. Thus, the strong localization of $\Delta\rho_i$ on atoms leads to small $V_{i,A}^{\alpha}$ values and hence, a small V_i^{α}.

On the other hand, in the case where $\Delta\rho_i$ is largely delocalized on a bond (Fig. 6(b)), $\Delta\rho_i$ overlaps significantly with the negative region of of $v_{\alpha,A}$ on the bond, while it overlaps slightly with the positive region of $v_{\alpha,A}$. Hence, the positive region of $\eta_{i,A}^{\alpha}$ is larger than the negative region, and $V_{i,A}^{\alpha}$ has a large positive value. Thus, the large delocalization of $\Delta\rho_i$ on bonds leads to large $V_{i,A}^{\alpha}$ values and consequently, a large V_i^{α}.

Examples of the former case (in which $\Delta\rho_i$ is strongly localized on atoms) are TPA, TPD, carbazole, and free-base porphin cations (Chapter 1–3 in Part I and Chapter 2 in Part III). Those of the latter case (in which $\Delta\rho_i$ is delocalized on bonds) are biphenyl, fluorene, and α-oligothiophenes cations (Chapter 3 in Part I and Chapter 1 in Part II).

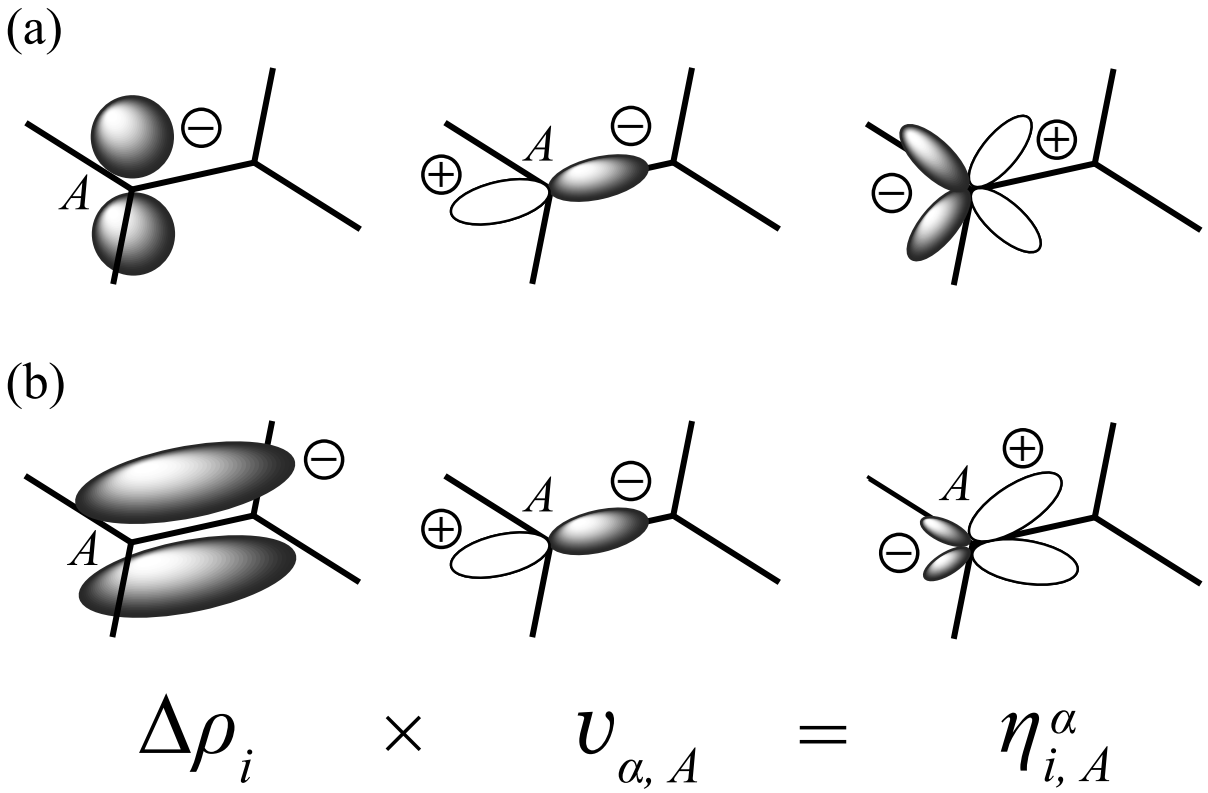

Figure 6: Schematic representation of atomic vibronic coupling density $\eta^{\alpha}_{i,A}$. (a) In the case where $\Delta\rho_i$ is strongly localized on the atom A; (b) in the case where $\Delta\rho_i$ is largely delocalized on the bond. $v_{\alpha,A}$ is a contribution of the atom A to the one-electron part of the derivative of the nuclear–electronic potential v_α (Eq. (11)). Dark-gray regions are negative; white regions are positive.

0.2.2 Non-equilibrium Green's Function Formalism

An IET spectrum can be calculated employing the NEGF method.[142] The NEGF method has been widely used to investigate an electronic transport through a molecular wire linked with electrodes. The Hamiltonian for an electrode-molecule-electrode junction is written in the second quantization form as

$$\mathcal{H} = \mathcal{H}_{\mathrm{e}} + \mathcal{V}_{\mathrm{L}} + \mathcal{V}_{\mathrm{R}} + \mathcal{H}_{\mathrm{vib}} + \mathcal{H}_{\mathrm{vibro}}, \tag{13}$$

where

$$\mathcal{H}_{\mathrm{e}} = \sum_{i} \epsilon_i c_i^{\dagger} c_i, \tag{14}$$

$$\mathcal{H}_{\mathrm{L}} = \sum_{l} \epsilon_l c_l^{\dagger} c_l, \tag{15}$$

$$\mathcal{H}_{\mathrm{R}} = \sum_{r} \epsilon_r c_r^{\dagger} c_r, \tag{16}$$

$$\mathcal{V}_{\mathrm{L}} = \sum_{i,l} \tau_{il} \left(c_i^{\dagger} c_l + c_l^{\dagger} c_i \right), \tag{17}$$

$$\mathcal{V}_{\mathrm{R}} = \sum_{i,r} \tau_{ir} \left(c_i^{\dagger} c_r + c_r^{\dagger} c_i \right), \tag{18}$$

$$\mathcal{H}_{\mathrm{vib}} = \sum_{\alpha} \hbar\omega_{\alpha} \left(b_{\alpha}^{\dagger} b_{\alpha} + \frac{1}{2} \right), \tag{19}$$

$$\mathcal{H}_{\mathrm{vibro}} = \sum_{i,\alpha} \lambda_i^{\alpha} c_i^{\dagger} c_i \left(b_{\alpha} + b_{\alpha}^{\dagger} \right). \tag{20}$$

$\mathcal{H}_{\mathrm{e}}$ is the electronic Hamiltonian for the molecule, $\mathcal{H}_{\mathrm{L/R}}$ is the electronic Hamiltonian for the left/right electrode, $\mathcal{H}_{\mathrm{vib}}$ is the Hamiltonian of the molecular vibrations, and $\mathcal{H}_{\mathrm{vibro}}$ is the vibronic couplings with the molecular vibrations. $\mathcal{V}_{\mathrm{L/R}}$ is the electronic coupling between the molecule and left/right electrode. $c_i^{\dagger}$ and c_i are electron creation and annihilation operators in the i^{th} molecular orbital, respectively, and $b_{\alpha}^{\dagger}$ and b_{α} denote a phonon creation/annihilation operators of the α^{th} mode, respectively. ϵ_i is the orbital energy of the molecule, $\epsilon_{l/r}$ is the eigenenergy of the left/right electrode, and ω_{α} is the frequency of the α^{th} mode. τ_{il} and τ_{ir} are the transfer integrals between the orbital states of the molecule and the electrodes. λ_i^{α} is the electron-phonon coupling constant, and can be written in terms of the VCC V_i^{α}:

$$\lambda_i^{\alpha} = \sqrt{\frac{\hbar}{2\omega_{\alpha}}} V_i^{\alpha}. \tag{21}$$

Heisenberg equations $i\hbar d\mathcal{O}/dt = [\mathcal{O}, \mathcal{H}]$ are obtained from Eq. (13) as

$$i\hbar\frac{d}{dt}c_i = \epsilon_i c_i + \sum_l \tau_{il}c_l + \sum_r \tau_{ir}c_r + \sum_\alpha \lambda_i^\alpha c_i \left(b_\alpha + b_\alpha^\dagger\right), \tag{22}$$

$$i\hbar\frac{d}{dt}c_l = \epsilon_l c_l + \sum_i \tau_{il}c_i, \tag{23}$$

$$i\hbar\frac{d}{dt}c_r = \epsilon_r c_r + \sum_i \tau_{ir}c_i, \tag{24}$$

$$i\hbar\frac{d}{dt}b_\alpha = \hbar\omega_\alpha b_\alpha + \sum_i \lambda_i^\alpha c_i^\dagger c_i. \tag{25}$$

Eq. (22) contains the electrode and vibration operators, c_l, c_r, $c_i b_\alpha$, and $c_i b_\alpha^\dagger$. Theses operators can be expressed employing Green's functions of the differential operators appearing in Eqs. (23)-(25).

The Green's functions for the differential equations appearing in Eqs. (23) and (24) are defined by

$$i\hbar\frac{d}{dt}g_{ll}^{\rm L}(t,t') - (\epsilon_l - i\eta)\, g_{ll}^{\rm L}(t,t') = \delta(t-t'), \tag{26}$$

$$i\hbar\frac{d}{dt}g_{rr}^{\rm R}(t,t') - (\epsilon_r - i\eta)\, g_{rr}^{\rm R}(t,t') = \delta(t-t'). \tag{27}$$

The solutions of Eqs. (26) and (27) are expressed as

$$g_{ll}^{\rm L}(t,t') = \frac{1}{i\hbar}\Theta(t-t')\exp\left[-i\frac{(\epsilon_l - i\eta)}{\hbar}\left(t-t'\right)\right], \tag{28}$$

$$g_{rr}^{\rm R}(t,t') = \frac{1}{i\hbar}\Theta(t-t')\exp\left[-i\frac{(\epsilon_r - i\eta)}{\hbar}\left(t-t'\right)\right]. \tag{29}$$

where $\Theta(t-t')$ is the Heaviside function,

$$\Theta(t-t') = \begin{cases} 1\left(t-t'>0\right), \\ 0\left(t-t'<0\right), \end{cases} \tag{30}$$

and η is a positive infinitesimal such that $\eta \times \infty = \infty$. The solutions of Eqs. (23) and (24) can be written as

$$c_l(t) = C_l(t) + \sum_j \int_{-\infty}^{+\infty} dt'\, g_{ll}^{\rm L}(t,t')\tau_{jl}c_j(t'), \tag{31}$$

$$c_r(t) = C_r(t) + \sum_j \int_{-\infty}^{+\infty} dt'\, g_{rr}^{\rm R}(t,t')\tau_{jr}c_j(t'). \tag{32}$$

Here C_l and C_r denote electron annihilation operators for the isolated left and right electrode, respectively:

$$i\hbar\frac{d}{dt}C_l = \epsilon_l C_l, \tag{33}$$

$$i\hbar\frac{d}{dt}C_r = \epsilon_r C_r. \tag{34}$$

The equation for $c_i b_\alpha$ is given by

$$\begin{aligned} i\hbar\frac{d}{dt}\left(c_i b_\alpha\right) &= \left(i\hbar\frac{d}{dt}c_i\right)b_\alpha + c_i\left(i\hbar\frac{d}{dt}b_\alpha\right) \\ &= \left\{\epsilon_i c_i + \sum_l \tau_{il}c_l + \sum_r \tau_{ir}c_r + \sum_\beta \lambda_i^\beta c_i\left(b_\beta + b_\beta^\dagger\right)\right\}b_\alpha \\ &\quad + c_i\left(\hbar\omega_\alpha b_\alpha + \sum_j \lambda_j^\alpha c_j^\dagger c_j\right). \end{aligned} \tag{35}$$

Using the following relations between the field operators

$$c_i^\dagger c_j + c_j c_i^\dagger = \delta_{ij}, \tag{36}$$

$$b_\alpha b_\beta^\dagger - b_\beta^\dagger b_\alpha = \delta_{\alpha\beta}, \tag{37}$$

and replacing the products of operators by their average values (it should be noted that $\langle c_l b_\alpha\rangle = 0$ and $\langle c_r b_\alpha\rangle = 0$), we can obtain

$$i\hbar\frac{d}{dt}\left(c_i b_\alpha\right) - \left(\epsilon_i + \hbar\omega_\alpha\right)c_i b_\alpha = \sum_{j,\beta}\lambda_i^\alpha\left(\left\langle b_\beta^\dagger b_\alpha\right\rangle\left\langle c_j^\dagger c_i\right\rangle + \left\langle c_i c_j^\dagger\right\rangle\left\langle b_\alpha b_\beta^\dagger\right\rangle\right)c_j. \tag{38}$$

The Green's function for the differential operator in Eq. (38) is defined by

$$i\hbar\frac{d}{dt}g_{i\alpha}^{(+)}(t,t') - \left(\epsilon_i + \hbar\omega_\alpha - i\eta\right)g_{i\alpha}^{(+)}(t,t') = \delta(t-t'), \tag{39}$$

and

$$g_{i\alpha}^{(+)}(t,t') = \frac{1}{i\hbar}\Theta(t-t')\exp\left[-i\frac{\left(\epsilon_i + \hbar\omega_\alpha - i\eta\right)}{\hbar}\left(t-t'\right)\right]. \tag{40}$$

Using the Green's function (40), the solution of Eq. (38) is given by

$$\begin{aligned} c_i(t)b_\alpha(t) &= C_i(t)B_\alpha(t) + \int_{-\infty}^{+\infty}dt'\sum_{j,\beta}c_j(t')\lambda_j^\beta g_{i\alpha}^{(+)}(t,t')\left\{\left\langle b_\beta^\dagger(t')b_\alpha(t')\right\rangle\left\langle c_j^\dagger(t')c_i(t')\right\rangle\right. \\ &\quad \left. + \left\langle c_i(t')c_j^\dagger(t')\right\rangle\left\langle b_\alpha(t')b_\beta^\dagger(t')\right\rangle\right\}, \end{aligned} \tag{41}$$

where

$$i\hbar\frac{d}{dt}\left\{C_i(t)B_\alpha(t)\right\} = \left(\epsilon_i + \hbar\omega_\alpha\right)C_i(t)B_\alpha(t). \tag{42}$$

Since, in the lowest-order,

$$g_{i\alpha}^{(+)}(t,t') \approx \frac{1}{i\hbar}\Theta(t-t'), \tag{43}$$

and

$$g_{i\alpha}^{(+)}(t,t')c_i(t')b_\alpha(t') \approx \frac{1}{i\hbar}\Theta(t-t')c_i(t')b_\alpha(t') = \frac{1}{i\hbar}\Theta(t-t')c_i(t)b_\alpha(t), \tag{44}$$

the solution for $c_i b_\alpha$ can be written as

$$\begin{aligned} c_i(t)b_\alpha(t) &= C_i(t)B_\alpha(t) + \int_{-\infty}^{+\infty} dt' \sum_{j,\beta} c_j(t')\lambda_j^\beta \frac{1}{i\hbar}\Theta(t-t') \left\{ \left\langle b_\beta^\dagger(t')b_\alpha(t) \right\rangle \left\langle c_j^\dagger(t')c_i(t) \right\rangle \right. \\ &\quad \left. + \left\langle c_i(t)c_j^\dagger(t') \right\rangle \left\langle b_\alpha(t)b_\beta^\dagger(t') \right\rangle \right\} \qquad (45) \\ &= C_i(t)B_\alpha(t) + \frac{\hbar}{i}\int_{-\infty}^{+\infty} dt' \sum_{j,\beta} c_j(t')\lambda_j^\beta \Theta(t-t') \left\{ G_{\alpha\beta}^{\rm ab}(t,t')G_{ij}^{\rm n}(t,t') \right. \\ &\quad \left. + G_{ij}^{\rm p}(t,t')G_{\alpha\beta}^{\rm em}(t,t') \right\}, \qquad (46) \end{aligned}$$

where

$$G_{\alpha\beta}^{\rm ab}(t,t') := \frac{\left\langle b_\beta^\dagger(t')b_\alpha(t) \right\rangle}{\hbar}, \qquad (47)$$

$$G_{\alpha\beta}^{\rm em}(t,t') := \frac{\left\langle b_\alpha(t)b_\beta^\dagger(t') \right\rangle}{\hbar}, \qquad (48)$$

$$G_{ij}^{\rm p}(t,t') := \frac{\left\langle c_i(t)c_j^\dagger(t') \right\rangle}{\hbar}, \qquad (49)$$

$$G_{ij}^{\rm n}(t,t') := \frac{\left\langle c_j^\dagger(t')c_i(t) \right\rangle}{\hbar}. \qquad (50)$$

$G^{\rm n}$ and $G^{\rm p}$ are called an electron and hole correlation function, respectively. $c_i b_\alpha^\dagger$ is obtained in a similar manner:

$$\begin{aligned} c_i(t)b_\alpha^\dagger(t) &= C_i(t)B_\alpha^\dagger(t) + \int_{-\infty}^{+\infty} dt' \sum_{j,\beta} c_j(t')\lambda_j^\beta g_{i\alpha}^{(-)}(t,t') \left\{ \left\langle b_\beta(t')b_\alpha^\dagger(t') \right\rangle \left\langle c_j^\dagger(t')c_i(t') \right\rangle \right. \\ &\quad \left. + \left\langle c_i(t')c_j^\dagger(t') \right\rangle \left\langle b_\alpha^\dagger(t')b_\beta(t') \right\rangle \right\}, \qquad (51) \end{aligned}$$

where

$$i\hbar\frac{d}{dt}\left\{ C_i(t)B_\alpha^\dagger(t) \right\} = \left(\epsilon_i - \hbar\omega_\alpha\right) C_i(t)B_\alpha^\dagger(t). \qquad (52)$$

Green's function $g_{i\alpha}^{(-)}(t,t')$ is defined by

$$i\hbar\frac{d}{dt}g_{i\alpha}^{(-)}(t,t') - \left(\epsilon_i - \hbar\omega_\alpha - i\eta\right) g_{i\alpha}^{(-)}(t,t') = \delta(t-t'), \qquad (53)$$

and

$$g_{i\alpha}^{(-)}(t,t') = \frac{1}{i\hbar}\Theta(t-t')\exp\left[-i\frac{\epsilon_i - \hbar\omega_\alpha - i\eta}{\hbar}\left(t-t'\right) \right]. \qquad (54)$$

Since, in the lowest-order,

$$g_{i\alpha}^{(-)}(t,t')c_i(t')b_\alpha^\dagger(t') \approx \frac{1}{i\hbar}\Theta(t-t')c_i(t')b_\alpha^\dagger(t') = \frac{1}{i\hbar}\Theta(t-t')c_i(t)b_\alpha^\dagger(t), \qquad (55)$$

the solution can be written as

$$c_i(t)b_\alpha^\dagger(t) = C_i(t)B_\alpha^\dagger(t) + \frac{\hbar}{i}\int_{-\infty}^{+\infty} dt' \sum_{j,\beta} c_j(t')\lambda_j^\beta \Theta(t-t') \Big\{ G_{\beta\alpha}^{\rm em}(t',t)G_{ij}^{\rm n}(t,t') + G_{ij}^{\rm p}(t,t')G_{\beta\alpha}^{\rm ab}(t',t)\Big\}. \quad (56)$$

Substituting (46) and (56) into (22), we obtain the following equation for the field operator c_i:

$$i\hbar\frac{d}{dt}c_i(t) - \epsilon_i c_i(t) - \sum_j \int_{-\infty}^{+\infty} dt' \Sigma_{ij}(t,t')c_j(t') = S_i(t), \quad (57)$$

where

$$\begin{aligned}
\mathbf{\Sigma}(t,t') &:= \mathbf{\Sigma}_{\rm L}(t,t') + \mathbf{\Sigma}_{\rm R}(t,t') + \mathbf{\Sigma}_{\rm S}(t,t'), && (58)\\
\mathbf{\Sigma}_{\rm L}(t,t') &:= \tau_{\rm L}\mathbf{g}_{\rm L}\tau_{\rm L}^\dagger, && (59)\\
\mathbf{\Sigma}_{\rm R}(t,t') &:= \tau_{\rm R}\mathbf{g}_{\rm R}\tau_{\rm R}^\dagger, && (60)\\
(\mathbf{g}_{\rm L})_{ll'}(t,t') &:= \delta_{ll'}g_{ll}^{\rm L}(t,t'), && (61)\\
(\mathbf{g}_{\rm R})_{rr'}(t,t') &:= \delta_{rr'}g_{rr}^{\rm R}(t,t'), && (62)\\
\mathbf{\Sigma}_{\rm S}(t,t') &:= \frac{\hbar}{i}\Theta(t-t')\sum_{\alpha,\beta}\lambda_i^\alpha\lambda_j^\beta \Big\{ G_{\alpha\beta}^{\rm ab}(t,t')G_{ij}^{\rm n}(t,t') + G_{ij}^{\rm p}(t,t')G_{\alpha\beta}^{\rm em}(t,t') \\
&\quad + G_{\beta\alpha}^{\rm em}(t',t)G_{ij}^{\rm n}(t,t') + G_{ij}^{\rm p}(t,t')G_{\beta\alpha}^{\rm ab}(t',t)\Big\}, && (63)\\
S_i(t) &:= S_i^{\rm L}(t) + S_i^{\rm R}(t) + S_i^{\rm S}(t), && (64)\\
S_i^{\rm L}(t) &:= \sum_l \tau_{il}C_l(t), && (65)\\
S_i^{\rm R}(t) &:= \sum_r \tau_{ir}C_r(t), && (66)\\
S_i^{\rm S}(t) &:= \sum_\alpha \lambda_i^\alpha C_i(t)\left\{B_\alpha(t) + B_\alpha^\dagger(t)\right\}. && (67)
\end{aligned}$$

$\mathbf{\Sigma}_{\rm L}$, $\mathbf{\Sigma}_{\rm R}$, and $\mathbf{\Sigma}_{\rm S}$ are self-energies for the left electrode, right electrode, and vibronic couplings, respectively, and $\mathbf{\Sigma}$ is a total self-energy. $S_i^{\rm L}$, $S_i^{\rm R}$, and $S_i^{\rm S}$ are source terms which represent an excitation from the left electrode, right electrode, and vibronic couplings, respectively, and S_i is a sum of these excitations.

The Green's function for the differential operator in Eq.(57) is defined by

$$i\hbar\frac{d}{dt}G_{ik}(t,t_1) - \epsilon_i G_{ik}(t,t_1) - \sum_j \int_{-\infty}^{+\infty} dt' \Sigma_{ij}(t,t')G_{jk}(t',t_1) = \delta_{ik}\delta(t-t_1). \quad (68)$$

Using the Green's function (68), the field operator c_i is obtained as

$$c_i(t) = \sum_k \int_{-\infty}^{+\infty} dt_1 G_{ik}(t,t_1)S_k(t_1). \quad (69)$$

Assuming the electrodes are in thermal equilibrium, electron correlation function $\mathbf{g}^{\mathrm{n}}_{\mathrm{L}}(t,t^{'})$ and hole correlation function $\mathbf{g}^{\mathrm{p}}_{\mathrm{L}}(t,t^{'})$ in the isolated left contact are given by

$$\begin{aligned}\left(\mathbf{g}^{\mathrm{n}}_{\mathrm{L}}\right)_{ll'}(t,t^{'}) &:= \frac{\left\langle C^{\dagger}_{l'}(t^{'})C_{l}(t)\right\rangle}{\hbar} \\ &= \delta_{ll'}\frac{f_l}{\hbar}\exp\left[-i\frac{\epsilon_l}{\hbar}\left(t-t^{'}\right)-\frac{\eta}{\hbar}\left|t-t^{'}\right|\right], \end{aligned} \tag{70}$$

and

$$\begin{aligned}\left(\mathbf{g}^{\mathrm{p}}_{\mathrm{L}}\right)_{ll'}(t,t^{'}) &:= \left\langle C_{l}(t)C^{\dagger}_{l'}(t^{'})\right\rangle \\ &= \delta_{ll'}\frac{1-f_l}{\hbar}\exp\left[-i\frac{\epsilon_l}{\hbar}\left(t-t^{'}\right)-\frac{\eta}{\hbar}\left|t-t^{'}\right|\right], \end{aligned} \tag{71}$$

respectively, where f_l is the left Fermi distribution function:

$$f_l = \frac{1}{1+\exp\left(\frac{\epsilon_l-\mu_{\mathrm{L}}}{k_{\mathrm{B}}T}\right)}. \tag{72}$$

Here μ_{L} is the electrochemical potential of the left electrode, k_{B} the Boltzmann constant, and T temperature of the entire system. Inscattering function and outscattering functions in the left electrode are defined by

$$\begin{aligned}\left(\mathbf{\Sigma}^{\mathrm{in}}_{\mathrm{L}}\right)_{ij}(t,t^{'}) &:= \frac{\left\langle S^{\mathrm{L}\dagger}_{j}(t^{'})S^{\mathrm{L}}_{i}(t)\right\rangle}{\hbar} \\ &= \sum_{l,l'}\tau_{il}\frac{\left\langle C^{\dagger}_{l'}(t^{'})C_{l}(t)\right\rangle}{\hbar}\tau_{jl'} \\ &= \sum_{l,l'}\tau_{il}\left(\mathbf{g}^{\mathrm{n}}_{\mathrm{L}}\right)_{ll'}(t,t^{'})\tau_{jl'}, \end{aligned} \tag{73}$$

and

$$\begin{aligned}\left(\mathbf{\Sigma}^{\mathrm{out}}_{\mathrm{L}}\right)_{ij}(t,t^{'}) &:= \frac{\left\langle S^{\mathrm{L}}_{i}(t)S^{\mathrm{L}\dagger}_{j}(t^{'})\right\rangle}{\hbar} \\ &= \sum_{l,l'}\tau_{il}\frac{\left\langle C_{l}(t)C^{\dagger}_{l'}(t^{'})\right\rangle}{\hbar}\tau_{jl'} \\ &= \sum_{l,l'}\tau_{il}\left(\mathbf{g}^{\mathrm{p}}_{\mathrm{L}}\right)_{ll'}(t,t^{'})\tau_{jl'}. \end{aligned} \tag{74}$$

In the matrix notation, the inscattering function and outscattering function can be written as

$$\mathbf{\Sigma}^{\mathrm{in}}_{\mathrm{L}}(t,t^{'}) = \tau_{\mathrm{L}}\mathbf{g}^{\mathrm{n}}_{\mathrm{L}}(t,t^{'})\tau^{\dagger}_{\mathrm{L}}, \tag{75}$$

$$\mathbf{\Sigma}_{\mathrm{L}}^{\mathrm{out}}(t,t^{'}) = \tau_{\mathrm{L}}\mathbf{g}_{\mathrm{L}}^{\mathrm{p}}(t,t^{'})\tau_{\mathrm{L}}^{\dagger}. \tag{76}$$

Inscattering function and outscattering function for the right electrode are defined by

$$\mathbf{\Sigma}_{\mathrm{R}}^{\mathrm{in}}(t,t^{'}) = \tau_{\mathrm{R}}\mathbf{g}_{\mathrm{R}}^{\mathrm{n}}(t,t^{'})\tau_{\mathrm{R}}^{\dagger}, \tag{77}$$

$$\mathbf{\Sigma}_{\mathrm{R}}^{\mathrm{out}}(t,t^{'}) = \tau_{\mathrm{R}}\mathbf{g}_{\mathrm{R}}^{\mathrm{p}}(t,t^{'})\tau_{\mathrm{R}}^{\dagger}, \tag{78}$$

where

$$\begin{aligned}
\left(\mathbf{g}_{\mathrm{R}}^{\mathrm{n}}\right)_{rr^{'}}(t,t^{'}) &:= \frac{\left\langle C_{r^{'}}^{\dagger}(t^{'})C_{r}(t)\right\rangle}{\hbar} \\
&= \delta_{rr^{'}}\frac{f_r}{\hbar}\exp\left[-i\frac{\epsilon_r}{\hbar}\left(t-t^{'}\right)-\frac{\eta}{\hbar}\left|t-t^{'}\right|\right],
\end{aligned} \tag{79}$$

and

$$\begin{aligned}
\left(\mathbf{g}_{\mathrm{R}}^{\mathrm{p}}\right)_{rr^{'}}(t,t^{'}) &:= \frac{\left\langle C_{r}(t)C_{r^{'}}^{\dagger}(t^{'})\right\rangle}{\hbar} \\
&= \delta_{rr^{'}}\frac{(1-f_r)}{\hbar}\exp\left[-i\frac{\epsilon_r}{\hbar}\left(t-t^{'}\right)-\frac{\eta}{\hbar}\left|t-t^{'}\right|\right].
\end{aligned} \tag{80}$$

Inscattering function and outscattering function for the vibronic couplings are defined by

$$\left(\mathbf{\Sigma}_{\mathrm{S}}^{\mathrm{in}}\right)_{ij}(t,t^{'}) := \frac{\left\langle S_j^{\mathrm{S}\dagger}(t^{'})S_i^{\mathrm{S}}(t)\right\rangle}{\hbar}, \tag{81}$$

and

$$\left(\mathbf{\Sigma}_{\mathrm{S}}^{\mathrm{out}}\right)_{ij}(t,t^{'}) := \frac{\left\langle S_i^{\mathrm{S}}(t)S_j^{\mathrm{S}\dagger}(t^{'})\right\rangle}{\hbar}, \tag{82}$$

which yields

$$\left(\mathbf{\Sigma}_{\mathrm{S}}^{\mathrm{in}}\right)_{ij}(t,t^{'}) = \hbar\sum_{\alpha,\beta}\lambda_i^{\alpha}\lambda_j^{\beta}\left\{G_{ij}^{\mathrm{n}}(t,t^{'})g_{\alpha\beta}^{\mathrm{ab}}(t,t^{'})+G_{ij}^{\mathrm{n}}(t,t^{'})g_{\beta\alpha}^{\mathrm{em}}(t^{'},t)\right\}, \tag{83}$$

$$\left(\mathbf{\Sigma}_{\mathrm{S}}^{\mathrm{out}}\right)_{ij}(t,t^{'}) = \hbar\sum_{\alpha,\beta}\lambda_i^{\alpha}\lambda_j^{\beta}\left\{G_{ij}^{\mathrm{p}}(t,t^{'})g_{\alpha\beta}^{\mathrm{em}}(t,t^{'})+G_{ij}^{\mathrm{p}}(t,t^{'})g_{\beta\alpha}^{\mathrm{ab}}(t^{'},t)\right\}, \tag{84}$$

where

$$g_{\alpha\beta}^{\mathrm{ab}}(t,t^{'}) = \delta_{\alpha\beta}\frac{N_\alpha}{\hbar}\exp\left[-i\omega_\alpha\left(t-t^{'}\right)-\frac{\eta}{\hbar}\left|t-t^{'}\right|\right], \tag{85}$$

$$g_{\alpha\beta}^{\mathrm{em}}(t,t^{'}) = \delta_{\alpha\beta}\frac{(N_\alpha+1)}{\hbar}\exp\left[-i\omega_\alpha\left(t-t^{'}\right)-\frac{\eta}{\hbar}\left|t-t^{'}\right|\right], \tag{86}$$

and N_α is the Bose distribution function:

$$N_\alpha = \frac{1}{\exp\left(\frac{\hbar\omega_\alpha}{k_{\mathrm{B}}T}\right)-1}. \tag{87}$$

Electron correlation function in the molecule is obtained as

$$\begin{aligned} G^{\mathrm{n}}_{ij}(t,t^{'}) &= \left\langle c^{\dagger}_{j}(t^{'})c_{i}(t)\right\rangle /\hbar \\ &= \sum_{m,n}\int_{-\infty}^{+\infty}dt_{1}\int_{-\infty}^{+\infty}dt_{2}G_{im}(t,t_{1})G^{*}_{jn}(t^{'},t_{2})\left\langle S^{\dagger}_{n}(t_{2})S_{m}(t_{1})\right\rangle /\hbar. \end{aligned} \tag{88}$$

This is written in the matrix form:

$$\mathbf{G}^{\mathrm{n}}(t,t^{'}) = \int_{-\infty}^{+\infty}dt_{1}\int_{-\infty}^{+\infty}dt_{2}\mathbf{G}(t,t_{1})\mathbf{\Sigma}^{\mathrm{in}}(t_{1},t_{2})\mathbf{G}^{\dagger}(t_{2},t^{'}), \tag{89}$$

where

$$\left(\mathbf{G}^{\dagger}\right)_{nj}(t_{2},t^{'}) := G^{*}_{jn}(t^{'},t_{2}), \tag{90}$$

and

$$\left(\mathbf{\Sigma}^{\mathrm{in}}\right)_{mn}(t_{1},t_{2}) := \left\langle S^{\dagger}_{n}(t_{2})S_{m}(t_{1})\right\rangle /\hbar, \tag{91}$$

which is called a total inscattering function. The total inscattering function can be written as

$$\mathbf{\Sigma}^{\mathrm{in}}(t_{1},t_{2}) = \mathbf{\Sigma}^{\mathrm{in}}_{\mathrm{L}}(t_{1},t_{2}) + \mathbf{\Sigma}^{\mathrm{in}}_{\mathrm{R}}(t_{1},t_{2}) + \mathbf{\Sigma}^{\mathrm{in}}_{\mathrm{S}}(t_{1},t_{2}). \tag{92}$$

Hole correlation function is written as

$$\begin{aligned} G^{\mathrm{p}}_{ij}(t,t^{'}) &= \left\langle c_{i}(t)c^{\dagger}_{j}(t^{'})\right\rangle /\hbar \\ &= \sum_{m,n}\int_{-\infty}^{+\infty}dt_{1}\int_{-\infty}^{+\infty}dt_{2}G^{*}_{jn}(t,t_{1})G_{jm}(t^{'},t_{2})\left\langle S_{m}(t_{1})S^{\dagger}_{n}(t_{2})\right\rangle /\hbar, \end{aligned} \tag{93}$$

which is written in the matrix form:

$$\mathbf{G}^{\mathrm{p}}(t,t^{'}) = \int_{-\infty}^{+\infty}dt_{1}\int_{-\infty}^{+\infty}dt_{2}\mathbf{G}(t,t_{1})\mathbf{\Sigma}^{\mathrm{out}}(t_{1},t_{2})\mathbf{G}^{\dagger}(t_{2},t^{'}), \tag{94}$$

where

$$\left(\mathbf{\Sigma}^{\mathrm{out}}\right)_{mn}(t_{1},t_{2}) := \left\langle S_{m}(t_{1})S^{\dagger}_{n}(t_{2})\right\rangle /\hbar. \tag{95}$$

$\mathbf{\Sigma}^{\mathrm{out}}$ is called a total outscattering function. The total outscattering function can be written as

$$\mathbf{\Sigma}^{\mathrm{out}}(t_{1},t_{2}) = \mathbf{\Sigma}^{\mathrm{out}}_{\mathrm{L}}(t_{1},t_{2}) + \mathbf{\Sigma}^{\mathrm{out}}_{\mathrm{R}}(t_{1},t_{2}) + \mathbf{\Sigma}^{\mathrm{out}}_{\mathrm{S}}(t_{1},t_{2}). \tag{96}$$

Broadening for the left electrode is given by

$$\mathbf{\Gamma}_{\mathrm{L}}(t,t^{'}) := i\left\{\mathbf{\Sigma}_{\mathrm{L}}(t,t^{'}) - \mathbf{\Sigma}_{\mathrm{L}}{}^{\dagger}(t,t^{'})\right\}, \tag{97}$$

where

$$\left(\mathbf{\Sigma}_{\mathrm{L}}{}^{\dagger}\right)_{ij}(t,t^{'}) := \left(\mathbf{\Sigma}_{\mathrm{L}}\right)^{*}_{ji}(t^{'},t). \tag{98}$$

Noting that

$$\mathbf{g}^{\mathrm{n}}_{\mathrm{L}}(t,t^{'}) + \mathbf{g}^{\mathrm{p}}_{\mathrm{L}}(t,t^{'}) = i\left\{\mathbf{g}_{\mathrm{L}}(t,t^{'}) - \mathbf{g}_{\mathrm{L}}{}^{\dagger}(t,t^{'})\right\}, \tag{99}$$

the following equation holds:

$$\begin{aligned}\mathbf{\Sigma}^{\mathrm{in}}_{\mathrm{L}}(t,t^{'}) + \mathbf{\Sigma}^{\mathrm{out}}_{\mathrm{L}}(t,t^{'}) &= i\left\{\mathbf{\Sigma}_{\mathrm{L}}(t,t^{'}) - \mathbf{\Sigma}_{\mathrm{L}}{}^{\dagger}(t,t^{'})\right\} \\ &= \mathbf{\Gamma}_{\mathrm{L}}(t,t^{'}),\end{aligned} \tag{100}$$

$$\left(\mathbf{\Sigma}^{\mathrm{in}}_{\mathrm{L}}\right)_{ll^{'}}(t,t^{'}) = \delta_{ll^{'}} f_l \left(\mathbf{\Gamma}_{\mathrm{L}}\right)_{ll^{'}}(t,t^{'}), \tag{101}$$

$$\left(\mathbf{\Sigma}^{\mathrm{out}}_{\mathrm{L}}\right)_{ll^{'}}(t,t^{'}) = \delta_{ll^{'}} \left(1-f_l\right) \left(\mathbf{\Gamma}_{\mathrm{L}}\right)_{ll^{'}}(t,t^{'}). \tag{102}$$

With the derivation similar to that used above, we obtain the following equations:

$$\mathbf{\Sigma}^{\mathrm{in}}_{\mathrm{R}}(t,t^{'}) + \mathbf{\Sigma}^{\mathrm{out}}_{\mathrm{R}}(t,t^{'}) = \mathbf{\Gamma}_{\mathrm{R}}(t,t^{'}), \tag{103}$$

$$\left(\mathbf{\Sigma}^{\mathrm{in}}_{\mathrm{R}}\right)_{rr^{'}}(t,t^{'}) = \delta_{rr^{'}} f_r \left(\mathbf{\Gamma}_{\mathrm{R}}\right)_{rr^{'}}(t,t^{'}), \tag{104}$$

$$\left(\mathbf{\Sigma}^{\mathrm{out}}_{\mathrm{R}}\right)_{rr^{'}}(t,t^{'}) = \delta_{rr^{'}} \left(1-f_r\right) \left(\mathbf{\Gamma}_{\mathrm{R}}\right)_{rr^{'}}(t,t^{'}), \tag{105}$$

where

$$\mathbf{\Gamma}_{\mathrm{R}}(t,t^{'}) = i\left\{\mathbf{\Sigma}_{\mathrm{R}}(t,t^{'}) - \mathbf{\Sigma}_{\mathrm{R}}{}^{\dagger}(t,t^{'})\right\}. \tag{106}$$

Broadening function for the vibronic couplings is defined by

$$\mathbf{\Gamma}_{\mathrm{S}}(t,t^{'}) := i\left(\mathbf{\Sigma}_{\mathrm{S}}(t,t^{'}) - \mathbf{\Sigma}^{\dagger}_{\mathrm{S}}(t,t^{'})\right). \tag{107}$$

Comparing the sum of (83) and (84) with (107),

$$\mathbf{\Gamma}_{\mathrm{S}}(t,t^{'}) = \mathbf{\Sigma}^{\mathrm{in}}_{\mathrm{S}}(t,t^{'}) + \mathbf{\Sigma}^{\mathrm{out}}_{\mathrm{S}}(t,t^{'}). \tag{108}$$

Two-time current is defined by

$$\begin{aligned} j(t,t^{'}) &= \sum_i \left(\frac{d}{dt} + \frac{d}{dt^{'}}\right)\left\langle c^{\dagger}_i(t^{'}) c_i(t)\right\rangle \\ &= \frac{1}{i\hbar}\mathrm{Tr}\left[\int_{-\infty}^{+\infty} dt_1 \left\{\mathbf{\Sigma}^{\mathrm{in}}(t,t_1)\mathbf{G}^{\dagger}(t_1,t^{'}) - \mathbf{G}(t,t_1)\mathbf{\Sigma}^{\mathrm{in}}(t_1,t^{'})\right.\right. \\ &\quad \left.\left. + \mathbf{\Sigma}(t,t_1)\mathbf{G}^{\mathrm{n}}(t_1,t^{'}) - \mathbf{G}^{\mathrm{n}}(t,t_1)\mathbf{\Sigma}^{\dagger}(t_1,t^{'})\right\}\right]. \end{aligned} \tag{109}$$

The right-hand side of Eq. (109) is the sum of the following three terms: $j(t,t^{'}) = j_{\rm L}(t,t^{'}) + j_{\rm R}(t,t^{'}) + j_{\rm S}(t,t^{'})$, where $j_{\rm L}$, $j_{\rm R}$, and $j_{\rm S}$ are defined by

$$\begin{aligned} j_{\rm L}(t,t^{'}) &= \frac{1}{i\hbar}{\rm Tr}\left[\int_{-\infty}^{+\infty} dt_1 \left\{ \mathbf{\Sigma}_{\rm L}^{\rm in}(t,t_1)\mathbf{G}^{\dagger}(t_1,t^{'}) - \mathbf{G}(t,t_1)\mathbf{\Sigma}_{\rm L}^{\rm in}(t_1,t^{'}) \right.\right. \\ &\left.\left. + \mathbf{\Sigma}_{\rm L}(t,t_1)\mathbf{G}^{\rm n}(t_1,t^{'}) - \mathbf{G}^{\rm n}(t,t_1){\mathbf{\Sigma}_{\rm L}}^{\dagger}(t_1,t^{'}) \right\}\right], \end{aligned} \tag{110}$$

$$\begin{aligned} j_{\rm R}(t,t^{'}) &= \frac{1}{i\hbar}{\rm Tr}\left[\int_{-\infty}^{+\infty} dt_1 \left\{ \mathbf{\Sigma}_{\rm R}^{\rm in}(t,t_1)\mathbf{G}^{\dagger}(t_1,t^{'}) - \mathbf{G}(t,t_1)\mathbf{\Sigma}_{\rm R}^{\rm in}(t_1,t^{'}) \right.\right. \\ &\left.\left. + \mathbf{\Sigma}_{\rm R}(t,t_1)\mathbf{G}^{\rm n}(t_1,t^{'}) - \mathbf{G}^{\rm n}(t,t_1){\mathbf{\Sigma}_{\rm R}}^{\dagger}(t_1,t^{'}) \right\}\right], \end{aligned} \tag{111}$$

$$\begin{aligned} j_{\rm S}(t,t^{'}) &= \frac{1}{i\hbar}{\rm Tr}\left[\int_{-\infty}^{+\infty} dt_1 \left\{ \mathbf{\Sigma}_{\rm S}^{\rm in}(t,t_1)\mathbf{G}^{\dagger}(t_1,t^{'}) - \mathbf{G}(t,t_1)\mathbf{\Sigma}_{\rm S}^{\rm in}(t_1,t^{'}) \right.\right. \\ &\left.\left. + \mathbf{\Sigma}_{\rm S}(t,t_1)\mathbf{G}^{\rm n}(t_1,t^{'}) - \mathbf{G}^{\rm n}(t,t_1){\mathbf{\Sigma}_{\rm S}}^{\dagger}(t_1,t^{'}) \right\}\right]. \end{aligned} \tag{112}$$

$j_{\rm L}$ and $j_{\rm R}$ represent the number of electrons entering into the molecule from the left and right electrodes per unit time, respectively. $j_{\rm S}$ represents the number of electrons that interact with the molecular vibrations per unit time. The current through the molecule is calculated from $j_{\rm L}$ or $j_{\rm R}$. Under the steady-state condition, all quantities depend only on the time difference between the two time variables. Thus, they can be Fourier transformed with respect to the time difference τ,

$$F(E) = \int_{-\infty}^{+\infty} d\tau \exp\left(i\frac{E}{\hbar}\tau\right) f(t, t-\tau). \tag{113}$$

From Eqs.(58) - (60),

$$\mathbf{\Sigma}(E) = \mathbf{\Sigma}_{\rm L}(E) + \mathbf{\Sigma}_{\rm R}(E) + \mathbf{\Sigma}_{\rm S}(E), \tag{114}$$

$$\mathbf{\Sigma}_{\rm L}(E) = \tau_{\rm L}\mathbf{g}_{\rm L}(E)\tau_{\rm L}^{\dagger}, \tag{115}$$

$$\mathbf{\Sigma}_{\rm R}(E) = \tau_{\rm R}\mathbf{g}_{\rm R}(E)\tau_{\rm R}^{\dagger}. \tag{116}$$

We adopt a surface Green's function of the electrode as $\mathbf{g}_{\rm L(R)}(E)$. The surface property of the electrodes are represented by $\mathbf{g}_{\rm L}(E)$ and $\mathbf{g}_{\rm R}(E)$. $\mathbf{\Sigma}_{\rm L}(E)$ and $\mathbf{\Sigma}_{\rm R}(E)$ incorporate the interaction of the molecule and the electrodes. From Eq.(97) and Eq.(106), the corresponding broadening matrices are given by

$$\mathbf{\Gamma}_{\rm L}(E) = i\left\{\mathbf{\Sigma}_{\rm L}(E) - \mathbf{\Sigma}_{\rm L}^{\dagger}(E)\right\}, \tag{117}$$

$$\mathbf{\Gamma}_{\rm R}(E) = i\left\{\mathbf{\Sigma}_{\rm R}(E) - \mathbf{\Sigma}_{\rm R}^{\dagger}(E)\right\}. \tag{118}$$

From Eqs.(101), (102), (104), and (105), the inscattering function and outscattering function in the electrodes are obtained as

$$\begin{aligned}
\mathbf{\Sigma}_{\mathrm{L}}^{\mathrm{in}}(E) &= f_{\mathrm{L}}(E)\,\mathbf{\Gamma}_{\mathrm{L}}(E), && (119)\\
\mathbf{\Sigma}_{\mathrm{L}}^{\mathrm{out}}(E) &= (1-f_{\mathrm{L}}(E))\,\mathbf{\Gamma}_{\mathrm{L}}(E), && (120)\\
\mathbf{\Sigma}_{\mathrm{R}}^{\mathrm{in}}(E) &= f_{\mathrm{R}}(E)\,\mathbf{\Gamma}_{\mathrm{R}}(E), && (121)\\
\mathbf{\Sigma}_{\mathrm{R}}^{\mathrm{out}}(E) &= (1-f_{\mathrm{R}}(E))\,\mathbf{\Gamma}_{\mathrm{R}}(E), && (122)
\end{aligned}$$

where

$$f_{\mathrm{L}}(E) = \frac{1}{1+\exp\left(\frac{E-\mu_{\mathrm{L}}}{k_{\mathrm{B}}T}\right)}, \tag{123}$$

$$f_{\mathrm{R}}(E) = \frac{1}{1+\exp\left(\frac{E-\mu_{\mathrm{R}}}{k_{\mathrm{B}}T}\right)}. \tag{124}$$

Here the electrochemical potentials μ_{L} and μ_{R} are given by

$$\begin{aligned}
\mu_{\mathrm{L}} &= E_{\mathrm{F}} + \frac{eV_{\mathrm{b}}}{2}, && (125)\\
\mu_{\mathrm{R}} &= E_{\mathrm{F}} - \frac{eV_{\mathrm{b}}}{2}. && (126)
\end{aligned}$$

E_{F} is the Fermi energy of electrode, e the elementary charge, and V_{b} an applied bias voltage. From Eqs. (83) and (84), inscattering function and outscattering function for the vibronic couplings can be written by

$$\begin{aligned}
\left(\mathbf{\Sigma}_{\mathrm{S}}^{\mathrm{in}}\right)_{ij}(E) &= \sum_{\alpha}\lambda_i^{\alpha}\lambda_j^{\alpha}\left\{(N_\alpha+1)\,G_{ij}^{\mathrm{n}}(E+\hbar\omega_\alpha)+N_\alpha G_{ij}^{\mathrm{n}}(E-\hbar\omega_\alpha)\right\}, && (127)\\
\left(\mathbf{\Sigma}_{\mathrm{S}}^{\mathrm{out}}\right)_{ij}(E) &= \sum_{\alpha}\lambda_i^{\alpha}\lambda_j^{\alpha}\left\{N_\alpha G_{ij}^{\mathrm{p}}(E+\hbar\omega_\alpha)+(N_\alpha+1)\,G_{ij}^{\mathrm{p}}(E-\hbar\omega_\alpha)\right\}. && (128)
\end{aligned}$$

The product $\lambda_i^{\alpha}\lambda_j^{\alpha}$ defines a scattering strength: $D_{ij}^{\alpha}=\lambda_i^{\alpha}\lambda_j^{\alpha}$. From Eq. (108),

$$\mathbf{\Gamma}_{\mathrm{S}}(E) = \mathbf{\Sigma}_{\mathrm{S}}^{\mathrm{in}}(E) + \mathbf{\Sigma}_{\mathrm{S}}^{\mathrm{out}}(E). \tag{129}$$

Fourier transformation of Eq. (68) gives

$$\mathbf{G}(E) = \left[E\mathbf{I} - \mathbf{H}_{\mathrm{e}} - \mathbf{\Sigma}(E)\right]^{-1}, \tag{130}$$

where $\mathbf{I}$ is a unit matrix and $\mathbf{H}_{\mathrm{e}}$ is the matrix representation of $\mathcal{H}_{\mathrm{e}}$ in Eq. (14). Spectral function is defined by

$$\mathbf{A}(E) := \mathbf{G}^{\mathrm{n}}(E) + \mathbf{G}^{\mathrm{p}}(E), \tag{131}$$

which is related to the Green's function $\mathbf{G}$ as follows

$$\mathbf{A}(E) = i\left\{\mathbf{G}(E) - \mathbf{G}^{\dagger}(E)\right\}. \tag{132}$$

From Eq. (89) and (94), electron correlation function and hole correlation function can be calculated from

$$\begin{aligned} \mathbf{G}^{\mathrm{n}}(E) &= \mathbf{G}(E)\mathbf{\Sigma}^{\mathrm{in}}(E)\mathbf{G}^{\dagger}(E), & (133)\\ \mathbf{G}^{\mathrm{p}}(E) &= \mathbf{G}(E)\mathbf{\Sigma}^{\mathrm{out}}(E)\mathbf{G}^{\dagger}(E), & (134) \end{aligned}$$

where

$$\begin{aligned} \mathbf{\Sigma}^{\mathrm{in}}(E) &= \mathbf{\Sigma}^{\mathrm{in}}_{\mathrm{L}}(E) + \mathbf{\Sigma}^{\mathrm{in}}_{\mathrm{R}}(E) + \mathbf{\Sigma}^{\mathrm{in}}_{\mathrm{S}}(E), & (135)\\ \mathbf{\Sigma}^{\mathrm{out}}(E) &= \mathbf{\Sigma}^{\mathrm{out}}_{\mathrm{L}}(E) + \mathbf{\Sigma}^{\mathrm{out}}_{\mathrm{R}}(E) + \mathbf{\Sigma}^{\mathrm{out}}_{\mathrm{S}}(E). & (136) \end{aligned}$$

Using Eqs. (97), (100), (103), (106), (131), and (132) after Fourier transformation of Eqs. (110) and (111), current per spin at each contact is obtained as

$$I_{\mathrm{L(R)}} = -e\int_{-\infty}^{+\infty} dE\left\{j^{\mathrm{in}}_{\mathrm{L(R)}}(E) - j^{\mathrm{out}}_{\mathrm{L(R)}}(E)\right\}. \tag{137}$$

Here we define influx and outflux of electrons at each contact:

$$\begin{aligned} j^{\mathrm{in}}_{\mathrm{L(R)}}(E) &= \frac{1}{2\pi\hbar}\mathrm{Tr}\left[\mathbf{\Sigma}^{\mathrm{in}}_{\mathrm{L(R)}}(E)\,\mathbf{G}^{\mathrm{p}}(E)\right], & (138)\\ j^{\mathrm{out}}_{\mathrm{L(R)}}(E) &= \frac{1}{2\pi\hbar}\mathrm{Tr}\left[\mathbf{\Sigma}^{\mathrm{out}}_{\mathrm{L(R)}}(E)\,\mathbf{G}^{\mathrm{n}}(E)\right]. & (139) \end{aligned}$$

Since the inscattering function $\mathbf{\Sigma}^{\mathrm{in}}_{\mathrm{L(R)}}$ and outscattering function $\mathbf{\Sigma}^{\mathrm{out}}_{\mathrm{L(R)}}$ are independent of the vibronic couplings, an effect of the vibronic couplings on current-voltage characteristics is described through the electron correlation function $\mathbf{G}^{\mathrm{n}}$ and hole correlation function $\mathbf{G}^{\mathrm{p}}$.

The current is calculated using (137), (138), and (139). The correlation functions $\mathbf{G}^{\mathrm{n}}(E)$ and $\mathbf{G}^{\mathrm{p}}(E)$ are evaluated using a scheme shown in Fig. 7. Figure 8 shows a schematic representation of the NEGF method. The second derivative of I with respect to V_{b} gives an IET spectrum.

Since the energy current at each electrode is given by

$$e_{\mathrm{L(R)}}(E) = E\left\{j^{\mathrm{in}}_{\mathrm{L(R)}}(E) - j^{\mathrm{out}}_{\mathrm{L(R)}}(E)\right\}, \tag{140}$$

we can calculate the power loss inside the molecule from

$$P = \int_{-\infty}^{+\infty} dE\left\{e_{\mathrm{L}}(E) + e_{\mathrm{R}}(E)\right\}. \tag{141}$$

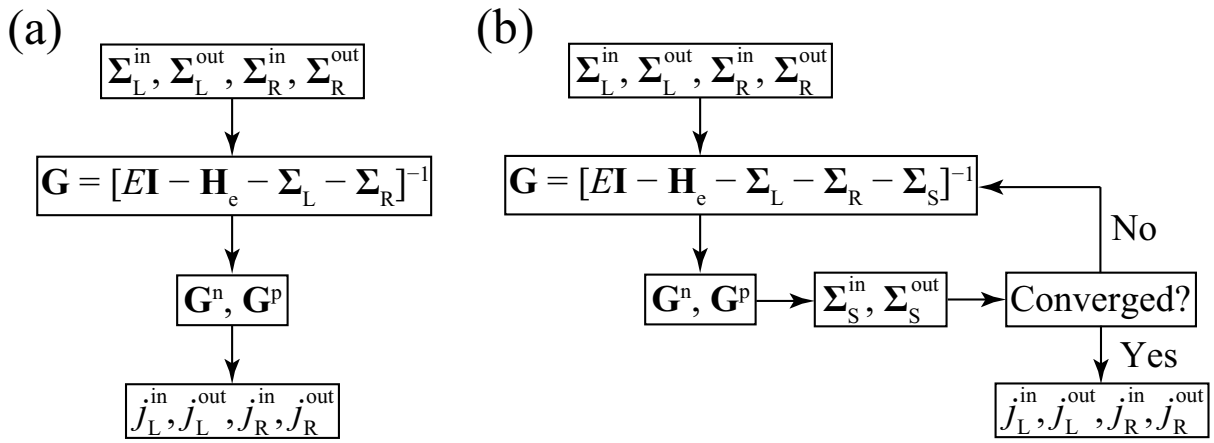

Figure 7: Calculation of correlation functions and inscattering functions (a) without an electron-phonon coupling and (b) with an electron-phonon coupling.

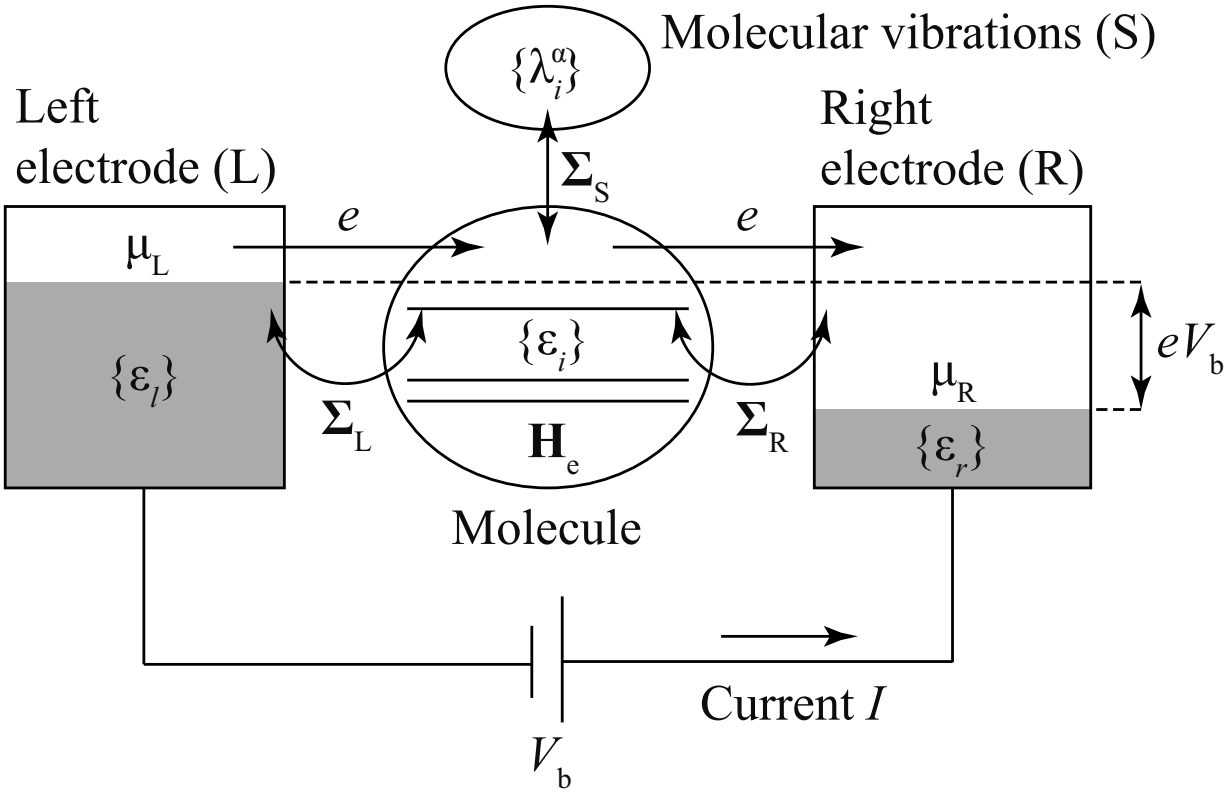

Figure 8: Schematic representation of an electrode-molecule-electrode system with vibronic couplings.

0.3 Contents of the Thesis

0.3.1 Part I

Part I deals with design of charge-transporting materials for OLEDs. We investigate effects of vibronic couplings in a charge-transport process and theoretically designs novel charge-transporting molecules for OLEDs.

In Chapter 1, VCCs in the TPD cation are calculated. The calculated constants are very small compared with other π conjugated systems such as oligothiophenes. The calculated constants are analyzed with the VCD concept. The VCD analysis clearly reveals that large contributions originate from the phenyl group and tolyl group. In addition, the hole-transport property of the electrode-TPD molecule-electrode system is investigated using the NEGF theory. Reflecting the small couplings, the current suppression and power loss are less than 1/2 compared with oligothiophenes.

In Chapter 2, to investigate the hole-transport properties of TPA and its derivatives, such as TPD, the relative order of VCCs for the TPA cation is analyzed using the VCD analysis. The VCD analysis reveals that strong localization of the electron-density difference $\Delta\rho$ in the N atoms reduces the reorganization energies for the TPA and TPD cations. For TPD, the vibronic couplings in not only central biphenyl unit but also tolyl and phenyl groups contribute to the reorganization energy.

In Chapter 3, density functional studies of the vibronic couplings in hole-transporting materials in OLEDs, carbazole, biphenyl and fluorene are investigated as well as Hartree-Fock calculations. The VCD analysis reveals that the strong localization of $\Delta\rho$ on the carbazole N atom is responsible for the small VCCs of carbazole. A heteroatom bridge such as an imino group is expected to enhance hole-transporting properties, and localized $\Delta\rho$ on the atom is expected to decrease the vibronic couplings. The difference between the density functional and Hartree-Fock calculations are discussed.

In Chapter 4, we investigate a relationship between the VCC and the extent of a distribution of $\Delta\rho$ using ethylene dimer as an example. Employing the VCD analysis, we show that the VCC is inversely proportional to the extent of the $\Delta\rho$ distribution, suggesting that we can tune the strength of vibronic coupling by controlling $\Delta\rho$ distribution. This finding opens new perspectives for designing functional materials such as charge-transporting materials.

In Chapter 5, we theoretically propose a hole-transporting molecule, hexaaza[1_6]para-biphenylophane (HAPBP) on the basis of the VCD. We calculate VCCs of HAPBP and compare them with those of other well-known hole-transporting materials, TPD, TAD, and α-NPD. HAPBP has smaller VCCs than TPD, TAD, and α-NPD. Employing the VCD analysis, we reveal the reason for the small VCCs of HAPBP. To investigate their single molecular hole-transporting properties, we calculate the current-voltage characteristics and power loss using the NEGF method taking into account inelastic scatterings due to the vibronic couplings. HAPBP, because of its small VCCs, exhibits more efficient hole-transporting properties and lower power-loss than TPD, TAD, and α-NPD. Furthermore, as a hole-transporting material, HAPBP has more suitable highest occupied and lowest unoccupied molecular orbital energies than TPD, TAD, and α-NPD when Alq_3 is employed as an emitter. HAPBP is a promising candidate for a hole-transporting material in OLEDs.

In Chapter 6, we theoretically propose a boron-containing molecule, hexaboracyclophane (HBCP), as an electron-transporting material with low power-loss. We calculate the vibronic couplings of HBCP, comparing them with those of other electron-transporting materials, Alq_3 and 3TPYMB. Using the NEGF method to evaluate their single molecular electron-transporting properties, we show that HBCP exhibits more efficient and lower-power consumption than Alq_3 and 3TPYMB. HBCP has suitable HOMO and LUMO energy levels as an electron-transport layer when Alq_3 is employed as an emitter.

In Chapter 7, the VCCs of hole-transporting molecules, 2,7-bis(phenyl-*m*-tolylamino)-fluorene (TPF) and 4,4′-di(*N*-carbazolyl)biphenyl (CBP), are estimated. Despite the planar structure of TPF, the calculated VCCs are close to those of nonplanar TPD. The origin of the vibronic couplings in TPF is investigated employing the VCD analysis. Based on a Hubbard Hamiltonian, electron-hole interactions are found to be crucial in the vibronic couplings. A large difference of on-site Coulomb interactions, or electron-hole interactions gives rise to a localization of $\Delta\rho$ on a site which can lead to small vibronic couplings.

0.3.2 Part II

Part II deals with the VCD analyses of molecular wires. In Chapter 1, the VCD analyses for the α,α'-oligothiophenes (denoted α-nT, where n stands for the number of thiophene

rings) cations are presented. We can gain a new insight for the reason why a polaronic defect of α-oligothiophenes occurs mainly in four thiophene rings for even n and at most five thiophene rings for odd n. A role of $\Delta\rho$ in the formation of polaronic defects is discussed.

In Chapter 2, we calculate the IET spectra for 2,5-dimercapto-1,3,4-thiadiazole (DMcT) and tetrathiafulvalene dithiol (TTF-DT) sandwiched between two gold electrodes using the NEGF theory. The calculated peak positions are in reasonable agreement with the experimental data. We also calculate the IET spectrum for thiophene dithiol (Th-DT) sandwiched between two gold electrodes and compare it with that for the Au/DMcT/Au junction. Th-DT and DMcT can be distinguished using the IET spectroscopy by the peak of the C−C stretching mode. The peak intensity in the IET spectra is analyzed using the VCD analysis. For the Au/DMcT/Au junction, the large distribution of $\Delta\rho$ on the C−N bond is responsible for the intense peak of the C−N stretching mode; on the other hand, for an Au/TTF-DT/Au junction, the large distribution of $\Delta\rho$ on the central C=C bond is responsible for the intense peak of the C=C stretching modes.

0.3.3 Part III

Part III deals with miscellaneous applications of the VCD analysis. In Chapter 1, reduced vibronic coupling density (RVCD) and reduced atomic vibronic coupling density (RAVCD) are introduced in order to discuss the origin of vibronic couplings in a molecule. As an example, the RVCDs and RAVCDs of the bis(ethylenedithio)tetrathiafulvalene (BEDT-TTF) cation are presented. The strongest vibronic coupling of the C=C stretching mode originates from the large $\Delta\rho$ on the C=C bond.

In Chapter 2, we calculate the VCCs and RVCDs of the free-base porphin (FBP) cation whose derivatives are employed as hole-transporting molecules in OFETs. The FBP cation has small VCCs as a π-conjugated molecule. VCD analysis reveals that strong localization of $\Delta\rho$ on the meso-carbon atoms between the cationic and neutral states leads to the small VCCs of the FBP cation.

Bibliography

[1] C. W. Tang and S. A. VanSlyke, Appl. Phys. Lett. **51**, 913 (1987).

[2] C. Adachi, S. Tokito, T. Tsutsui, and S. Saito, Jpn. J. Appl. Phys. **27**, L269 (1988).

[3] J. Kido, M. Kimura, and K. Nagai, Science **267**, 1332 (1995).

[4] C. Adachi, K. Nagai, and N. Tamoto, Appl. Phys. Lett. **66**, 2679 (1995).

[5] V. Bulović, G. Gu, P. E. Burrows, S. R. Forrest, and M. E. Thompson, Nature **380**, 29 (1996).

[6] N. Tamoto, C. Adachi, and K. Nagai, Chem. Mater. **9**, 1077 (1997).

[7] D. F. O'Brien, P. E. Burrows, S. R. Forrest, B. E. Koene, D. E. Loy, and M. E. Thompson, Adv. Mater. **10**, 1108 (1998).

[8] H. Ishii, K. Sugiyama, E. Ito, and K. Seki, Adv. Mater. **11**, 605 (1999).

[9] A. Tsumura, H. Koezuka, and T. Ando, Appl. Phys. Lett. **49**, 1210 (1986).

[10] L. Torsi, A. Dodabalapur, L. J. Rothberg, A. W. P. Fung, and H. E. Katz, Science **272**, 1462 (1996).

[11] A. Brown, C. Jarrett, D. de Leeuw, and M. Matters, Synth. Met. **88**, 37 (1997).

[12] G. Horowitz, Adv. Mater. **10**, 365 (1998).

[13] M. Muccini, Nat. Mater. **5**, 605 (2006).

[14] C. A. Mirkin and M. A. Ratner, Annu. Rev. Phys. Chem. **43**, 719 (1992).

[15] A. Nitzan, Annu. Rev. Phys. Chem. **52**, 681 (2001).

[16] J. M. Tour, Acc. Chem. Res. **33**, 791 (2000).

[17] W. Ho, J. Chem. Phys. **117**, 11033 (2002).

[18] J. R. Heath and M. A. Ratner, Phys. Today **56**, 43 (2003).

[19] R. L. McCreery, Chem. Mater. **16**, 4477 (2004).

[20] C. Joachim and M. A. Ratner, Proc. Natl. Acad. Sci. USA **102**, 8801 (2005).

[21] Y. Selzer and D. L. Allara, Annu. Rev. Phys. Chem. **57**, 593 (2006).

[22] M. Galperin, M. A. Ratner, and A. Nitzan, J. Phys.: Condensed Matter **19**, 103201 (2007).

[23] M. E. Kozlov, K. I. Pokhodnia, and A. A. Yurchenko, Spectrochim. Acta A **45**, 437 (1989).

[24] M. Lannoo, G. A. Baraff, M. Schlüter, and D. Tomanek, Phys. Rev. B **44**, 12106 (1991).

[25] C. M. Varma, J. Zaanen, and K. Raghavachari, Science **254**, 989 (1991).

[26] J. C. Faulhaber, D. Y. Ko, and P. R. Briddon, Synth. Met. **60**, 227 (1993).

[27] J. C. R. Faulhaber, D. Y. K. Ko, and P. R. Briddon, Phys. Rev. B **48**, 661 (1993).

[28] O. Gunnarsson, H. Handschuh, P. S. Bechthold, B. Kessler, G. Ganteför, and W. Eberhardt, Phys. Rev. Lett. **74**, 1875 (1995).

[29] O. Gunnarsson, Rev. Mod. Phys. **69**, 575 (1997).

[30] A. Devos and M. Lannoo, Phys. Rev. B **58**, 8236 (1998).

[31] G. Visentini, M. Masino, C. Bellitto, and A. Girlando, Phys. Rev. B **58**, 9460 (1998).

[32] M. Taniguchi, Y. Misaki, and K. Tanaka, Solid State Commun. **114**, 75 (2000).

[33] T. Kato and T. Yamabe, J. Chem. Phys. **115**, 8592 (2001).

[34] T. Kato, M. Kondo, K. Yoshizawa, and T. Yamabe, Synth. Met. **126**, 75 (2002).

[35] T. Kato, K. Yoshizawa, and K. Hirao, J. Chem. Phys. **116**, 3420 (2002).

[36] T. Kato and T. Yamabe, J. Chem. Phys. **120**, 3311 (2004).

[37] T. Kato and T. Yamabe, J. Phys. Chem. A **110**, 2785 (2006).

[38] N. E. Gruhn, D. A. da Silva Filho, T. G. Bill, M. Malagoli, V. Coropceanu, A. Kahn, and J.-L. Bredas, J. Am. Chem. Soc. **124**, 7918 (2002).

[39] V. Coropceanu, M. Malagoli, J. M. André, and J. L. Brédas, J. Chem. Phys. **115**, 10409 (2001).

[40] V. Coropceanu, M. Malagoli, D. A. da Silva Filho, N. E. Gruhn, T. G. Bill, and J.-L. Brédas, Phys. Rev. Lett. **89**, 275503 (2002).

[41] V. Coropceanu, M. Malagoli, J. M. André, and J. L. Brédas, J. Am. Chem. Soc. **124**, 10519 (2002).

[42] V. Coropceanu, J. André, M. Malagoli, and J.-L. Brédas, Theor. Chem. Acc. **110**, 59 (2003).

[43] J.-L. Brédas, D. Beljonne, V. Coropceanu, and J. Cornil, Chem. Rev. **104**, 4971 (2004).

[44] V. Coropceanu, N. Gruhn, S. Barlow, C. Lambert, J. Durivage, T. Bill, G. Nöll, S. Marder, and J.-L. Brédas, J. Am. Chem. Soc. **126**, 2727 (2004).

[45] V. Lemaur, D. A. da Silva Filho, V. Coropceanu, M. Lehmann, Y. Geerts, J. Piris, M. G. Debije, A. M. van de Craats, K. Senthilkumar, L. D. A. Siebbeles, J. M. Warman, J.-L. Bredas, and J. Cornil, J. Am. Chem. Soc. **126**, 3271 (2004).

[46] V. Coropceanu, J. Cornil, D. A. da Silva Filho, Y. Olivier, R. Silbey, and J.-L. Brédas, Chem. Rev. **107**, 926 (2007).

[47] D. A. da Silva Filho, V. Coropceanu, D. Fichou, N. E. Gruhn, T. G. Bill, J. Gierschner, J. Cornil, and J.-L. Brédas, Philos. Trans. R. Soc. London, A **365**, 1435 (2007).

[48] E.-G. Kim, V. Coropceanu, N. E. Gruhn, R. S. Sánchez-Carrera, R. Snoeberger, A. J. Matzger, and J.-L. Brédas, J. Am. Chem. Soc. **129**, 13072 (2007).

[49] V. Coropceanu, R. S. Sánchez-Carrera, P. Paramonov, G. M. Day, and J. L. Brédas, J. Phys. Chem. C **113**, 4679 (2009).

[50] K. Clark, A. Hassanien, S. Khan, K.-F. Braun, H. Tanaka, and S.-W. Hla, Nat. Nanotechnol. **5**, 261 (2010).

[51] L.-Z. Zhang, C.-W. Chen, C.-F. Lee, C.-C. Wu, and T.-Y. Luh, Chem. Commun. 2336 (2002).

[52] P. Strohriegl and J. V. Grazulevicius, Adv. Mater. **14**, 1439 (2002).

[53] M. Thelakkat, Macromol. Mater. Eng. **287**, 442 (2002).

[54] Y. Shirota, J. Mater. Chem. **15**, 75 (2005).

[55] K. Okumoto, H. Kanno, Y. Hamada, H. Takahashi, and K. Shibata, J. Appl. Phys. **100**, 044507 (2006).

[56] T. P. I. Saragi, T. Fuhrmann-Lieker, and J. Salbeck, Adv. Funct. Mater. **16**, 966 (2006).

[57] T. P. I. Saragi, T. Spehr, A. Siebert, T. Fuhrmann-Lieker, and J. Salbeck, Chem. Rev. **107**, 1011 (2007).

[58] Y. Shirota and H. Kageyama, Chem. Rev. **107**, 953 (2007).

[59] H. Tsuji, C. Mitsui, L. Ilies, Y. Sato, and E. Nakamura, J. Am. Chem. Soc. **129**, 11902 (2007).

[60] M. Stolka, J. F. Yanus, and D. M. Pai, J. Phys. Chem. **88**, 4707 (1984).

[61] J. Kido, C. Ohtaki, K. Hongawa, K. Okuyama, and K. Nagai, Jpn. J. Appl. Phys. **32**, L917 (1993).

[62] Y. Qiu and J. Qiao, Thin Solid Films **372**, 265 (2000).

[63] S. A. VanSlyke, C. H. Chen, and C. W. Tang, Appl. Phys. Lett. **69**, 2160 (1996).

[64] C. W. Tang, S. A. VanSlyke, and C. H. Chen, J. Appl. Phys. **65**, 3610 (1989).

[65] S. Naka, H. Okada, H. Onnagawa, Y. Yamaguchi, and T. Tsutsui, Synth. Met. **111-112**, 331 (2000).

[66] K. Tamao, M. Uchida, T. Izumizawa, K. Furukawa, and S. Yamaguchi, J. Am. Chem. Soc. **118**, 11974 (1996).

[67] H. Murata, G. G. Malliaras, M. Uchida, Y. Shen, and Z. H. Kafafi, Chem. Phys. Lett. **339**, 161 (2001).

[68] M. Uchida, T. Izumizawa, T. Nakano, S. Yamaguchi, K. Tamao, and K. Furukawa, Chem. Mater. **13**, 2680 (2001).

[69] A. J. Mäkinen, M. Uchida, and Z. H. Kafafi, Appl. Phys. Lett. **82**, 3889 (2003).

[70] L. C. Palilis, A. J. Mäkinen, M. Uchida, and Z. H. Kafafi, Appl. Phys. Lett. **82**, 2209 (2003).

[71] C. Risko, G. P. Kushto, Z. H. Kafati, and J. L. Brédas, J. Chem. Phys. **121**, 9031 (2004).

[72] J. Kido and T. Matsumoto, Appl. Phys. Lett. **73**, 2866 (1998).

[73] S. Naka, H. Okada, H. Onnagawa, and T. Tsutsui, Appl. Phys. Lett. **76**, 197 (2000).

[74] J. Huang, M. Pfeiffer, A. Werner, J. Blochwitz, K. Leo, and S. Liu, Appl. Phys. Lett. **80**, 139 (2002).

[75] X. Zhou, M. Pfeiffer, J. S. Huang, J. Blochwitz-Nimoth, D. S. Qin, A. Werner, J. Drechsel, B. Maennig, and K. Leo, Appl. Phys. Lett. **81**, 922 (2002).

[76] Y. Kijima, N. Asai, and S. ichiro Tamura, Jpn. J. Appl. Phys. **38**, 5274 (1999).

[77] D. F. O'Brien, M. A. Baldo, M. E. Thompson, and S. R. Forrest, Appl. Phys. Lett. **74**, 442 (1999).

[78] T. Yasuda, Y. Yamaguchi, D.-C. Zou, and T. Tsutsui, Jpn. J. Appl. Phys. **41**, 5626 (2002).

[79] C. Adachi, T. Tsutsui, and S. Saito, Appl. Phys. Lett. **55**, 1489 (1989).

[80] C. Adachi, T. Tsutsui, and S. Saito, Appl. Phys. Lett. **56**, 799 (1990).

[81] C. Adachi, T. Tsutsui, and S. Saito, Appl. Phys. Lett. **57**, 531 (1990).

[82] M. Era, C. Adachi, T. Tsutsui, and S. Saito, Chem. Phys. Lett. **178**, 488 (1991).

[83] J. Kido, K. Nagai, Y. Okamoto, and T. Skotheim, Chem. Lett. **20**, 1267 (1991).

[84] Y. Hamada, C. Adachi, T. Tsutsui, and S. Saito, Jpn. J. Appl. Phys. **31**, 1812 (1992).

[85] H. Tokuhisa, M. Era, T. Tsutsui, and S. Saito, Appl. Phys. Lett. **66**, 3433 (1995).

[86] J. Bettenhausen and P. Strohriegl, Adv. Mater. **8**, 507 (1996).

[87] J. Bettenhausen, P. Strohriegl, W. Brütting, H. Tokuhisa, and T. Tsutsui, J. Appl. Phys. **82**, 4957 (1997).

[88] Y. Kawabe and J. Abe, Appl. Phys. Lett. **81**, 493 (2002).

[89] T. Noda and Y. Shirota, J. Am. Chem. Soc. **120**, 9714 (1998).

[90] S. Yamaguchi, S. Akiyama, and K. Tamao, J. Am. Chem. Soc. **122**, 6335 (2000).

[91] Q. Wu, M. Esteghamatian, N.-X. Hu, Z. Popovic, G. Enright, Y. Tao, M. D'Iorio, and S. Wang, Chem. Mater. **12**, 79 (2000).

[92] M. Kinoshita and Y. Shirota, Chem. Lett. **30**, 614 (2001).

[93] M. Kinoshita, H. Kita, and Y. Shirota, Adv. Funct. Mater. **12**, 780 (2002).

[94] D. Tanaka, T. Takeda, T. Chiba, S. Watanabe, and J. Kido, Chem. Lett. **36**, 262 (2007).

[95] N. Chopra, J. Lee, Y. Zheng, S.-H. Eom, J. Xue, and F. So, Appl. Mater. Interfaces **1**, 1169 (2009).

[96] R. Madru, G. Guillaud, M. A. Sadoun, M. Maitrot, J. J. Andr , J. Simon, and R. Even, Chem. Phys. Lett. **145**, 343 (1988).

[97] Z. Bao, A. J. Lovinger, and A. Dodabalapur, Appl. Phys. Lett. **69**, 3066 (1996).

[98] Z. Bao, Y. Feng, A. Dodabalapur, V. R. Raju, and A. J. Lovinger, Chem. Mater. **9**, 1299 (1997).

[99] Z. Bao, A. J. Lovinger, and J. Brown, J. Am. Chem. Soc. **120**, 207 (1998).

[100] H. Tada, H. Touda, M. Takada, and K. Matsushige, Appl. Phys. Lett. **76**, 873 (2000).

[101] M. Kitamura, T. Imada, S. Kako, and Y. Arakawa, Jpn. J. Appl. Phys. **43**, 2326 (2004).

[102] H. Ohta, T. Kambayashi, K. Nomura, M. Hirano, K. Ishikawa, H. Takezoe, and H. Hosono, Adv. Mater. **16**, 312 (2004).

[103] R. W. I. de Boer, A. F. Stassen, M. F. Craciun, C. L. Mulder, A. Molinari, S. Rogge, and A. F. Morpurgo, Appl. Phys. Lett. **86**, 262109 (2005).

[104] D. G. de Oteyza, E. Barrena, J. O. Ossó, H. Dosch, S. Meyer, and J. Pflaum, Appl. Phys. Lett. **87**, 183504 (2005).

[105] R. Zeis, T. Siegrist, and C. Kloc, Appl. Phys. Lett. **86**, 022103 (2005).

[106] P. G. Schouten, J. M. Warman, M. P. de Haas, M. A. Fox, and H. L. Pan, Nature **353**, 736 (1991).

[107] Y.-Y. Noh, J.-J. Kim, Y. Yoshida, and K. Yase, Adv. Mater. **15**, 699 (2003).

[108] P. Checcoli, G. Conte, S. Salvatori, R. Paolesse, A. Bolognesi, M. Berliocchi, F. Brunetti, A. D'Amico, A. D. Carlo, and P. Lugli, Synth. Met. **138**, 261 (2003).

[109] S. Aramaki, Y. Sakai, and N. Ono, Appl. Phys. Lett. **84**, 2085 (2004).

[110] P. B. Shea, J. Kanicki, and N. Ono, J. Appl. Phys. **98**, 014503 (2005).

[111] P. B. Shea, A. R. Johnson, N. Ono, and J. Kanicki, IEEE Trans. Electron Dev. **52**, 1497 (2005).

[112] P. B. Shea, J. Kanicki, L. R. Pattison, P. Petroff, M. Kawano, H. Yamada, and N. Ono, J. Appl. Phys. **100**, 034502 (2006).

[113] P. B. Shea, C. Chen, J. Kanicki, L. R. Pattison, P. Petroff, H. Yamada, and N. Ono, Appl. Phys. Lett. **90**, 233107 (2007).

[114] P. B. Shea, L. R. Pattison, M. Kawano, C. Chen, J. Chen, P. Petroff, D. C. Martin, H. Yamada, N. Ono, and J. Kanicki, Synth. Met. **157**, 190 (2007).

[115] T. Minari, M. Seto, T. Nemoto, S. Isoda, K. Tsukagoshi, and Y. Aoyagi, Appl. Phys. Lett. **91**, 123501 (2007).

[116] A. S. Dhoot, S. Aramaki, D. Moses, and A. J. Heeger, Adv. Mater. **19**, 2914 (2007).

[117] C.-M. Che, H.-F. Xiang, S. S.-Y. Chui, Z.-X. Xu, V. A. L. Roy, J. J. Yan, W.-F. Fu, P. T. Lai, and I. D. Williams, Chem. Asian J. **3**, 1092 (2008).

[118] P. Ma, Y. Chen, X. Cai, H. Wang, Y. Zhang, Y. Gao, and J. Jiang, Synth. Met. **160**, 510 (2010).

[119] D. Fichou, J. Mater. Chem. **10**, 571 (2000).

[120] G. Horowitz, D. Fichou, and F. Garnier, Solid State Commun. **70**, 385 (1989).

[121] X. Peng, G. Horowitz, D. Fichou, and F. Garnier, Appl. Phys. Lett. **57**, 2013 (1990).

[122] H. Akimichi, K. Waragai, S. Hotta, H. Kano, and H. Sakaki, Appl. Phys. Lett. **58**, 1500 (1991).

[123] F. Garnier, A. Yassar, R. Hajlaoui, G. Horowitz, F. Deloffre, B. Servet, S. Ries, and P. Alnot, J. Am. Chem. Soc. **115**, 8716 (1993).

[124] B. Servet, G. Horowitz, S. Ries, O. Lagorsse, P. Alnot, A. Yassar, F. Deloffre, P. Srivastava, R. Hajlaoui, P. Lang, and F. Garnier, Chem. Mater. **6**, 1809 (1994).

[125] G. Horowitz, F. Garnier, A. Yassar, R. Hajlaoui, and F. Kouki, Adv. Mater. **8**, 52 (1996).

[126] R. Hajlaoui, G. Horowitz, F. Garnier, A. Arce-Brouchet, L. Laigre, A. E. Kassmi, F. Demanze, and F. Kouki, Adv. Mater. **9**, 387 (1997).

[127] R. Hajlaoui, D. Fichou, G. Horowitz, B. Nessakh, M. Constant, and F. Garnier, Adv. Mater. **9**, 557 (1997).

[128] H. E. Katz, J. Mater. Chem. **7**, 369 (1997).

[129] F. Garnier, G. Horowitz, D. Fichou, and A. Yassar, Supramol. Sci. **4**, 155 (1997).

[130] H. E. Katz, A. J. Lovinger, and J. G. Laquindanum, Chem. Mater. **10**, 457 (1998).

[131] G. Horowitz, R. Hajlaoui, and F. Kouki, Eur. Phys. J. Appl. Phys. **1**, 361 (1998).

[132] G. Horowitz and M. E. Hajlaoui, Adv. Mater. **12**, 1046 (2000).

[133] G. Horowitz, D. Fichou, X. Peng, Z. Xu, and F. Garnier, Solid State Commun. **72**, 381 (1989).

[134] O. D. Jurchescu, J. Baas, and T. T. M. Palstra, Appl. Phys. Lett. **84**, 3061 (2004).

[135] V. Podzorov, E. Menard, A. Borissov, V. Kiryukhin, J. A. Rogers, and M. E. Gershenson, Phys. Rev. Lett. **93**, 086602 (2004).

[136] R. A. Marcus, J. Electroanal. Chem. **483**, 2 (2000).

[137] R. A. Marcus, J. Electroanal. Chem. **438**, 251 (1997).

[138] R. A. Marcus and N. Sutin, Biochim. Biophys. Acta **811**, 265 (1985).

[139] R. A. Marcus, J. Chem. Phys. **43**, 679 (1965).

[140] R. A. Marcus, J. Chem. Phys. **24**, 966 (1956).

[141] P. F. Barbara, T. J. Meyer, and M. A. Ratner, J. Phys. Chem. **100**, 13148 (1996).

[142] S. Datta, *Quantum Transport: Atom to Transistor* (Cambridge University Press, Cambridge, 2005).

[143] W. P. Su, J. R. Schrieffer, and A. J. Heeger, Phys. Rev. Lett. **42**, 1698 (1979).

[144] W. P. Su, J. R. Schrieffer, and A. J. Heeger, Phys. Rev. B **22**, 2099 (1980).

[145] W. P. Su and J. R. Schrieffer, Proc. Natl. Acad. Sci. U.S.A. **77**, 5626 (1980).

[146] R. C. Jaklevic and J. Lambe, Phys. Rev. Lett. **17**, 1139 (1966).

[147] J. Kirtley, D. J. Scalapino, and P. K. Hansma, Phys. Rev. B **14**, 3177 (1976).

[148] S. Gregory, Phys. Rev. Lett. **64**, 689 (1990).

[149] B. C. Stipe, M. A. Rezaei, and W. Ho, Rev. Sci. Instrum. **70**, 137 (1999).

[150] J. Gaudioso, L. J. Lauhon, and W. Ho, Phys. Rev. Lett. **85**, 1918 (2000).

[151] R. H. M. Smit, Y. Noat, C. Untiedt, N. D. Lang, M. C. van Hemert, and J. M. van Ruitenbeek, Nature **419**, 906 (2002).

[152] A. Troisi, M. A. Ratner, and A. Nitzan, J. Chem. Phys. **118**, 6072 (2003).

[153] W. Wang, T. Lee, I. Kretzschmar, and M. A. Reed, Nano Lett. **4**, 643 (2004).

[154] J. G. Kushmerick, J. Lazorcik, C. H. Patterson, R. Shashidhar, D. S. Seferos, and G. C. Bazan, Nano Lett. **4**, 639 (2004).

[155] R. Jorn and T. Seideman, J. Chem. Phys. **124**, 084703 (2006).

[156] J. G. Kushmerick, A. S. Blum, and D. P. Long, Anal. Chim. Acta **568**, 20 (2006).

[157] D. P. Long, J. L. Lazorcik, rent A. Mantooth, M. H. Moore, M. A. Ratner, A. Troisi, Y. Yao, J. W. Ciszek, J. M. Tour, and R. Shashidhar, Nat. Mater. **5**, 901 (2006).

[158] A. Troisi and M. A. Ratner, Phys. Rev. B **72**, 033408 (2005).

[159] A. Troisi and M. A. Ratner, Small **2**, 172 (2006).

[160] A. Troisi and M. A. Ratner, Nano Lett. **6**, 1784 (2006).

[161] A. Troisi and M. A. Ratner, J. Chem. Phys. **125**, 214709 (2006).

[162] J. M. Beebe, H. J. Moore, T. R. Lee, and J. G. Kushmerick, Nano Lett. **7**, 1364 (2007).

[163] A. Troisi and M. A. Ratner, Phys. Chem. Chem. Phys. **9**, 2421 (2007).

[164] A. Troisi, J. Phys.: Condens. Matter **20**, 374111 (2008).

[165] M. Tsutsui, M. Taniguchi, K. Shoji, K. Yokota, and T. Kawai, Nanoscale **1**, 164 (2009).

[166] N. Okabayashi, Y. Konda, and T. Komeda, Phys. Rev. Lett. **100**, 217801 (2008).

[167] N. Okabayashi, M. Paulsson, H. Ueba, Y. Konda, and T. Komeda, Phys. Rev. Lett. **104**, 077801 (2010).

[168] T. Sato, K. Tokunaga, and K. Tanaka, J. Chem. Phys. **124**, 024314 (2006).

[169] K. Tokunaga, T. Sato, and K. Tanaka, J. Chem. Phys. **124**, 154303 (2006).

[170] K. Tokunaga, T. Sato, and K. Tanaka, J. Mol. Struct. **838**, 116 (2007).

[171] T. Sato, K. Tokunaga, N. Iwahara, K. Shizu, and K. Tanaka, *Vibronic coupling constant and vibronic coupling density* in *The Jahn-Teller-Effect - Fundamentals and Implications for Physics and Chemistry,* H. Köppel, D. R. Yarkony, and H. Barentzen (Eds) (Springer-Verlag, Berlin and Heidelberg, 2009).

Part I

Design of Charge-Transporting Materials in Organic Light-Emitting Diodes

Chapter 1

Electron-Vibration Interactions in Carrier-Transport Material: Vibronic Coupling Density Analysis in TPD

1.1 Introduction

Hole-transport materials have been investigated as a component of multi-layer structures in organic light-emitting devices (OLED).[1–8] Aromatic amines have been employed as hole-transport materials with a high carrier mobility.[9–13] N,N'-diphenyl-N,N'-di(m-tolyl)benzidine (TPD, Fig. 1.1(a)) is one of the hole-transport materials employed in the OLED.[2,4,5,8] In 1984, Stolka *et al.* have reported that TPD/polycarbonate solid solutions have a high carrier mobility.[9] Kaji *et al.* have observed ^{15}N NMR spectra, and compared with their density functional calculations.[13] They have found that a TPD molecule in the amorphous phase is similar in geometry to the free molecule.

A high carrier mobility and a low power loss are required in the development of carrier transport materials in OLED. A mobility measurement on TPD has revealed that the hole transport in this material can be described by the simple disorder-controlled hopping model without a polaron formation.[10] Sakanoue *et al.* have obtained the small reorganization energy of an aromatic amine, triphenyl amine (TPA), based on the Marcus theory employing theoretical calculations.[12]

One of the important factors determining these properties is a vibronic coupling, or electron-vibration interaction. Small vibronic couplings in a molecule should result in a high mobility, a small reorganization energy,[12,14] and a low power loss, in other words, a low heat dissipation. It is one of the necessary conditions for hole-transport materials that a molecule has small intramolecular vibronic couplings. To design efficient hole-transport materials in a molecular level, we should elucidate the reason why aromatic amines such as TPD have small vibronic coupling constants (VCC). Sato *et al.* have proposed a new method of the calculation for VCC and a concept of vibronic coupling density (VCD) which enables us to analyze the calculated result on the basis of the electronic and vibrational structures.[15–18]

Recently theoretical calculations of carrier transport through a single molecule including the electron-molecular vibration interaction have been reported based on the non-equilibrium Green's function (NEGF) theory.[19]

In this chapter, we address the reason of the small couplings in TPD employing the VCD analysis and calculate a current suppression through a single TPD molecule due to the vibronic coupling based on the NEGF theory.

1.2 Method of calculation

The electronic and vibrational structures were calculated using GAMESS.[20] We adopted the calculation method for the VCC and VCD described in Ref. 18. The optimized structure $\mathbf{R}_0$ and vibrational structure of the neutral molecule were calculated using restricted Hartree-Fock (RHF) method with 6-31G basis set including the first derivatives which ensure the Hellmann-Feynman theorem applicable in the calculation. Vibronic coupling constants V_i of the vibrational mode i were calculated from vibronic integrals:

$$V_i = \left\langle \Phi_{N-1}(\mathbf{r}, \mathbf{R}_0) \left| \left(\frac{\partial U}{\partial Q_i} \right)_{\mathbf{R}_0} \right| \Phi_{N-1}(\mathbf{r}, \mathbf{R}_0) \right\rangle, \tag{1.1}$$

where Φ_{N-1} is a restricted open Hartree-Fock (ROHF) wavefunction of the ionized state with $N-1$ electrons at the equilibrium configuration $\mathbf{R}_0$ of the neutral molecule, Q_i normal coordinate, U potential, and

$$\left(\frac{\partial U}{\partial Q_i} \right)_{\mathbf{R}_0}$$

is the electronic part of the vibronic coupling operator:

$$\left(\frac{\partial U}{\partial Q_i}\right)_{\mathbf{R}_0} Q_i$$

appearing in the Hertzberg-Teller expansion.[21] In the present calculation, orbitals should have a correct symmetry. The ROHF method is appropriate since unrestricted methods such as UHF and UB3LYP yield orbitals with a broken symmetry.[15]

Vibronic coupling density $\eta_i(\mathbf{x})$ is defined by

$$\eta_i(\mathbf{x}) = \Delta\rho(\mathbf{x})\, v_i(\mathbf{x}), \tag{1.2}$$

where $\Delta\rho(\mathbf{x})$ is an electron density difference between the neutral and ionized state

$$\Delta\rho(\mathbf{x}) = \rho_+(\mathbf{x}) - \rho_0(\mathbf{x}), \tag{1.3}$$

and $\mathbf{x} = (x, y, z)$. For comparison, frozen density difference is defined using the HOMO ψ_{HOMO} of the neutral molecule by

$$\Delta\rho_{\mathrm{F}}(\mathbf{x}) = -\psi^*_{\mathrm{HOMO}}(\mathbf{x})\psi_{\mathrm{HOMO}}(\mathbf{x}). \tag{1.4}$$

The density difference defined in Eq. (1.3) is called relaxed density difference $\Delta\rho_R$. $v_i(\mathbf{x})$ denotes a potential derivative with respect to a normal coordinate Q_i:

$$v_i(\mathbf{x}) = \sum_\mu \left[\frac{\partial}{\partial Q_i}\frac{Z_\mu}{|\mathbf{x} - \mathbf{X}_\mu|}\right]_{\mathbf{R}_0}, \tag{1.5}$$

where $\mathbf{X}_\mu = (X_\mu, Y_\mu, Z_\mu)$ denotes the Cartesian coordinate of nucleus μ. Note that v_i is a one-electron operator. The vibronic coupling density gives a local map of the interaction, since the integration of $\eta_i(\mathbf{x})$ over the whole space yields the vibronic coupling constant V_i:

$$V_i = \int \eta_i(\mathbf{x}) d\mathbf{x}. \tag{1.6}$$

Orbital vibronic coupling constant of molecular orbital k for vibrational mode i is defined by

$$\beta_{ik} = \langle \psi_k(\mathbf{x}) | v_i(\mathbf{x}) | \psi_k(\mathbf{x}) \rangle \,. \tag{1.7}$$

The sum of β_{ik} over the occupied orbitals yields the electronic component of the vibronic coupling constant V_i in the Hartree-Fock approximation. Atomic vibronic coupling constant $\alpha_{i\mu}$ of atom μ for vibrational mode i is defined by

$$\alpha_{i\mu} = \left(\sum_{k\in\mathrm{occ}} \left\langle \psi_k(\mathbf{x}) \left| \left\{ \nabla_\mu \left(-\frac{Z_\mu}{|\mathbf{x} - \mathbf{X}_\mu|} \right) \right\}_{\mathbf{R}_0} \right| \psi_k(\mathbf{x}) \right\rangle + \sum_\nu \left\{ \nabla_\mu \left(-\frac{Z_\nu Z_\mu}{|\mathbf{X}_\nu - \mathbf{X}_\mu|} \right) \right\}_{\mathbf{R}_0} \right) \cdot \frac{\mathbf{u}^i_\mu}{\sqrt{M_\mu}}, \tag{1.8}$$

where $\mathbf{u}_\mu^i$ is the μ component of a vibrational vector in mass-weighted coordinates and M_μ the mass of atom μ. Within the Hartree-Fock approximation, the sum of $\alpha_{i\mu}$ over the atoms also yields the electronic component of the vibronic coupling constant V_i. The atomic vibronic coupling constant $\alpha_{i\mu}$ indicates a contribution of the atom μ to the vibronic coupling of the mode i.

Transport properties were calculated based on Ref. 19.

1.3 Results and discussion

We obtained a C_2 structure as an optimized structure, and performed vibrational analysis for the C_2 structure to confirm that it is a minimum. Since the electronic structure has no degeneracy, only the a_g vibrational modes have a non-zero vibronic coupling. Couplings of b_g modes are zero because of the symmetry. Figure 1.1 (b) shows the calculated vibronic coupling constant of the a_g modes. Vibrational modes with the strong coupling and their assignment are tabulated in Table 1.1. The order of the strongest one is at most of 10^{-5} a.u., which is smaller than those of typical π conjugated systems such as oligothiophenes and oligoynes by one order.[22] Relatively strong couplings occur bending modes around 735 cm^{-1} and 1326 cm^{-1}. The strongest coupling mode is depicted in Fig. 1.1 (c). We concentrate ourselves on the strongest mode shown in Fig. 1.1 (c).

Table 1.1: Vibrational modes with a strong vibronic coupling and their assignment. Frequencies are in cm^{-1} and vibronic coupling constants are in 10^{-5}a.u.

Frequency	VCC	Assignment
735	7.58	phenylene in-plane bending, phenyl in-plane bending, tolyl in-plane bending, C-N stretching
820	7.01	phenylene in-plane bending, phenyl C-H out-of-plane bending, tolyl in-plane bending
856	7.17	phenylene in-plane bending, phenyl C-H out-of-plane bending, tolyl C-H out-of-plane bending bending
1326	7.45	phenylene ring stretching, phenyl C-H in-plane bending, tolyl C-H in-plane bending, C-N stretching

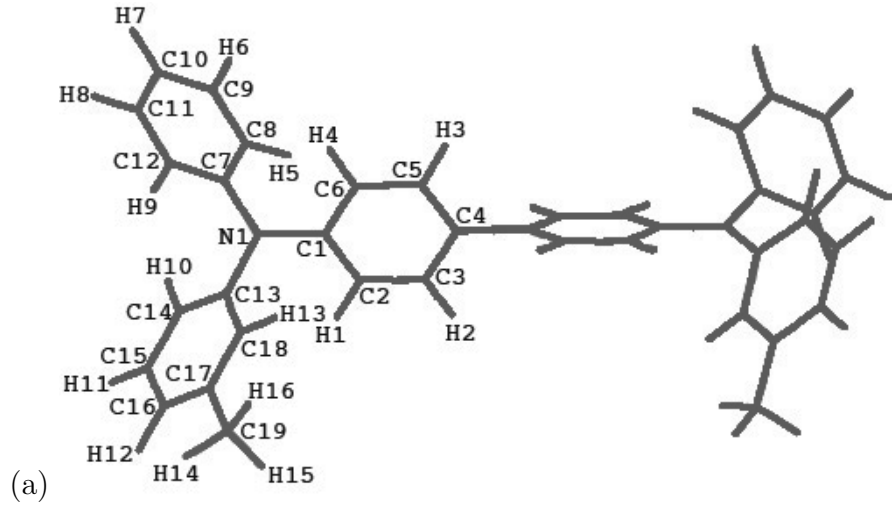

(a)

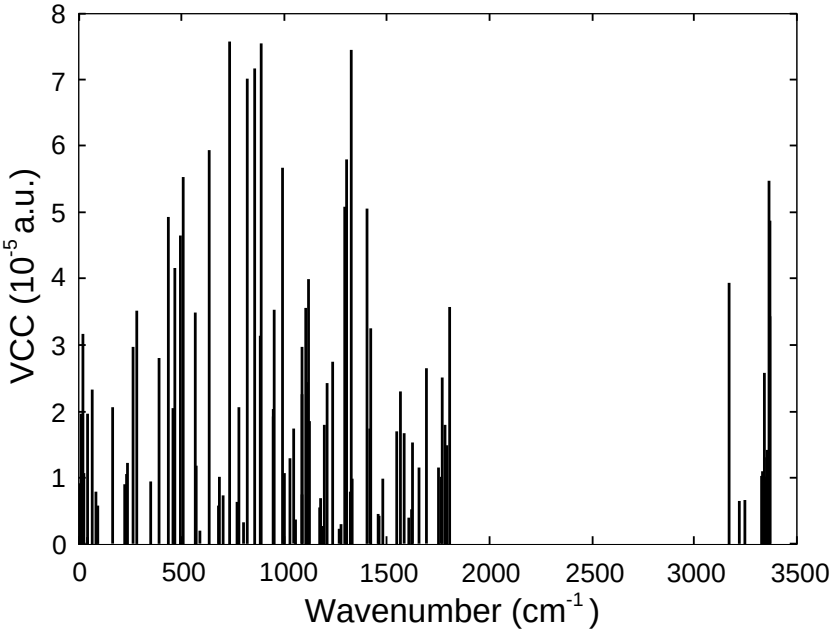

(b)

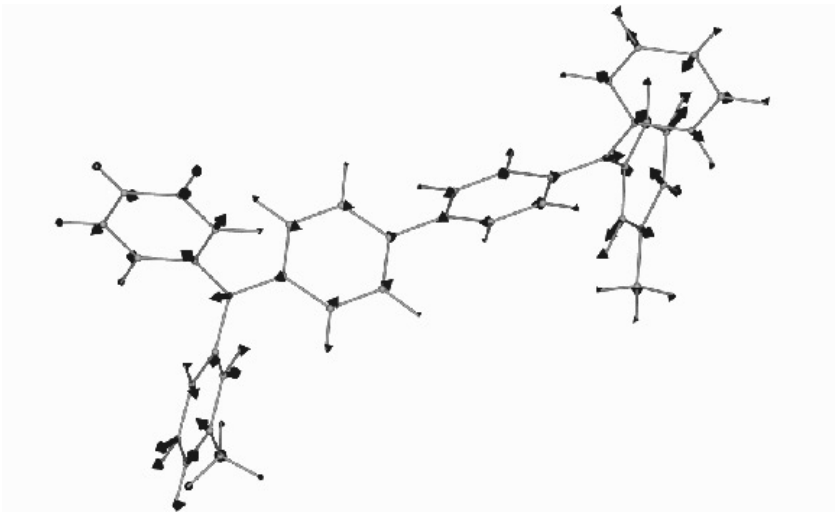

(c)

Figure 1.1: (a) Structure of TPD, (b) calculated vibronic coupling constants, and (c) vibrational mode (735 cm^{-1}) with the strongest coupling in TPD cation.

Though the mode shown in Fig. 1.1(c) is the strongest in TPD cation, order of the coupling is small compared with other π conjugated systems by one order. The reason can be realized with the aid of the vibronic coupling density which yields a local map of a vibronic coupling on the basis of the electron density difference $\Delta\rho$ and the potential derivative v_i.

The potential derivative v_i of the strongest mode is shown in Fig. 1.2. Reflecting the vibrational vector of the mode, v_i takes large values on the phenyl, tolyl groups, and the nitrogen atoms. Figure 1.3 (a) shows the relaxed electron density difference $\Delta\rho_R$. We can see that the electron density difference greatly lies on the nitrogen atoms, and small portion resides on the phenyl and tolyl groups.

Vibronic coupling density is defined as a product of $\Delta\rho$ and v_i. Electron density difference is also related to geometry change via vibronic coupling. The structural change upon oxidation in organic molecules has been discussed[23,24] The vibronic coupling density η_{R} of the strongest mode is shown in Fig. 1.3 (b). It should be noted that the coupling density is localized mostly on the nitrogen atoms. However, since the coupling density is distributed symmetrically around the nitrogen atoms with the positive and negative signs, the contribution near the nitrogen atoms to the coupling constant is quite small. On the other hand, since $\Delta\rho$ is distributed asymmetrically on the phenyl and the tolyl groups, the coupling density is distributed in an asymmetric manner with a little cancellation. Thus, the coupling density on these groups greatly contributes to the vibronic coupling. In Table 1.2, atomic vibronic coupling constant and their summation over the groups are tabulated. It is found that the main contribution originates from the phenyl and the tolyl groups. The electron density difference which is symmetrically localized on the nitrogen affords a little contribution to the vibronic coupling. This is the reason why the TPD cation has the small vibronic couplings.

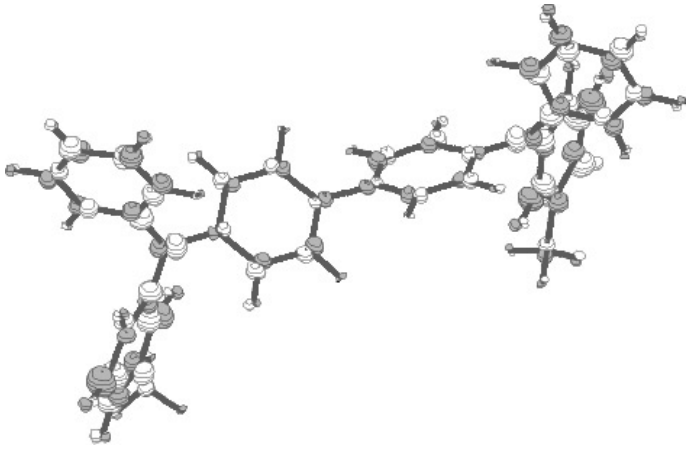

Figure 1.2: Potential derivative $v_i(\mathbf{x})$ with respect to the normal coordinate of 735 cm^{-1} mode. White is positive, and gray negative.

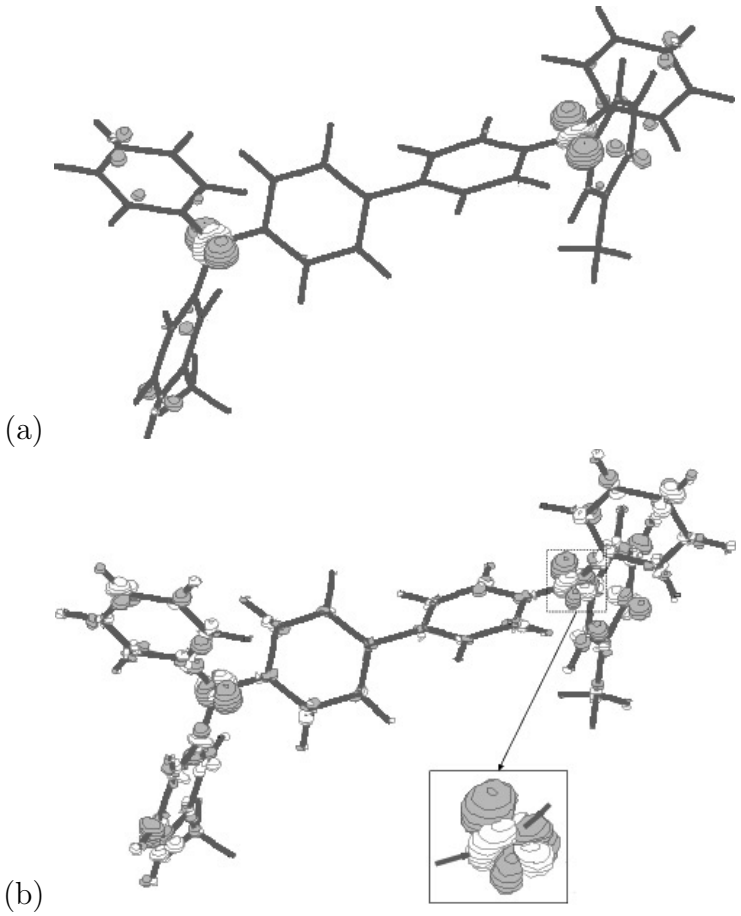

Figure 1.3: (a) Relaxed density difference $\Delta\rho_{\mathrm{R}}(\mathbf{x})$ and (b) vibronic coupling density $\eta_{i\mathrm{R}}(\mathbf{x})$ of 735 cm^{-1} mode. White is positive, and gray negative.

Table 1.2: Atomic vibronic coupling constant in 10^{-5}a.u. The numbers of the atoms are defined in Fig. 1.1(a).

Phenylene		Phenyl		Tolyl		Nitrogen	
C1	0.381	C7	-0.680	C13	-0.522	N1	-0.314
C2	0.096	C8	-0.735	C14	-0.097		
C3	0.090	C9	-0.182	C15	-0.246		
C4	-0.209	C10	-0.163	C16	-0.233		
C5	0.104	C11	-0.120	C17	-0.154		
C6	0.149	C12	-0.235	C18	-0.608		
H1	0.008	H5	-0.032	C19	-0.056		
H2	0.031	H6	-0.077	H10	0.063		
H3	0.049	H7	0.060	H11	-0.041		
H4	-0.003	H8	0.001	H12	0.037		
		H9	-0.048	H13	-0.083		
				H14	0.021		
				H15	-0.024		
				H16	-0.020		
Sum	0.696		-2.211		-1.963		-0.314

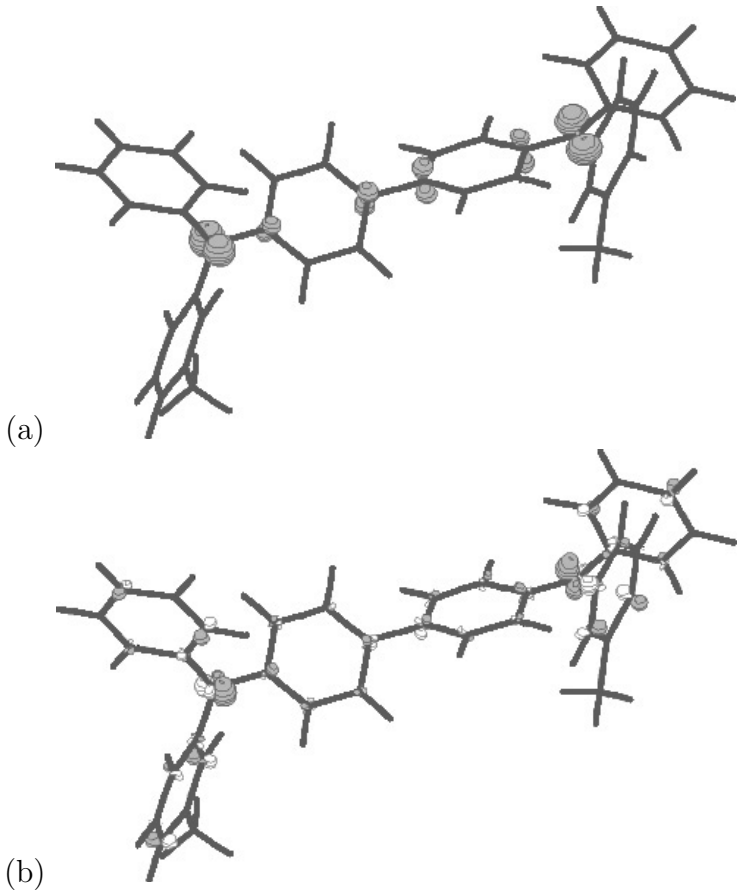

Figure 1.4: (a) Frozen density difference $\Delta\rho_{\rm F}(\mathbf{x})$ and (b) vibronic coupling density $\eta_{i\rm F}(\mathbf{x})$ of 735 $\rm cm^{-1}$ mode. White is positive, and gray negative.

Figures 1.4 show (a) the frozen electron density difference $\Delta\rho_F$ and (b) vibronic coupling density $\eta_{\rm F}$ employing $\Delta\rho_F$. It is found that the density difference and the coupling density reside on the phenylene group, which is completely different from the results obtained from $\Delta\rho_R$. This means that we cannot discuss vibronic coupling on the basis of a frontier orbital only. The use of relaxed density is crucial in the calculation of vibronic coupling.[18]

The calculated $I-V$ characteristics and the power loss are shown in Figs. 1.5(a) and (b). Note that we do not intend to simulate an $I-V$ characteristics observed in bulk systems. Our interest lies in a suppression effect on current due to the electron-vibration interaction in the TPD molecule. The suppression of the current and the power loss is less than 1/2 compared with other π conjugated systems such as oligothiophenes.[22] This could be one of the reasons that TPD is one of good hole-transport materials.

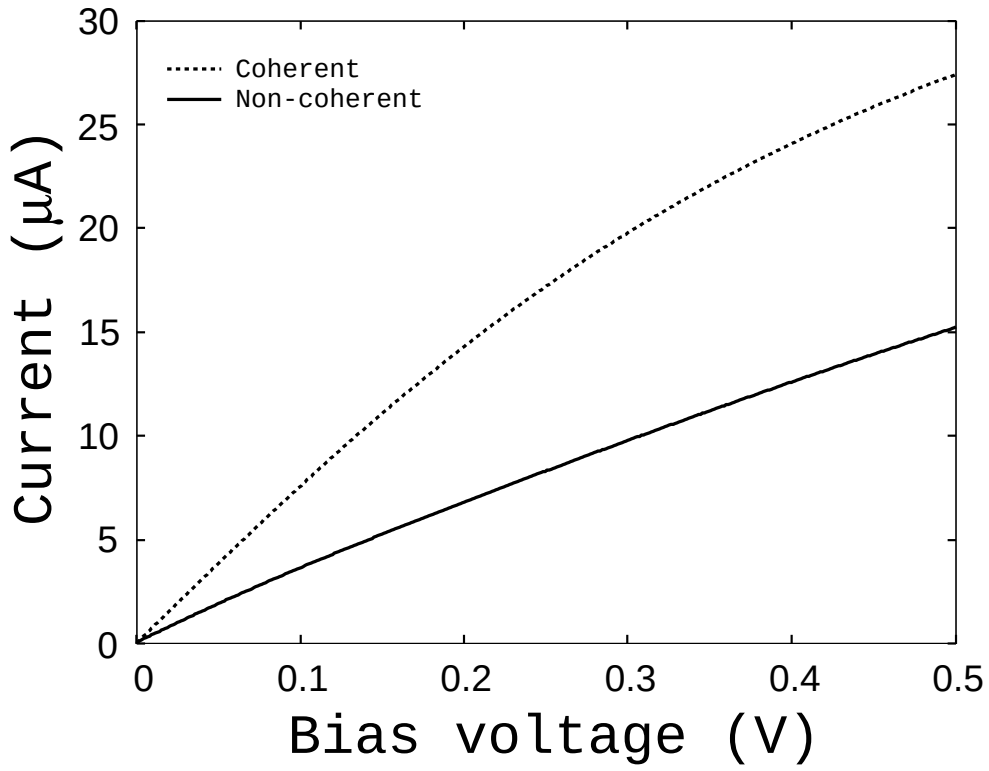

(a)

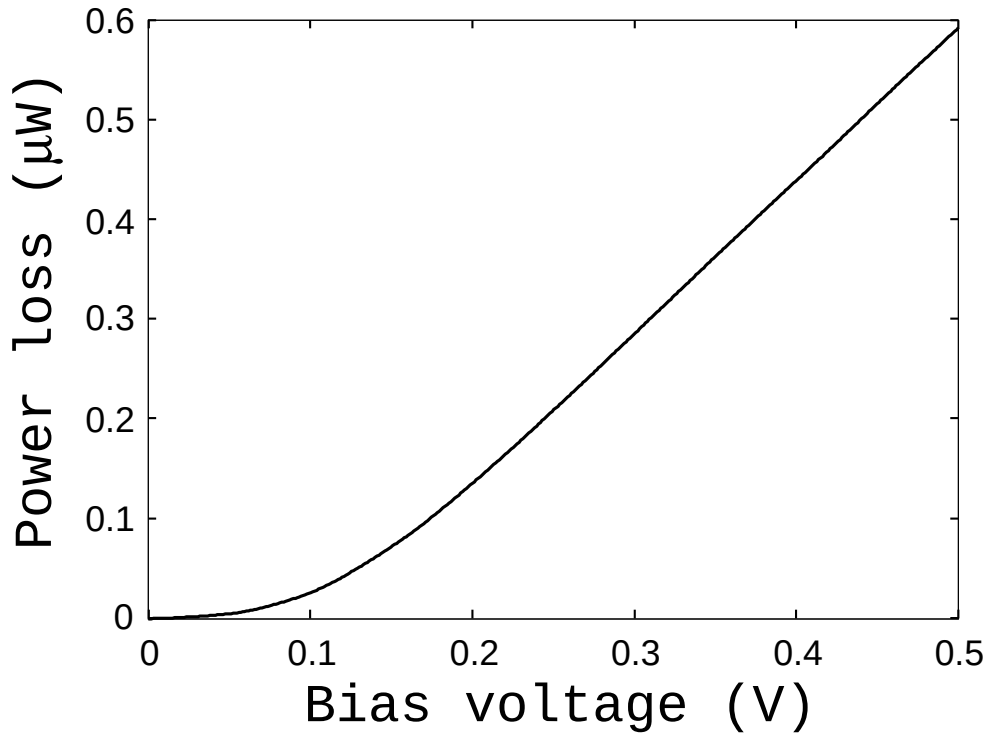

(b)

Figure 1.5: Transport properties through a TPD molecule. (a) $I-V$ characteristics (solid line: with the vibronic couplings, dotted line: without vibronic couplings) and (b) power loss.

1.4 Conclusion

We calculated the vibronic coupling, or electron-vibration coupling constants in N, N'-diphenyl-N, N'-di(m-tolyl)benzidine (TPD) cation from the evaluation of vibronic coupling integrals. The calculated constants were very small compared with other π conjugated systems. The calculated constants were analyzed on the basis of the vibronic coupling density (VCD). The VCD analysis clearly reveals that large contributions originate from the phenyl group and the tolyl group. The excess carrier density is accommodated on the nitrogen atoms. However, the density difference on the nitrogen atoms cannot contribute to the vibronic coupling, since the symmetric density distribution around the atoms are canceled. In addition, the hole transport property of electrode-TPD molecule-electrode system was investigated using Non-equilibrium Green Function (NEGF) theory. Reflecting the small coupling, the current suppression and power loss are less than 1/2 compared with other π conjugated systems such as oligothiophenes.

There would be two approaches to reduce the inelastic current and power loss: one is to make the low frequency higher, and the other is to reduce the large vibronic coupling. For the latter approach, the vibronic coupling density analysis could be helpful in the molecular design for carrier-transport materials.

Bibliography

[1] C. W. Tang and S. A. VanSlyke, Appl. Phys. Lett. **51**, 913 (1987).

[2] C. Adachi, S. Tokito, T. Tsutsui, and S. Saito, Jpn. J. Appl. Phys. **27**, L269 (1988).

[3] J. Kido, M. Kimura, and K. Nagai, Science **267**, 1332 (1995).

[4] C. Adachi, K. Nagai, and N. Tamoto, Appl. Phys. Lett. **66**, 2679 (1995).

[5] V. Bulović, G. Gu, P. E. Burrows, S. R. Forrest, and M. E. Thompson, Nature **380**, 29 (1996).

[6] N. Tamoto, C. Adachi, and K. Nagai, Chem. Mater. **9**, 1077 (1997).

[7] D. F. O'Brien, P. E. Burrows, S. R. Forrest, B. E. Koene, D. E. Loy, and M. E. Thompson, Adv. Mater. **10**, 1108 (1998).

[8] H. Ishii, K. Sugiyama, E. Ito, and K. Seki, Adv. Mater. **11**, 605 (1999).

[9] M. Stolka, J. F. Yanus, and D. M. Pai, J. Phys. Chem. **88**, 4707 (1984).

[10] S. Heun and P. M. Borsenberger, Chem. Phys. **200**, 245 (1995).

[11] R. H. Young and J. J. Fitzgerald, J. Phys. Chem. **99**, 4230 (1995).

[12] K. Sakanoue, M. Motoda, M. Sugimoto, and S. Sakaki, J. Phys. Chem. A **103**, 5551 (1999).

[13] H. Kaji, T. Yamada, N. Tsukamoto, and F. Horii, Chem. Phys. Lett. **401**, 246 (2005).

[14] V. Coropceanu, J. Cornil, D. A. da Silva Filho, Y. Olivier, R. Silbey, and J.-L. Brédas, Chem. Rev. **107**, 926 (2007).

[15] T. Sato, K. Tokunaga, and K. Tanaka, J. Chem. Phys. **124**, 024314 (2006).

[16] K. Tokunaga, T. Sato, and K. Tanaka, J. Chem. Phys. **124**, 154303 (2006).

[17] K. Tokunaga, T. Sato, and K. Tanaka, J. Mol. Struct. **838**, 116 (2007).

[18] T. Sato, K. Tokunaga, and K. Tanaka, J. Phys. Chem. A **112**, 758 (2008).

[19] S. Datta, *Quantum Transport: Atom to Transistor* (Cambridge University Press, Cambridge, 2005).

[20] M. W. Schmidt, K. K. Baldridge, J. A. Boatz, S. T. Elbert, M. S. Gordon, J. H. Jensen, S. Koseki, N. Matsunaga, K. A. Nguyen, S. J. Su, T. L. Windus, M. Dupins, and J. A. Montgomery, J. Comput. Chem. **14**, 1347 (1993).

[21] G. Fischer, *Vibronic Coupling: The Interaction Between the Electronic and Nuclear Motions* (Academic, London, 1984).

[22] T. Sato, K. Shizu, T. Kuga, K. Tanaka, and H. Kaji, Chem. Phys. Lett. **458**, 152 (2008).

[23] M. C. Díaz, B. M. Illescas, N. Martín, R. Viruela, P. M. Viruela, E. Ortí, O. Brede, I. Zilbermann, and D. M. Guldi, Chem. Eur. J. **10**, 2067 (2004).

[24] C. Desmarets, B. Champagne, A. Walcarius, C. Bellouard, R. Omar-Amrani, A. Ahajji, Y. Fort, and R. Schneider, J. Org. Chem. **71**, 1351 (2006).

Chapter 2

Electron-Vibration Interactions in Triphenylamine Cation: Why Are Triphenylamine-Based Molecules Good Hole-Transport Materials?

2.1 Introduction

Molecules containing a triphenylamine (TPA) moiety,[1–5] such as N,N'-diphenyl-N,N'-di(m-tolyl)benzidine[6–8] (TPD) and N,N'-di(naphthalene-1-yl)-N,N'-diphenyl-benzidine[9–13] (α-NPD), are used as hole-transport layers in multilayer organic light-emitting diodes (OLEDs)[14–17] because of their high hole mobility. Large energy dissipation occurs when a carrier transmits through a molecule having large vibronic coupling constants (VCCs). Since vibronic (electron–phonon) coupling lowers the efficiency of hole transport and causes energy dissipation in a molecule, a detailed understanding of vibronic coupling is needed for designing new hole-transport materials with high carrier mobility. In Chapter I, we showed that localization of electron-density differences on N atoms is responsible for the small VCCs, and therefore high hole mobility of TPD cation.[18]

The Marcus theory[19–24] has been applied to investigate charge transport in hole-/electron-transport materials. In this theory, reorganization energy ΔE plays an im-

portant role. $\Delta E/4$ corresponds to the activation energy for carrier transfer between molecules; thus, molecules with small ΔE could prove good for charge transport. Several authors have calculated ΔE for TPA derivatives in the hole-transport process.[25–28] Wang and co-workers showed that for TPD, conformational changes in tolyl and phenyl groups as well as central biphenyl unit contribute to ΔE.[25]

In the hole-transport process, ΔE is two times the stabilization energy of the cationic state. The stabilization energy can be written in terms of VCCs,[29] and a molecule with large/small VCCs has large/small ΔE. Hence, an understanding of VCC ordering clarifies the reason for the size of the stabilization energy, and therefore the magnitude of ΔE. In this chapter, we investigate vibronic coupling in TPA cation as a prototypical example of triarylamine-based molecules, and calculate its VCCs at the *ab initio* level. VCC ordering of TPA cation is discussed in detail using vibronic coupling density (VCD) analysis,[30–34] which reveals a local picture of vibronic coupling in a molecule. Finally, we calculate and compare the reorganization energies for effective modes of TPA, TPD, and biphenyl cations. The reorganization energy for TPD cation is shown to be influenced by the contribution from the tolyl and phenyl groups as well as the biphenyl moiety.

2.2 Theory

The Hamiltonian of a molecule is given by

$$\mathcal{H}\left(\mathbf{r},\mathbf{R}\right)=\mathcal{H}_{\mathrm{e}}\left(\mathbf{r},\mathbf{R}\right)+\mathcal{T}_{\mathrm{n}}\left(\mathbf{R}\right), \tag{2.1}$$

where $\mathcal{H}_{\mathrm{e}}\left(\mathbf{r},\mathbf{R}\right)$ is an electronic Hamiltonian, $\mathcal{T}_{\mathrm{n}}\left(\mathbf{R}\right)$ is the nuclear kinetic energy, and $\mathbf{r}$ and $\mathbf{R}$ are sets of electronic and nuclear coordinates, respectively. The VCC for the i^{th} totally symmetric mode is expressed in terms of a set of mass-weighted normal coordinates $\{Q_i\}$,

$$V_i=\left\langle \Psi^{+}\left(\mathbf{r},\mathbf{R_0}\right)\left|\left(\frac{\partial\mathcal{H}_{\mathrm{e}}\left(\mathbf{r},\mathbf{R}\right)}{\partial Q_i}\right)_{\mathbf{R_0}}\right|\Psi^{+}\left(\mathbf{r},\mathbf{R_0}\right)\right\rangle, \tag{2.2}$$

where $\mathbf{R_0}$ is the set of nuclear coordinates of the equilibrium geometry in the neutral state, and $\Psi^{+}\left(\mathbf{r},\mathbf{R_0}\right)$ is the electronic wave function of the cationic state at the equilibrium geometry. We can express eq. 2.2 in the form

$$V_i \;=\; \sum_A \frac{1}{\sqrt{M_A}}\mathbf{e}_A^{(i)}\cdot\left\langle \Psi^{+}\left(\mathbf{r},\mathbf{R_0}\right)\left|\left(\frac{\partial\mathcal{H}_{\mathrm{e}}\left(\mathbf{r},\mathbf{R}\right)}{\partial\mathbf{R}}\right)_{\mathbf{R_0}}\right|\Psi^{+}\left(\mathbf{r},\mathbf{R_0}\right)\right\rangle$$

$$= \sum_A V_{i,A}, \tag{2.3}$$

where M_A is the mass of nucleus A, and $\mathbf{e}_A^{(i)}$ is the A^{th} component of a vibrational vector of the i^{th} vibrational mode in mass-weighted coordinates $\mathbf{e}^{(i)}$. The direction $\mathbf{e}^{(i)}$ is chosen such that V_i is negative. $V_{i,A}$ is called the atomic vibronic coupling constant (AVCC) for atom A. The sum of the AVCCs $V_{i,A}$ gives the VCC V_i. Hence, the AVCC $V_{i,A}$ represents the contribution to the VCC V_i from atom A.

Under the condition that the Hellmann–Feynman theorem[35] holds, V_i can be written in terms of the electron-density difference $\Delta\rho$ and the derivative of the nuclear–electronic potential v_i:[30–34]

$$V_i = \int \Delta\rho\left(\mathbf{x}\right) \times v_i\left(\mathbf{x}\right) d\mathbf{x}, \tag{2.4}$$

where

$$\Delta\rho\left(\mathbf{x}\right) = \rho^{+}\left(\mathbf{x}\right) - \rho\left(\mathbf{x}\right), \tag{2.5}$$

$$v_i\left(\mathbf{x}\right) = -\sum_A \frac{Z_A}{\sqrt{M_A}} \mathbf{e}_A^{(i)} \cdot \frac{\mathbf{x} - \mathbf{R}_A}{\left|\mathbf{x} - \mathbf{R}_A\right|^3}, \tag{2.6}$$

where $\rho^{+}\left(\mathbf{x}\right)$ and $\rho\left(\mathbf{x}\right)$ are the electron densities for the cationic and neutral states, respectively. $\mathbf{x}$ denotes a position in three-dimensional space. The VCD $\eta_i\left(\mathbf{x}\right)$ is defined by

$$\eta_i\left(\mathbf{x}\right) = \Delta\rho\left(\mathbf{x}\right) \times v_i\left(\mathbf{x}\right), \tag{2.7}$$

which gives a local picture of the vibronic coupling in a molecule.[30–34]

An effective mode of geometric deformation $\mathbf{e}_s$ is defined by

$$\mathbf{e}_s = -\sum_i \frac{V_i}{|\mathbf{V}|} \mathbf{e}^{(i)}, \tag{2.8}$$

where the i^{th} component of $\mathbf{V}$ is equal to V_i, and

$$|\mathbf{V}| = \sqrt{\sum_i V_i^2}. \tag{2.9}$$

Within the harmonic and crude adiabatic (CA) approximations, the energy of the cationic state E^{+} takes the form[36]

$$E^{+} = E^{0} + \sum_i V_i Q_i + \frac{1}{2} \sum_i \omega_i^2 Q_i^2, \tag{2.10}$$

where

$$E^0 = \left\langle \Psi^+ (\mathbf{r}, \mathbf{R_0}) \left| \mathcal{H}_\mathrm{e} (\mathbf{r}, \mathbf{R_0}) \right| \Psi^+ (\mathbf{r}, \mathbf{R_0}) \right\rangle . \tag{2.11}$$

Since Q_i can be expressed as

$$Q_i = -\frac{V_i}{|\mathbf{V}|} Q_s, \tag{2.12}$$

E^+ can be written as

$$E^+ = E^0 + \frac{1}{2}\omega_s^2 \left(Q_s + \frac{V_s}{\omega_s^2} \right)^2 - \frac{V_s^2}{2\omega_s^2}, \tag{2.13}$$

where

$$V_s = -\left| \mathbf{V} \right| , \tag{2.14}$$

$$\omega_s = \frac{\sum_i V_i^2 \omega_i^2}{V_s^2}. \tag{2.15}$$

V_s and ω_s are the VCC and frequency, respectively, of the effective mode. Eq. 2.13 means that the geometric deformation is expressed in terms of the single effective mode $\mathbf{e}_s$. The stabilization energy of the cationic state for the effective mode ΔE_s can be written as

$$\Delta E_s = \frac{V_s^2}{2\omega_s^2}, \tag{2.16}$$

and the contribution to ΔE_s from the i^{th} mode is given by

$$\Delta E_{s,i} = \frac{V_i^2}{2\omega_s^2}. \tag{2.17}$$

2.3 Method of Calculation

To satisfy the Hellmann–Feynman theorem,[35] the 6-31G basis set with first derivatives of the functions it contains[37] (denoted as 6-31G+der) was used. Geometry optimization and vibrational analysis for the neutral states were performed with the RHF/6-31G+der level of the theory. Electronic structures of the cationic states were calculated at the ROHF/6-31G+der level using the optimized geometries of the neutral states. All *ab initio* calculations were performed with the GAMESS computational chemistry software program.[38]

2.4 Results and Discussion

2.4.1 Vibronic Coupling Constant

Figure 2.1 shows the optimized geometry with the atomic numbering scheme, bond lengths, and bond angles for neutral TPA. The geometry was optimized assuming D_3 symmetry. The C_3 axis was observed in a jet-cooled TPA.[39] The propeller-like structure of TPA is due to steric hindrance between neighboring phenyl groups. The N1, C1, C7, and C13 atoms are coplanar. The calculated dihedral angle between the phenyl ring and the plane formed by the C1, C7, and C13 atoms is 45.9°. Dihedral angles of 50°[39] and 44°[40] were observed in the gas and solid crystalline phases, respectively. Four independent TPA molecules exist in the solid crystalline phase.[40] Mean values for the geometrical parameters of the four independent TPA molecules are written in parentheses in Fig. 2.1 and are in satisfactory agreement with our calculated results.

The calculated frequencies and VCCs for the totally symmetric modes of neutral TPA are listed in Table 2.1. Vibrational modes that include C−N stretching vibrations have relatively large VCCs, suggesting that vibronic coupling occurs mainly around the central N atom; the out-of-plane bending and C−H stretching modes have small VCCs. This is often observed in the VCCs for π conjugated systems.[31–34] The magnitude of the VCCs is at most 1.374×10^{-4} a.u., and the vibronic coupling in TPA cation is weak. For TPD cation, since $\Delta\rho$ is delocalized in two TPA moieties,[18] it is smaller than for TPA cation. As a result, the VCDs and VCCs are smaller for TPD cation than for TPA cation.

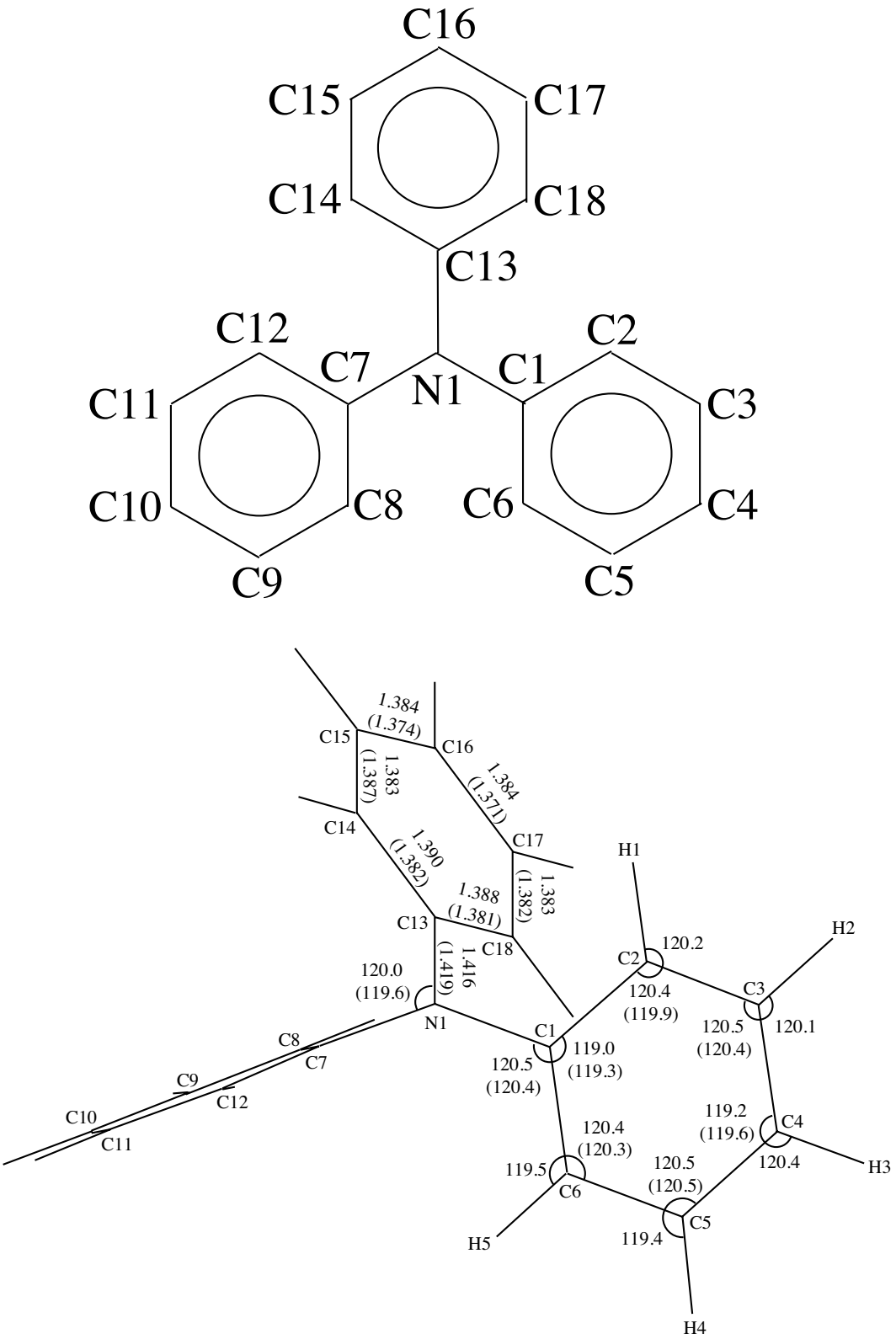

Figure 2.1: 6-31G+der optimized geometry with atomic numbering scheme, bond lengths, and bond angles for neutral TPA. Bond lengths are in Å; bond angles are in degrees. Numbers in parentheses are experimental values.[40]

Table 2.1: Calculated frequencies in cm^{-1}, vibronic coupling constants (VCCs) in 10^{-4} a.u., and descriptions for totally symmetric modes of TPA. str, bend, oop, and ip indicate stretching, bending, out-of-plane, and in-plane, respectively.

Mode	Wavenumber	VCC	Assignment
$a_1\,(1)$	72.59	−0.174	ring torsion
$a_1\,(2)$	301.17	−0.540	C−N str
$a_1\,(3)$	466.41	−0.660	ring oop bend
$a_1\,(4)$	780.20	−1.374	C−N str, ring ip bend
$a_1\,(5)$	955.88	−0.378	C−H oop bend
$a_1\,(6)$	1088.29	−0.652	ring ip bend
$a_1\,(7)$	1114.40	−0.342	C−H oop bend
$a_1\,(8)$	1122.91	−0.457	ring ip bend
$a_1\,(9)$	1285.21	−0.371	C−N str, ring ip bend, C−H ip bend
$a_1\,(10)$	1296.64	−1.198	C−N str, ring str
$a_1\,(11)$	1660.28	−0.492	C−N str, ring ip bend, C−H ip bend
$a_1\,(12)$	1798.63	−0.606	C−N str, ring str, C−H ip bend
$a_1\,(13)$	3331.10	−0.432	C−H str
$a_1\,(14)$	3354.13	−0.030	C−H str
$a_1\,(15)$	3366.18	−0.774	C−H str

2.4.2 Vibronic Coupling Density Analysis

In this subsection, we discuss the reason for the VCC ordering using VCD analysis. Figure 2.2a shows the electron density of the highest occupied molecular orbital (HOMO). The HOMO electron density has a π-orbital character. The main portion of the HOMO electron density is located on the N1 atom, and the remaining density is distributed over the phenyl rings. The π conjugation does not extend so much over the phenyl rings because of the propeller-like structure of TPA.

Figure 2.2b shows the electron-density difference $\Delta\rho$ upon ionization. The distribution pattern for $\Delta\rho$ is similar to that for the HOMO electron density: $\Delta\rho$ is located mostly on the N1 atom and is small on the phenyl rings. Note that a region with positive $\Delta\rho$ exists. Positive $\Delta\rho$ in the C1–C7–C13 plane decreases repulsion between the negative regions above and below the plane, and has a σ-character. As in the case of negative $\Delta\rho$, positive $\Delta\rho$ is also localized around the N1, C1, C7, and C13 atoms. Positive $\Delta\rho$ arises from an orbital relaxation due to the ionization. In the phenyl rings, $\Delta\rho$ is quite small on the meta carbons (the C3 and C5 atoms).

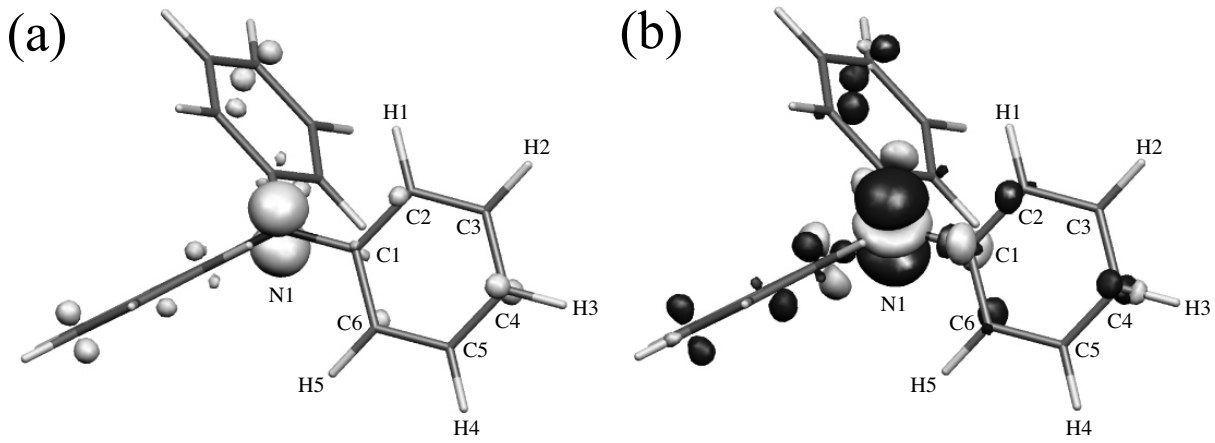

Figure 2.2: (a) Electron density of HOMO; (b) Electron-density difference $\Delta\rho$ at an isosurface value of 0.008 a.u. Dark gray shows where values are negative; light gray shows where values are positive.

Figure 2.3 shows some of the totally symmetric modes. Significantly, the N1 atom is not displaced in these modes. Figures 2.4 and 2.5 show derivatives of the nuclear–electronic potential v_i and VCDs η_i, respectively, for the $a_1\,(3)$, $a_1\,(4)$, $a_1\,(6)$, $a_1\,(8)$, $a_1\,(10)$, and $a_1\,(15)$ modes. Since the N1 atom is not displaced, v_i is small near the N1 atom (Figs. 2.4a–f). The VCCs and AVCCs for various atoms for these modes are listed in Table 2.2.

The largest VCC (-1.374×10^{-4} a.u.) corresponds to the $a_1\,(4)$ mode, involving displacements of all the carbon atoms (Fig. 2.3b), and v_4 is large on the phenyl rings (Fig. 2.4b). $\Delta\rho$ overlaps with v_4 in the phenyl rings, leading to the η_4 distribution around the carbon atoms (Fig. 2.5b). This distribution pattern is reflected in the size of the AVCCs. The C1 atom has a large AVCC (-0.160×10^{-4} a.u.); the other carbon atoms have relatively large AVCCs (Table 2.2). η_4 is also large on the N1 atom, but the η_4 distribution on the N1 atom is due to the overlap between $\Delta\rho$ on the N1 atom and v_4 resulting from the displacement of the C1, C7, and C13 atoms, and not from the displacement of the N1 atom. The η_4 distribution on the N1 atom contributes not to the AVCC for the N1 atom but to the AVCCs for the C1, C7, and C13 atoms. Significantly, the AVCC for the nitrogen atom $V_{4,\mathrm{N1}}$ is 0 a.u. This is because the N1 atom is not displaced, and $\mathbf{e}_{\mathrm{N1}}^{(15)} = \mathbf{0}$, per eq. 2.3.

The second largest VCC (-1.198×10^{-4} a.u.) corresponds to the $a_1(10)$ mode, involving C$-$N stretching and ring stretching vibrations. By comparing v_{10} (Fig. 2.4e) with v_4 (Fig. 2.4b), we find that v_{10} is smaller than v_4 around the C2, C3, C4, C5, and C6 atoms, and hence, η_{10} (Fig. 2.5e) is smaller than η_4 (Fig. 2.5b) on these atoms. This is why AVCCs for the carbon atoms other than the C1 atom are smaller for the $a_1(10)$ mode than for the $a_1(4)$ mode. Displacements of the hydrogen atoms associated with ring stretching vibration cause η_{10} distribution around the hydrogen atoms to be large, but the increase in the AVCCs for the hydrogen atoms does not compensate for the decrease in the AVCCs for the carbon atoms. Consequently, the VCC is smaller for the $a_1(10)$ mode than for the $a_1(4)$ mode.

The $a_1(3)$ mode is a ring out-of-plane bending mode. v_3 is distributed vertically and almost antisymmetrically with respect to the phenyl rings (Fig. 2.4a). Overlap between v_3 and $\Delta\rho$ is large only on the C2 and C6 atoms. Hence, AVCCs for the other atoms are small, and the $a_1(3)$ mode has a small VCC (-0.660×10^{-4} a.u.).

The $a_1(6)$ mode is a ring in-plane bending mode. In contrast to the $a_1(4)$ and $a_1(10)$ modes, C−N displacements are small (Fig. 2.3c). v_6 is large around the C2, C4, and C6 atoms (the ortho and para carbons); it is quite small around the C1 atom (Fig. 2.4c). v_6 overlaps significantly with $\Delta\rho$ on the C2, C4, and C6 atoms. On the C1−C2 bond, $\Delta\rho$ is negative, whereas v_6 is positive. Hence, around the C2 and C6 atoms, regions where η_6 is negative are larger than regions where it is positive (Fig. 2.5c), leading to negative VCCs for the C2 and C6 atoms. In contrast, around the C1 and C4 atoms, regions where η_6 is positive are larger than regions where it is negative. Hence, AVCCs for the C1 and C4 atoms are positive, and they cancel the AVCCs for the C2 and C6 atoms. This is why the VCC magnitude for the $a_1(6)$ mode is small compared with those for the $a_1(4)$ and $a_1(10)$ modes.

Such a cancellation of AVCCs also occurs for the $a_1(8)$ mode. AVCCs for the C2 and C3 atoms cancel, and those for the H1 and H2 atoms cancel. Hence, the VCC for the $a_1(8)$ mode is quite small (-0.457×10^{-4} a.u.).

The $a_1(15)$ mode is a C−H stretching mode, and v_{15} is localized on the C−H bonds (Fig. 2.4f). Figure 2.5f shows η_{15}. Since $\Delta\rho$ is large only on the C4−H3 bond among the C-H bonds, the η_{15} distribution is localized on that bond. The η_{15} distribution on the N1 atom is due to overlap between $\Delta\rho$ on the N1 atom and the v_{15} distribution resulting from displacement of the H1 and H5 atoms. Because the overlap between $\Delta\rho$ and v_{15} is small, regions where the VCD value is large are smaller for η_{15} than for η_4 and η_{10}. Consequently, the AVCCs, and hence the VCC, for the $a_1(15)$ mode are small. This explanation for small VCC (-0.774×10^{-4} a.u.) also applies to the other C−H stretching modes.

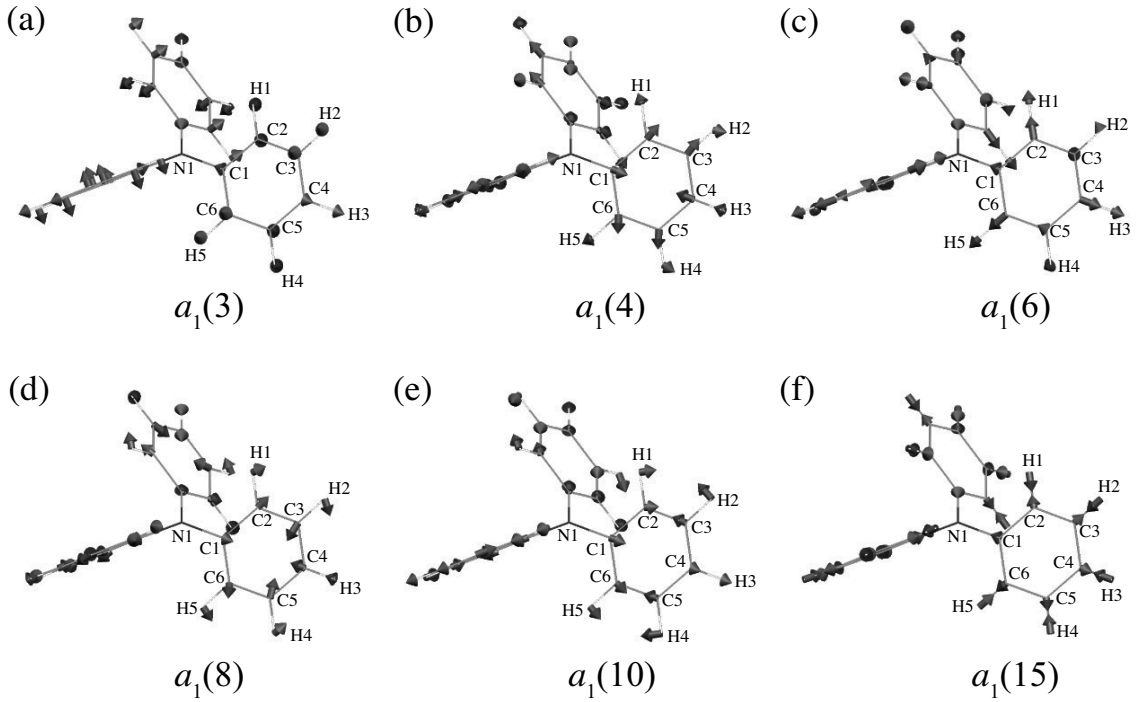

Figure 2.3: Various totally symmetric vibrational modes for neutral TPA: (a) $a_1(3)$; (b) $a_1(4)$; (c) $a_1(6)$; (d) $a_1(8)$; (e) $a_1(10)$; (f) $a_1(15)$.

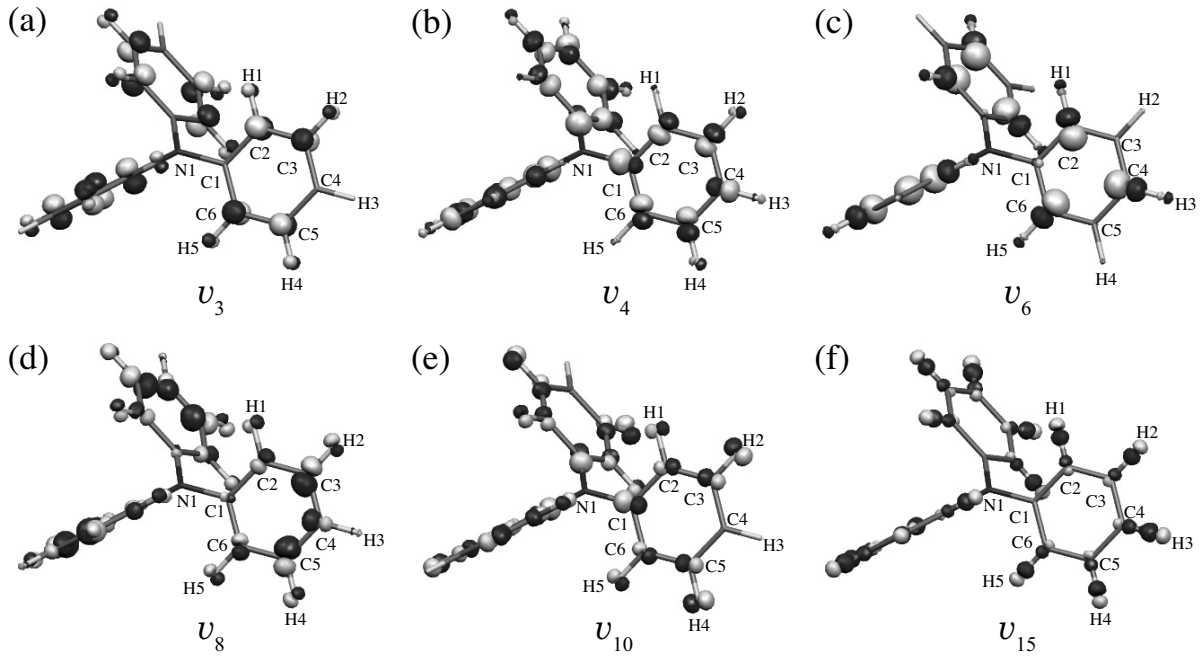

Figure 2.4: Derivative of nuclear–electronic potential v at an isosurface value of 0.01 a.u. for various modes: (a) $a_1(3)$; (b) $a_1(4)$; (c) $a_1(6)$; (d) $a_1(8)$; (e) $a_1(10)$; (f) $a_1(15)$. Dark gray shows where values are negative; light gray shows where values are positive.

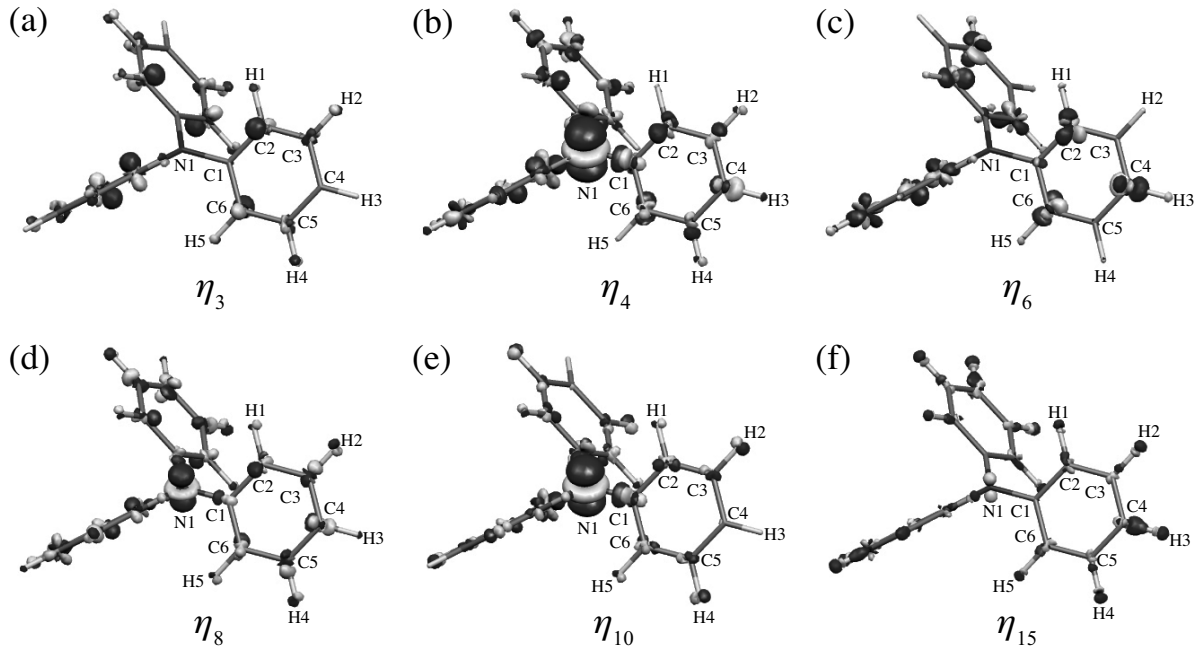

Figure 2.5: Vibronic coupling density η at an isosurface value of 5×10^{-5} a.u. for various modes: (a) $a_1(3)$; (b) $a_1(4)$; (c) $a_1(6)$; (d) $a_1(8)$; (e) $a_1(10)$; (f) $a_1(15)$. Dark gray shows where values are negative; light gray shows where values are positive.

Table 2.2: Vibronic coupling constants and atomic vibronic coupling constants in 10^{-4} a.u. for the $a_1\,(3)$, $a_1\,(4)$, $a_1\,(6)$, $a_1\,(8)$, $a_1\,(10)$, and $a_1\,(15)$ modes.

	$a_1\,(3)$	$a_1\,(4)$	$a_1\,(6)$	$a_1\,(8)$	$a_1\,(10)$	$a_1\,(15)$
N1	0.000	0.000	0.000	0.000	0.000	0.000
C1	0.006	−0.160	0.024	−0.039	−0.154	0.004
C2(C6)	−0.082	−0.092	−0.164	−0.064	−0.001	−0.039
C3(C5)	−0.029	−0.057	0.000	0.068	−0.019	−0.015
C4	0.000	−0.057	0.079	−0.035	0.004	0.022
H1(H5)	0.009	0.002	−0.003	−0.049	−0.050	0.003
H2(H4)	−0.011	0.032	−0.002	0.009	−0.054	−0.066
H3	0.000	−0.012	0.017	−0.008	0.001	−0.049
VCC	−0.660	−1.374	−0.652	−0.457	−1.198	−0.774

2.4.3 Reorganization Energy

Within the harmonic and CA approximations[36] employed here, the stabilization energy for the cationic state for the effective mode ΔE_s can be written as $\Delta E_s = V_s^2/2\omega_s^2$, per eq. 2.16. Calculated values for ΔE_s for TPA, TPD, and biphenyl cations are 0.031, 0.034, and 0.176 eV, respectively. Within the Born-Oppenheimer (BO) approximation, the estimated reorganization energies for these cations are 0.12, 0.36, and 0.29 eV,[27] respectively, and are larger than ours. Our calculation is based purely on linear vibronic coupling, whereas calculations within the BO approximation inevitably include higher-order vibronic coupling effects. The difference in the reorganization energies originates from higher-order vibronic coupling terms. First, we should consider the influence of linear vibronic coupling on charge-transport properties, and hence the reorganization energy originating from linear vibronic coupling.

Significantly, ΔE_s for TPD cation is close to that for TPA cation, because the VCC spectrum for TPD cation[18] is similar to that for TPA cation. In contrast, ΔE_s for biphenyl is five times larger than those for TPA and TPD cations. The large ΔE_s for biphenyl cation comes from the contribution from the C−C stretching mode, for which the VCC is large (-6.088×10^{-4} a.u.). Since $\Delta\rho$ on the N atoms in TPD is localized[18] and vibronic coupling in the biphenyl unit is weakened, TPD cation has small VCCs and ΔE_s, as for TPA cation. Such localization of $\Delta\rho$ does not occur for biphenyl cation; consequently, VCCs and ΔE_s are large for biphenyl cation.

Figures 2.6a–c show the contribution to ΔE_s from each mode for TPA, TPD, and biphenyl cations. For the TPA and TPD cations, low-frequency modes contribute significantly to ΔE_s (Fig. 2.6a,b); for biphenyl cation the main contribution comes from a C−C stretching mode (Fig. 2.6c). The difference in the ΔE_s peak pattern suggests that vibronic coupling in TPD cation occurs around the N atoms and not in the biphenyl unit.

$\Delta E_{s,i}$ values are smaller for TPD cation than for TPA cation. For TPD cation, since $\Delta\rho$ is distributed on the two N atoms, $\Delta\rho$ is small compared with the value for TPA cation. Hence, η is also smaller for TPD cation than for TPA cation, leading to small VCCs and $\Delta E_{s,i}$ for TPD cation. However, the number of vibrational modes is larger for TPD than for TPA, so ΔE for TPD cation is comparable to that for TPA cation.

Figures 2.6d–f show three vibrational modes for TPD with large $\Delta E_{s,i}$. The mode of wavenumber 391.33 cm^{-1} is an out-of-plane bending mode (Fig. 2.6d). The N atoms

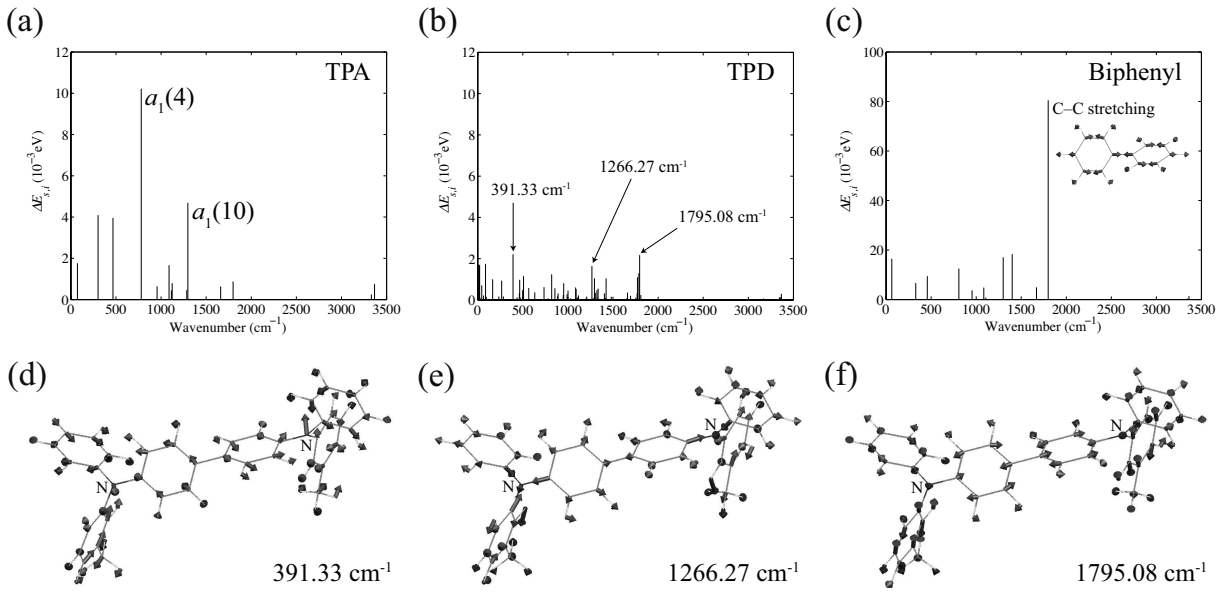

Figure 2.6: Contribution to ΔE_s from each mode for various cations: (a) TPA; (b) TPD; (c) Biphenyl. Various vibrational modes of TPD: (d) 391.33 cm^{-1}; (e) 1266.27 cm^{-1}; (f) 1795.08 cm^{-1}.

are greatly displaced and have large AVCCs. The AVCCs of the N atoms contribute significantly to the VCC for this mode, and hence, vibronic coupling for this mode occurs mainly on the N atoms. Figure 2.6e shows a C−N stretching mode. Tolyl and phenyl groups make large contributions to $\Delta E_{s,i}$, and the contribution from the biphenyl unit is small. Figure 2.6f shows a C−C stretching mode. Contributions from the tolyl, phenyl, and biphenyl moieties are large, suggesting that $\Delta E_{s,i}$ is not influenced by the biphenyl moiety only. This is because the electron-density difference $\Delta\rho$ of TPD cation is localized on the N atoms, and vibronic coupling in the biphenyl is weak. If vibronic coupling is strong in the biphenyl unit, the C−C stretching mode (Fig. 2.6f) has a large $\Delta E_{s,i}$, as in the case of biphenyl (Fig. 2.6c). In conclusion, ΔE_s for TPD cation is not influenced by the contribution from the biphenyl moiety only, which is consistent with the results obtained by Wang and co-workers using a different method.[25]

2.5 Conclusions

We calculated the vibronic coupling constants of TPA in the cation state and discussed their relative ordering by means of vibronic coupling density analysis. The small overlap between the electron-density difference and the derivative of the nuclear–electronic potential in the phenyl groups is responsible for the weak vibronic coupling in TPA cation. The vibronic coupling constants of the TPA cation are small. We calculated the reorganization energies ΔE_s for the effective modes for TPA cations and compared them with those for TPD and biphenyl cations. Tolyl and phenyl groups as well as central biphenyl unit contribute to ΔE_s for TPD cation. This is because the electron-density difference $\Delta\rho$ of TPD cation localizes on the N atoms, and vibronic coupling in the biphenyl moiety is weak. The localization of $\Delta\rho$ on the N atoms leads to a small reorganization energy for TPD cation.

Bibliography

[1] H. Kageyama, H. Ohishi, M. Tanaka, Y. Ohmori, and Y. Shirota, Appl. Phys. Lett. **94**, 063304 (2009).

[2] C. H. Cheung, K. C. Kwok, S. C. Tse, and S. K. So, J. Appl. Phys. **103**, 093705 (2008).

[3] S. K. So, S. C. Tse, , and K. L. Tong, J. Disp. Technol. **3**, 225 (2007).

[4] Y. Shirota and H. Kageyama, Chem. Rev. **107**, 953 (2007).

[5] H. Ohishi, M. Tanaka, H. Kageyama, and Y. Shirota, Chem. Lett. **33**, 1266 (2004).

[6] K. Okumoto and Y. Shirota, Mater. Sci. Eng. **B85**, 135 (2001).

[7] S. Heun and P. M. Borsenberger, Chem. Phys. **200**, 245 (1995).

[8] M. Stolka, J. F. Yanus, and D. M. Pai, J. Phys. Chem. **88**, 4707 (1984).

[9] K. L. Tong, S. W. Tsang, K. K. Tsung, S. C. Tse, and S. K. So, J. Appl. Phys. **102**, 093705 (2007).

[10] S. C. Tse, K. C. Kwok, and S. K. So, Appl. Phys. Lett. **89**, 262102 (2006).

[11] B.-X. Mi, P.-F. Wang, M.-W. Liu, H.-L. Kwong, N.-B. Wong, C.-S. Lee, and S.-T. Lee, Chem. Mater. **15**, 3148 (2003).

[12] Z. Deng, S. T. Lee, D. P. Webb, Y. C. Chan, and W. A. Gambling, Synth. Met. **107**, 107 (1999).

[13] S. A. VanSlyke, C. H. Chen, and C. W. Tang, Appl. Phys. Lett. **69**, 2160 (1996).

[14] C. Adachi, K. Nagai, and N. Tamoto, Appl. Phys. Lett. **66**, 2679 (1995).

[15] C. W. Tang, S. A. VanSlyke, and C. H. Chen, J. Appl. Phys. **65**, 3610 (1989).

[16] C. Adachi, S. Tokito, T. Tsutsui, and S. Saito, Jpn. J. Appl. Phys. **27**, L269 (1988).

[17] C. W. Tang and S. A. VanSlyke, Appl. Phys. Lett. **51**, 913 (1987).

[18] T. Sato, K. Shizu, T. Kuga, K. Tanaka, and H. Kaji, Chem. Phys. Lett. **458**, 152 (2008).

[19] R. A. Marcus, J. Electroanal. Chem. **483**, 2 (2000).

[20] R. A. Marcus, J. Electroanal. Chem. **438**, 251 (1997).

[21] R. A. Marcus and N. Sutin, Biochim. Biophys. Acta **811**, 265 (1985).

[22] R. A. Marcus, J. Chem. Phys. **43**, 679 (1965).

[23] R. A. Marcus, J. Chem. Phys. **24**, 966 (1956).

[24] P. F. Barbara, T. J. Meyer, and M. A. Ratner, J. Phys. Chem. **100**, 13148 (1996).

[25] J.-H. Pan, Y.-M. Chou, H.-L. Chiu, and B.-C. Wang, J. Phys. Org. Chem. **20**, 743 (2007).

[26] B. C. Lin, C. P. Cheng, and Z. P. M. Lao, J. Phys. Chem. A **107**, 5241 (2003).

[27] M. Malagoli and J.-L. Brédas, Chem. Phys. Lett. **327**, 13 (2000).

[28] K. Sakanoue, M. Motoda, M. Sugimoto, and S. Sakaki, J. Phys. Chem. A **103**, 5551 (1999).

[29] V. Coropceanu, J. Cornil, D. A. da Silva Filho, Y. Olivier, R. Silbey, and J.-L. Brédas, Chem. Rev. **107**, 926 (2007).

[30] T. Sato, K. Tokunaga, N. Iwahara, K. Shizu, and K. Tanaka, *Vibronic coupling constant and vibronic coupling density* in *The Jahn-Teller-Effect - Fundamentals and Implications for Physics and Chemistry,* H. Köppel, D. R. Yarkony, and H. Barentzen (Eds) (Springer-Verlag, Berlin and Heidelberg, 2009).

[31] T. Sato, K. Tokunaga, and K. Tanaka, J. Phys. Chem. A **112**, 758 (2008).

[32] K. Tokunaga, T. Sato, and K. Tanaka, J. Mol. Struct. **838**, 116 (2007).

[33] K. Tokunaga, T. Sato, and K. Tanaka, J. Chem. Phys. **124**, 154303 (2006).

[34] T. Sato, K. Tokunaga, and K. Tanaka, J. Chem. Phys. **124**, 024314 (2006).

[35] R. P. Feynman, Phys. Rev. **56**, 340 (1939).

[36] G. Fischer, *Vibronic Coupling: The Interaction Between the Electronic and Nuclear Motions* (Academic, London, 1984).

[37] H. Nakatsuji, K. Kanda, and T. Yonezawa, Chem. Phys. Lett. **75**, 340 (1980).

[38] M. W. Schmidt, K. K. Baldridge, J. A. Boatz, S. T. Elbert, M. S. Gordon, J. H. Jensen, S. Koseki, N. Matsunaga, K. A. Nguyen, S. J. Su, T. L. Windus, M. Dupins, and J. A. Montgomery, J. Comput. Chem. **14**, 1347 (1993).

[39] G. Meijer, G. Berden, W. L. Meerts, H. E. Hunziker, M. S. de Vries, and H. R. Wendt, Chem. Phys. **163**, 209 (1992).

[40] A. N. Sobolev, V. K. Belsky, I. P. Romm, N. Y. Chernikova, and E. N. Guryanova, Acta Crystallogr., Sect. C **41**, 967 (1985).

Chapter 3

Vibronic Coupling Density Analysis of Hole-Transporting Materials: Electron-Density Difference in DFT and HF Methods

3.1 Introduction

Organic light-emitting diodes (OLEDs)[1,2] have attracted much attention because of their potential application in flat-panel devices. A typical OLED has a multilayer structure consisting of, for example, an indium tin oxide (ITO) anode, a hole-transporting layer, an emitting layer, an electron-transporting layer, and a cathode. Hole-transporting materials require efficient hole injection from the ITO surface, high hole mobility, and thermal stability. Hole-injection efficiency depends on the difference between a work function of the ITO surface and ionization potential of the hole-transporting molecule. Molecules with low ionization potentials, such as 4,4′,4″-tris(3-methylphenylphenylamino)triphenylamine (*m*-MTDATA), exhibit efficient hole injections from the ITO electrode.[3–5]

Interaction between carrier and molecular vibration (vibronic coupling) causes an inelastic scattering and decreases current. The extent of the suppression of the current is governed by the magnitude of the vibronic coupling constant (VCC) of a molecule, and molecules with small VCCs are good for charge-transporting materials. Marcus' theory[6–11] has been used to estimate the charge-transfer rate constant k between molecules. In the

theory, the rate constant is related to the reorganization energy,[12] and a molecule with a small reorganization energy has large k and is good for charge-transporting material. In this chapter, we adopted the non-equilibrium Green's function (NEGF) theory[13] to investigate the carrier-transporting properties. In the NEGF theory, VCC plays a crucial role in a mechanism of the inelastic scattering, and hence, it is important to understand the factors that change the magnitude of VCC in order to design new hole-transporting materials. In addition, reorganization energy can be evaluated from the VCCs and vibrational frequencies. In this sense, a fundamental understanding of the vibronic interaction is necessary.

Sato *et al.* have shown that VCC can be expressed as a space integration of the vibronic coupling density (VCD) η, which gives a local picture of vibronic coupling in a molecule.[14–18] VCD is the product of the electron-density difference $\Delta\rho$ and the derivative of the nuclear–electronic potential v. $\Delta\rho$ is the electron-density difference between the ionic and neutral states. The magnitude of η depends on the degree of overlap between $\Delta\rho$ and v. A molecule with small overlap has small VCCs and is expected to be good for charge-transporting material. We have calculated the VCDs of N,N'-bis(3-methylphenyl)-N,N'-diphenyl-[1,1′-biphenyl]-4,4′-diamine (TPD) cation and reported that localization of $\Delta\rho$ on N atoms makes η small, which results in small VCCs for the cation.[19] The good transport property of TPD originates from the small VCCs. The importance of N atom in a mechanism of hole-transporting process has been discussed elsewhere.[20,21] The VCD analysis further suggests that conformational change in tolyl and phenyl groups as well as central biphenyl unit contributes to the reorganization energy.[21] This result is consistent with that obtained by Wang and co-workers using a different method.[22]

Various carbazole derivatives having good thermal stability have been synthesized and used as hole-transporting materials.[23–25] Carbazole N atom is expected to localize $\Delta\rho$, reduce VCCs, and enhance the hole-mobility. In this chapter, we calculate VCDs for biphenyl, fluorene, and carbazole (Fig. 3.1) cations and investigate the reason for the VCC ordering by analyzing VCDs. Because methylene- and imino-bridging of biphenyl yields fluorene and carbazole, respectively, we investigate the effect of the methylene and imino on the VCDs and VCCs.

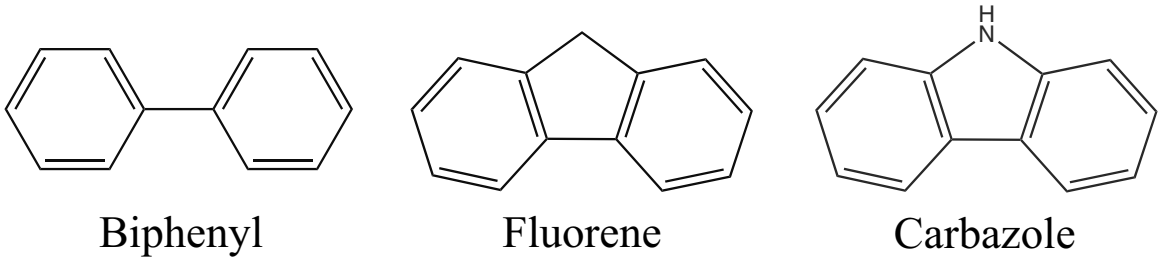

Figure 3.1: Structural formulas for biphenyl, fluorene, and carbazole.

3.2 Theory

The Hamiltonian of a molecule is expressed as

$$\mathcal{H}\left(\mathbf{r},\mathbf{R}\right)=\mathcal{H}_{\mathrm{e}}\left(\mathbf{r},\mathbf{R}\right)+\mathcal{T}_{\mathrm{n}}\left(\mathbf{R}\right), \tag{3.1}$$

where $\mathcal{H}_{\mathrm{e}}\left(\mathbf{r},\mathbf{R}\right)$ is an electronic Hamiltonian, $\mathcal{T}_{\mathrm{n}}\left(\mathbf{R}\right)$ is the nuclear kinetic energy, and $\mathbf{r}$ and $\mathbf{R}$ denote sets of electronic and nuclear coordinates, respectively. Herzberg−Teller expansion of the electronic Hamiltonian yields

$$\mathcal{H}_{\mathrm{e}}\left(\mathbf{r},\mathbf{R}\right)=\mathcal{H}_{\mathrm{e}}\left(\mathbf{r},\mathbf{R_0}\right)+\sum_{i}\left(\frac{\partial\mathcal{H}_{\mathrm{e}}\left(\mathbf{r},\mathbf{R}\right)}{\partial Q_i}\right)_{\mathbf{R_0}}Q_i+\cdots, \tag{3.2}$$

where $\{Q_i\}$ is a set of mass-weighted normal coordinates for the i^{th} vibrational mode and $\mathbf{R_0}$ is the nuclear configuration of the equilibrium geometry in the neutral state. The VCC for the i^{th} mode is defined by

$$V_i=\left\langle\Psi^{+}\left(\mathbf{r},\mathbf{R_0}\right)\left|\left(\frac{\partial\mathcal{H}_{\mathrm{e}}\left(\mathbf{r},\mathbf{R}\right)}{\partial Q_i}\right)_{\mathbf{R_0}}\right|\Psi^{+}\left(\mathbf{r},\mathbf{R_0}\right)\right\rangle, \tag{3.3}$$

where $\Psi^{+}\left(\mathbf{r},\mathbf{R_0}\right)$ is the electronic wave function of the cation state at the equilibrium geometry in the neutral state. Eq. 3.3 can be written as

$$\begin{aligned}V_i &= \sum_{A}\frac{1}{\sqrt{M_A}}\mathbf{e}_A^{(i)}\cdot\left\langle\Psi^{+}\left(\mathbf{r},\mathbf{R_0}\right)\left|\left(\frac{\partial\mathcal{H}_{\mathrm{e}}\left(\mathbf{r},\mathbf{R}\right)}{\partial\mathbf{R}}\right)_{\mathbf{R_0}}\right|\Psi^{+}\left(\mathbf{r},\mathbf{R_0}\right)\right\rangle \\ &= \sum_{A}V_{i,A},\end{aligned} \tag{3.4}$$

where M_A is the mass of nucleus A. $\mathbf{e}_A^{(i)}$ is the mass-weighted 3D component of atom A of the i^{th} vibrational mode Q_i, and denotes the relative magnitude of displacement of nucleus A. The direction of $\mathbf{e}^{(i)}$ is defined such that V_i becomes negative; that is, structural deformation toward $\mathbf{e}^{(i)}$ lowers the energy of the cationic state. $V_{i,A}$ is called the atomic

vibronic coupling constant (AVCC) of the A^{th} atom and represents the contribution from the A^{th} atom to VCC V_i.

When the Hellmann–Feynman theorem[26] holds, V_i can be expressed in terms of the electron-density difference $\Delta\rho$ and the derivative of the nuclear–electronic potential v_i:[14–18]

$$V_i = \int \Delta\rho\left(\mathbf{x}\right) \times v_i\left(\mathbf{x}\right) d\mathbf{x}, \tag{3.5}$$

where

$$\Delta\rho\left(\mathbf{x}\right) = \rho^{+}\left(\mathbf{x}\right) - \rho\left(\mathbf{x}\right), \tag{3.6}$$

$$v_i\left(\mathbf{x}\right) = \sum_A v_{i,A}\left(\mathbf{x}\right) = \sum_A -\frac{Z_A}{\sqrt{M_A}}\mathbf{e}_A^{(i)} \cdot \frac{\mathbf{x}-\mathbf{R}_A}{\left|\mathbf{x}-\mathbf{R}_A\right|^3}, \tag{3.7}$$

where Z_A is atomic number, $\rho^{+}\left(\mathbf{x}\right)$ and $\rho\left(\mathbf{x}\right)$ are electron densities for the cationic and neutral states, respectively, and $\mathbf{x}$ denotes a position in 3D space. The product $\Delta\rho\left(\mathbf{x}\right) \times v_i\left(\mathbf{x}\right)$ is called the VCD[14–18] and is denoted by $\eta_i\left(\mathbf{x}\right)$,

$$\eta_i\left(\mathbf{x}\right) = \Delta\rho\left(\mathbf{x}\right) \times v_i\left(\mathbf{x}\right), \tag{3.8}$$

which gives a local picture of the vibronic couplings in the molecule.

Atomic vibronic coupling density (AVCD) $\eta_{i,A}$ is defined by

$$\eta_{i,A}\left(\mathbf{x}\right) = \Delta\rho\left(\mathbf{x}\right) \times v_{i,A}\left(\mathbf{x}\right) = \Delta\rho\left(\mathbf{x}\right) \times \left(-\frac{Z_A}{\sqrt{M_A}}\mathbf{e}_A^{(i)} \cdot \frac{\mathbf{x}-\mathbf{R}_A}{\left|\mathbf{x}-\mathbf{R}_A\right|^3}\right). \tag{3.9}$$

AVCD represents the contribution from the A^{th} atom to η_i. Space integration gives the AVCC $V_{i,A}$:

$$V_{i,A} = \int \eta_{i,A}\left(\mathbf{x}\right) d\mathbf{x}. \tag{3.10}$$

The sum of the AVCDs is equal to the VCD η_i,

$$\eta_i\left(\mathbf{x}\right) = \sum_A \eta_{i,A}\left(\mathbf{x}\right). \tag{3.11}$$

3.3 Method of Calculation

We used the 6-31G basis set with their first derivatives[27] (denoted as 6-31G+der) so as to satisfy the Hellmann–Feynman theorem,[26] and confirmed that the theorem was satisfied for all systems. We optimized the structures of neutral biphenyl, fluorene, and carbazole

at the B3LYP/6-31G+der level of theory. We assumed D_2 symmetry for biphenyl and C_{2v} symmetry for fluorene and carbazole, and confirmed by vibrational analysis that they are stationary minima. A scaling factor of 0.963[28] was used for B3LYP/6-31G+der theoretical frequencies. We calculated electronic structures of the cationic states at the UB3LYP/6-31G+der level using the optimized geometries of the neutral states. All the DFT calculations were done using Gaussian 03 software.[29] Current and power loss calculations were performed based on Datta.[13] Neighboring molecules are considered as electrodes with the Fermi levels which are set to the HOMO levels shown in Fig. 3.3. We employed the electronic coupling $\tau = 0.5$ eV and temperature $T = 298$ K.

3.4 Results and Discussion

3.4.1 Equilibrium Geometries

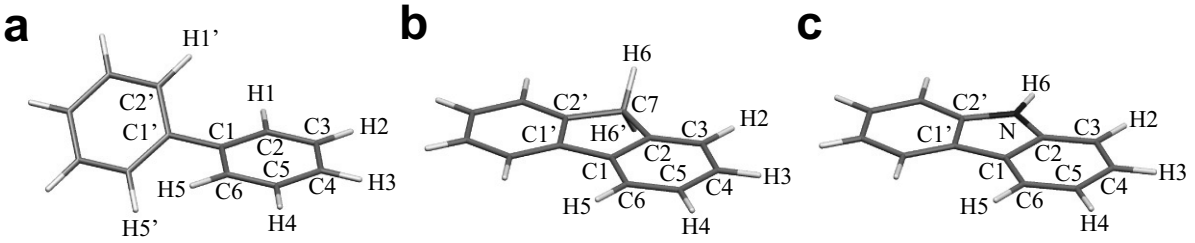

Figure 3.2: Geometries optimized at the B3LYP/6-31G+der level of theory with the atomic numbering scheme for various neutral moieties: (a) Biphenyl; (b) Fluorene; (c) Carbazole.

Figure 3.2 shows B3LYP/6-31G+der optimized geometries for neutral biphenyl, fluorene, and carbazole with an atomic numbering scheme. Biphenyl has a twisted structure (Fig. 3.2a). Deviation from planarity is due to steric repulsion between H1−H1' atoms and H5−H5' atoms. In a planar structure, the calculated distance between H1 and H1' atoms is 1.949 Å; in the twisted conformation, the estimated distance is 2.403 Å. The calculated torsion angle between the two benzene rings of biphenyl is 40.3°, being small compared with experimental values of 44.4°[30] and 45±10°[31] determined by gas-phase electron diffraction. In solutions, the estimated twisted angles are 19−26°;[32] in a solid crystalline form at room temperature, the two benzene rings are coplanar.[33–36] These facts suggest that intermolecular interaction overcomes steric repulsion between H atoms. Our calculated

geometrical parameters are listed in Table 3.1, along with experimental results obtained by X-ray analysis for crystalline biphenyl at 110K.[37] Although calculated and experimental results are not in agreement, especially for the dihedral angle between the two benzene rings, nonplanarity does not affect VCC ordering for the biphenyl cation, as discussed in Section 3.4.2.

The carbon skeleton of fluorene is calculated to be coplanar (Fig. 3.2b). Whether it is coplanar or bent has been controversial in experiments. By X-ray analysis of crystalline fluorene, Brown *et al.*[38] and Belsky *et al.*[39] determined that it is coplanar, while Gerkin *et al.* determined that it is bent.[40] Although lack of planarity can arise from intermolecular interaction between the H6 atom of one molecule and the C1 and C1' atoms of a neighboring molecule, our calculation does not consider such interactions. Our calculated geometrical parameters, listed in Table 3.1, are in good agreement with experimental results.[40] The molecular structure of carbazole resembles that of fluorene, with the methylene group replaced by an imino group. In their solid crystalline forms, intermolecular interactions cause both fluorene and carbazole to be slightly bent,[41,42] whereas the optimized geometry of carbazole is planar (Fig. 3.2c). Differences in the geometrical parameters of carbazole and fluorene are observed in five-membered rings; the C2−N bond is much shorter than the C2−C7 bond because of π delocalization in the pyrrole ring. Our calculated bond lengths and angles, listed in Table 3.1, are in satisfactory agreement with experimental results.[41]

Figure 3.3 shows orbital energy levels of HOMOs and lowest unoccupied molecular orbitals (LUMOs) for biphenyl, fluorene, and carbazole together with those for TPD, CBP, and meridional tris(8-quinolinolato)aluminum (*mer*-Alq_3). TPD and CBP are widely used as hole-transporting materials, and Alq_3 as an emitting material and electron-transporting material.[1] HOMOs and LUMOs were calculated at the RHF/6-31G+der level using General Atomic and Molecular Electronic Structure System (GAMESS) general *ab initio* quantum chemistry package program.[43] Experimental work functions with opposite signs to those for ITO thin film[44] and Mg:Ag alloy[45] are also shown in the figure as Fermi energies of ITO and Mg:Ag electrode surfaces. ITO and Mg:Ag electrodes are widely used as anodes and cathodes, respectively, in multilayer OLEDs. Carbazole has a higher HOMO energy level than do biphenyl and fluorene, suggesting that it exhibits higher hole-injection efficiency.

Table 3.1: Geometrical parameters of optimized structures of neutral biphenyl, fluorene, and carbazole calculated at the B3LYP/6-31G+der level. Numbers in parentheses are experimental values.[37,40,41] Bond lengths are in Å; bond angles and dihedral angles are in degrees.

	Biphenyl	Fluorene	Carbazole
Bond lengths			
C1−C2	1.403(1.394)	1.409(1.397)	1.419(1.401)
C2−C3	1.392(1.391)	1.389(1.386)	1.395(1.393)
C3−C4	1.394(1.379)	1.397(1.385)	1.391(1.373)
C4−C5	1.394(1.390)	1.397(1.385)	1.404(1.394)
C5−C6	1.392(1.385)	1.394(1.390)	1.390(1.379)
C6−C1	1.403(1.399)	1.395(1.387)	1.399(1.388)
C1−C1'	1.484(1.496)	1.469(1.472)	1.450(1.4151)
C2−C7(N)		1.515(1.504)	1.388(1.387)
C2−H1	1.084(1.04)		
C3−H2	1.084(1.08)	1.085(1.00)	1.084(1.00)
C4−H3	1.084(1.05)	1.084(1.00)	1.084(0.96)
C5−H4	1.084(1.04)	1.084(0.99)	1.083(1.02)
C6−H5	1.084(0.96)	1.084(0.97)	1.084(1.01)
C7(N)−H6		1.096(1.01)	1.004(0.98)
Bond angles			
C1−C2−C3	120.9(120.57)	120.5(120.5)	121.6(122.3)
C2−C3−C4	120.2(120.98)	119.1(118.7)	117.7(116.7)
C3−C4−C5	119.5(118.91)	120.5(120.9)	121.3(122.0)
C4−C5−C6	120.2(120.43)	120.7(120.7)	120.8(121.0)
C5−C6−C1	120.9(121.25)	118.9(118.5)	119.2(118.4)
C6−C1−C2	118.2(117.86)	120.4(120.7)	119.2(119.7)
C2−C1−C1'	120.9(120.63)	108.6(108.3)	106.7(106.6)
C1−C2−C7(N)		110.0(110.4)	108.5(109.0)
C2−C7(N)−C2'		102.8(102.7)	109.6(108.7)

C7(N)−C2−C3		129.5(129.1)	129.7(128.7)
H1−C2−C1	119.4(122.0)		
H1−C2−C3	119.7(117.3)		
H2−C3−C2	119.7(118.9)	120.8(119.5)	121.3(121)
H2−C3−C4	120.0(120.1)	120.1(121.8)	121.0(122)
H3−C4−C3	120.3(120.6)	119.8(119.2)	119.3(119)
H3−C4−C5	120.3(120.5)	119.7(119.8)	119.4(119)
H4−C5−C4	120.0(117.3)	119.6(119.3)	119.4(118)
H4−C5−C6	119.7(122.3)	119.7(119.9)	119.8(121)
H5−C6−C5	119.7(115.6)	120.2(121.2)	120.3(124)
H5−C6−C1	119.4(122.9)	120.8(120.3)	120.5(118)
C1'−C1−C6	120.9(121.5)	131.0(131.0)	134.1(133.7)
H6−C7(N)−C2		111.9(111.9)	125.2
H6−C7−H6'		106.5(105)	
Dihedral angles			
C1−C2−C3−C4	−0.1	0.0	0.0
C2−C3−C4−C5	0.0	0.0	0.0
C3−C4−C5−C6	0.0	0.0	0.0
C4−C5−C6−C1	−0.1	0.0	0.0
C5−C6−C1−C2	0.0	0.0	0.0
C6−C1−C2−C3	0.0	0.0	0.0
C2′−C1′−C1−C6	139.7	180.0	180.0
C1′−C1−C2−C7(N)		0.0	0.0
C1−C2−C7(N)−H6		120.3	180.0
C2′−C7(N)−H6−C2		114.7	180.0
C6−C1−C2−H1	178.3		
C1−C2−C3−H2	179.4	180.0	180.0
C2−C3−C4−H3	180.0	180.0	180.0
C3−C4−C5−H4	−179.4	180.0	180.0
C4−C5−C6−H5	−178.3	180.0	180.0

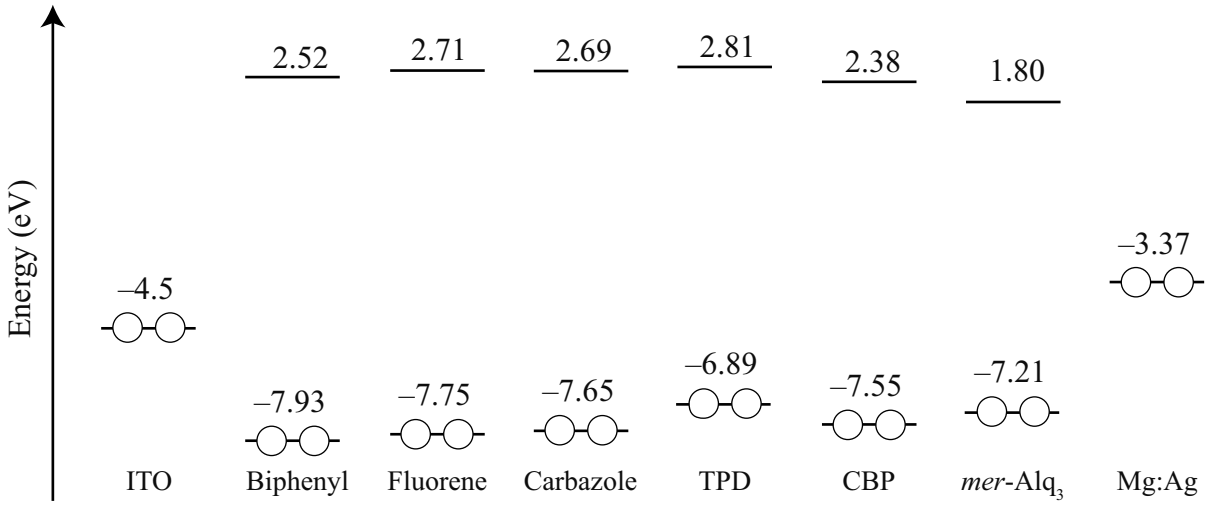

Figure 3.3: HOMO/LUMO energy-level diagrams for neutral biphenyl, fluorene, carbazole, TPD, CBP, and *mer*-Alq_3 calculated at the RHF/6-31G+der level of theory. Experimental work functions with opposite signs of an ITO thin film[44] and Mg:Ag alloy[45] are also shown as the Fermi energies of ITO and Mg:Ag electrode surfaces.

3.4.2 Vibronic Coupling Density Analysis

Figure 3.4 shows calculated VCCs for biphenyl, fluorene, and carbazole cations. VCCs are smaller for carbazole than for the others. The trend in VCC ordering for fluorene is similar to that for biphenyl. For both biphenyl and fluorene, the largest VCC corresponds to a C−C stretching mode (1589.13 and 1594.25 cm^{-1}, respectively). The experimental frequencies are 1610[46] and 1612[47] cm^{-1}, respectively, which are in satisfactory agreement with our theoretical results; for carbazole, the largest two VCCs correspond to a C−C stretching mode (1608.91 cm^{-1}) and a N−H stretching mode (3529.22 cm^{-1}). The calculated frequencies are in agreement with the experimental frequencies of 1625 and 3421[48] cm^{-1}. These various C−C stretching modes are clearly different; the associated VCCs are -4.192×10^{-4} au for biphenyl, -3.440×10^{-4} au for fluorene, and -2.390×10^{-4} au for carbazole. In spite of their similarities in molecular structure, the largest VCC for carbazole is small compared with those for biphenyl and fluorene, suggesting that carbazole is the superior transporting material. The reorganization energy for biphenyl is calculated to be 0.387 eV, which is close to the value calculated using the different basis set (0.36 eV).[49]

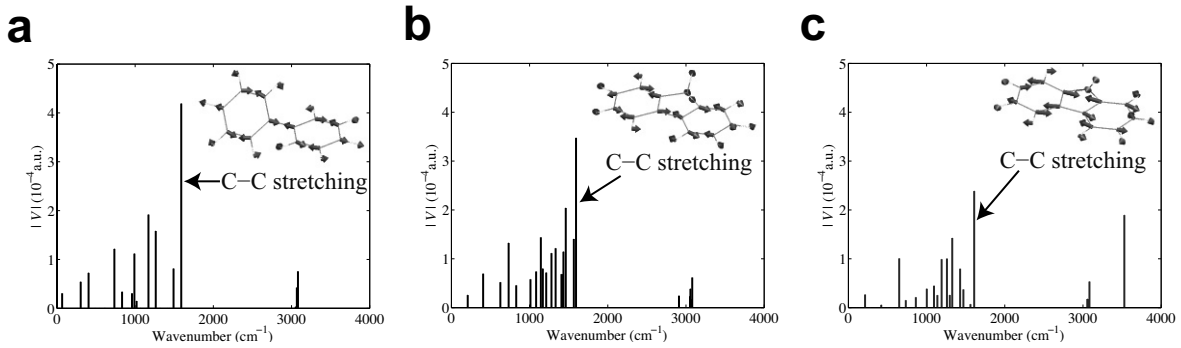

Figure 3.4: Absolute values of vibronic coupling constants $|V|$ for various cations calculated at the UB3LYP/6-31G+der level of theory: (a) Biphenyl; (b) Fluorene; (c) Carbazole.

Figure 3.5a1–c1 shows the (largest-VCC) C−C stretching modes for biphenyl, fluorene, and carbazole cations. Note that these modes involve inter-ring C−C (C1−C1') stretching and intra-ring C−C (C2−C3 and C5−C6) stretching vibrations. For biphenyl and fluorene, the mode directions correspond to a quinoid deformation, which converts the molecular geometry from benzenoid to quinoid. The C1−C1', C2−C3, and C5−C6 bonds shorten, while the C1−C2, C3−C4, C4−C5, and C6−C1 bonds lengthen. Since we have defined the mode directions such that their VCCs become negative, quinoid deformations stabilize the cationic states. For carbazole, the vibration phase is the opposite: the C1−C1', C2−C3, and C5−C6 bonds lengthen, while the C1−C2, C3−C4, C4−C5, and C6−C1 bonds shorten. Quinoid deformation does not occur, and the optimized structure of carbazole cation is not quinoid-like. The AVCCs of the three C−C stretching modes in the figure are listed in Table 3.2. Values for the C1 and C3 atoms are much smaller for carbazole than for biphenyl and fluorene. A value for the carbazole C5 atom is much smaller for the biphenyl C5 atom. Values for the carbazole C4 and C6 atoms are comparable to those for the fluorene C4 and biphenyl C6 atoms. Contributions to the VCCs from H and C7 (N) atoms are small. Hence, the smaller VCC of the carbazole C−C stretching mode is due to the C1, C3, and C5 atoms. We can understand the reason for this result by considering VCD distributions.

Figure 3.5a2–c2 shows derivatives of nuclear–electronic potential v for C−C stretching modes with the same isosurface value. The distribution of v_i reflects the vibrational mode; v_i around atom A is distributed along a component of vibrational vector $\mathbf{e}_A^{(i)}$,

and is large around an atom for which $|\mathbf{e}_A^{(i)}|$ is large (eq. 3.7). $|\mathbf{e}_A^{(i)}|$ is the relative magnitude of displacement of nucleus A toward a negative (dark gray) region around it. For in-plane modes, v_i has a large negative value at which interatomic distance is small. Values of $|\mathbf{e}_A^{(i)}|$ for the three C−C stretching modes in Fig. 3.5a1–c1 are listed in Table 3.3. For biphenyl and fluorene, v_i distributions of the C−C stretching modes are similar because the associated $|\mathbf{e}_A^{(i)}|$ values resemble. Large negative v_i values (dark-gray regions in Fig. 3.5a2,b2) are observed for the C1−C1', C2−C3, and C5−C6 bonds (that is, the bond lengths are shorter), and large positive values are observed for the C1−C2, C3−C4, C4−C5, and C6−C1 bonds. For carbazole, the phase of v_i is opposite to that for biphenyl and fluorene, but the magnitudes of $\mathbf{e}_A^{(i)}$ is comparable to that for fluorene. Thus, the $|v_i|$ distribution for carbazole is almost identical to that for fluorene, suggesting that differences in VCC magnitude among the three molecules is due to the differences in the distribution patterns of the electron-density difference $\Delta\rho$.

Figure 3.5a3–c3 shows electron-density difference $\Delta\rho$. For biphenyl, $\Delta\rho$ is large across the C1−C2 and C6−C1 bonds and C4 atom (Fig. 3.5a3). For fluorene, $\Delta\rho$ is similarly distributed (Fig. 3.5b3) and, on the C1−C2 and C6−C1 bonds, greatly overlaps with v_i. $\Delta\rho$ is small on fluorene's methylene group. In contrast, for carbazole, $\Delta\rho$ distribution changes as a result of imino-group substitution. $\Delta\rho$ is large on the N atom; it is also large on the benzene ring C3 and C5 atoms (where, for biphenyl and fluorene, it is small) and relatively small on the benzene ring C1 and C2 atoms. For carbazole, $\Delta\rho$ is limited around the N, C3, and C5 atoms, whereas for biphenyl and fluorene, it extends over the C1−C2 and C6−C1 bonds. This difference affects the degree of overlap between $\Delta\rho$ and v_i.

Figure 3.5a4–c4 shows vibronic coupling densities η_i. For biphenyl and fluorene, since v_i and $\Delta\rho$ overlap significantly on the C1−C2 and C6−C1 bonds, the AVCDs of the C1, C2, and C6 atoms are large. The sums of the AVCCs of the C1, C1', C2, C2', C6 and C6' atoms are -2.864×10^{-4} au for biphenyl and -2.580×10^{-4} au for fluorene, corresponding to 68.3 and 75.0% of their respective VCCs. This result suggests that vibronic coupling in biphenyl and fluorene occurs mainly on the C1−C2 and C6−C1 bonds, where η_i is large. However, around the C4 atom, although $\Delta\rho$ is large, since v_i is small, η_i is small, which explains why the associated AVCCs are small. For fluorene, since the methylene group's $\Delta\rho$ and v_i are small, its η_i is also small.

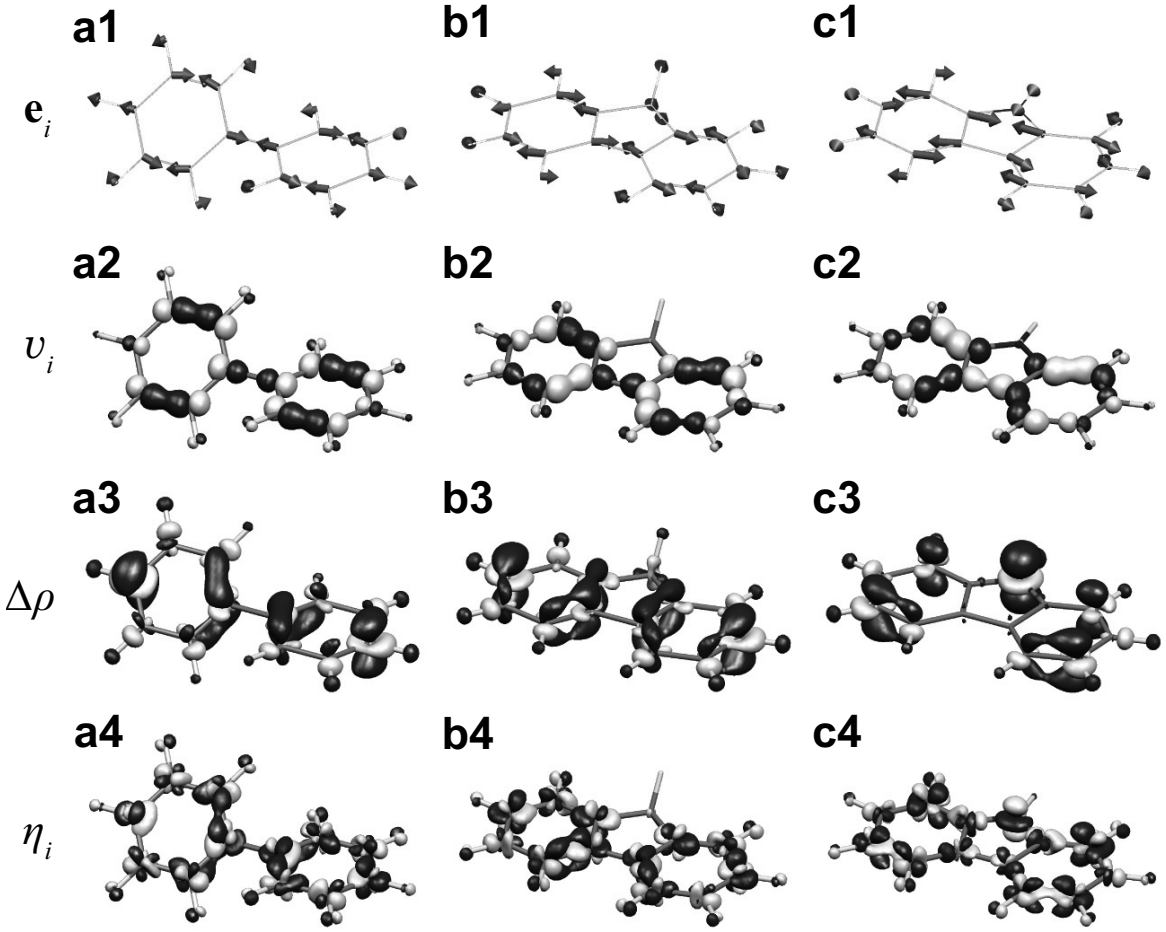

Figure 3.5: (a1)−(c1) C−C stretching modes for biphenyl, fluorene, and carbazole. (a2)−(c2) Corresponding nuclear–electronic potential derivatives at an isosurface value of 0.01 au. (a3)−(c3) Electron-density differences due to ionization at an isosurface value of 0.04 au. (a4)−(c4) Vibronic coupling densities of the C−C stretching modes at an isosurface value of 2.0×10^{-5} au. Dark gray shows where values are negative; light gray shows where values are positive.

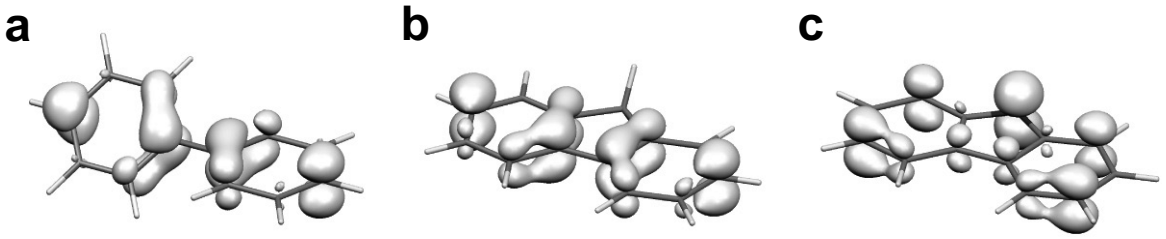

Figure 3.6: HOMO electron-density distributions for various neutral moieties at an isosurface value of 0.04 au: (a) Biphenyl; (b) Fluorene; (c) Carbazole.

Table 3.2: Atomic vibronic coupling constants for C−C stretching modes shown in Fig. 3.5a1–c1. Atomic vibronic coupling constants are in 10^{-4} au.

	Biphenyl	Fluorene	Carbazole
C1	−0.582	−0.628	−0.335
C2	−0.425	−0.127	−0.140
C3	−0.334	−0.269	−0.105
C4	−0.051	0.030	0.042
C5	−0.334	−0.206	−0.153
C6	−0.425	−0.535	−0.505
C7(N)		−0.003	−0.027
H1	0.023		
H2	0.004	0.001	0.014
H3	0.001	0.000	−0.007
H4	0.004	−0.002	0.003
H5	0.023	0.009	−0.003
H6		0.000	0.015
total	−4.192	−3.440	−2.390

Table 3.3: Values of $|\mathbf{e}_A^{(i)}|$ for the three C−C stretching modes in Fig. 3.5a1–c1.

	Biphenyl	Fluorene	Carbazole
C1	0.296	0.309	0.316
C2	0.311	0.279	0.315
C3	0.268	0.320	0.317
C4	0.133	0.169	0.170
C5	0.268	0.190	0.174
C6	0.311	0.337	0.317
C7(N)		0.012	0.011
H1	0.133		
H2	0.099	0.126	0.117
H3	0.045	0.060	0.059
H4	0.099	0.069	0.063
H5	0.133	0.146	0.137
H6		0.010	0.006

Figure 3.6 shows HOMO electron densities for neutral biphenyl, fluorene, and carbazole. The HOMO electron densities have a π-orbital character. By comparing Fig. 3.6a–c with Fig. 3.5a3–c3, we find that regions where $\Delta\rho$ is negative also have a π-orbital character, with similar distribution patterns, suggesting that electron difference comes mainly from the HOMOs. In addition, regions where $\Delta\rho$ is positive have a σ-orbital character, due to relaxation of the occupied molecular orbitals other than the HOMOs. The positive $\Delta\rho$ reduces Coulomb repulsion from the negative $\Delta\rho$ of the π-orbitals.

Figures 3.7 and 3.8 show the AVCDs and reduced AVCDs (RAVCDs), respectively, of the C and N atoms for the C−C stretching mode for carbazole. The AVCD $\eta_{i,A}$ contains contributions for which the space integrals vanish because of symmetries of basis functions and $v_{i,A}$. The RAVCD $\bar{\eta}_{i,A}$ is calculated by subtracting such contributions from the AVCD $\eta_{i,A}$.[50] Hence, the space integrals of the AVCDs and RAVCDs give the corresponding AVCCs:

$$\int \eta_{i,A}(\mathbf{x})\, d\mathbf{x} = \int \bar{\eta}_{i,A}(\mathbf{x})\, d\mathbf{x} = V_{i,A}. \tag{3.12}$$

The distribution pattern for $\bar{\eta}_{i,A}$ is simpler than that for $\eta_{i,A}$. For carbazole, the C1 and C6 atoms contribute significantly to the VCCs (Table 3.2). On the C1 atom, although $\Delta\rho$ is relatively small, since v_i is large, the AVCD $\eta_{i,\mathrm{C1}}$ gives a large positive or negative value around the C1 atom (Fig. 3.7a). The region where values are negative is larger than the region where they are positive. This feature is also observed for $\bar{\eta}_{i,\mathrm{C1}}$ (Fig. 3.8a). On the C1 atom, the region where $\bar{\eta}_{i,\mathrm{C1}}$ is negative is large, so the AVCC is large and negative (-0.335×10^{-4} au). Similarly, on the C6 atom above and below the benzene ring, overlap between v_i and $\Delta\rho$ gives a negative distribution, so the C6 atom has a large negative AVCC (-0.505×10^{-4} au), whose contribution is clearly seen for $\bar{\eta}_{i,\mathrm{C6}}$ (Fig. 3.8f).

On the C5 atom, since $\Delta\rho$ is large, $\bar{\eta}_{i,\mathrm{C5}}$ is also large (Fig. 3.8e). The region where values are negative is larger than the region where they are positive, so the AVCC is negative (-0.153×10^{-4} au). However, since the difference between the negative and positive regions is small, the AVCC is smaller for the C5 atom than for the C1 and C6 atoms.

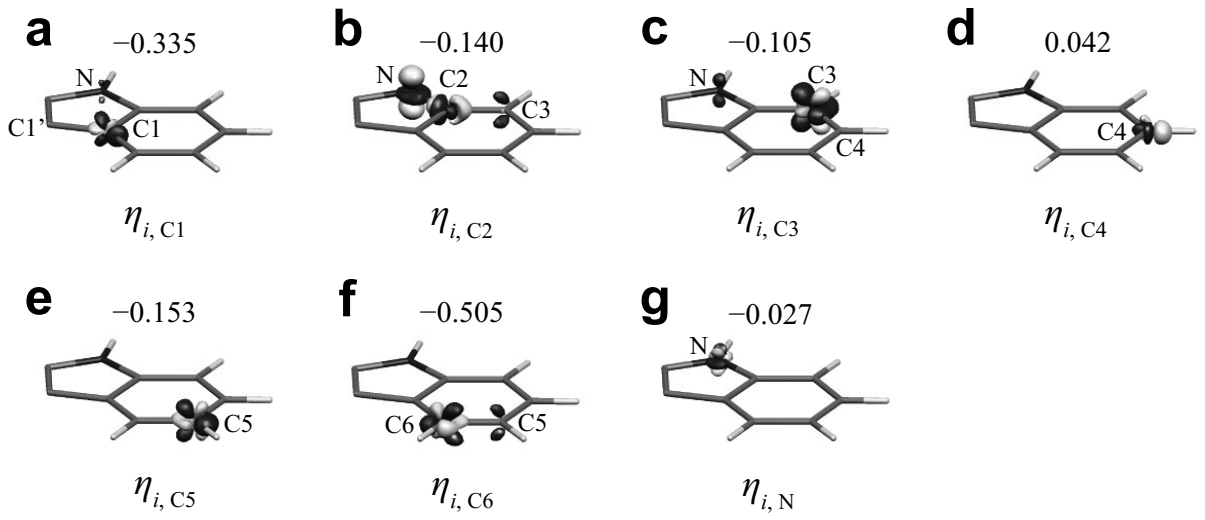

Figure 3.7: Atomic vibronic coupling densities $\eta_{i,A}$ of the C and N atoms for the C−C stretching mode of carbazole at an isosurface value of 2.0×10^{-5} au. Dark gray shows where values are negative; light gray shows where values are positive. The number above each figure is the corresponding atomic vibronic coupling constant.

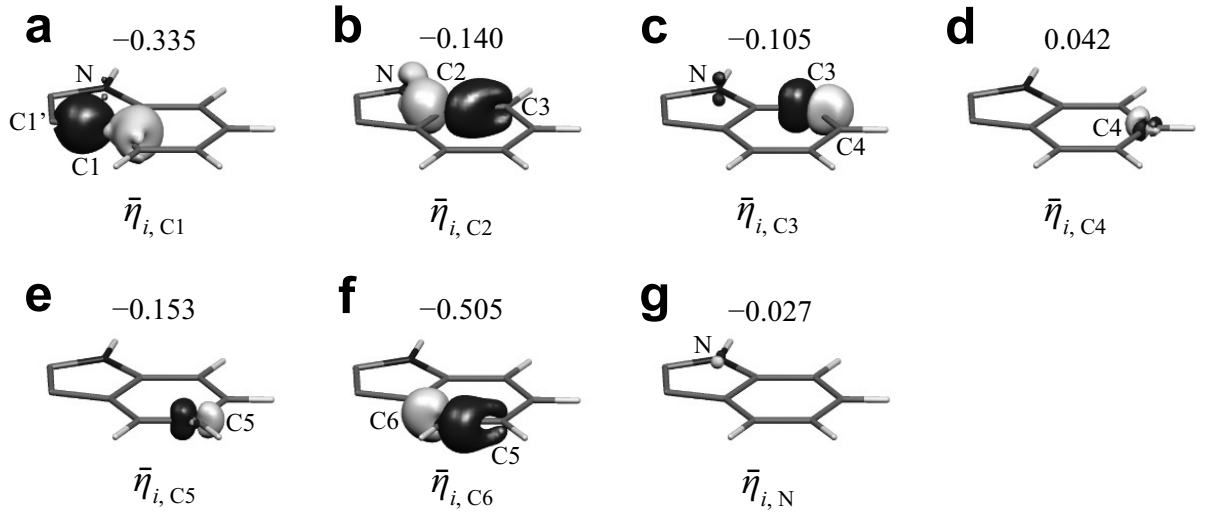

Figure 3.8: Reduced atomic vibronic coupling densities $\bar{\eta}_{i,A}$ of the C and N atoms for the C−C stretching mode of carbazole at an isosurface value of 2.0×10^{-5} au. Dark gray shows where values are negative; light gray shows where values are positive. The number above each figure is the corresponding atomic vibronic coupling constant.

The AVCC of the C3 atom (-0.105×10^{-4} au) is close to that of the C5 atom. This is because the distribution pattern for $\eta_{i,\mathrm{C3}}$ (Fig. 3.7c) is similar to that for $\eta_{i,\mathrm{C5}}$ (Fig. 3.7e). $\eta_{i,\mathrm{C3}}$ and $\bar{\eta}_{i,\mathrm{C3}}$ are negative for the N atom because the C3 atom is located nearby. The region where values are negative is slightly larger than the region where they are positive, which explains why the C3 atom has a small negative AVCC (Fig. 3.8c).

$\Delta\rho$ has a small positive value on the C4−H3 bond. Hence, around the C4 atom, $\eta_{i,\mathrm{C4}}$ and $\bar{\eta}_{i,\mathrm{C4}}$ are small (Fig. 3.7d,3.8d). Because the positive region of $\eta_{i,\mathrm{C4}}$ is larger than the negative region, the C4 atom has a small positive AVCC (0.042×10^{-4} au).

For the C2 atom, both negative and positive $\bar{\eta}_{i,\mathrm{C2}}$ (Fig. 3.8b) regions are largely distributed on the C2−N and C2−C3 bonds. The small AVCC for the C2 atom results from cancellation of these positive and negative regions on the C2−N and C2−C3 bonds.

By comparing $\eta_{i,\mathrm{C2}}$ (Fig. 3.7b) with η_i (Fig. 3.5c4), we find that for the N atom, the η_i distribution comes from $\eta_{i,\mathrm{C2}}$ and not $\eta_{i,\mathrm{N}}$ (Fig. 3.7g). The latter is considerably small because v_i is negligibly small. The small overlap between $\Delta\rho$ and v_i is responsible for the small AVCC of the N atom. v_i for the N−H stretching mode (Fig. 3.4c) is distributed on the N−H6 bond and can overlap with $\Delta\rho$ around the N atom. However, since the overlap region is limited on the N−H6 bond, the VCC of the N−H stretching mode is not large (1.894×10^{-4} au). Thus, imino-bridging changes the $\Delta\rho$ distribution pattern and weakens vibronic coupling in the benzene rings.

We calculated current through a single fluorene and carbazole molecule employing the NEGF theory including inelastic scattering.[13] Here, we consider a suppression effect originating from the intramolecular vibronic coupling on the current. Actually, in the bulk systems, intermolecular vibronic coupling can be a dominant factor governing the suppression effect. However, the small intramolecular vibronic coupling is a necessary condition for design of transporting materials and first, we should consider the suppression effect due to the intramolecular vibronic coupling.

Figure 3.9a shows $I-V$ characteristics. The solid line shows the $I-V$ characteristics in the absence of vibronic coupling; the dot-dashed and dashed lines show the $I-V$ characteristics for carbazole and fluorene, respectively, in the presence of the vibronic coupling. Figure 3.9a shows that the vibronic coupling reduces the current and the suppression effect is larger for fluorene (having the large VCCs) than for carbazole (having the small VCCs). Figure 3.9b shows power loss due to the vibronic coupling. Note that,

without vibronic coupling, the power loss dose not occur. At $V = 2$ V, the power loss in carbazole is about half that in fluorene. Figure 3.9 suggests that a molecule with small VCCs is good charge-transporting and low power-loss material. The carbazole N atom can weaken the vibronic coupling and enhance hole-transporting property.

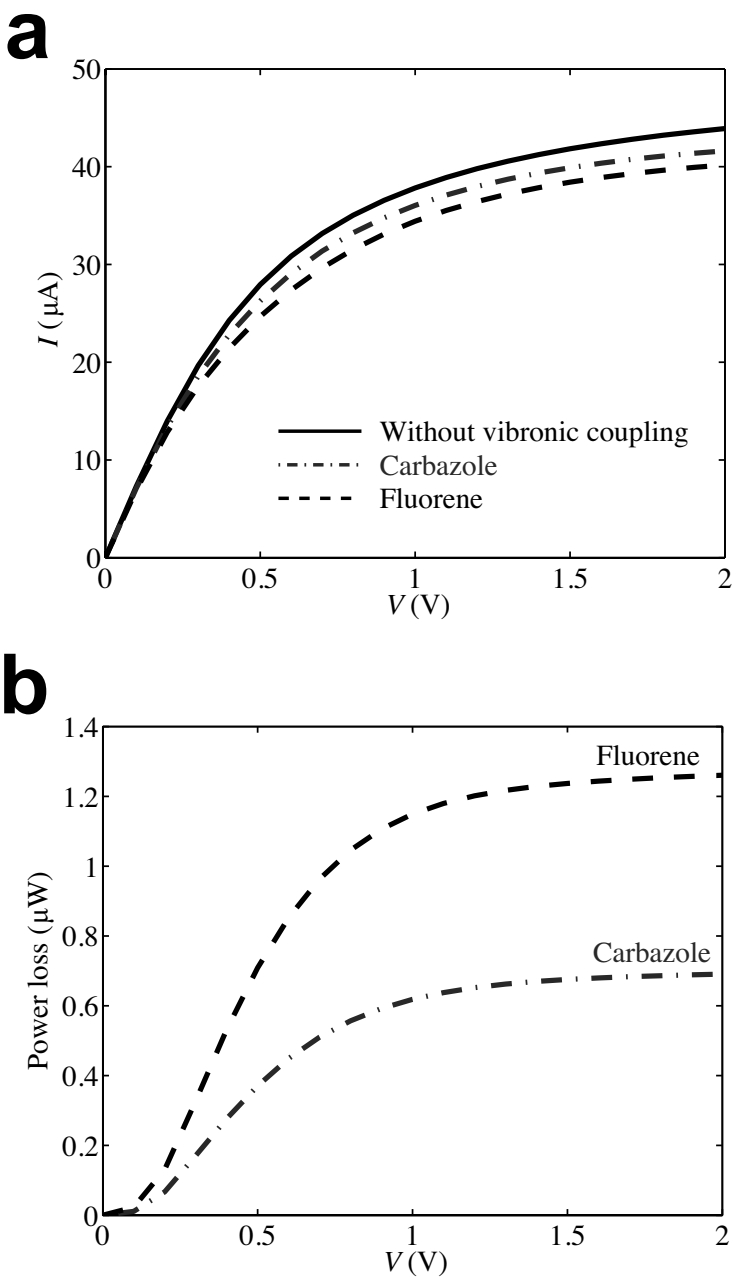

Figure 3.9: (a) Current-voltage characteristics and (b) power loss.

Figure 3.10a1–c1 shows Hartree-Fock (HF) VCCs for biphenyl, fluorene, and carbazole cations. Geometry optimization and vibrational analysis for neutral biphenyl, fluorene, and carbazole were done at the RHF/6-31G+der level of theory. Cationic states of the molecules were calculated at the UHF/6-31G+der level of theory. A scaling factor of 0.8929[51] was used for RHF/6-31G+der theoretical frequencies. All the HF calculations were done using GAMESS package program. The trend in VCC ordering in Fig. 3.10a1–c1 is similar to that in Fig. 3.4a–c; for biphenyl and fluorene, the largest VCC corresponds to a C−C stretching mode (1608.87 and 1610.88 cm^{-1}, respectively); for carbazole, the largest two VCCs correspond to a C−C stretching mode (1620.01 cm^{-1}) and a N−H stretching mode (3490.04 cm^{-1}). The C−C stretching modes having the large VCCs are shown in Fig. 3.10a1–c1. Comparing Fig. 3.10a1–c1 with Fig. 3.4a–c, the VCCs calculated at the UHF/6-31G+der level are large compared with those calculated at the UB3LYP/6-31G+der level. We can understand the reason for the difference in VCC size using the VCD analysis.

Figure 3.10a2–c2 shows v_i for the modes shown in Fig. 3.10a1–c1. Comparing Fig. 3.10a2–c2 with Fig. 3.5a2–c2, v_i calculated using the HF method is as large as that calculated using the B3LYP method, suggesting that electron correlation does not influence v_i distribution significantly.

Figure 3.10a3–c3 shows $\Delta\rho$ for biphenyl, fluorene, and carbazole. The isosurface value in Fig. 3.10a3–c3 is the same in Fig. 3.5a3–c3. $\Delta\rho$ calculated using the HF method has a large value. This is because without electron correlation, electron delocalization is underestimated. $\Delta\rho$ across the C1−C2 and C6−C1 bonds is larger in Fig. 3.10a3 than in Fig. 3.5a3; $\Delta\rho$ across the C1−C2 and C6−C1 bonds is larger in Fig. 3.10b3 than in Fig. 3.5b3; $\Delta\rho$ on the N atom is larger in Fig. 3.10c3 than in Fig. 3.5c3.

Figure 3.10a4–c4 shows η_i calculated at the UHF/6-31G+der level of theory. Large $\Delta\rho$ leads to large η_i and consequently large VCCs. Since $\Delta\rho$ is less delocalized for carbazole than for biphenyl and fluorene, electron correlation effects on $\Delta\rho$ is smaller. Hence, for carbazole, the differences between η_i calculated using the UB3LYP and UHF methods are small compared with those for biphenyl and fluorene. For biphenyl and fluorene, the HF method significantly overestimates the VCCs because $\Delta\rho$ is highly delocalized. The AVCC of the C1 atom of biphenyl and fluorene calculated using the HF method are -1.263×10^{-4} and -1.346×10^{-4} au, respectively, which are more than twice those

calculated using the B3LYP method (-0.582×10^{-4} and -0.628×10^{-4} au, respectively). The VCCs are closely related to the reorganization energy; Large/Small VCCs give a large/small reorganization energy. The overestimation of the reorganization energy with the HF method has been reported by Sancho-García *et al.*[52] For vibronic coupling calculations, the UHF/6-31G+der level of theory gives qualitatively good results, and sometimes quantitative results.

3.5 Conclusions

We calculated the VCDs of biphenyl, fluorene, and carbazole cations. VCD analysis reveals that strong localization of the electron-density difference on the N atom leads to the small VCCs of carbazole. In general, localized electron-density differences on an atom decreases the vibronic coupling and enhances hole mobility. Substituting the biphenyl or fluorenyl moieties in the molecule with the carbazolyl moiety can weaken vibronic coupling in the molecule and improve hole mobility. This guiding principle opens a new way for molecular design of carrier-transporting materials based on VCD analysis. Though the HF method gives qualitatively good results, it sometimes yields overestimated VCC. This is because the electron-density difference calculated by the HF method is highly delocalized over the bonds, compared with the DFT method. Therefore, for carbazole, the HF method yield quantitatively good result, since the electron-density difference in carbazole does not largely delocalized over the bonds.

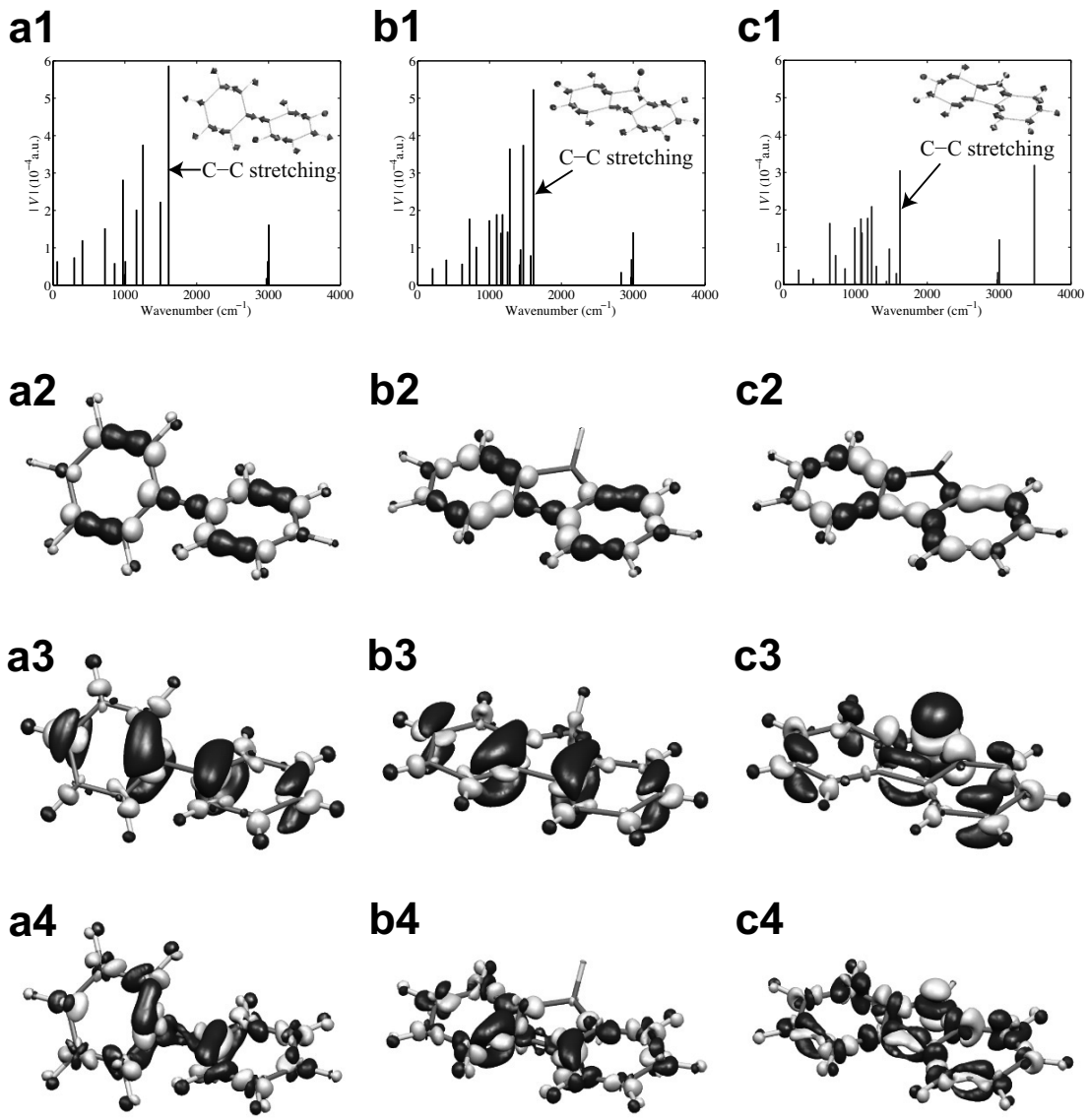

Figure 3.10: Absolute values of vibronic coupling constants $|V|$ for various cations calculated at the UHF/6-31G+der level of theory: (a1) Biphenyl; (b1) Fluorene; (c1) Carbazole. (a2)−(c2) Nuclear–electronic potential derivatives of the modes shown in (a1)−(c1) at an isosurface value of 0.01 au. (a3)−(c3) Electron-density differences due to ionization at an isosurface value of 0.04 au. (a4)−(c4) Vibronic coupling densities at an isosurface value of 2.0×10^{-5} au. Dark gray shows where values are negative; light gray shows where values are positive.

Bibliography

[1] C. W. Tang, S. A. VanSlyke, and C. H. Chen, J. Appl. Phys. **65**, 3610 (1989).

[2] C. W. Tang and S. A. VanSlyke, Appl. Phys. Lett. **51**, 913 (1987).

[3] Y. Shirota, Y. Kuwabara, D. Okuda, R. Okuda, H. Ogawa, H. Inada, T. Wakimoto, H. Nakada, Y. Yonemoto, S. Kawami, and K. Imai, J. Lumin. **72-74**, 985 (1997).

[4] Y. Hamada, T. Sano, K. Shibata, and K. Kuroki, Jpn. J. Appl. Phys. **34**, L824 (1995).

[5] Y. Shirota, Y. Kuwabara, H. Inada, T. Wakimoto, H. Nakada, Y. Yonemoto, S. Kawami, and K. Imai, Appl. Phys. Lett. **65**, 807 (1994).

[6] R. A. Marcus, J. Electroanal. Chem. **483**, 2 (2000).

[7] R. A. Marcus, J. Electroanal. Chem. **438**, 251 (1997).

[8] R. A. Marcus and N. Sutin, Biochim. Biophys. Acta **811**, 265 (1985).

[9] R. A. Marcus, J. Chem. Phys. **43**, 679 (1965).

[10] R. A. Marcus, J. Chem. Phys. **24**, 966 (1956).

[11] P. F. Barbara, T. J. Meyer, and M. A. Ratner, J. Phys. Chem. **100**, 13148 (1996).

[12] V. Coropceanu, N. Gruhn, S. Barlow, C. Lambert, J. Durivage, T. Bill, G. Nöll, S. Marder, and J.-L. Brédas, J. Am. Chem. Soc. **126**, 2727 (2004).

[13] S. Datta, *Quantum Transport: Atom to Transistor* (Cambridge University Press, Cambridge, 2005).

[14] T. Sato, K. Tokunaga, and K. Tanaka, J. Phys. Chem. A **112**, 758 (2008).

[15] K. Tokunaga, T. Sato, and K. Tanaka, J. Mol. Struct. **838**, 116 (2007).

[16] K. Tokunaga, T. Sato, and K. Tanaka, J. Chem. Phys. **124**, 154303 (2006).

[17] T. Sato, K. Tokunaga, and K. Tanaka, J. Chem. Phys. **124**, 024314 (2006).

[18] T. Sato, K. Tokunaga, N. Iwahara, K. Shizu, and K. Tanaka, *Vibronic coupling constant and vibronic coupling density* in *The Jahn-Teller-Effect - Fundamentals and Implications for Physics and Chemistry,* H. Köppel, D. R. Yarkony, and H. Barentzen (Eds) (Springer-Verlag, Berlin and Heidelberg, 2009).

[19] T. Sato, K. Shizu, T. Kuga, K. Tanaka, and H. Kaji, Chem. Phys. Lett. **458**, 152 (2008).

[20] B.-C. Wang, H.-R. Liao, J.-C. Chang, L. Chen, and J.-T. Yeh, J. Lumin. **124**, 333 (2007).

[21] K. Shizu, T. Sato, K. Tanaka, and H. Kaji, Chem. Phys. Lett. **486**, 130 (2010).

[22] J.-H. Pan, Y.-M. Chou, H.-L. Chiu, and B.-C. Wang, J. Phys. Org. Chem. **20**, 743 (2007).

[23] Q. Zhang, J. Chen, Y. Cheng, L. Wang, D. Ma, X. Jing, and F. Wang, J. Mater. Chem. **14**, 895 (2004).

[24] B. E. Koene, D. E. Loy, and M. E. Thompson, Chem. Mater. **10**, 2235 (1998).

[25] V. Rani and K. Santhanam, J. Solid State Electrochem. **2**, 99 (1998).

[26] R. P. Feynman, Phys. Rev. **56**, 340 (1939).

[27] H. Nakatsuji, K. Kanda, and T. Yonezawa, Chem. Phys. Lett. **75**, 340 (1980).

[28] G. Rauhut and P. Pulay, J. Phys. Chem. **99**, 3093 (1995).

[29] M. J. Frisch, G. W. Trucks, H. B. Schlegel, G. E. Scuseria, M. A. Robb, J. R. Cheeseman, J. A. Montgomery, Jr., T. Vreven, K. N. Kudin, J. C. Burant, J. M. Millam, S. S. Iyengar, J. Tomasi, V. Barone, B. Mennucci, M. Cossi, G. Scalmani, N. Rega, G. A. Petersson, H. Nakatsuji, M. Hada, M. Ehara, K. Toyota, R. Fukuda, J. Hasegawa, M. Ishida, T. Nakajima, Y. Honda, O. Kitao, H. Nakai, M. Klene, X.

Li, J. E. Knox, H. P. Hratchian, J. B. Cross, V. Bakken, C. Adamo, J. Jaramillo, R. Gomperts, R. E. Stratmann, O. Yazyev, A. J. Austin, R. Cammi, C. Pomelli, J. W. Ochterski, P. Y. Ayala, K. Morokuma, G. A. Voth, P. Salvador, J. J. Dannenberg, V. G. Zakrzewski, S. Dapprich, A. D. Daniels, M. C. Strain, O. Farkas, D. K. Malick, A. D. Rabuck, K. Raghavachari, J. B. Foresman, J. V. Ortiz, Q. Cui, A. G. Baboul, S. Clifford, J. Cioslowski, B. B. Stefanov, G. Liu, A. Liashenko, P. Piskorz, I. Komaromi, R. L. Martin, D. J. Fox, T. Keith, M. A. Al-Laham, C. Y. Peng, A. Nanayakkara, M. Challacombe, P. M. W. Gill, B. Johnson, W. Chen, M. W. Wong, C. Gonzalez, and J. A. Pople, GAUSSIAN 03, Revision D.02, Gaussian, Inc., Wallingford, CT, 2004.

[30] A. Almenningen, O. Bastiansen, L. Fernholt, B. N. Cyvin, S. J. Cyvin, and S. Samdal, J. Mol. Struct. **128**, 59 (1985).

[31] O. Bastiansen, Acta Chem. Scand. **3**, 408 (1949).

[32] H. Suzuki, Bull. Chem. Soc. Jpn. **32**, 1340 (1959).

[33] G. P. Charbonneau and Y. Delugeard, Acta Crystallogr., Sect. B **33**, 1586 (1977).

[34] A. Hargreaves and S. H. Rizvi, Acta Crystallogr. **15**, 365 (1962).

[35] J. Trotter, Acta Crystallogr. **14**, 1135 (1961).

[36] G. Robertson., Nature **191**, 593 (1961).

[37] G. P. Charbonneau and Y. Delugeard, Acta Crystallogr., Sect. B **32**, 1420 (1976).

[38] G. M. Brown and M. H. Bortner, Acta Crystallogr. **7**, 139 (1954).

[39] V. K. Belsky, V. E. Zavodnik, and V. M. Vozzhennikov, Acta Crystallogr., Sect. C **40**, 1210 (1984).

[40] R. E. Gerkin, A. P. Lundstedt, and W. J. Reppart, Acta Crystallogr., Sect. C **40**, 1892 (1984).

[41] R. E. Gerkin and W. J. Reppart, Acta Crystallogr., Sect. C **42**, 480 (1986).

[42] M. Kurahashi, M. Fukuyo, A. Shimada, A. Furusaki, and I. Nitta, Bull. Chem. Soc. Jpn. **42**, 2174 (1969).

[43] M. W. Schmidt, K. K. Baldridge, J. A. Boatz, S. T. Elbert, M. S. Gordon, J. H. Jensen, S. Koseki, N. Matsunaga, K. A. Nguyen, S. J. Su, T. L. Windus, M. Dupins, and J. A. Montgomery, J. Comput. Chem. **14**, 1347 (1993).

[44] Y. Park, V. Choong, Y. Gao, B. R. Hsieh, and C. W. Tang, Appl. Phys. Lett. **68**, 2699 (1996).

[45] P. A. Lane, G. P. Kushto, and Z. H. Kafafi, Appl. Phys. Lett. **90**, 023511 (2007).

[46] A. Bree, C. Y. Pang, and L. Rabeneck, Spectrochim. Acta A **27**, 1293 (1971).

[47] A. Bree and R. Zwarich, J. Chem. Phys. **51**, 912 (1969).

[48] A. Bree and R. Zwarich, J. Chem. Phys. **49**, 3344 (1968).

[49] M. Malagoli and J.-L. Brédas, Chem. Phys. Lett. **327**, 13 (2000).

[50] K. Shizu, T. Sato, and K. Tanaka, Chem. Phys. **369**, 108 (2010).

[51] J. A. Pople, M. Head-Gordon, D. J. Fox, K. Raghavachari, and L. A. Curtiss, J. Chem. Phys. **90**, 5622 (1989).

[52] J. C. Sancho-García and A. J. Pérez-Jiménez, J. Chem. Phys. **129**, 024103 (2008).

Chapter 4

Inverse Proportionality between Vibronic Coupling Constant and Electron-Density Difference Distribution

4.1 Introduction

Vibronic coupling or electron-phonon coupling plays an important role in charge transport, superconductivity, chemical reaction, luminescence, etc. In charge transport process, for example, vibronic coupling inhibits carrier transport, and creates Joule heat. Hence, molecules exhibiting weak vibronic coupling are preferable as charge-transporting materials. Although much effort has been directed towards effects of vibronic coupling in charge-transport process,[1,2] little attention has been paid to designing charge-transporting materials by controlling vibronic coupling.

We have theoretically investigated a hole-transporting material, N,N'-diphenyl-N,N'-di(m-tolyl)benzidine[3–5] (TPD), which has been widely used as a hole-transport layer in multilayer organic light-emitting diodes (OLEDs).[6–9] We have shown that the localization of the electron-density difference $\Delta\rho$ on the two N atoms is responsible for the weak vibronic coupling in TPD cation, and it is one origin of high mobility of TPD.[10] This result suggests that the extent of $\Delta\rho$ distribution significantly influences the strength of vibronic coupling and charge-transport property.

The relationship between extent of π-conjugation and strength of vibronic coupling has been investigated by Devos and Lannoo.[11] They have shown that stabilization energy due to vibronic coupling is inversely proportional to the number of π-bonded carbon atoms N_π. This $1/N_\pi$ relationship of the stabilization energy approximately holds for various π-conjugated compounds up to $N_\pi = 60$.[11–13]

In this chapter, we investigate the relationship between the vibronic coupling and the extent of $\Delta\rho$ distribution. We construct ideal models with a localized and delocalized electronic state using ethylene dimer cations as an example, and calculate their vibronic coupling constants (VCCs). The difference between the VCCs of the two electronic states is analyzed employing vibronic coupling density analysis,[10] which describes local properties of vibronic coupling based on the electronic and vibrational structures. The vibronic coupling density analysis gives a clear explanation of the reason for the $1/N_\pi$ relationship.

4.2 Vibronic Coupling Density Analysis

The VCC V_i for the ith normal mode is defined by

$$V_i = \left\langle \Psi^+(\mathbf{r}, \mathbf{R_0}) \left| \left(\frac{\partial \mathcal{H}_\mathrm{e}(\mathbf{r}, \mathbf{R})}{\partial Q_i} \right)_{\mathbf{R_0}} \right| \Psi^+(\mathbf{r}, \mathbf{R_0}) \right\rangle, \tag{4.1}$$

where $\mathbf{r}$ and $\mathbf{R}$ denote sets of electronic and nuclear coordinates, respectively, $\mathbf{R_0}$ is an equilibrium geometry of the neutral state, $\mathcal{H}_\mathrm{e}(\mathbf{r}, \mathbf{R})$ is the electronic Hamiltonian, Q_i is a mass-weighted normal coordinate for the ith mode, and $\Psi^+(\mathbf{r}, \mathbf{R_0})$ is the electronic wave function of the cationic state at the equilibrium geometry $\mathbf{R_0}$. Only totally symmetric modes have non-zero VCCs.

V_i can be written as[14]

$$V_i = \int \Delta\rho(\mathbf{x}) \times v_i(\mathbf{x})\, d\mathbf{x}, \tag{4.2}$$

where $\mathbf{x}$ is a position in the three-dimensional space, $\Delta\rho$ is the electron-density difference between the cationic and neutral states at $\mathbf{R_0}$ and satisfies the following relation

$$\int \Delta\rho(\mathbf{x})\, d\mathbf{x} = -1. \tag{4.3}$$

v_i is the one-electron part of the derivative of the nuclear–electronic potential and written as

$$v_i(\mathbf{x}) = \sum_A -\frac{Z_A}{\sqrt{M_A}} \mathbf{e}_A^{(i)} \cdot \frac{\mathbf{x} - \mathbf{R}_A}{|\mathbf{x} - \mathbf{R}_A|^3}, \tag{4.4}$$

where M_A and Z_A are the mass and charge of the Ath nucleus, respectively, $\mathbf{e}_A^{(i)}$ is the Ath component of the ith vibrational mode in the mass-weighted coordinates Q_i, and $\mathbf{R}_A$ is the position of the Ath nucleus. The set of $\mathbf{e}^{(i)}$ is orthonormalized:

$$\mathbf{e}^{(i)} \cdot \mathbf{e}^{(j)} = \delta_{ij}. \tag{4.5}$$

$\Delta\rho \times v_i$ in Eq. (4.2) contains components of which the integral over space vanishes. Reduced vibronic coupling density[15] (RVCD) $\bar{\eta}_i$ is obtained by subtracting those vanishing components which are not essential to the vibronic coupling, from $\Delta\rho \times v_i$. Integral over space of $\bar{\eta}_i$ gives again V_i:

$$V_i = \int \bar{\eta}_i \left(\mathbf{x}\right) d\mathbf{x}. \tag{4.6}$$

$\bar{\eta}_i$ gives a local picture of vibronic coupling in a molecule. Analyses based on the vibronic coupling density have revealed the reason for VCC magnitudes[14,16,17] and enable us to relate the VCC to $\Delta\rho$ and v_i.

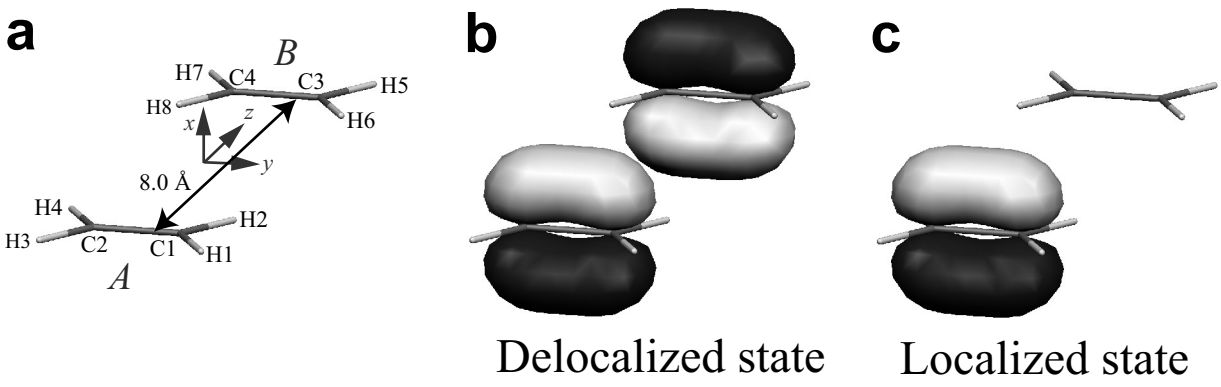

Figure 4.1: (a) Assumed structure of ethylene dimer with an atomic numbering scheme. The two ethylene molecules lie in the yz plane and the centers of mass of them are placed on the z axis. HOMOs of the ethylene dimers: (b) delocalized state; (c) localized state. The isosurface values for (b) and (c) are $0.08/\sqrt{2}$ and 0.08 a.u., respectively.

4.3 Method of Calculation

First, we optimized the structure of neutral ethylene monomer assuming D_{2h} symmetry. Employing vibrational analysis, we confirmed that the optimized geometry is a stationary minima. The cationic state is calculated at the equilibrium geometry. The electronic structures of the neutral and cationic states were calculated at the B3LYP/6-311+G(d) and UB3LYP/6-311+G(d) levels of theory, respectively. A scaling factor of 0.963 was used for B3LYP/6-311+G(d) theoretical frequencies.[18]

Second, we calculated electronic structures of ethylene dimer. Fig. 4.1a shows a nuclear configuration of the ethylene dimer with the labeling of the ethylene molecules. In the following, the two ethylene molecules are referred to as ethylene A and B. Both ethylene A and B lie in the yz plane and the centers of mass of them are placed on the z axis. The distance between the centers of mass is set to be 8.0 Å.

We calculated the electronic states in which wave functions are delocalized over the two ethylene molecules (Fig. 4.1b) by setting the geometrical parameters of the two ethylene molecules to be the same as those of the optimized ethylene monomer. The geometry of the dimer belongs to the D_{2h} point group. We calculated the electronic states in which wave functions are strongly localized on the ethylene A (Fig. 4.1c) by setting the C3−C4 bond to be 0.001 Å shorter than the C1−C2 bond and assuming C_{2v} symmetry. The wave functions of the neutral and cationic states and vibrational modes were calculated using these two geometries. The dimers were also calculated at the same level of theory as the monomer.

All the *ab initio* calculations were done employing Gaussian 03 software.[19]

4.4 Results and Discussion

The optimized C=C and C−H bond lengths of the ethylene monomer are 1.3288 and 1.0859 Å, respectively. The calculated C−H bond length is within the error bar of the experimental value determined from the rotational constants of deuterated ethylenes,[20] while the calculated C=C bond length is about 0.009 Å too long. The optimized CCH angle is 121.84°, which is about 0.56° too large. Calculated frequencies ω_i and VCCs V_i of totally symmetric modes of the ethylene monomer and dimers are listed in Tables 4.1 and 4.2, respectively. In Table 4.2, superscripts deloc and loc mean delocalized (Fig. 4.1b)

and localized states (Fig. 4.1c), respectively. We use this notation in the following.

The optimized structure of the ethylene monomer belongs to D_{2h} symmetry, leading to the following normal mode distribution

$$\Gamma_{\text{vib}}\left(D_{2h}\right) = 3A_g + A_u + 2B_{1u} + B_{2g} + 2B_{2u} + 2B_{3g} + B_{3u}. \tag{4.7}$$

The three a_g modes are C−H bending ($a_g(1)$), C=C stretching ($a_g(2)$), and C−H stretching ($a_g(3)$) modes, respectively (Table 4.1). The frequency of the $a_g(1)$ mode is calculated to be about 13 cm^{-1} smaller than the experimental value, while those of the $a_g(2)$ and $a_g(3)$ modes are in good agreement with the experimental values.[21] The C=C stretching and C−H bending modes have the large VCCs while the C−H stretching mode has the small VCC. This trend in the VCCs is supported by a photoelectron spectrum[22] and consistent with theoretical results calculated at the Hartree-Fock level.[23]

The normal mode distribution of the delocalized state of the dimer is as follows:

$$\Gamma_{\text{vib}}^{\text{deloc}}\left(D_{2h}\right) = 6A_g + 3A_u + 2B_{1g} + 5B_{1u} + 2B_{2g} + 5B_{2u} + 5B_{3g} + 2B_{3u}. \tag{4.8}$$

All the vibrations are delocalized over the ethylene A and B. The $a_g^{\text{deloc}}(3)$, $a_g^{\text{deloc}}(4)$, and $a_g^{\text{deloc}}(5)$ modes are C−H bending, C=C stretching, and C−H stretching modes, respectively, and are in-phase combinations of the $a_g(1)$, $a_g(2)$, and $a_g(3)$ modes of the monomer. Out-of-phase combinations of these modes give non-totally symmetric C−H bending, C=C stretching, and C−H stretching modes of the dimer. Hence, their VCCs vanish. The $a_g^{\text{deloc}}(3)$ and $a_g^{\text{deloc}}(4)$ modes have the large VCCs, of which values are roughly $1/\sqrt{2}$ of those of $a_g(1)$ and $a_g(2)$ modes of the monomer: $V_1/\sqrt{2} = -2.92 \times 10^{-4}$ a.u. $\approx V_3^{\text{deloc}}$; $V_2/\sqrt{2} = -5.54 \times 10^{-4}$ a.u. $\approx V_4^{\text{deloc}}$. Since the stabilization energy due to the vibronic coupling of the ith mode is expressed as $V_i^2/2\omega_i^2$,[10] the stabilization energies of $a_g^{\text{deloc}}(3)$ and $a_g^{\text{deloc}}(4)$ modes are 1/2 of those of $a_g(1)$ and $a_g(2)$ modes, respectively. In other words, stabilization energy is inversely proportional to the number of atoms N over which HOMO is delocalized: $N = 2$ for the monomer; $N = 4$ for the delocalized state of the dimer (Fig. 4.1b). This $1/N$ relationship of the vibronic coupling has been observed for various π-conjugated systems.[11–13] By contrast, the VCCs of the C−H stretching modes of the monomer and dimer are comparable and hence, do not satisfy the $1/N$ relationship.

The VCCs of the $a_g^{\text{deloc}}(1)$, $a_g^{\text{deloc}}(2)$, and $a_g^{\text{deloc}}(6)$ modes are quite small. This is because these modes are combinations of the modes of the monomer of which VCCs vanish: the

$a_g^{\mathrm{deloc}}(1)$ mode is a combination of the translational mode of the monomer along the z axis, in which the intermonomer distance changes; the $a_g^{\mathrm{deloc}}(2)$ and $a_g^{\mathrm{deloc}}(6)$ modes are combinations of the b_{2u} modes of the monomer. The VCCs of the translational and b_{2u} modes of the monomer are vanishing.

The normal mode distribution of the localized state of the dimer is as follows:

$$\Gamma_{\mathrm{vib}}^{\mathrm{loc}}\left(C_{2v}\right) = 11A_1 + 5A_2 + 4B_1 + 10B_2. \tag{4.9}$$

The number of totally symmetric modes of the localized state is about twice that of the delocalized state, since one of the C_2 axes disappears by setting the C3−C4 bond to be shorter than the C1−C2 bond. The $a_1^{\mathrm{loc}}(1)$ mode is a translational mode, in which the intermonomer distance changes. The vibration of the $a_1^{\mathrm{loc}}(1)$ mode is delocalized over the two ethylene molecules. The remaining ten totally symmetric modes are classified with respect to two types of vibration (Table 4.2): vibrations strongly localized on the ethylene A (marked with the superscript A) and those strongly localized on the ethylene B (marked with the superscript B). As is observed for the delocalized state, $a_1^{\mathrm{loc}}(2)$, $a_1^{\mathrm{loc}}(3)$, $a_1^{\mathrm{loc}}(10)$, and $a_1^{\mathrm{loc}}(11)$ modes that are combinations of the b_{2u} modes of the monomer have quite small VCCs.

The $a_1^{\mathrm{loc}}(4)$, $a_1^{\mathrm{loc}}(5)$, $a_1^{\mathrm{loc}}(6)$, $a_1^{\mathrm{loc}}(7)$, $a_1^{\mathrm{loc}}(8)$, and $a_1^{\mathrm{loc}}(9)$ modes are combinations of the $a_g(1)$, $a_g(2)$, and $a_g(3)$ modes of the monomer. The VCCs of the $a_1^{\mathrm{loc}}(4)$, $a_1^{\mathrm{loc}}(6)$, and $a_1^{\mathrm{loc}}(8)$ modes are approximately equal to those of $a_g(1)$, $a_g(2)$, and $a_g(3)$ modes. For the localized state, since the HOMO is dominantly distributed on the ethylene A (Fig. 4.1c), $N = 2$ (the same N value for the monomer). Hence, the $1/N$ relationship holds also for this case. The VCCs of the $a_1^{\mathrm{loc}}(5)$, $a_1^{\mathrm{loc}}(7)$, and $a_1^{\mathrm{loc}}(9)$ modes are quite small, suggesting that the vibronic coupling is weak on the ethylene B.

Table 4.1: Calculated frequencies ω_i (cm^{-1}) and vibronic coupling constants V_i (10^{-4} a.u.) of totally symmetric modes of the ethylene monomer. Bend. and str. mean bending and stretching modes, respectively.

Mode	ω_i	V_i	
$a_g(1)$	1330.63	-4.124	C−H bend.
$a_g(2)$	1627.46	-7.838	C=C str.
$a_g(3)$	3021.50	-1.458	C−H str.

Table 4.2: Calculated frequencies ω_i (cm^{-1}) and vibronic coupling constants V_i (10^{-4} a.u.) of totally symmetric modes of the ethylene dimers. Superscripts deloc and loc mean the delocalized and localized states, respectively. Trans., bend., and str. mean translational, bending, and stretching modes, respectively.

Delocalized state				Localized state			
Mode	$\omega_i^{\mathrm{deloc}}$	V_i^{deloc}		Mode	ω_i^{loc}	V_i^{loc}	
$a_g^{\mathrm{deloc}}(1)$	1.66	-0.056	Trans.	$a_1^{\mathrm{loc}}(1)$	1.66	-0.001	Trans.
$a_g^{\mathrm{deloc}}(2)$	809.10	-0.057	C−H bend.	$a_1^{\mathrm{loc}}(2)$	808.53	-0.008	C−H bend.^{A}
				$a_1^{\mathrm{loc}}(3)$	809.03	-0.049	C−H bend.^{B}
$a_g^{\mathrm{deloc}}(3)$	1330.79	-2.686	C−H bend.	$a_1^{\mathrm{loc}}(4)$	1329.27	-4.052	C−H bend.^{A}
				$a_1^{\mathrm{loc}}(5)$	1330.63	-0.636	C−H bend.^{B}
$a_g^{\mathrm{deloc}}(4)$	1627.59	-5.135	C=C str.	$a_1^{\mathrm{loc}}(6)$	1624.44	-7.713	C=C str.^{A}
				$a_1^{\mathrm{loc}}(7)$	1627.46	-0.213	C=C str.^{B}
$a_g^{\mathrm{deloc}}(5)$	3021.69	-1.818	C−H str.	$a_1^{\mathrm{loc}}(8)$	3021.62	-1.418	C−H str.^{A}
				$a_1^{\mathrm{loc}}(9)$	3021.68	-0.121	C−H str.^{B}
$a_g^{\mathrm{deloc}}(6)$	3102.84	-0.012	C−H str.	$a_1^{\mathrm{loc}}(10)$	3102.74	-0.167	C−H str.^{B}
				$a_1^{\mathrm{loc}}(11)$	3102.93	-0.070	C−H str.^{A}

Let us now discuss the reason for the $1/N$ relationship employing the vibronic coupling density analysis for the C=C stretching modes of the dimers. Figs. 4.2a and 4.2b show the $a_g^{\mathrm{deloc}}(4)$ and $a_1^{\mathrm{loc}}(6)$ modes, respectively. In the $a_1^{\mathrm{loc}}(6)$ mode, the displacement of the nuclei of the ethylene A is large while that of the ethylene B is quite small, reflecting that half of components of $\mathbf{e}^{(i)}$ (corresponding to the ethylene A) are large and the remaining components (corresponding to the ethylene B) are quite small. In the $a_g^{\mathrm{deloc}}(4)$ mode, the nuclei of the ethylene A and B are symmetrically displaced, reflecting that all the components of $\mathbf{e}^{(i)}$ have values. Since $\mathbf{e}^{(i)}$ is normalized by the condition (4.5), the components of $\mathbf{e}^{(i)}$ for the $a_g^{\mathrm{deloc}}(4)$ mode are $1/\sqrt{2}$ of those of the $a_1^{\mathrm{loc}}(6)$ mode.

Fig. 4.2 shows this relation. Each number in Fig. 4.2 is the norm of the Ath component of the ith vibrational mode in the mass-weighted coordinates $\left|\mathbf{e}_A^{(i)}\right|$. By comparing the $\left|\mathbf{e}_A^{(i)}\right|$ for the C1 and H1 atoms, the values for the delocalized state are almost $1/\sqrt{2}$ of those for the localized state: $0.60/\sqrt{2} = 0.42 \approx 0.43$; $0.26/\sqrt{2} = 0.18$. Hence, v_i for the $a_g^{\mathrm{deloc}}(4)$ mode (v_4^{deloc}) is nearly $1/\sqrt{2}$ of that for the $a_1^{\mathrm{loc}}(6)$ mode (v_6^{loc}), per Eq. (4.4). Figs. 4.3a and 4.3b show v_4^{deloc} and v_6^{loc}, respectively. The isosurface value for v_4^{deloc} is set to be $1/\sqrt{2}$ of that for v_6^{loc}. Around the ethylene A, the shape of the isosurface in Fig. 4.3a is almost the same as that in Fig. 4.3b, reflecting that around the ethylene A, v_4^{deloc} is nearly $1/\sqrt{2}$ of v_6^{loc}. Since the $a_1^{\mathrm{loc}}(6)$ mode is strongly localized on the ethylene A, $\left|\mathbf{e}_A^{(i)}\right|$ values for the ethylene B are almost 0, and hence, v_6^{loc} is quite small around the ethylene B.

Fig. 4.4 shows the electron-density difference $\Delta\rho$. The negative $\Delta\rho$ (the dark-gray region) is largely distributed over the C=C bonds. Comparing Fig. 4.4a with Fig. 4.1b and Fig. 4.4b with Fig. 4.1c, the distribution pattern of the negative $\Delta\rho$ is similar to that of the HOMOs, reflecting that an electron is removed dominantly from the HOMOs. The positive $\Delta\rho$ (the light-gray region) is distributed between the negative regions and relaxes the Coulomb repulsion between them. σ-bond-like shape of the positive $\Delta\rho$ originates from the orbital relaxation of doubly-occupied orbitals other than the HOMOs.

In Fig. 4.4, the isosurface value for $\Delta\rho^{\mathrm{deloc}}$ is set to be 1/2 of that for $\Delta\rho^{\mathrm{loc}}$. Around the ethylene A, the shape of isosurface in Fig. 4.4a is almost the same as that in Fig. 4.4b, reflecting that around the ethylene A, $\Delta\rho^{\mathrm{deloc}}$ is smaller by a factor of 2 than $\Delta\rho^{\mathrm{loc}}$. Not that the space integration of $\Delta\rho$ is equal to -1 regardless of its distribution pattern,

per Eq. (4.3):

$$\int \Delta\rho^{\mathrm{deloc}} d\mathbf{x} = \int \Delta\rho^{\mathrm{loc}} d\mathbf{x} = -1. \tag{4.10}$$

$\Delta\rho^{\mathrm{loc}}$ is almost equivalently distributed around the H1 and H2 atoms, while $\Delta\rho^{\mathrm{deloc}}$ is distributed more largely around the H1 atom than around the H2 atom, which is due to the Coulomb repulsion between excess charges on the two ethylene molecules.

The reduced vibronic coupling density $\bar{\eta}_i$ is proportional to the product $\Delta\rho \times v_i$. Around the ethylene A, since $\Delta\rho^{\mathrm{deloc}} \approx \Delta\rho^{\mathrm{loc}}/2$ and $v_4^{\mathrm{deloc}} \approx v_6^{\mathrm{loc}}/\sqrt{2}$,

$$\bar{\eta}_4^{\mathrm{deloc}} \approx \frac{1}{2\sqrt{2}} \bar{\eta}_6^{\mathrm{loc}}. \tag{4.11}$$

Fig. 4.5 shows this relation: the distribution range of $\bar{\eta}_4^{\mathrm{deloc}}$ around the ethylene A/B (of which isosurface value is set to be $1/2\sqrt{2}$ of that for $\bar{\eta}_6^{\mathrm{loc}}$) is almost identical with that of $\bar{\eta}_6^{\mathrm{loc}}$ around the ethylene A. $\bar{\eta}_4^{\mathrm{deloc}}$ is distributed twice as widely as $\bar{\eta}_6^{\mathrm{loc}}$. Hence,

$$\int \bar{\eta}_4^{\mathrm{deloc}} d\mathbf{x} \approx \frac{1}{\sqrt{2}} \int \bar{\eta}_6^{\mathrm{loc}} d\mathbf{x}, \tag{4.12}$$

that is, $V_4^{\mathrm{deloc}} \approx V_6^{\mathrm{loc}}/\sqrt{2}$. Thus, delocalization of $\Delta\rho$ decreases $\bar{\eta}_i$ and consequently, V_i. We can rephrase the $1/N_\pi$ relationship proposed by Devos and Lannoo[11] as follows: magnitude of vibronic coupling constant is inversely proportional to the square root of the number of atoms over which $\Delta\rho$ is distributed. Using this guiding principle, we can design molecules with small VCCs by delocalizing $\Delta\rho$ over equivalent fragments. Thus, we can tune vibronic coupling and design functional materials such as charge-transporting materials through controlling $\Delta\rho$ distribution. Actually, we have succeeded in designing an efficient electron-transporting material consisting of six equivalent triphenylborane units with low-power consumption.[24]

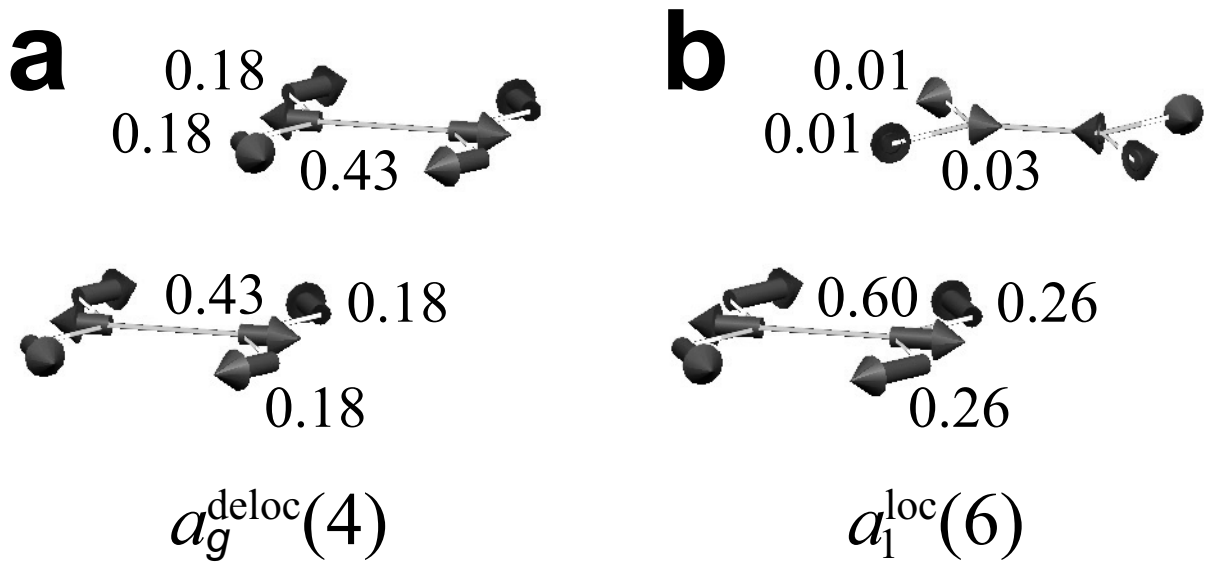

Figure 4.2: Vibrational modes of the ethylene dimers: (a) $a_g^{\mathrm{deloc}}(4)$ mode for the delocalized state; (b) $a_1^{\mathrm{loc}}(6)$ mode for the localized state. Numbers are the components of the ith vibrational mode in the mass-weighted coordinates $\left|\mathbf{e}_A^{(i)}\right|$.

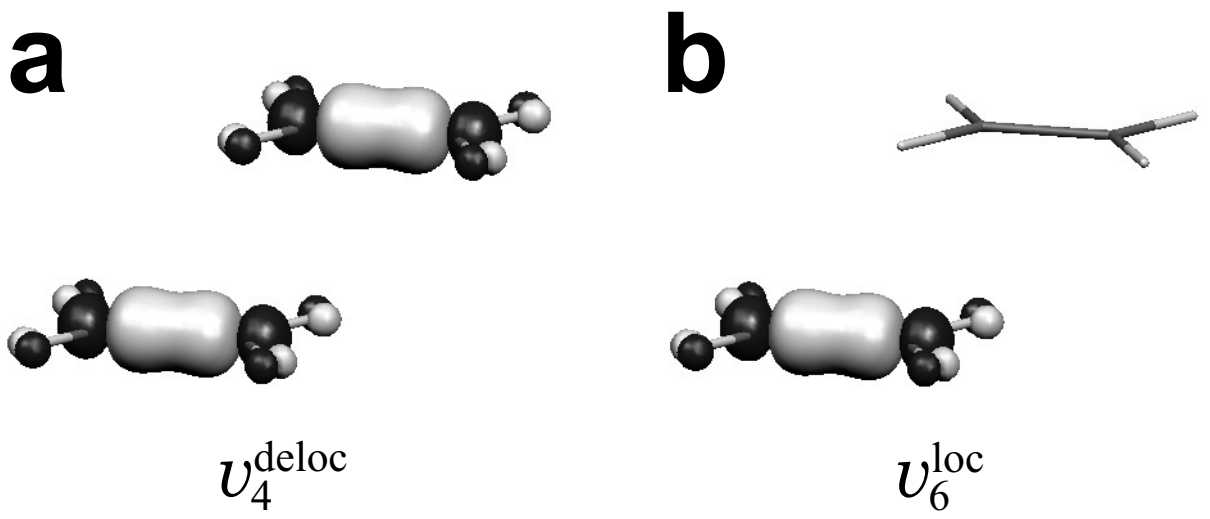

Figure 4.3: One-electron part of derivative of nuclear–electronic potential v_i of the ethylene dimers: (a) v_4^{deloc}; (b) v_6^{deloc}. The isosurface values for (a) and (b) are $0.02/\sqrt{2}$ and 0.02 a.u., respectively. Dark gray shows where values are negative; light gray shows where values are positive.

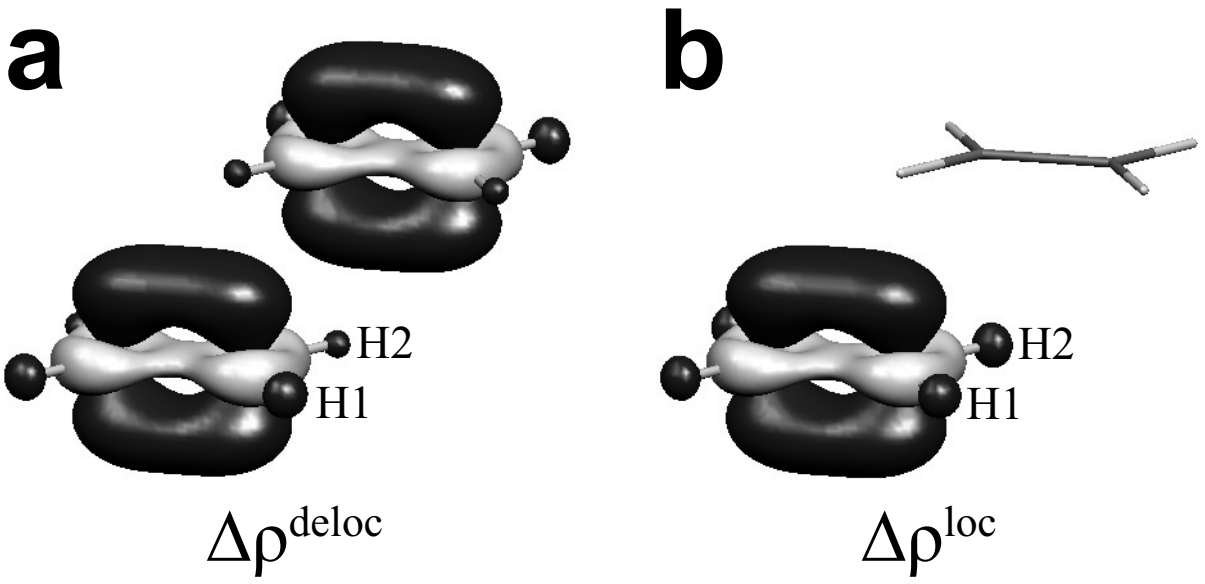

Figure 4.4: Electron-density difference $\Delta\rho$ of the ethylene dimers: (a) $\Delta\rho^{\mathrm{deloc}}$; (b) $\Delta\rho^{\mathrm{loc}}$. The isosurface values for (a) and (b) are 0.01/2 and 0.01 a.u., respectively. Dark gray shows where values are negative; light gray shows where values are positive.

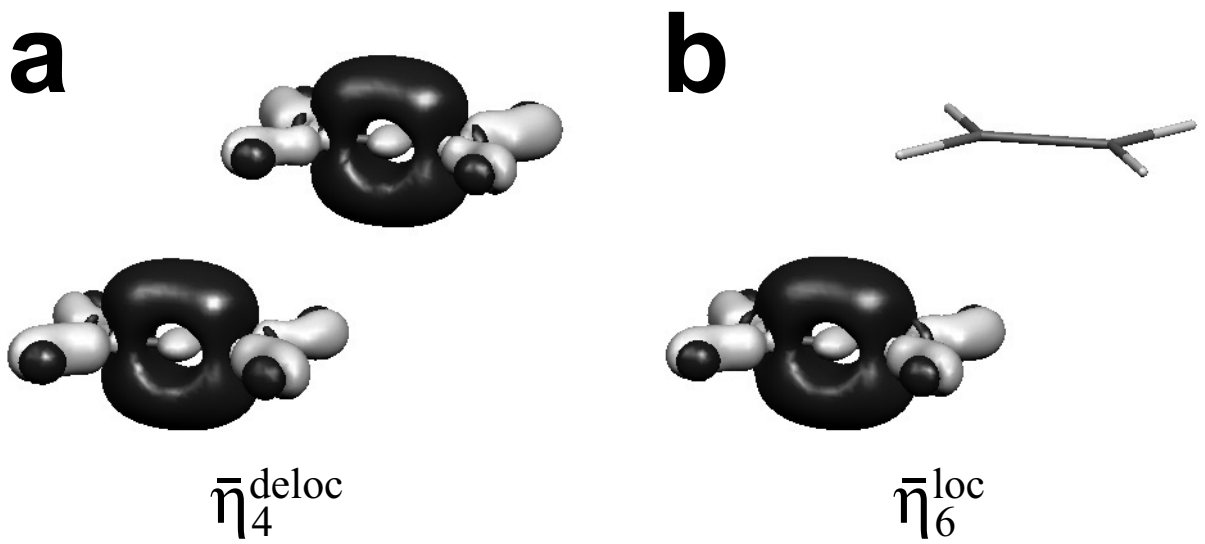

Figure 4.5: Reduced vibronic coupling density $\bar{\eta}_i$ of the ethylene dimers: (a) $\bar{\eta}_4^{\mathrm{deloc}}$ for the delocalized state; (b) $\bar{\eta}_6^{\mathrm{loc}}$ for the localized state. The isosurface values for (a) and (b) are $1/2\sqrt{2}\times10^{-4}$ and 1×10^{-4} a.u., respectively. Dark gray shows where values are negative; light gray shows where values are positive.

4.5 Conclusions

We investigated the relation between the strength of vibronic coupling and the extent of $\Delta\rho$ distribution by choosing ethylene dimer as an example. We calculated and compared vibronic coupling constants of the state in which $\Delta\rho$ is delocalized over the two ethylene molecules and those in which it is strongly localized on one of the ethylene molecule. Our major finding is that the vibronic coupling constants for the delocalized $\Delta\rho$ case are $1/\sqrt{2}$ of those for the localized $\Delta\rho$ case. In other words, magnitude of vibronic coupling constant is inversely proportional to the square root of the number of atoms over which $\Delta\rho$ is distributed. This finding may open the way to tuning vibronic coupling through controlling $\Delta\rho$ distribution and enable us to design functional materials such as charge-transporting molecules.

Bibliography

[1] J.-L. Brédas, D. Beljonne, V. Coropceanu, and J. Cornil, Chem. Rev. **104**, 4971 (2004).

[2] V. Coropceanu, J. Cornil, D. A. da Silva Filho, Y. Olivier, R. Silbey, and J.-L. Brédas, Chem. Rev. **107**, 926 (2007).

[3] K. Okumoto and Y. Shirota, Mater. Sci. Eng. **B85**, 135 (2001).

[4] S. Heun and P. M. Borsenberger, Chem. Phys. **200**, 245 (1995).

[5] M. Stolka, J. F. Yanus, and D. M. Pai, J. Phys. Chem. **88**, 4707 (1984).

[6] C. Adachi, K. Nagai, and N. Tamoto, Appl. Phys. Lett. **66**, 2679 (1995).

[7] C. W. Tang, S. A. VanSlyke, and C. H. Chen, J. Appl. Phys. **65**, 3610 (1989).

[8] C. Adachi, S. Tokito, T. Tsutsui, and S. Saito, Jpn. J. Appl. Phys. **27**, L269 (1988).

[9] C. W. Tang and S. A. VanSlyke, Appl. Phys. Lett. **51**, 913 (1987).

[10] T. Sato, K. Tokunaga, N. Iwahara, K. Shizu, and K. Tanaka, *Vibronic coupling constant and vibronic coupling density* in *The Jahn-Teller-Effect - Fundamentals and Implications for Physics and Chemistry,* H. Köppel, D. R. Yarkony, and H. Barentzen (Eds) (Springer-Verlag, Berlin and Heidelberg, 2009).

[11] A. Devos and M. Lannoo, Phys. Rev. B **58**, 8236 (1998).

[12] V. Coropceanu, M. Malagoli, D. A. da Silva Filho, N. E. Gruhn, T. G. Bill, and J.-L. Brédas, Phys. Rev. Lett. **89**, 275503 (2002).

[13] E.-G. Kim, V. Coropceanu, N. E. Gruhn, R. S. Sánchez-Carrera, R. Snoeberger, A. J. Matzger, and J.-L. Brédas, J. Am. Chem. Soc. **129**, 13072 (2007).

[14] T. Sato, K. Shizu, T. Kuga, K. Tanaka, and H. Kaji, Chem. Phys. Lett. **458**, 152 (2008).

[15] K. Shizu, T. Sato, and K. Tanaka, Chem. Phys. Lett. **491**, 65 (2010).

[16] K. Shizu, T. Sato, K. Tanaka, and H. Kaji, Chem. Phys. Lett. **486**, 130 (2010).

[17] K. Shizu, T. Sato, K. Tanaka, and H. Kaji, Org. Electron. **11**, 1277 (2010).

[18] G. Rauhut and P. Pulay, J. Phys. Chem. **99**, 3093 (1995).

[19] M. J. Frisch, G. W. Trucks, H. B. Schlegel, G. E. Scuseria, M. A. Robb, J. R. Cheeseman, J. A. Montgomery, Jr., T. Vreven, K. N. Kudin, J. C. Burant, J. M. Millam, S. S. Iyengar, J. Tomasi, V. Barone, B. Mennucci, M. Cossi, G. Scalmani, N. Rega, G. A. Petersson, H. Nakatsuji, M. Hada, M. Ehara, K. Toyota, R. Fukuda, J. Hasegawa, M. Ishida, T. Nakajima, Y. Honda, O. Kitao, H. Nakai, M. Klene, X. Li, J. E. Knox, H. P. Hratchian, J. B. Cross, V. Bakken, C. Adamo, J. Jaramillo, R. Gomperts, R. E. Stratmann, O. Yazyev, A. J. Austin, R. Cammi, C. Pomelli, J. W. Ochterski, P. Y. Ayala, K. Morokuma, G. A. Voth, P. Salvador, J. J. Dannenberg, V. G. Zakrzewski, S. Dapprich, A. D. Daniels, M. C. Strain, O. Farkas, D. K. Malick, A. D. Rabuck, K. Raghavachari, J. B. Foresman, J. V. Ortiz, Q. Cui, A. G. Baboul, S. Clifford, J. Cioslowski, B. B. Stefanov, G. Liu, A. Liashenko, P. Piskorz, I. Komaromi, R. L. Martin, D. J. Fox, T. Keith, M. A. Al-Laham, C. Y. Peng, A. Nanayakkara, M. Challacombe, P. M. W. Gill, B. Johnson, W. Chen, M. W. Wong, C. Gonzalez, and J. A. Pople, GAUSSIAN 03, Revision D.02, Gaussian, Inc., Wallingford, CT, 2004.

[20] E. Hirota, Y. Endo, S. Saito, K. Yoshida, I. Yamaguchi, and K. Machida, J. Mol. Spectrosc. **89**, 223 (1981).

[21] W. Knippers, K. V. Helvoort, S. Stolte, and J. Reuss, Chem. Phys. **98**, 1 (1985).

[22] R. Stockbauer and M. G. Inghram, J. Electron Spectrosc. Relat. Phenom. **7**, 492 (1975).

[23] H. Köppel, W. Domcke, L. S. Cederbaum, and W. von Niessen, J. Chem. Phys. **69**, 4252 (1978).

[24] K. Shizu, T. Sato, K. Tanaka, and H. Kaji, Appl. Phys. Lett. **97**, 142111 (2010).

Chapter 5

Theoretical Design of a Hole-Transporting Molecule: Hexaaza[1_6]parabiphenylophane

5.1 Introduction

Organic light-emitting diodes (OLEDs) have received considerable attention because of their potential application to full-color flat-panel displays, backlight for liquid crystal displays, and paper thin-light sources.[1,2] A typical multi-layer OLED consists of an indium-tin-oxide (ITO) anode, a hole-transport layer, an emitting layer, an electron-transport layer, and a cathode. Amorphous molecular materials or molecular glasses are attractive candidates for materials in OLEDs.[3–11]

The hole-transport layers in OLEDs play a role of assisting hole injection from the anode, preventing electrons from escaping from the emitting layer (blocking electrons), and transporting holes to the emitting layer. Hence, the hole-transporting molecules should have a highest occupied molecular orbital (HOMO) energy close to the Fermi level of the anode and a lowest unoccupied molecular orbital (LUMO) energy higher than that of the emitting molecule, and exhibit high-hole mobility. Since hole-transporting materials in OLEDs are used in their amorphous state, they should also exhibit a high glass transition temperature T_g to keep a device durability.

A number of compounds have been synthesized and used as the hole-transporting materials for OLEDs.[3–8,10,11] Among them, N,N'-bis(3-methylphenyl)-N,N'-diphenyl-

[1,1′-biphenyl]-4,4′-diamine (TPD) has been one of the most widely used hole-transporting material because of its high-hole mobility (1.0×10^{-3} $cm^2V^{-1}s^{-1}$ at an electric field 1.5×10^5 Vcm^{-1} obtained using time-of-flight (TOF) technique) and electron-blocking property.[12,13] However, since TPD exhibits a low glass transition temperature T_g (= 62°C), it lacks thermal stability.[8,14] N,N,N',N'-tetraphenylbenzidine (TAD), which has a chemical structure similar to that of TPD, exhibits a hole-transporting property, but is easily crystallized because of its low T_g (= 70°C).[8] N,N'-di(1-naphthyl)-N,N'-diphenyl-[1,1′-biphenyl]-4,4′-diamine (α-NPD), which exhibits higher T_g (= 95°C) and better thermal stability than TPD, has been also used as a hole-transporting material in OLEDs.[14,15] The hole mobility of α-NPD measured using TOF technique is about half that of TPD using the same method.[16,17] By contrast, hole mobilities of these two molecules using field-effect transistor (FET) technique are almost the same.[8]

One of the factors that influence charge-transport properties is an intramolecular vibronic coupling (electron-molecular vibration interaction). An inelastic scattering of charge carriers due to the vibronic coupling inhibits charge transport, and lowers charge mobility and performance of OLEDs. The inelastic scattering is weak when the charge carriers transmit through molecules exhibiting weak vibronic coupling, in other words, molecules with small vibronic coupling constants (VCCs). Hence, small VCCs are preferable in charge-transporting properties.

We have theoretically investigated the vibronic couplings in triphenylamine (TPA), carbazole, and TPD cations employing vibronic coupling density (VCD) analysis, and reveals that strong localization of the electron-density difference $\Delta\rho$ on the N atoms is responsible for the weak vibronic coupling of these molecules.[18–20] This result indicates that the TPA and carbazole moieties play an important role in facilitating hole transport. The VCD analysis provides an effective method for designing charge-transporting materials as well as investigating vibronic coupling. Employing the analysis, we have succeeded in designing an efficient electron-transporting material, haxaboracyclophane (HBCP).[21] The theoretically proposed HBCP has suitable HOMO and LUMO energy levels and exhibits lower-power consumption than tris-(8-hydroxyquinoline) aluminum(III) (Alq_3) and tris[3-(3-pyridyl)mesityl]borane (3TPYMB), which are good electron-transporting materials.[22]

In this chapter, using the VCD analysis, we theoretically propose a hole-transporting macrocyclic amine, hexaaza[1_6]parabiphenylophane (HAPBP, Fig. 5.1). HAPBP consists of three TAD moieties. Recently synthesized hexaaza[1_6]paracyclophane, in which the biphenyl moieties and phenyl groups are replaced by phenyl and *p*-methoxyphenyl groups, respectively, exhibits low oxidation potential and good electron-donating ability.[23] We calculate the VCCs of HAPBP cation and compare them with those of the well-known hole-transporting materials, TPD, TAD, and α-NPD. To investigate their single molecular hole-transporting properties, we calculate current-voltage characteristics and power loss using the non-equilibrium Green's function (NEGF) method[24] taking into account the inelastic scattering due to the vibronic couplings. We analyze hole-injecting and electron-blocking properties of HAPBP by calculating the HOMO and LUMO energy levels of HAPBP and comparing them with those of TPD, TAD, and α-NPD.

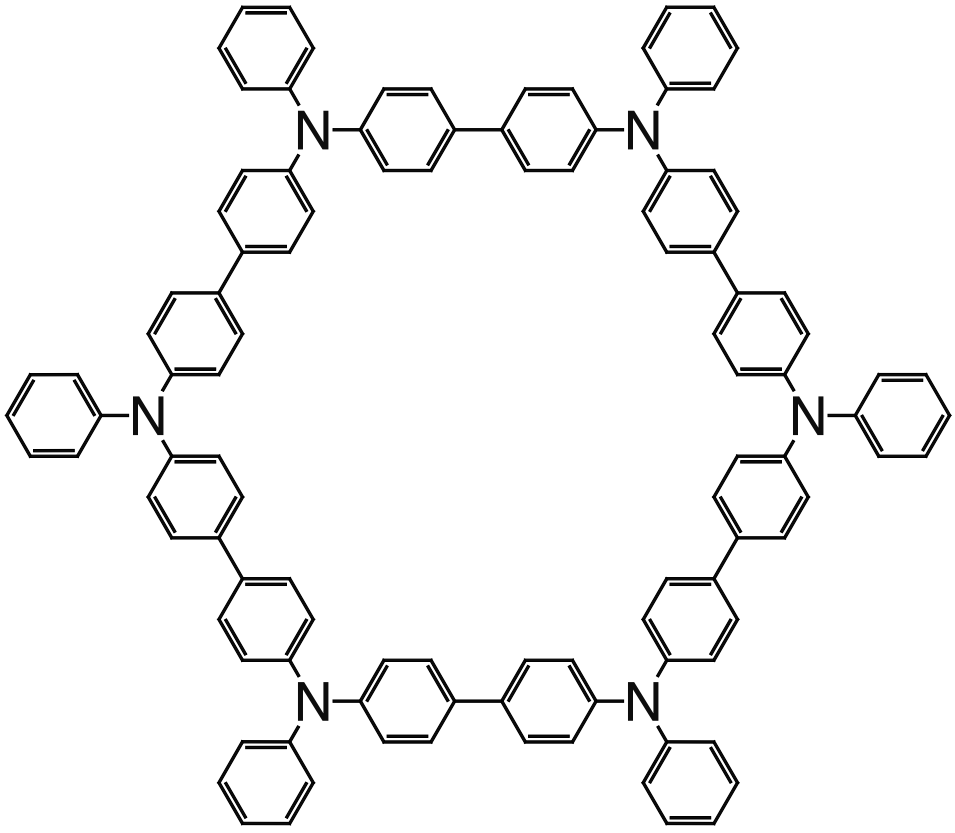

HAPBP

Figure 5.1: Chemical structure of HAPBP.

5.2 Vibronic coupling density analysis

The intramolecular VCC for the ith mode V_i can be expressed as

$$V_i = \int \eta_i(\mathbf{x})\, d\mathbf{x}, \tag{5.1}$$

where η_i is called a VCD for the ith mode and $\mathbf{x}$ denotes a position in the 3D space. In a hole-transport process, η_i can be expressed in terms of the electron-density difference between the cationic and neutral states $\Delta\rho(\mathbf{x})$ and the one-electron part of the derivative of the nuclear–electronic potential with respect to the normal coordinate of the ith mode $v_i(\mathbf{x})$:

$$\eta_i(\mathbf{x}) = \Delta\rho(\mathbf{x}) \times v_i(\mathbf{x}), \tag{5.2}$$

where

$$\Delta\rho(\mathbf{x}) = \rho^+(\mathbf{x}) - \rho(\mathbf{x}), \tag{5.3}$$

$$v_i(\mathbf{x}) = \sum_A -\frac{Z_A}{\sqrt{M_A}}\mathbf{e}_A^{(i)} \cdot \frac{\mathbf{x}-\mathbf{R}_A}{|\mathbf{x}-\mathbf{R}_A|^3}. \tag{5.4}$$

Here, $\rho^+(\mathbf{x})$ and $\rho(\mathbf{x})$ are electron densities for cationic and neutral states, respectively, at the equilibrium geometry of the neutral state. Z_A, M_A, and $\mathbf{R}_A$ are the atomic number, mass, and position of the Ath nucleus, respectively, and $\mathbf{e}_A^{(i)}$ is the mass-weighted 3D component of the Ath nucleus of the ith vibrational mode Q_i. The details of derivation of Eqs. (5.1–5.4) has been described elsewhere.[25,26] $\Delta\rho$ satisfies the following relation

$$\int \Delta\rho(\mathbf{x})\, d\mathbf{x} = -1, \tag{5.5}$$

and the set of $\mathbf{e}^{(i)}$ is orthonormalized:

$$\mathbf{e}^{(i)} \cdot \mathbf{e}^{(j)} = \delta_{ij}. \tag{5.6}$$

Significantly, only the totally symmetric modes have non-zero VCCs.

η_i contains vanishing components that make no contribution to V_i and are not essential to vibronic couplings. A reduced vibronic coupling density (RVCD) $\bar{\eta}_i$ is obtained by subtracting those vanishing components from η_i.[27] The space integral of $\bar{\eta}_i$ gives again V_i:

$$\int \bar{\eta}_i(\mathbf{x})\, d\mathbf{x} = V_i. \tag{5.7}$$

$\bar{\eta}_i$ gives a local picture of the vibronic coupling in a molecule. Since $\Delta\rho$ represents change in the electronic structure while v_i represents the vibrational structure, we can relate V_i to the electronic and vibrational structures by analyzing $\bar{\eta}_i$.

5.3 Method of calculation

Geometry optimizations and vibrational analyses of TPD, TAD, α-NPD, and HAPBP were carried out at the density functional (DFT) level employing Gaussian 03 software.[28] It has been shown that the DFT-optimized structure of an isolated TPD is in good agreement with that in an amorphous state.[29] In the DFT method calculations, we used Becke's three parameter exchange functional[30] with the Lee-Yang-Parr correlation functional[31] and 6-31G(d,p) basis set.[32] We confirmed that the optimized geometries are stationary minima. Calculated frequencies were uniformly scaled by 0.963.[33]

To investigate the single molecular hole-transporting properties of TPD, TAD, α-NPD, and HAPBP, we calculated the current-voltage characteristics and the power loss of a single TPD/TAD/α-NPD/HAPBP molecule employing the NEGF method taking into account inelastic scatterings due to the vibronic couplings.[24] The details of the NEGF method has been described elsewhere.[34]

5.4 Results and discussion

Stable structures of TPD and α-NPD belong to C_2 point group, while that of TAD belongs to D_2 point group. The number of totally symmetric modes, that is, the number of modes that couple to the electronic states are 106, 48, and 115 for TPD, TAD, and α-NPD, respectively. TAD has the smaller number of totally symmetric modes than TPD and α-NPD because of its higher symmetry.

Fig. 5.2 shows calculated VCCs of TPD, TAD, and α-NPD. The VCCs of these three molecules show a similar trend: C−C stretching modes have the largest VCCs; inter-ring C−C stretching and C−H in-plane bending modes have relatively large VCCs; C−H stretching and out-of-plane bending modes have small VCCs. This similarity in the VCCs originates from the similarity of geometric structures: TPD, TAD, and α-NPD consist of the two TPA moieties. The VCCs of C−H bending and inner-ring C−C stretching modes of α-NPD are slightly larger than those of TPD and TAD. However, the VCCs are at most 1.4×10^{-4} a.u. and small as a π-conjugated system.

The VCC values are about one third of those of the biphenyl cation calculated at the DFT level,[20] suggesting that the vibronic couplings in biphenyl moieties of TPD, TAD, and α-NPD cations are weaker than those in the biphenyl cation. In Chapter 1 and 2, we

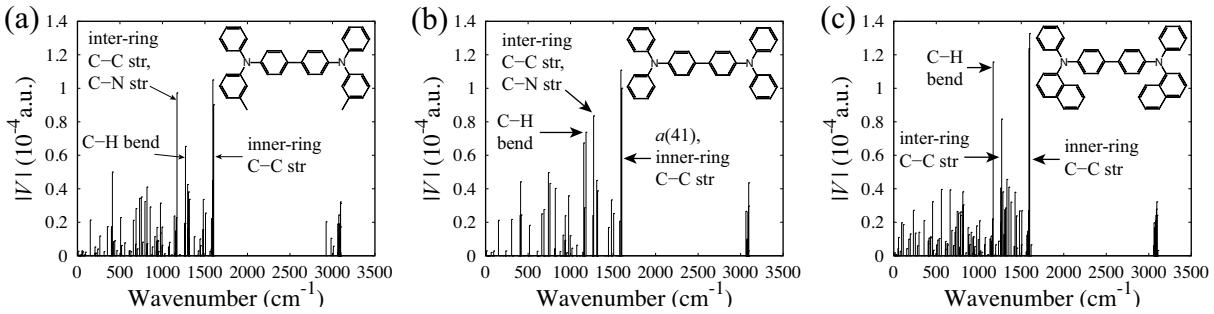

Figure 5.2: Vibronic coupling constants $|V|$ for the various cations calculated at the UB3LYP/6-31G(d,p) level of theory: (a) TPD, (b) TAD, and (c) α-NPD. Str and bend mean stretching and bending, respectively.

have shown that strong localization of $\Delta\rho$ on the N atoms weakens the vibronic couplings in the biphenyl moiety and is responsible for the weak vibronic coupling in the TPD cation.[18,19] This explanation is also true for the TAD and α-NPD cations. The strong localization of $\Delta\rho$ on the N atoms reduces VCCs and consequently, improves the hole mobilities.

Stabilization energy ΔE due to the vibronic couplings of a π-conjugated molecule is inversely proportional to its molecular size. This relationship first mentioned by Devos and Lannoo roughly holds for various π-conjugated compounds.[35–37] Since the stabilization energy ΔE due to the vibronic couplings is related to V_i and an angular frequency ω_i as follows[38]

$$\Delta E = \sum_i \frac{V_i^2}{2\omega_i^2}, \tag{5.8}$$

the relationship indicates that the size of VCCs of a π-conjugated molecule decreases as its molecular size increases. This provides a strategy for designing molecules with small VCCs. Using this strategy, we have theoretically proposed an efficient electron-transporting material exhibiting weak vibronic coupling.[21] In addition, we utilize a selection rule to design a molecule.

In the following, we show how to design a hole-transporting molecule exhibiting weaker vibronic coupling than TPD, TAD, and α-NPD employing the VCD analysis. Figure 5.1 shows the chemical structure of HAPBP. HAPBP consists of the three symmetrically arranged TAD moieties. The optimized structure of HAPBP belongs to D_6 symmetry and the structures of six TPA moieties are equivalent. In spite of the large molecular size,

HAPBP has only 46 totally symmetric modes because of its high symmetric structure:

$$\Gamma_{\mathrm{vib}}\left(D_6\right) = 46A_1 + 48A_2 + 46B_1 + 50B_2 + 188E_1 + 192E_2. \tag{5.9}$$

The remaining 524 non-totally symmetric modes make no contribution to the vibronic couplings. The number of totally symmetric modes of HAPBP is smaller than that of the parent compound, TAD, which corresponds to the one-third-sized fragment of HAPBP. The normal modes of TAD are as follows:

$$\Gamma_{\mathrm{vib}}\left(D_2\right) = 48A_1 + 46B_1 + 49B_2 + 49B_3. \tag{5.10}$$

Thus, using high symmetry, we can design a molecule with small number of modes that cause the vibronic couplings.

Figs. 5.3(a) and (b) show $\Delta\rho$ for HAPBP and TAD, respectively. $\Delta\rho$ for HAPBP/TAD is distributed equivalently over six/two TPA moieties. An isosurface value of $\Delta\rho$ for HAPBP ($|\Delta\rho| = 1 \times 10^{-3}$ a.u.) is set to be one third of that for TAD ($|\Delta\rho| = 3 \times 10^{-3}$ a.u.). Comparing Figs. 5.3(a) and (b), the distribution range of $\Delta\rho$ is approximately the same, suggesting that $\Delta\rho$ of HAPBP is about one third of that of TAD. This result is easily understood by noting that the molecular size of HAPBP is three times larger than that of TAD, the three TAD moieties of HAPBP are equivalent, and $\int \Delta\rho d\mathbf{x} = -1$. Optimized dihedral angles between the adjacent phenyl rings in the biphenyl moieties for HAPBP and TAD are 58.4 and 35.8°, respectively. The biphenyl moieties are more twisted for HAPBP than for TAD.

$\Delta\rho$ for the HAPBP and TAD cations show similar trend, which is also observed for the TPD cation:[18] $\Delta\rho$ is distributed dominantly on the N atoms and the remaining $\Delta\rho$ is distributed on the biphenyl and phenyl groups. Significantly, $\Delta\rho$ on C−C bonds is quite small. As mentioned in Chapter 3, a vibronic coupling is strong when $\Delta\rho$ is largely distributed on bonds, while it is weak when $\Delta\rho$ is strongly localized on atoms.[20] The N atoms have a role to localize $\Delta\rho$, and reduce the VCCs. The small VCCs of the TAD cation (Fig. 5.2(b)) originate from this effect of the N atoms. The negative $\Delta\rho$ on the N atoms shows that an electron removed dominantly from the N atoms. $\Delta\rho$ around the N atoms has also a σ character, and the positive $\Delta\rho$ originates from orbital relaxations of the doubly occupied molecular orbitals other than HOMOs. The positive regions have a role of relaxing Coulomb repulsions between the negative regions on the N atoms.

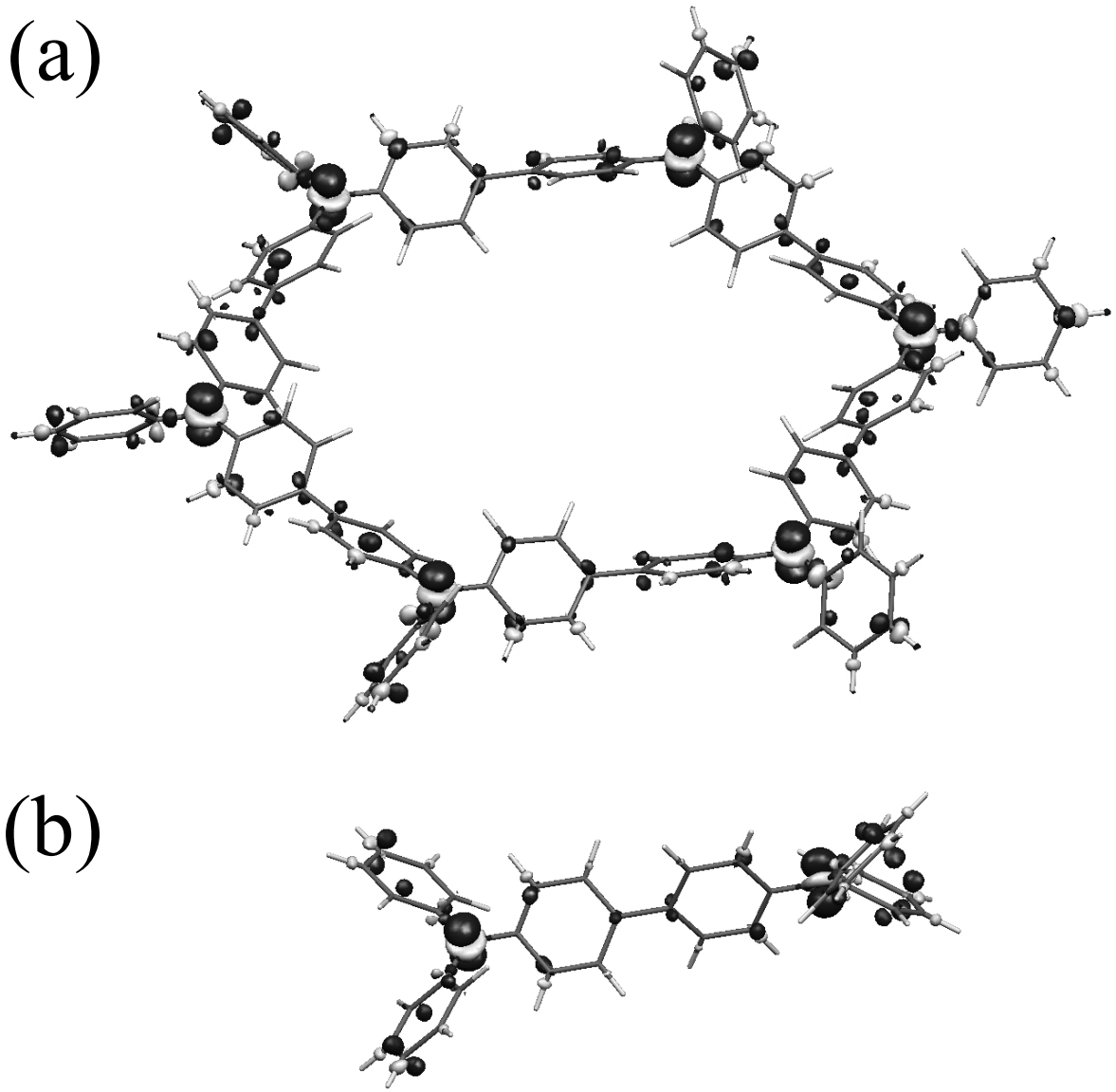

Figure 5.3: Electron-density difference $\Delta\rho$ due to ionization for (a) HAPBP at an isosurface value of 1.0×10^{-3} a.u. and (b) TAD at an isosurface value of 3.0×10^{-3} a.u. Dark gray shows where values are negative; light gray shows where values are positive.

To investigate the vibronic coupling in the HAPBP cation, we compare the vibronic coupling for C−C stretching modes of HAPBP and TAD (Fig. 5.4). Figs. 5.4(a) and (b) show the $a_1(39)$ mode of HAPBP and the $a(41)$ mode of TAD. The $a_1(39)$ mode has the largest VCC of the HAPBP cation while the $a(41)$ mode has the second largest VCC of the TAD cation. The $a_1(39)$ mode of HAPBP is considered as an in-phase combination of the three $a(41)$ modes of TAD. The $a_1(39)$ and $a(41)$ modes include the inner-ring C−C stretching vibration associated with the inter-ring C−C stretching and in-plane C−H bending vibrations.

Figs. 5.5(a) and (b) show v_{39} for HAPBP and v_{41} for TAD. v reflects the vibrational mode: v is negative in the regions where the bonds shorten (dark-gray regions); v is positive in the regions where the bonds lengthen (light-gray regions). In Fig. 5.5, an isosurface value of v_{39} ($|v_{39}| = 8/\sqrt{3} \times 10^{-3}$ a.u.) is set to be $1/\sqrt{3}$ of v_{41} ($|v_{41}| = 8 \times 10^{-3}$ a.u.). Comparing Figs. 5.5(a) and (b), the distribution ranges of v_{39} and v_{41} are approximately the same, suggesting that v_{39} is about $1/\sqrt{3}$ of v_{41}. Since HAPBP is about three times as large as TAD, the dimension of $\mathbf{e}^{(39)}$ of HAPBP is also about three times as large as that of $\mathbf{e}^{(41)}$ of TAD. Hence, the components of the orthonormalized $\mathbf{e}^{(39)}$ are about $1/\sqrt{3}$ of those of $\mathbf{e}^{(41)}$. Consequently, v_{39} is approximately $1/\sqrt{3}$ of v_{41}, per Eq. (5.4).

Significantly, an overlap between $\Delta\rho$ and v_i is small for HAPBP and TAD because the distribution patterns of $\Delta\rho$ and v_i are clearly different. On the N atoms, $\Delta\rho$ is large but v_i is small; on the C−C bonds v_i is large but $\Delta\rho$ is small. Consequently, $\Delta\rho$ and v_i overlap only on the atoms, and the distribution of $\bar{\eta}_i$ does not extend over the bonds so much. This mismatch between the $\Delta\rho$ and v_i distributions leads to small $\bar{\eta}_i$ values and consequently, the small VCCs of HAPBP and TAD. Since $\Delta\rho$ and v_i for HAPBP are approximately 1/3 and $1/\sqrt{3}$ of those for TAD, $\bar{\eta}_i$ for HAPBP is approximately $1/3\sqrt{3}$ of that for TAD. Fig. 5.6 shows this feature. In Fig. 5.6, an isosurface value of v_{39} ($|v_{39}| = 8/3\sqrt{3} \times 10^{-6}$ a.u.) is set to be $1/3\sqrt{3}$ of v_{41} ($|v_{41}| = 8 \times 10^{-6}$ a.u.). The distribution of $\bar{\eta}_{39}$ in Fig. 5.6(a) is similar to that of $\bar{\eta}_{41}$ in Fig. 5.6(b), suggesting that $\bar{\eta}_{39}$ is about $1/3\sqrt{3}$ of $\bar{\eta}_{41}$. The small value of $\bar{\eta}_{39}$ leads to the small V_{39}. V_{39} ($= 8.78 \times 10^{-5}$ a.u.) is actually smaller than V_{41} ($= 1.00 \times 10^{-4}$ a.u.). Thus, we can reduce the VCCs by arranging three equivalent TAD moieties symmetrically.

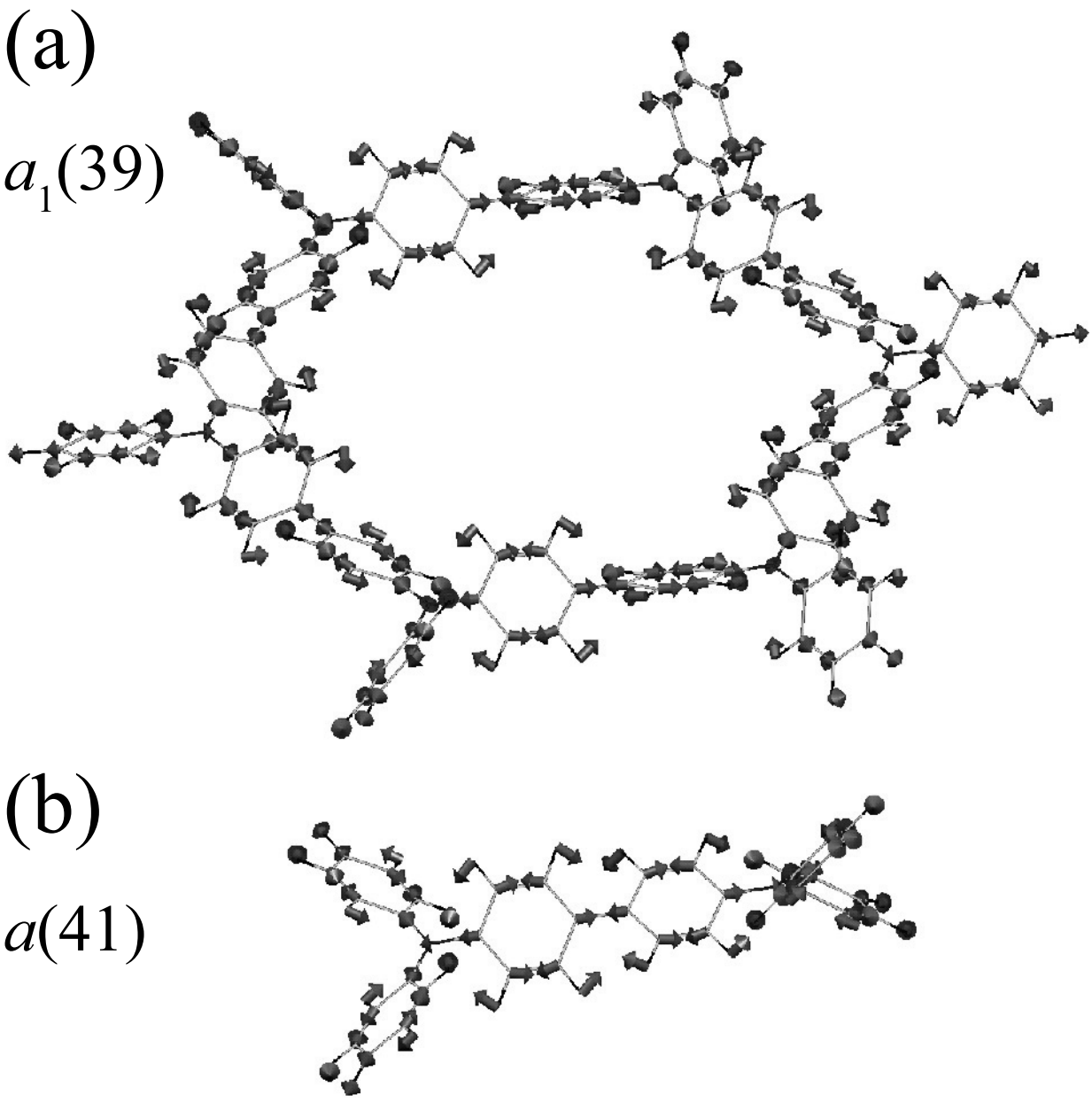

Figure 5.4: C−C stretching modes of HAPBP and TAD: (a) $a_1(39)$ mode of HAPBP and (b) $a(41)$ mode of TAD. The $a_1(39)$ mode has the largest VCC of HAPBP cation; the $a(41)$ mode has the second largest VCC of TAD cation.

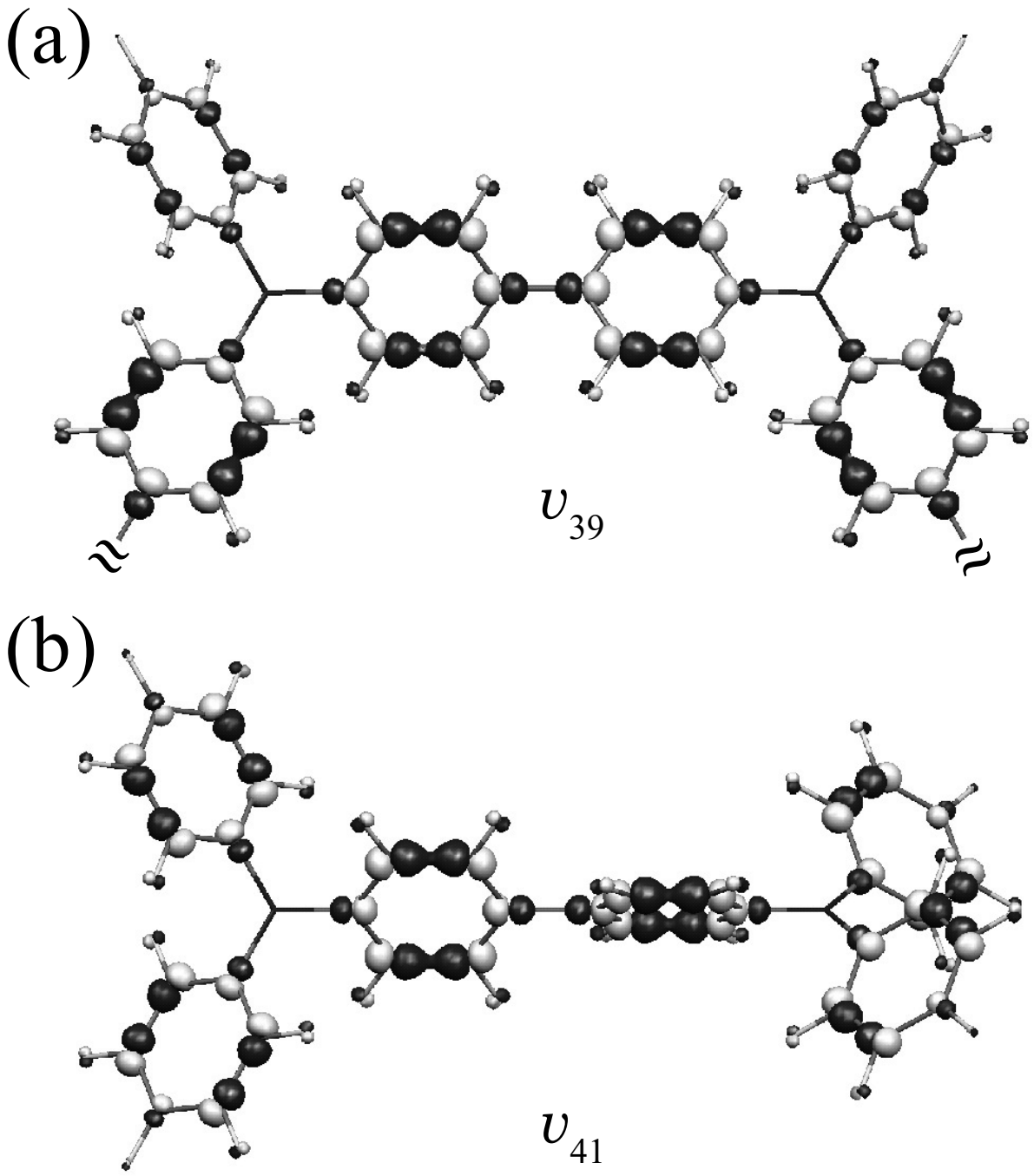

Figure 5.5: One-electron part of derivative of nuclear–electronic potential v_i for the $a_1(39)$ mode of HAPBP and the $a(41)$ mode of TAD: (a) v_{39} for HAPBP at an isosurface value of $8/\sqrt{3} \times 10^{-3}$ a.u. and (b) v_{41} for TAD at an isosurface value of 8×10^{-3} a.u. Dark gray shows where values are negative; light gray shows where values are positive.

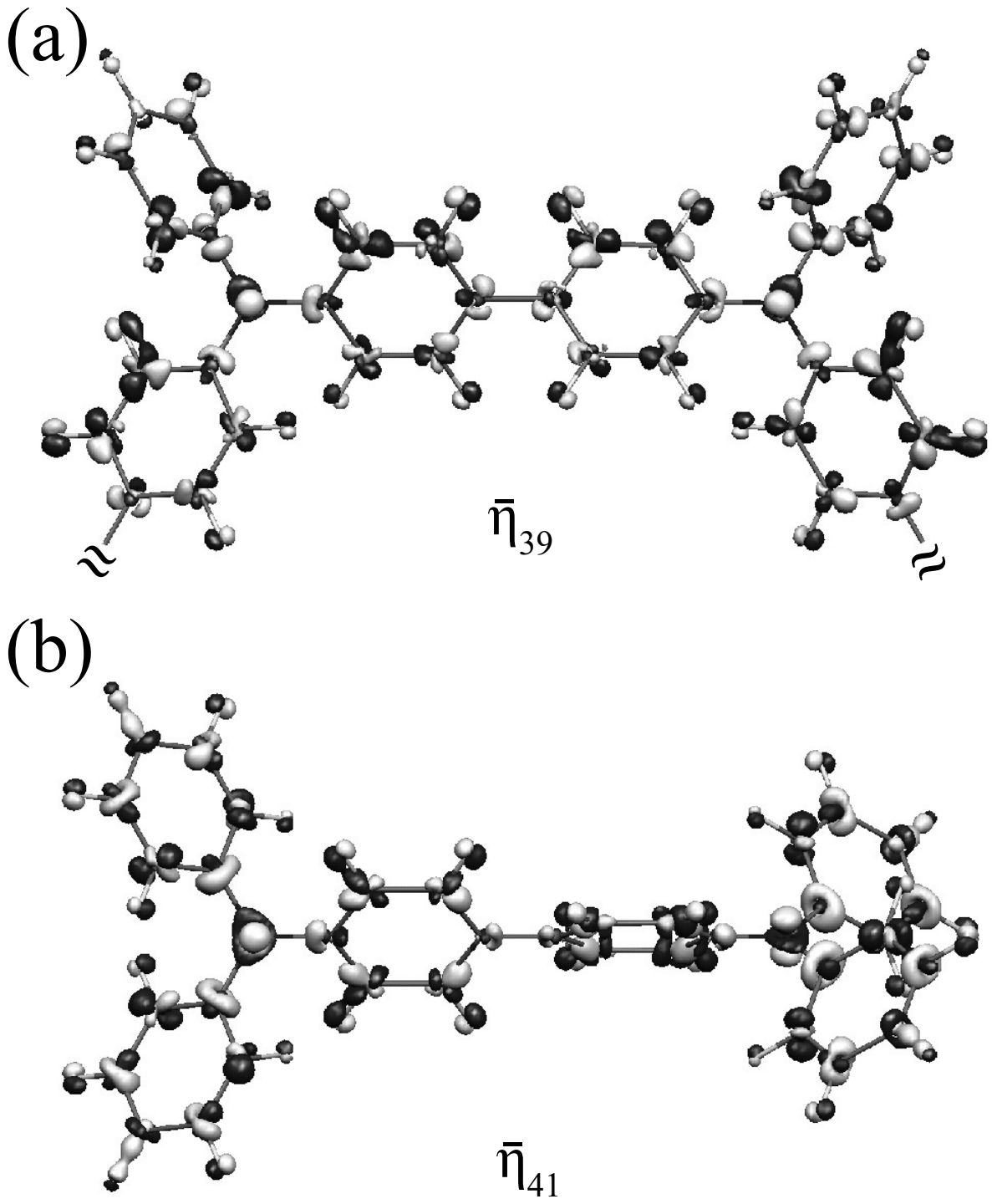

Figure 5.6: Reduce vibronic coupling density of $\bar{\eta}_i$ for the $a_1(39)$ mode of HAPBP and the $a(41)$ mode of TAD: (a) $\bar{\eta}_{39}$ for HAPBP at an isosurface value of $8/3\sqrt{3} \times 10^{-6}$ a.u. and (b) $\bar{\eta}_{41}$ for TAD at an isosurface value of 8×10^{-6} a.u. Dark gray shows where values are negative; light gray shows where values are positive.

Fig. 5.7 shows the VCCs of the HAPBP cation. All the VCCs are smaller than 1.0×10^{-4} a.u. and quite small as a π-conjugated system. It is pointed out again that, in spite of the large molecular size, HAPBP has only 46 totally symmetric modes because of its high-symmetric structure. Comparing Fig. 5.7 with Figs. 5.2(a–c), the VCCs of HAPBP are smaller than those of TPD, TAD, and α-NPD over the whole-frequency region. The small number of totally symmetric modes and small VCCs make HAPBP a promising candidate for a hole-transporting material with low-power loss.

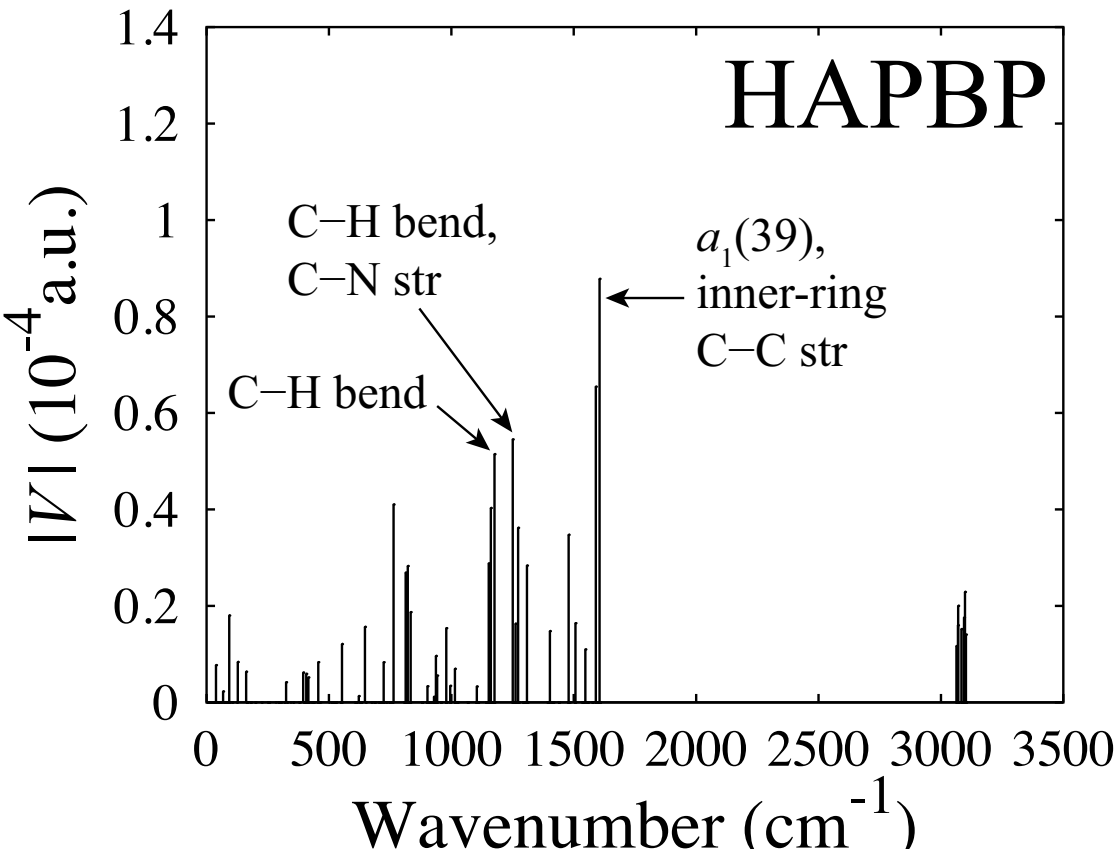

Figure 5.7: Vibronic coupling constants $|V|$ for the HAPBP cation calculated at the UB3LYP/6-31G(d,p) level of theory. Str and bend mean stretching and bending, respectively.

Fig. 5.8 shows the HOMO and LUMO energy levels of HAPBP, TPD, TAD, α-NPD, and *mer*-Alq_3 calculated at the B3LYP/6-31G(d,p) level of theory and the Fermi energy of the ITO electrode, which is a typical anode for OLEDs. The Fermi energy shown in Fig. 5.8 is the experimental work function of the ITO thin film with the opposite sign.[39] Here, we assume that Alq_3 is employed as an emitter. The HOMO energy level of HAPBP is closest to the Fermi energy of the ITO electrode. Hence, the energy barrier of hole injection is smaller for HAPBP than for TPD, TAD, and α-NPD. In addition, since HAPBP has the highest LUMO energy level, the energy barrier of electron transfer from *mer*-Alq_3 is largest for HAPBP. Hence, HAPBP is expected to exhibit higher-electron-blocking property than TPD, TAD, and α-NPD. Overall, HAPBP has more suitable HOMO and LUMO energy levels than TPD, TAD, and α-NPD as a hole-transporting material when Alq_3 is employed as an emitter.

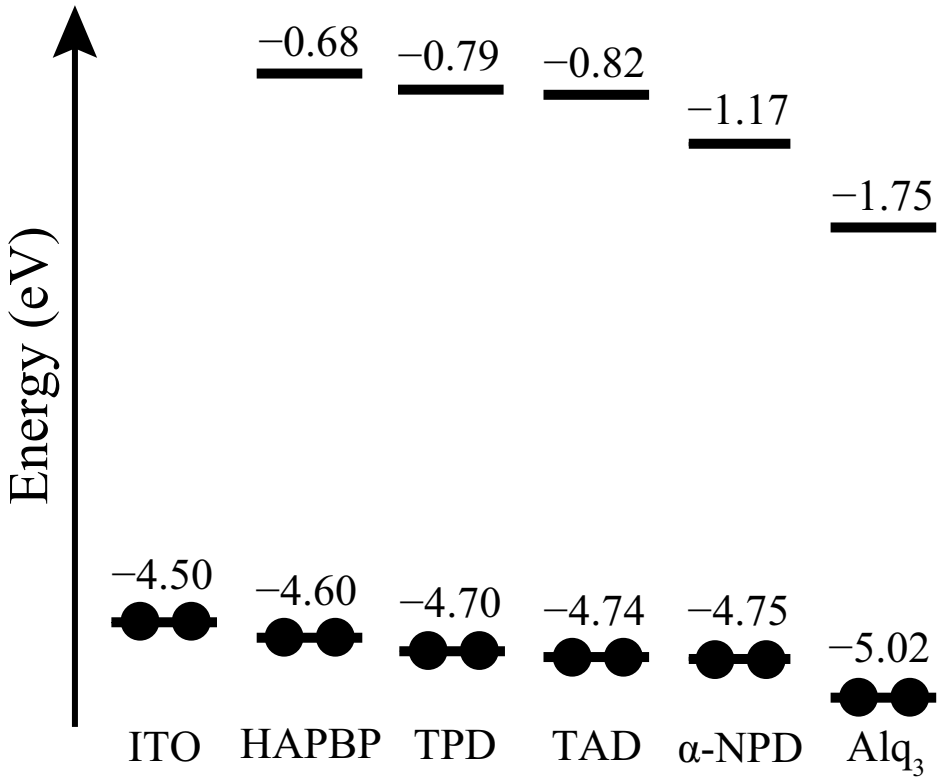

Figure 5.8: HOMO/LUMO energy-level diagrams for HAPBP, TPD, TAD, α-NPD, and *mer*-Alq_3 calculated at the B3LYP/6-31G(d,p) level of theory. Experimental work function with opposite sign of an ITO thin film[39] is also shown as the Fermi energies of ITO electrode surface.

We calculated current-voltage ($I - V_{\rm b}$) characteristics and power loss for a single HAPBP/TPD/TAD/α-NPD molecule using the NEGF method[24] to investigate a suppression effect due to the vibronic couplings on conducting properties. For the sake of simplicity, we considered neighboring molecules in a solid as a part of electrodes. In addition, the Fermi levels of the electrodes are set to be the HOMO levels shown in Fig. 5.8. We used the electronic coupling $\tau = -0.5$ eV and temperature $T = 298$ K.

Fig. 5.9(a) shows the $I - V_{\rm b}$ characteristics for HAPBP (solid line), TPD (dashed line), TAD (dot-dashed line), and α-NPD (dotted line). Significantly, HAPBP exhibits the largest I, suggesting that for HAPBP, the suppression effect of the vibronic couplings on the electric current is small compared with TPD, TAD, and α-NPD. This result indicates that HAPBP is expected to exhibit higher-hole mobility than TPD, TAD, and α-NPD. This small suppression effect of HAPBP originates from the small number of totally symmetric modes and small VCCs of HAPBP. The weak vibronic coupling leads to low-power loss. Fig. 5.9(b) shows the power loss in a single HAPBP/TPD/TAD/α-NPD molecule. HAPBP exhibits the smallest-power loss, that is, the lowest-power consumption. α-NPD exhibits the strongest vibronic coupling among the four molecules, which leads to the smallest current and largest power loss. The strength of the vibronic couplings of TPD and TAD are comparable and hence, they exhibit the similar current and power-loss. In Fig. 5.9(a), the $I - V_{\rm b}$ curves for TPD and TAD almost coincide.

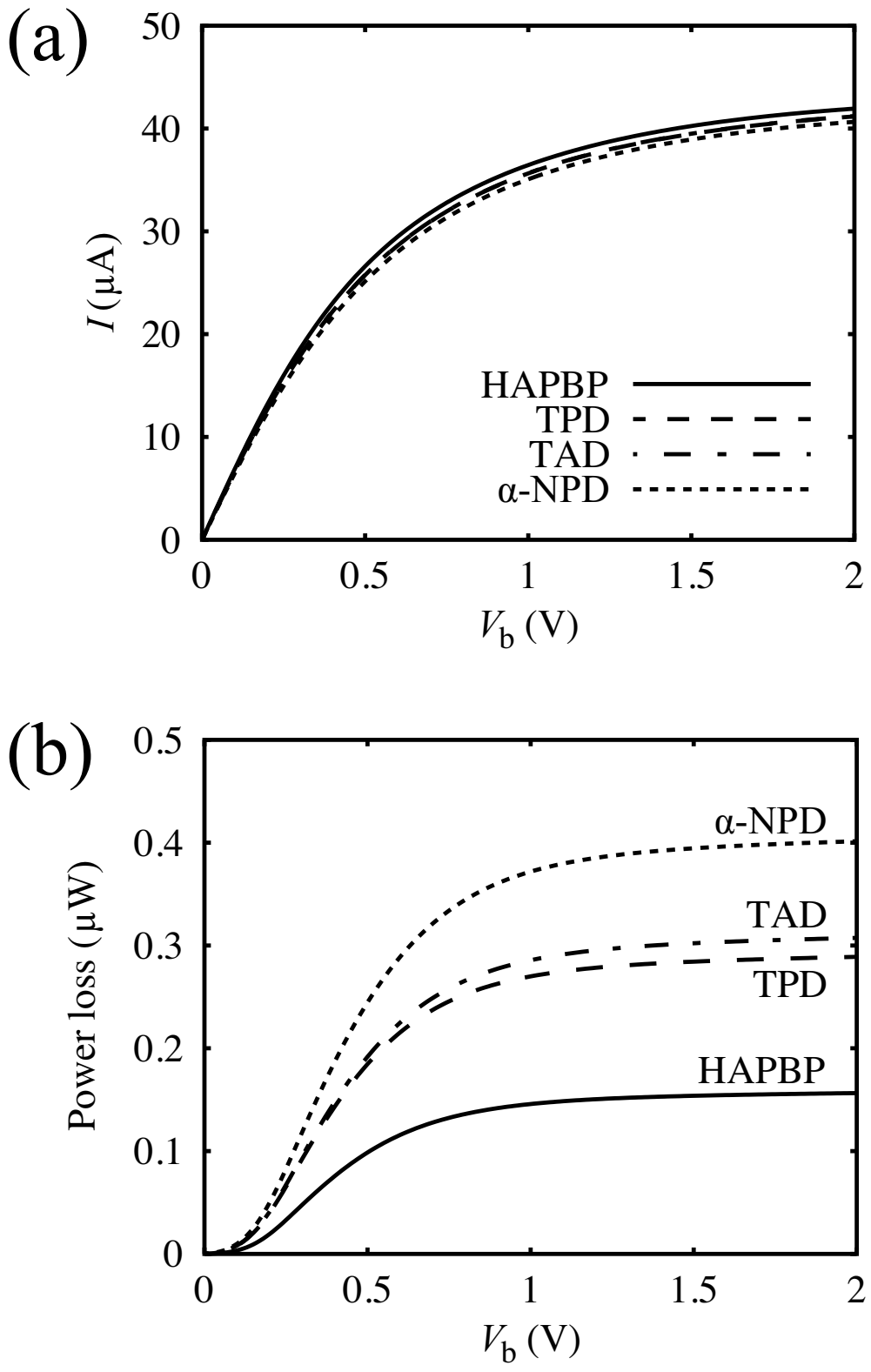

Figure 5.9: (a) Current-voltage characteristics and (b) power loss for HAPBP (solid lines), TPD (dashed lines), TAD (dot-dashed lines), and α-NPD (dotted lines).

5.5 Conclusion

We theoretically designed a hole-transporting molecule, HAPBP. HAPBP exhibits the weaker vibronic coupling and higher hole-transporting properties than the well-known hole-transporting materials, TPD, TAD, and α-NPD. HAPBP has the smaller number of vibronically active mode than TPD, TAD, and α-NPD because of its high symmetric structure. Furthermore, the VCCs of the HAPBP cation are smaller than those of the TPD, TAD, and α-NPD cations because the electron-density difference of the HAPBP cation is localized on six N atoms equivalently and quite small. The weak vibronic coupling of the HAPBP cation is due to the small number of vibronically active mode resulting from the selection rule for the vibronic coupling and the small VCCs originating from the symmetrically delocalized distributions of VCDs. In addition, HAPBP has the higher HOMO and LUMO energy levels than TPD, TAD, and α-NPD, suggesting that HAPBP exhibits superior hole-injecting and electron-blocking properties to TPD, TAD, and α-NPD. For these reasons, HAPBP is expected to be a candidate for a hole-transporting material.

Bibliography

[1] C. W. Tang and S. A. VanSlyke, Appl. Phys. Lett. **51**, 913 (1987).

[2] J. Kido, M. Kimura, and K. Nagai, Science **267**, 1332 (1995).

[3] L.-Z. Zhang, C.-W. Chen, C.-F. Lee, C.-C. Wu, and T.-Y. Luh, Chem. Commun. 2336 (2002).

[4] P. Strohriegl and J. V. Grazulevicius, Adv. Mater. **14**, 1439 (2002).

[5] M. Thelakkat, Macromol. Mater. Eng. **287**, 442 (2002).

[6] Y. Shirota, J. Mater. Chem. **15**, 75 (2005).

[7] K. Okumoto, H. Kanno, Y. Hamada, H. Takahashi, and K. Shibata, J. Appl. Phys. **100**, 044507 (2006).

[8] T. P. I. Saragi, T. Fuhrmann-Lieker, and J. Salbeck, Adv. Funct. Mater. **16**, 966 (2006).

[9] T. P. I. Saragi, T. Spehr, A. Siebert, T. Fuhrmann-Lieker, and J. Salbeck, Chem. Rev. **107**, 1011 (2007).

[10] Y. Shirota and H. Kageyama, Chem. Rev. **107**, 953 (2007).

[11] H. Tsuji, C. Mitsui, L. Ilies, Y. Sato, and E. Nakamura, J. Am. Chem. Soc. **129**, 11902 (2007).

[12] M. Stolka, J. F. Yanus, and D. M. Pai, J. Phys. Chem. **88**, 4707 (1984).

[13] J. Kido, C. Ohtaki, K. Hongawa, K. Okuyama, and K. Nagai, Jpn. J. Appl. Phys. **32**, L917 (1993).

[14] Y. Qiu and J. Qiao, Thin Solid Films **372**, 265 (2000).

[15] S. A. VanSlyke, C. H. Chen, and C. W. Tang, Appl. Phys. Lett. **69**, 2160 (1996).

[16] B. Chen, C.-S. Lee, S.-T. Lee, P. Webb, Y.-C. Chan, W. Gambling, H. Tian, and W. Zhu, Jpn. J. Appl. Phys. **39**, 1190 (2000).

[17] S. Naka, H. Okada, H. Onnagawa, Y. Yamaguchi, and T. Tsutsui, Synth. Met. **111-112**, 331 (2000).

[18] T. Sato, K. Shizu, T. Kuga, K. Tanaka, and H. Kaji, Chem. Phys. Lett. **458**, 152 (2008).

[19] K. Shizu, T. Sato, K. Tanaka, and H. Kaji, Chem. Phys. Lett. **486**, 130 (2010).

[20] K. Shizu, T. Sato, K. Tanaka, and H. Kaji, Org. Electron. **11**, 1277 (2010).

[21] K. Shizu, T. Sato, K. Tanaka, and H. Kaji, Appl. Phys. Lett. **97**, 142111 (2010).

[22] D. Tanaka, T. Takeda, T. Chiba, S. Watanabe, and J. Kido, Chem. Lett. **36**, 262 (2007).

[23] A. Ito, Y. Yokoyama, R. Aihara, K. Fukui, S. Eguchi, K. Shizu, T. Sato, and K. Tanaka, Angew. Chem., Int. Ed. **49**, 8205 (2010).

[24] S. Datta, *Quantum Transport: Atom to Transistor* (Cambridge University Press, Cambridge, 2005).

[25] T. Sato, K. Tokunaga, and K. Tanaka, J. Phys. Chem. A **112**, 758 (2008).

[26] T. Sato, K. Tokunaga, N. Iwahara, K. Shizu, and K. Tanaka, *Vibronic coupling constant and vibronic coupling density* in *The Jahn-Teller-Effect - Fundamentals and Implications for Physics and Chemistry,* H. Köppel, D. R. Yarkony, and H. Barentzen (Eds) (Springer-Verlag, Berlin and Heidelberg, 2009).

[27] K. Shizu, T. Sato, and K. Tanaka, Chem. Phys. Lett. **491**, 65 (2010).

[28] M. J. Frisch, G. W. Trucks, H. B. Schlegel, G. E. Scuseria, M. A. Robb, J. R. Cheeseman, J. A. Montgomery, Jr., T. Vreven, K. N. Kudin, J. C. Burant, J. M. Millam, S. S. Iyengar, J. Tomasi, V. Barone, B. Mennucci, M. Cossi, G. Scalmani, N. Rega, G. A. Petersson, H. Nakatsuji, M. Hada, M. Ehara, K. Toyota, R. Fukuda, J. Hasegawa, M. Ishida, T. Nakajima, Y. Honda, O. Kitao, H. Nakai, M. Klene, X.

Li, J. E. Knox, H. P. Hratchian, J. B. Cross, V. Bakken, C. Adamo, J. Jaramillo, R. Gomperts, R. E. Stratmann, O. Yazyev, A. J. Austin, R. Cammi, C. Pomelli, J. W. Ochterski, P. Y. Ayala, K. Morokuma, G. A. Voth, P. Salvador, J. J. Dannenberg, V. G. Zakrzewski, S. Dapprich, A. D. Daniels, M. C. Strain, O. Farkas, D. K. Malick, A. D. Rabuck, K. Raghavachari, J. B. Foresman, J. V. Ortiz, Q. Cui, A. G. Baboul, S. Clifford, J. Cioslowski, B. B. Stefanov, G. Liu, A. Liashenko, P. Piskorz, I. Komaromi, R. L. Martin, D. J. Fox, T. Keith, M. A. Al-Laham, C. Y. Peng, A. Nanayakkara, M. Challacombe, P. M. W. Gill, B. Johnson, W. Chen, M. W. Wong, C. Gonzalez, and J. A. Pople, GAUSSIAN 03, Revision D.02, Gaussian, Inc., Wallingford, CT, 2004.

[29] H. Kaji, T. Yamada, N. Tsukamoto, and F. Horii, Chem. Phys. Lett. **401**, 246 (2005).

[30] A. D. Becke, J. Chem. Phys. **98**, 5648 (1993).

[31] C. Lee, W. Yang, and R. G. Parr, Phys. Rev. B **37**, 785 (1988).

[32] P. C. Hariharan and J. A. Pople, Theoret. Chim. Acta **28**, 213 (1973).

[33] G. Rauhut and P. Pulay, J. Phys. Chem. **99**, 3093 (1995).

[34] K. Shizu, T. Sato, and K. Tanaka, Nanoscale **2**, 2186 (2010).

[35] A. Devos and M. Lannoo, Phys. Rev. B **58**, 8236 (1998).

[36] V. Coropceanu, M. Malagoli, D. A. da Silva Filho, N. E. Gruhn, T. G. Bill, and J.-L. Brédas, Phys. Rev. Lett. **89**, 275503 (2002).

[37] E.-G. Kim, V. Coropceanu, N. E. Gruhn, R. S. Sánchez-Carrera, R. Snoeberger, A. J. Matzger, and J.-L. Brédas, J. Am. Chem. Soc. **129**, 13072 (2007).

[38] V. Coropceanu, J. Cornil, D. A. da Silva Filho, Y. Olivier, R. Silbey, and J.-L. Brédas, Chem. Rev. **107**, 926 (2007).

[39] Y. Park, V. Choong, Y. Gao, B. R. Hsieh, and C. W. Tang, Appl. Phys. Lett. **68**, 2699 (1996).

Chapter 6

A Boron-Containing Molecule as an Efficient Electron-Transporting Material with Low-Power Consumption

Organic light-emitting diodes (OLEDs) have been of great interest because of their potential application for large-area full-color flat-panel displays. To enhance device efficiency it is necessary to develop electron-transporting materials with high-electron mobility and improve charge balance in OLEDs.[1] Alq_3 is one of the most widely used electron-transporting material in OLEDs and also used as a green emitter.[2,3] On the other hand, various boron-containing π-conjugated systems have electron-transporting property,[4–9] suggesting that boron plays a key role in electron-transporting process. Recently, Tanaka *et al.* have reported that tris[3-(3-pyridyl)mesityl]borane (3TPYMB) exhibits electron mobility about ten times higher than that of Alq_3 and has hole-blocking property.[9]

One of the factors that controls the electron mobility is intramolecular vibronic coupling (electron–molecular vibration interaction). Inelastic scattering due to vibronic coupling not only inhibits electron transport and reduces electron mobility but also causes Joule heat or power loss. Crystallization or melting of organic materials due to Joule heat is an origin of the instability of OLEDs.[10] Hence, molecules with weak vibronic coupling are favorable for electron-transporting material. In this chapter, we theoretically propose a boron-containing electron-transporting material, hexaboracyclophane (HBCP, Fig. 6.1)

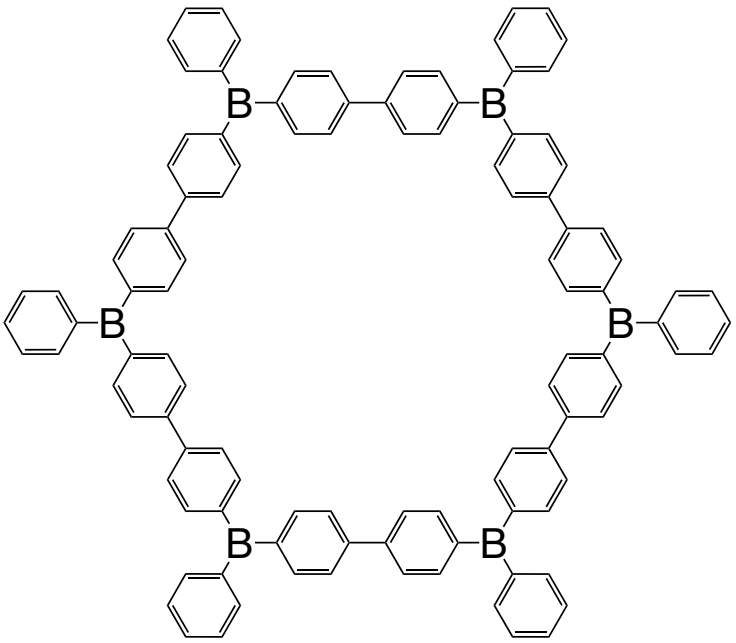

HBCP

Figure 6.1: Chemical structure of HBCP.

and compare its vibronic coupling, electron-transporting property, and hole-blocking character with those of *mer*-Alq_3 and 3TPYMB.

The strength of vibronic coupling of the i^{th} mode is controlled by the vibronic coupling constant (VCC) V_i. V_i can be expressed as $V_i = \int \Delta\rho \times v_i d\tau$, where $\Delta\rho$ is an electron-density difference between neutral and anion states and v_i is one-electron part of the derivative of the nuclear–electronic potential with respect to the i^{th} normal coordinate.[11] Note that only totally symmetric modes couple to the electronic states and have non-zero V_i values. Geometry optimization and vibrational analysis for neutral *mer*-Alq_3, 3TPYMB, and HBCP were done at the B3LYP/3-21G level of theory. We assumed C_1, C_3, and D_6 symmetries for *mer*-Alq_3, 3TPYMB, and HBCP, respectively. The electronic structures of anionic states for these molecules were calculated at the UB3LYP/3-21G level of theory using the optimized geometries of the neutral states. A scaling factor of 0.963[12] was used for B3LYP/3-21G theoretical frequencies. All the *ab initio* calculations were done using Gaussian 03 software.[13] We calculated current through a single *mer*-Alq_3/3TPYMB/HBCP molecule employing the non-equilibrium Green's function (NEGF) method taking into account inelastic scattering due to vibronic coupling.[14]

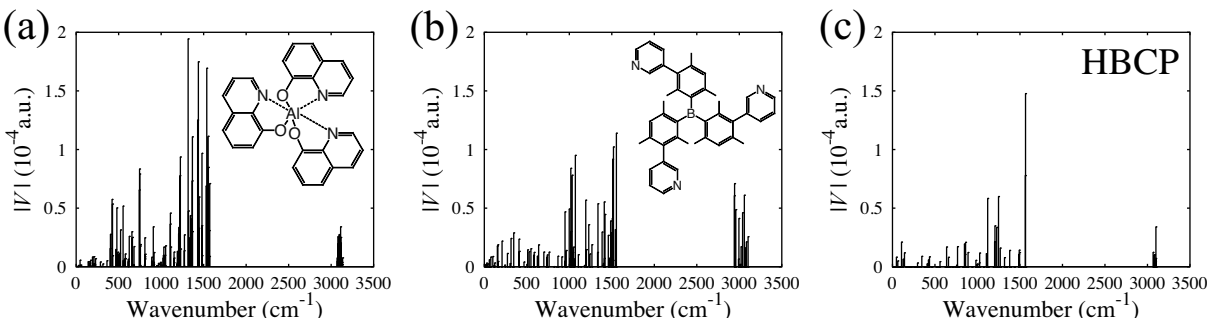

Figure 6.2: Vibronic coupling constants of (a) *mer*-Alq_3, (b) 3TPYMB, and (c) HBCP.

Figures 6.2(a)–6.2(c) show VCCs of *mer*-Alq_3, 3TPYMB, and HBCP. *mer*-Alq_3 has the largest V_i and exhibits the strongest vibronic coupling among them. Since *mer*-Alq_3 belongs to C_1 symmetry, all the vibrational modes (150 modes) have non-zero V_i. Low-symmetry molecular structure and not small V_i values lead to stronger vibronic coupling of *mer*-Alq_3 than those of 3TPYMB and HBCP. However, the largest V_i of *mer*-Alq_3 is at most 2.0×10^{-4} a.u., which is small compared with biphenyl, fluorene, and carbazole,[15] indicating that the vibronic coupling in *mer*-Alq_3 is weak as a π-conjugated system.

The largest V_i of 3TPYMB is about 1.2×10^{-4} a.u. (Fig. 6.2(b)). This value is quite small and comparable to the vibronic coupling in the cationic state of N,N'-bis(3-methylphenyl)-N,N'-diphenyl-[1,1′-biphenyl]-4,4′-diamine (TPD),[11] which is a widely used hole-transporting material in OLEDs. The number of vibrational modes of 3TPYMB (258 modes) is larger than that of *mer*-Alq_3. However, the number of totally symmetric modes of 3TPYMB (86 modes) is smaller than that of *mer*-Alq_3 because of the existence of the C_3 axis. The smaller V_i values and number of totally symmetric modes are responsible for the weaker vibronic coupling in 3TPYMB than in *mer*-Alq_3.

Figure 6.2(c) shows V_i of HBCP. Although HBCP has the largest molecular size and the number of vibrational modes (570 modes) among the three molecules, it has the smallest number of totally symmetric modes (46 modes) because of its high symmetry. Thus, high symmetry reduces the number of totally symmetric modes, and consequently, weakens the vibronic coupling as a whole. Furthermore, the largest V_i of HBCP is relatively small (1.6×10^{-4} a.u.) and the other V_i values are of the order of 1×10^{-5} a.u. and quite small. The high symmetry and small V_i values of HBCP make it a promising candidate for an electron-transporting material.

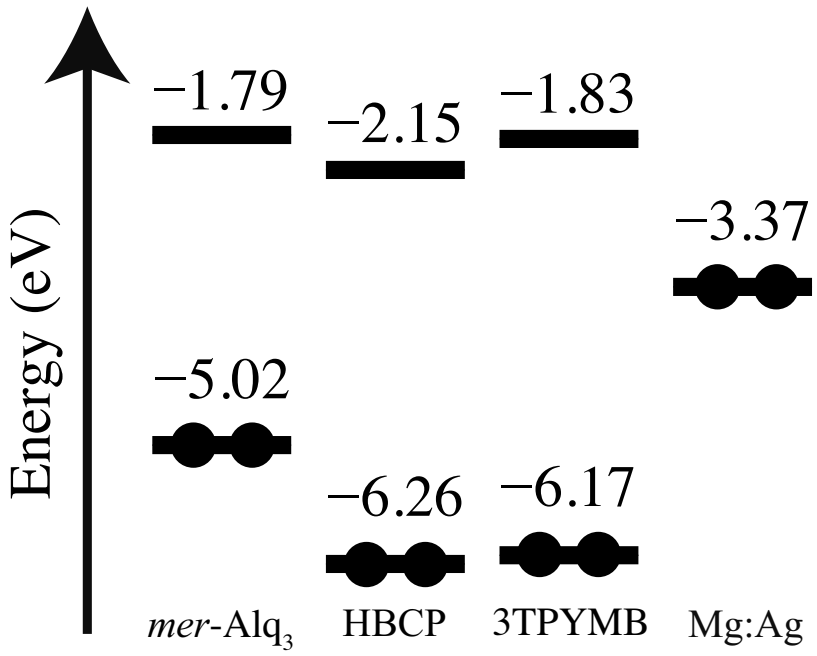

Figure 6.3: HOMO/LUMO energy-level diagrams for *mer*-Alq_3, 3TPYMB, and HBCP calculated at the B3LYP/3-21G level of theory. The experimental work function with opposite sign of an Mg:Ag alloy (see Ref. 16) is shown as the Fermi energy of Mg:Ag electrode surface.

Figure 6.3 shows HOMO and LUMO energy levels of *mer*-Alq_3, 3TPYMB, and HBCP calculated at the B3LYP/3-21G level of theory and Fermi energy of the Mg:Ag electrode, which is a typical cathode for OLEDs. The Fermi energy shown here is the experimental work function of the Mg:Ag alloy with the opposite sign.[16] The HOMO/LUMO energy level of HBCP is lower than that of 3TPYMB and hence, HBCP is expected to be a better electron-injecting and hole-blocking material than 3TPYMB when *mer*-Alq_3 is used as an emitting layer.

To investigate a suppression effect of vibronic coupling on electric current we calculated current-voltage ($I - V_b$) characteristics for a single *mer*-Alq_3/3TPYMB/HBCP molecule using the NEGF method.[14] Here, we considered neighboring molecules in a solid as a part of electrodes and set their Fermi levels to be the HOMO levels shown in Fig. 6.3. We used the electronic coupling $\tau = 0.5$ eV and temperature $T = 298$ K. In the NEGF method, the $I - V_b$ characteristics are influenced by τ and V_i. Since we focus on a suppression effect due to the vibronic coupling on $I - V_b$ characteristics, τ was set to be the same value for the three molecules.

Figure 6.4(a) shows the $I - V_{\mathrm{b}}$ characteristics for *mer*-Alq_3 (dotted line), 3TPYMB (dashed line), and HBCP (solid line). Significantly, HBCP exhibits the largest I, suggesting that for HBCP, the suppression effect due to vibronic coupling is weak compared with *mer*-Alq_3 and 3TPYMB, and HBCP can be a superior electron-transporting material than *mer*-Alq_3 and 3TPYMB. The large I originates from the high-symmetry and small V_i values of HBCP. Since the vibronic coupling in 3TPYMB is weaker than in *mer*-Alq_3, 3TPYMB exhibits larger I than *mer*-Alq_3. This result is consistent with the experimental observation that 3TPYMB exhibits higher electron mobility than *mer*-Alq_3.[9] The weak vibronic coupling is an origin of the high electron mobility of 3TPYMB. Inelastic scattering due to vibronic coupling causes power loss, in other words, heat generation. Figure 6.4(b) shows power loss in a single *mer*-Alq_3/3TPYMB/HBCP molecule. The power loss decreases in the following order: *mer*-Alq_3 > 3TPYMB > HBCP, suggesting that molecules with weak vibronic coupling exhibit low power consumption.

In conclusion, we designed the boron-containing molecule with high-symmetry, HBCP. The theoretically designed HBCP exhibits weaker vibronic coupling and higher electron-transporting property than *mer*-Alq_3 and 3TPYMB. Furthermore, since the HOMO/LUMO energy level of HBCP is lower than that of 3TPYMB, HBCP can be a superior electron-injecting and hole-blocking material than 3TPYMB when *mer*-Alq_3 is used as an emitting layer. In actual synthesis, it is necessary to protect the boron atoms, for instance, by introducing the methyl group at the ortho positions of the phenyl and phenylene groups. Such a chemical modification would change torsion angles between phenyl rings, but would not impair the electron-transporting and hole-blocking properties of HBCP so much. We calculated reorganization energies and HOMO/LUMO energy levels at the B3LYP/3-21G and UB3LYP/3-21G levels of theory for one-third-sized fragments of unsubstituted and methyl-substituted HBCP. The difference between the reorganization energies and HOMO/LUMO energy levels for the two molecules are 24 meV and 0.09/0.42 eV, respectively, suggesting that the electron-transporting and hole-blocking properties of HBCP are not influenced significantly by the methyl substitution. Usually, amorphous materials have been used in OLEDs. HBCP might be highly crystalline in nature because of its high symmetry. Amorphous HBCP-based materials would be obtained, for example, by introducing bulky substituents into HBCP.

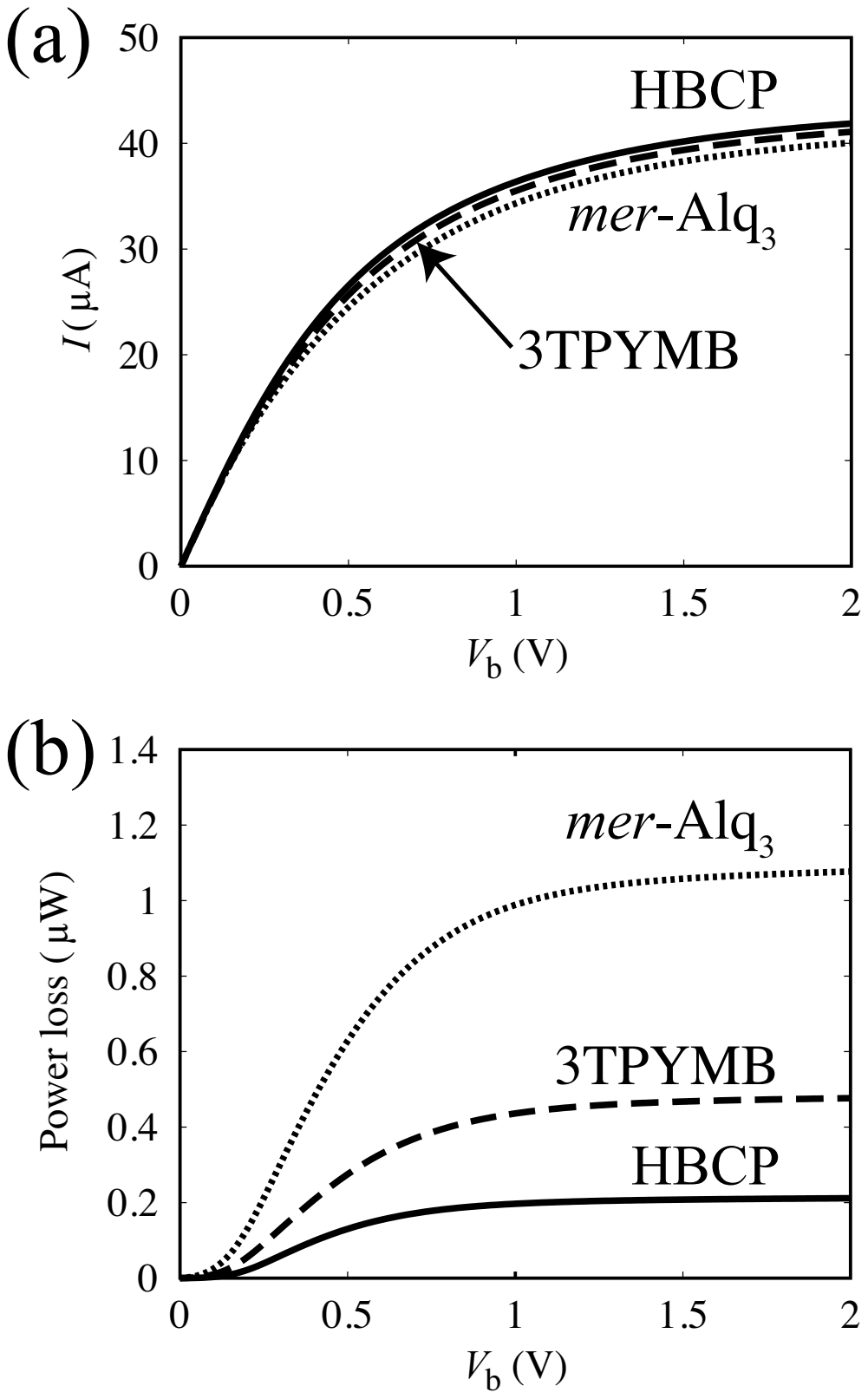

Figure 6.4: (a) Current-voltage characteristics and (b) power loss for *mer*-Alq_3 (dotted lines), 3TPYMB (dashed lines), and HBCP (solid lines).

Bibliography

[1] N. Chopra, J. Lee, Y. Zheng, S.-H. Eom, J. Xue, and F. So, Appl. Mater. Interfaces **1**, 1169 (2009).

[2] C. W. Tang and S. A. VanSlyke, Appl. Phys. Lett. **51**, 913 (1987).

[3] C. W. Tang, S. A. VanSlyke, and C. H. Chen, J. Appl. Phys. **65**, 3610 (1989).

[4] T. Noda and Y. Shirota, J. Am. Chem. Soc. **120**, 9714 (1998).

[5] S. Yamaguchi, S. Akiyama, and K. Tamao, J. Am. Chem. Soc. **122**, 6335 (2000).

[6] Q. Wu, M. Esteghamatian, N.-X. Hu, Z. Popovic, G. Enright, Y. Tao, M. D'Iorio, and S. Wang, Chem. Mater. **12**, 79 (2000).

[7] M. Kinoshita and Y. Shirota, Chem. Lett. **30**, 614 (2001).

[8] M. Kinoshita, H. Kita, and Y. Shirota, Adv. Funct. Mater. **12**, 780 (2002).

[9] D. Tanaka, T. Takeda, T. Chiba, S. Watanabe, and J. Kido, Chem. Lett. **36**, 262 (2007).

[10] Y. Shirota, Y. Kuwabara, D. Okuda, R. Okuda, H. Ogawa, H. Inada, T. Wakimoto, H. Nakada, Y. Yonemoto, S. Kawami, and K. Imai, J. Lumin. **72-74**, 985 (1997).

[11] T. Sato, K. Shizu, T. Kuga, K. Tanaka, and H. Kaji, Chem. Phys. Lett. **458**, 152 (2008).

[12] G. Rauhut and P. Pulay, J. Phys. Chem. **99**, 3093 (1995).

[13] M. J. Frisch, G. W. Trucks, H. B. Schlegel, G. E. Scuseria, M. A. Robb, J. R. Cheeseman, J. A. Montgomery, Jr., T. Vreven, K. N. Kudin, J. C. Burant, J. M. Millam, S. S. Iyengar, J. Tomasi, V. Barone, B. Mennucci, M. Cossi, G. Scalmani,

N. Rega, G. A. Petersson, H. Nakatsuji, M. Hada, M. Ehara, K. Toyota, R. Fukuda, J. Hasegawa, M. Ishida, T. Nakajima, Y. Honda, O. Kitao, H. Nakai, M. Klene, X. Li, J. E. Knox, H. P. Hratchian, J. B. Cross, V. Bakken, C. Adamo, J. Jaramillo, R. Gomperts, R. E. Stratmann, O. Yazyev, A. J. Austin, R. Cammi, C. Pomelli, J. W. Ochterski, P. Y. Ayala, K. Morokuma, G. A. Voth, P. Salvador, J. J. Dannenberg, V. G. Zakrzewski, S. Dapprich, A. D. Daniels, M. C. Strain, O. Farkas, D. K. Malick, A. D. Rabuck, K. Raghavachari, J. B. Foresman, J. V. Ortiz, Q. Cui, A. G. Baboul, S. Clifford, J. Cioslowski, B. B. Stefanov, G. Liu, A. Liashenko, P. Piskorz, I. Komaromi, R. L. Martin, D. J. Fox, T. Keith, M. A. Al-Laham, C. Y. Peng, A. Nanayakkara, M. Challacombe, P. M. W. Gill, B. Johnson, W. Chen, M. W. Wong, C. Gonzalez, and J. A. Pople, GAUSSIAN 03, Revision D.02, Gaussian, Inc., Wallingford, CT, 2004.

[14] S. Datta, *Quantum Transport: Atom to Transistor* (Cambridge University Press, Cambridge, 2005).

[15] K. Shizu, T. Sato, K. Tanaka, and H. Kaji, Org. Electron. **11**, 1277 (2010).

[16] P. A. Lane, G. P. Kushto, and Z. H. Kafafi, Appl. Phys. Lett. **90**, 023511 (2007).

Chapter 7

Vibronic Interactions in Hole-Transporting Molecules: An Interplay with Electron-Hole Interactions

7.1 Introduction

Hole-transporting (HT) materials have been attracted much attentions since they consist one of the building blocks in organic light-emitting diodes (OLED).[1–9] Among them, N,N'-diphenyl-N,N'-di(m-tolyl)benzidine (TPD, Fig. 7.1a) is well known as a HT material with highly-efficient HT properties in OLED.[10,11]

In the molecular level, the key interactions in carrier transport phenomena are electronic couplings among neighboring molecules and vibronic (electron-vibration) couplings. Large vibronic couplings give rise to a low mobility and energy dissipation. Therefore, a molecule with small vibronic couplings can be a candidate for a HT material. We have developed vibronic coupling density (VCD) analysis to investigate the vibronic couplings from relations between electronic and vibrational structures.[12,13] We have found that vibronic couplings are decreased if the electron-density difference between the neutral and ionic states is strongly localized not on bonds but on atoms.[14–16] We have investigated that the highly-efficient HT properties in TPD is ascribed to the electron-density difference which is strongly localized on the nitrogen atoms. Moreover, we have succeeded

in designing a highly-efficient electron-transporting molecule on the basis of the VCD concept.[17]

Though the highest occupied molecular orbital (HOMO) of TPD is delocalized over the molecule, the electron-density difference whose main source should arise from the HOMO is localized mainly on the nitrogen atoms.[14] The deficiency of the electron-density difference on the biphenyl group in TPD is still an open problem.

In this chapter, to clarify the problem, we analyze the vibronic coupling constants (VCC) in TPD derivatives, 4,4′-di(*N*-carbazolyl)biphenyl (CBP, Fig. 7.1b)[18] and 2,7-bis(phenyl-*m*-tolylamino)fluorene (TPF, Fig. 7.1c)[19] in terms of the VCD analysis. The replacement of the phenyl and tolyl groups in TPD by the carbazolyl group gives CBP, while the replacement of the biphenyl group in TPD by the fluorenyl group gives TPF. CBP has also been employed as a host for phosphorescent materials.[20–26] We also investigate the influence of electron-hole interactions on the vibronic couplings employing a Hubbard Hamiltonian. The finding in this chapter is one of the guiding principles which enable us to control the vibronic couplings.

7.2 Theory

A vibronic coupling between the electronic state and the ith vibrational mode of the molecule is described by the VCC V_i. V_i can be expressed as the space integral of the VCD of the ith vibrational mode η_i:[12,13]

$$V_i = \int \eta_i(\mathbf{x})\, d\mathbf{x}, \tag{7.1}$$

where $\mathbf{x}$ denotes a position in the 3D space.

The VCD η_i can be expressed as the product of the electron-density difference between the cationic and neutral states $\Delta\rho(\mathbf{x})$ and the one-electron part of the derivative of the nuclear–electronic potential with respect to the normal coordinate of the ith mode $v_i(\mathbf{x})$:

$$\eta_i(\mathbf{x}) = \Delta\rho(\mathbf{x}) \times v_i(\mathbf{x}), \tag{7.2}$$

where

$$\Delta\rho(\mathbf{x}) = \rho_{\text{cationic}}(\mathbf{x}) - \rho_{\text{neutral}}(\mathbf{x}), \tag{7.3}$$

$$v_i(\mathbf{x}) = \sum_A v_{i,A}(\mathbf{x}) = \sum_A -\frac{Z_A}{\sqrt{M_A}} \mathbf{e}_A^{(i)} \cdot \frac{\mathbf{x} - \mathbf{R}_A}{|\mathbf{x} - \mathbf{R}_A|^3}. \tag{7.4}$$

Here, $\mathbf{x}$ denotes a position in the space, $\rho_{\text{cationic}}(\mathbf{x})$ and $\rho_{\text{neutral}}(\mathbf{x})$ are electron densities for the cationic and neutral states, respectively, at the equilibrium geometry of the neutral state. Z_A, M_A, and $\mathbf{R}_A$ are the atomic number, mass, and position of the Ath nucleus, respectively, and $\mathbf{e}_A^{(i)}$ is the mass-weighted 3D component of the Ath atom of the ith vibrational mode Q_i. Only the totally symmetric modes are vibronically active and yield non-zero VCCs. $v_{i,A}$ is the contribution from the Ath atom to v_i and represents a distribution of v_i around the Ath atom.

An atomic vibronic coupling constant (AVCC) $V_{i,A}$ of the Ath atom is defined by

$$V_{i,A} = \int \Delta\rho(\mathbf{x}) \times v_{i,A}(\mathbf{x})\, d\mathbf{x}. \tag{7.5}$$

The sum of $V_{i,A}$ over A gives again V_i:

$$\sum_A V_{i,A} = V_i. \tag{7.6}$$

7.3 Method of calculation

We employed the RHF method for the geometry optimizations and vibrational analyses of the neutral CBP and TPF molecules. We confirmed that the optimized geometries are stationary minima. Employing the 6-31G basis set with their first derivatives[27] (denoted as 6-31G+der), we confirmed that the Hellmann-Feynman theorem[28] is satisfied. We calculated the VCCs for the CBP and TPF cations using the wavefunctions of the cationic states at the ROHF/6-31G+der level of theory for the optimized geometries of their neutral state. The method of calculation is the same as used for TPD in Chapter I for comparison.[14] All the *ab initio* calculations were performed using GAMESS package.[29]

7.4 Results and discussion

Optimized geometries of CBP and TPF are shown in Fig. 7.1. The structure of TPD is also shown for comparison. The symmetries of the optimized structures are C_2 for TPF and TPD and D_2 for CBP. The carbazolyl group in CBP and the carbon backbone of the fluorenyl group in TPF are almost coplanar. The dihedral angles C1−C7−C13−N1 and C7−N1−C1−C2 for TPD, CBP, and TPF are tabulated in Table 7.1. The dihedral angle C1−C7−C13−N1 for CBP is 0.0°, suggesting that the N1 atom is located on the plane formed by the C1, C7, and C13 atoms. For TPD and TPF, the position of the N1 atom is slightly deviated from the C1−C7−C13 plane. The dihedral angle C7−N1−C1−C2 for TPF (131.3°) is close to that for TPD (128.3°), suggesting that the replacement of the central biphenyl unit by the fluorenyl unit has little effect on the dihedral angle C7−N1−C1−C2. By contrast, the dihedral angle C7−N1−C1−C2 decreases to 107.3° by replacing the diphenylamino groups by the carbazolyl groups.

Table 7.1: Dihedral angles in degree. The atomic labels are shown in Fig. 7.1. The structure of TPD is taken from Chapter 1.[14]

	C1−C7−C13−N1	C7−N1−C1−C2
TPD	−0.6	128.3
CBP	0.0	107.3
TPF	0.3	−131.3

Fig. 7.2a shows the VCCs in the CBP cation. The maximum-coupling one is 1805 cm^{-1} mode which corresponds to a quinoid deformation (Fig. 7.2b). Note that the number of the active modes is small in the CBP cation. CBP has the smaller number of active modes than TPF because CBP belongs to the higher-symmetry point group (D_2) than TPF (C_2). Consequently, the reorganization energy for hole transfer in CBP is calculated to be smaller than that of TPF. We found the maximum-coupling mode in the TPD cation (1795 cm^{-1}) corresponds to this mode. Since the VCCs of these modes are 2.1×10^{-4} a.u. and 9.9×10^{-5} a.u. for CBP and TPD, respectively, the VCC in CBP is twice as large as that of TPD.

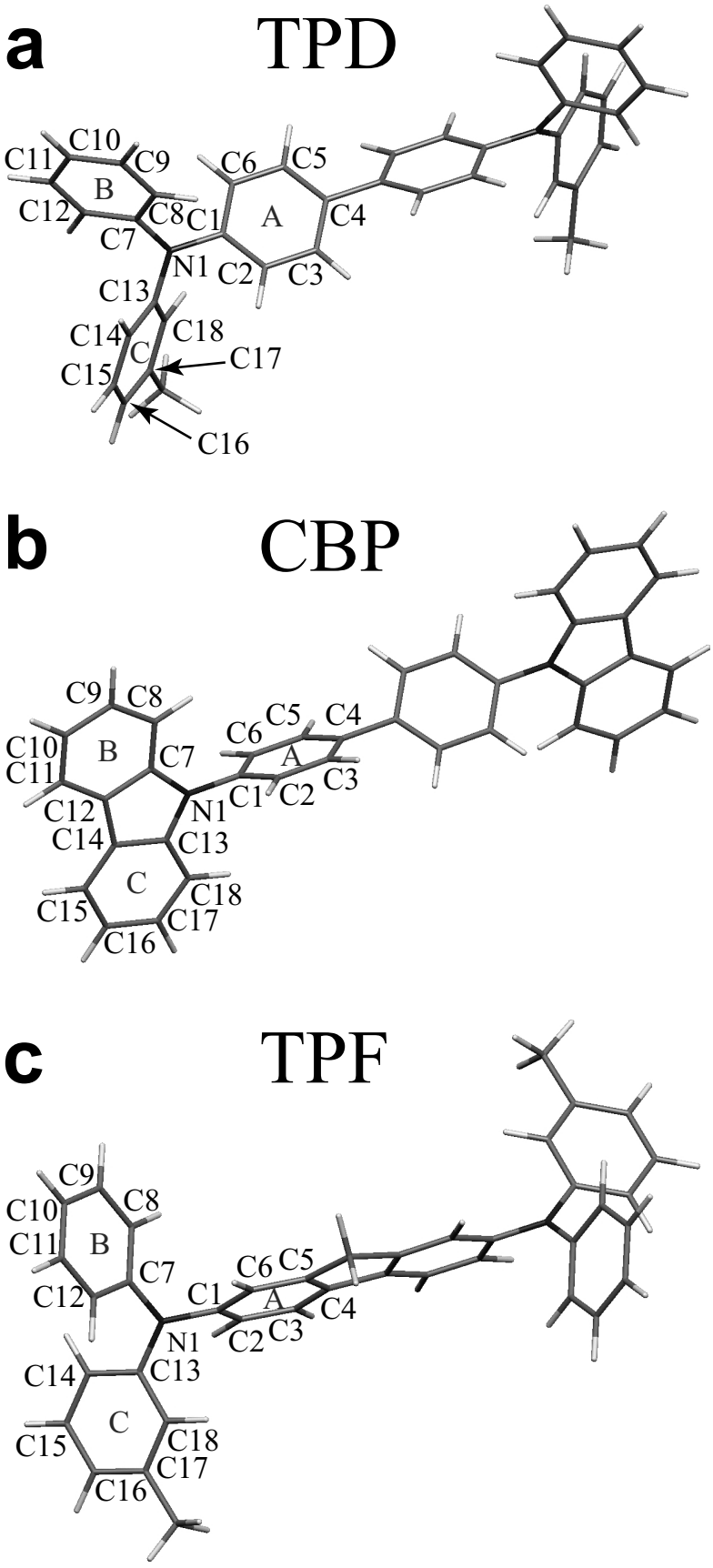

Figure 7.1: Molecular structures of (a) TPD, (b) CBP, and (c) TPF with atomic and ring labeling schemes.

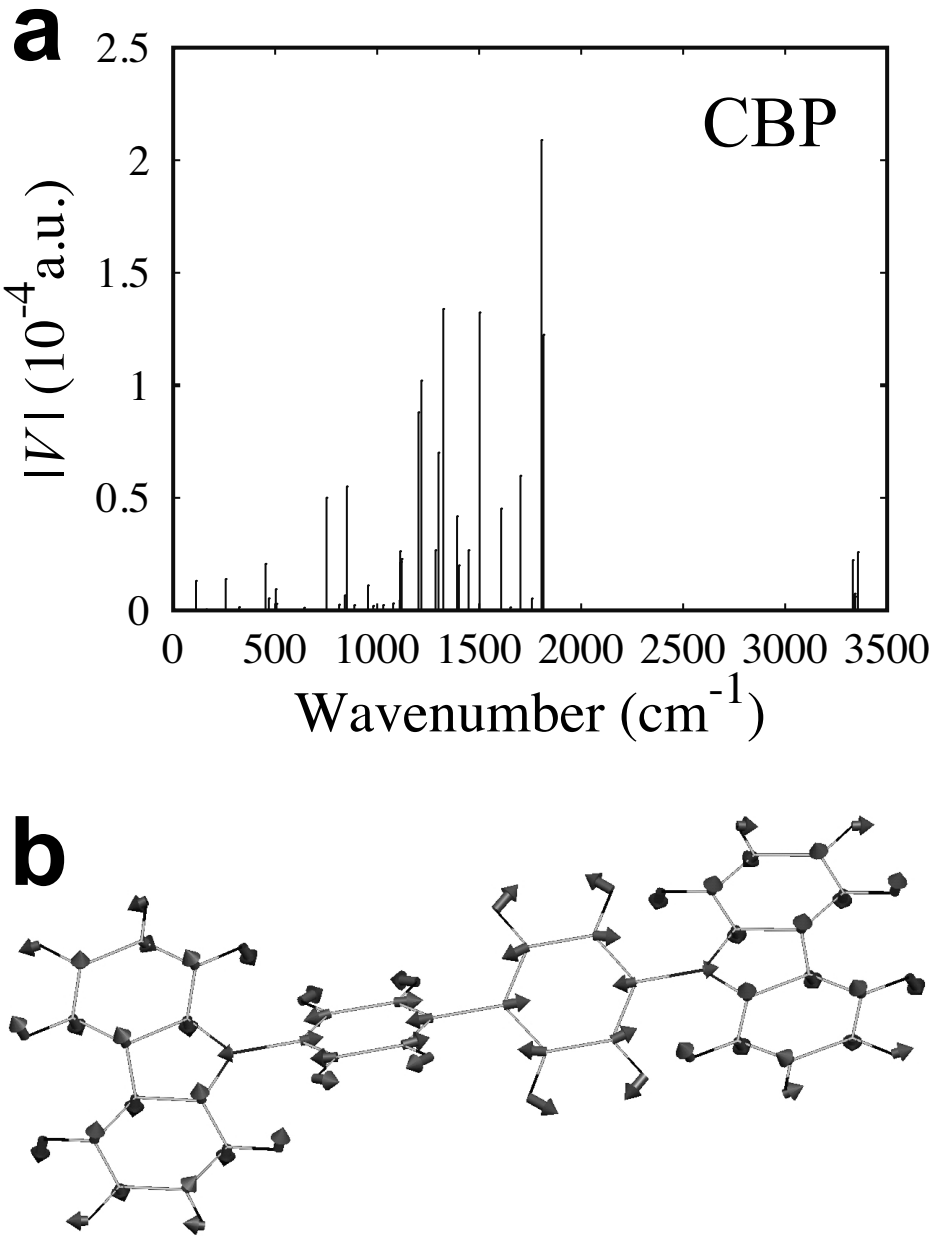

Figure 7.2: (a) Vibronic coupling constants and (b) the mode which exhibits the maximum vibronic coupling in CBP ($\omega = 1805$ cm^{-1}, $V = 2.1 \times 10^{-4}$ a.u.).

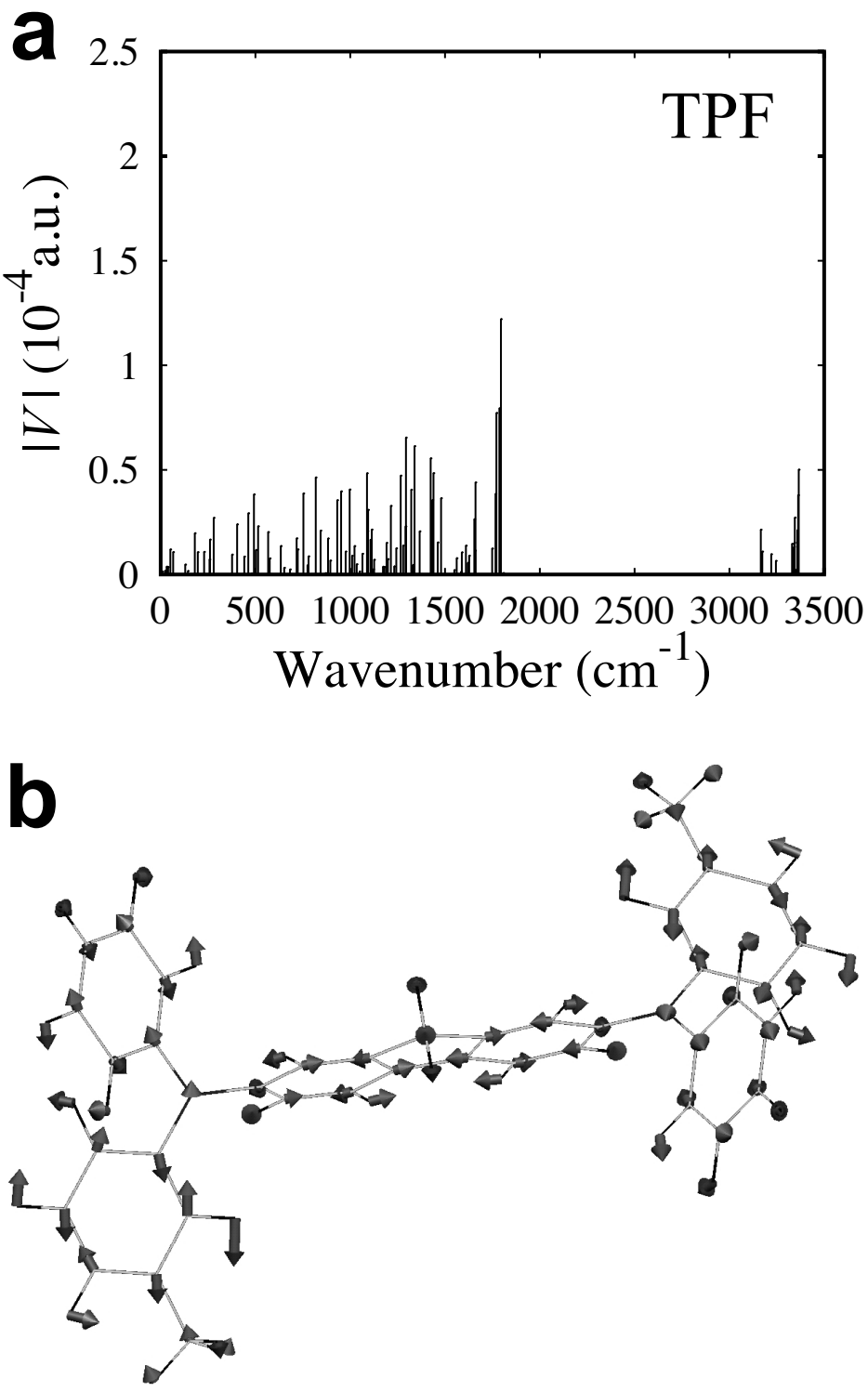

Figure 7.3: (a) Vibronic coupling constants and (b) the mode which exhibits the maximum vibronic coupling in TPF ($\omega = 1795$ cm^{-1}, $V = 1.2 \times 10^{-4}$ a.u.).

On the other hand, the maximum-coupling modes in TPF and TPD are almost the same in the vibrational frequency and VCC. The frequencies are 1795 cm^{-1} for both molecules, and the VCCs are 1.2×10^{-4} a.u. and 9.9×10^{-5} a.u. (Fig. 7.3a). This mode also corresponds to the maximum-coupling mode in CBP (Fig. 7.3b). Moreover, it should be noted that the whole VCC spectrum of TPF resembles to that of TPD.

The AVCCs of CBP and TPF are tabulated in Table 7.2 and 7.3, respectively. In the CBP cation, the carbazolyl groups (ring B and C) have larger AVCCs than those of the phenyl (-1.851×10^{-5} a.u.) and tolyl (-2.852×10^{-5} a.u.) groups in TPD.[14] On the other hand, in the TPF cation, the fluorenyl group (ring A) has small AVCCs. In other words, the bridge in TPF has little effect on the VCCs.

Fig. 7.4 shows the VCD analyses of the maximum-coupling modes in the CBP and TPF cations. Figs. 7.4a and b show the electron-density difference $\Delta\rho$ for CBP and TPF, respectively. $\Delta\rho$ is strongly localized on the nitrogen atoms for each cation as it is in TPD. The increase of the VCCs in CBP is ascribed to large $\Delta\rho$ on the carbazolyl group. The distribution of $\Delta\rho$ in TPF is almost the same as that in TPD,[14] in spite of the planarity of the fluorenyl group. This is the reason why the VCC spectrum of TPF is similar to that of TPD.

Strong and symmetric localization of $\Delta\rho$ on atoms give rise to the reduction of VCCs. Figs. 7.4c and d are the potential derivative v_i with respect to the maximum-coupling mode shown in Figs. 7.2b and 7.3b, respectively. v_i is delocalized over the cations. The VCD η_i for the CBP and TPF cations are shown in Figs. 7.4e and f, respectively. η_i on the terminal diphenylamino groups (ring B and C) are large, and the biphenyl unit (ring A) has small η_i. It should be noted that the central biphenyl unit has small $\Delta\rho$. This leads to the reduction of the VCD on the biphenyl or fluorenyl unit. Accordingly, the VCC becomes small.

Table 7.2: Atomic vibronic coupling constants (10^{-5} a.u.) of the maximum-coupling mode (1805 cm^{-1}) in CBP. The atomic and ring labels are shown in Fig. 7.1.

ring A		ring B		ring C		Nitrogen	
C1	−0.785	C7	−0.613	C13	−0.613	N1	−0.235
C2	−0.197	C8	−0.298	C14	−1.098		
C3	−0.040	C9	0.161	C15	−1.801		
C4	−0.213	C10	−0.522	C16	−0.522		
C5	−0.040	C11	−1.801	C17	0.161		
C6	−0.197	C12	−1.098	C18	−0.298		
Sum	−1.472		−4.171		−4.171		−0.235

Table 7.3: Atomic vibronic coupling constants (10^{-5} a.u.) of the maximum-coupling mode (1795 cm^{-1}) in TPF. The atomic and ring labels are shown in Fig. 7.1.

ring A		ring B		ring C		Nitrogen	
C1	0.033	C7	0.601	C13	0.837	N1	0.005
C2	0.090	C8	0.617	C14	0.124		
C3	0.054	C9	0.412	C15	0.778		
C4	0.533	C10	0.000	C16	−0.239		
C5	0.147	C11	0.392	C17	0.062		
C6	0.016	C12	0.396	C18	1.505		
Sum	0.873		2.418		3.067		0.005

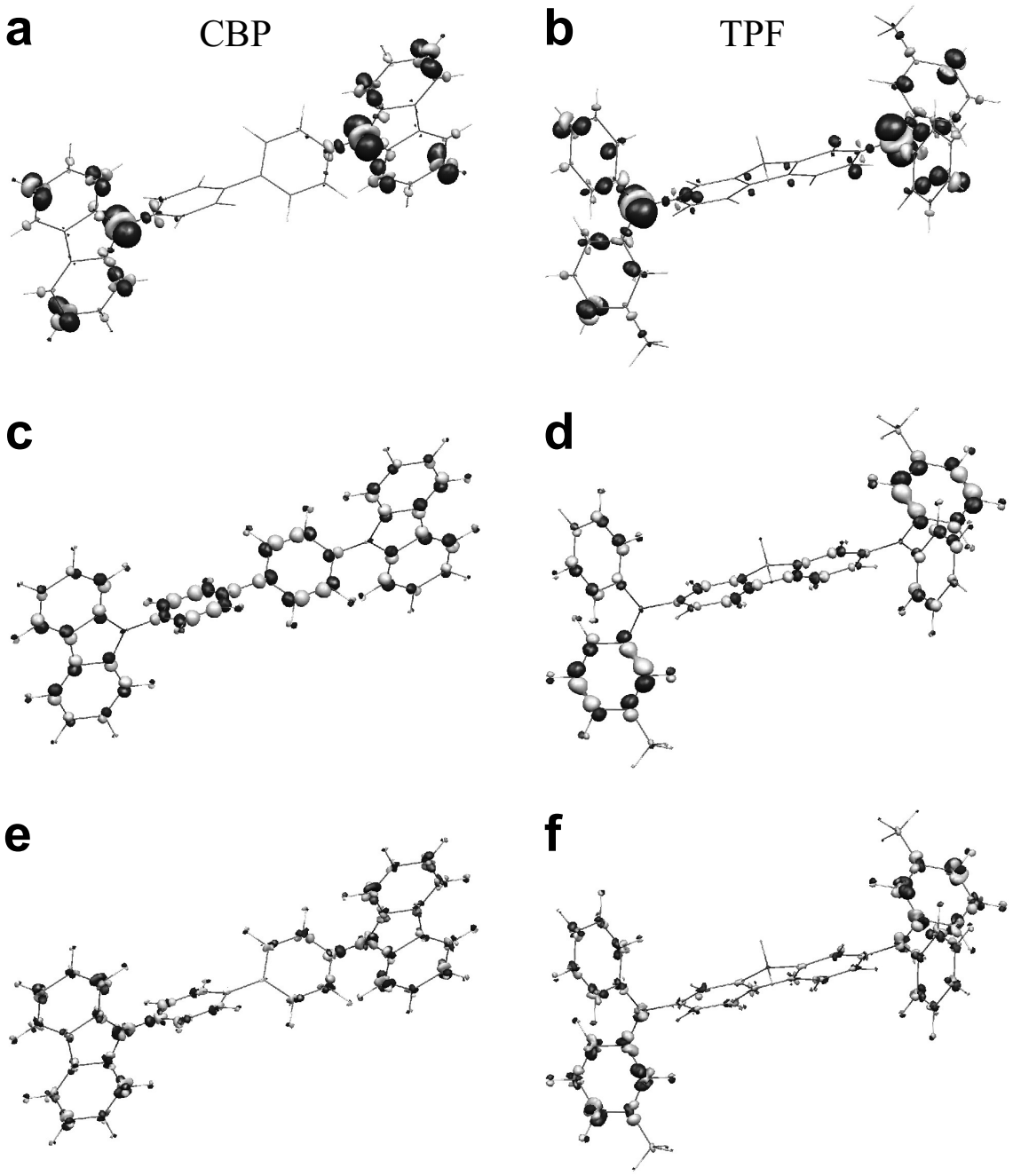

Figure 7.4: Electron-density difference $\Delta\rho$ in (a) the CBP cation and (b) TPF cation. Potential derivative v_i with respect to the maximum-coupling modes in (c) the CBP cation and (d) TPF cation. Vibronic coupling density η_i of the maximum-coupling modes in (e) the CBP cation and (f) TPF cation.

In order to investigate the deficiency of $\Delta\rho$ on the fluorenyl unit in the TPF cation, fragment molecular orbital (FMO) analysis was employed for the TPF cation using the extended Hückel method.[30] The cation is divided at the C−N bonds into three parts: the fluorenyl unit and two diphenylamino groups. It should be noted that, since the energy levels of the HOMOs of the fragments are close, the fragment HOMOs are hybridized. Therefore, the HOMO−2 and HOMO of TPF has almost the same orbital pattern on the fluorenyl unit. We projected the Hartree–Fock MOs of the TPF cation onto those of the neutral molecule. It is found the major components of the HOMO in the cation are the HOMO−2 and HOMO of the neutral molecule. When the molecule acquires a hole, the hole is affected by the strong electron-hole interaction between the HOMO−2 and HOMO because of the same orbital pattern on the fluorenyl group. The hole increases the orbital coefficients on the fluorenyl group of the HOMO−2. This increase compensates the electron removal from the HOMO on the fluorenyl unit.

The HOMO of the neutral TPF is delocalized on the fluorenyl unit. However, $\Delta\rho$ is deficient on the fluorenyl unit. In addition to the above mean field picture, we employed the following Hubbard Hamiltonian to investigate further the effect of electron-hole interactions on $\Delta\rho$:

$$H = \sum_{\sigma=\uparrow,\downarrow}\sum_{i=a,b}\epsilon_i a^\dagger_{i\sigma}a_{i\sigma} + \sum_{\sigma=\uparrow,\downarrow}\sum_{i,j=a,b} t a^\dagger_{i\sigma}a_{j\sigma} + \sum_{i=a,b} U_i a^\dagger_{i\uparrow}a_{i\uparrow}a^\dagger_{i\downarrow}a_{i\downarrow}, \tag{7.7}$$

where ϵ_i is the energy level of the fragment HOMOs, χ_a and χ_b, of the fragment $i = a, b$ (in the case of TPF, fragment a is the terminal groups of two diphenylamino groups, and fragment b is the central fluorenyl unit), t the transfer integral between the fragment HOMOs, and U_i the on-site Coulomb interaction on the site i. An electronic configuration is written as $|\text{site}\quad a, \text{site}\quad b\rangle$. The neutral state is written as $|\uparrow\downarrow,\uparrow\downarrow\rangle$, the cationic state in which a hole is localized on fragment a, $|\uparrow\quad,\uparrow\downarrow\rangle$, and the cationic state in which a hole is localized on fragment b, $|\uparrow\downarrow,\uparrow\quad\rangle$. The expectation value for the neutral state is $E_0 = \langle\uparrow\downarrow,\uparrow\downarrow|H|\uparrow\downarrow,\uparrow\downarrow\rangle = 2\epsilon_a + 2\epsilon_b + U_a + U_b$. The Hamiltonian matrix for the cationic state is written as

$$H_{\text{cat}} = \begin{pmatrix} E_0 - \epsilon_a - U_a & t \\ t & E_0 - \epsilon_b - U_b \end{pmatrix}. \tag{7.8}$$

The eigen state is expressed by $C^a_\pm|\uparrow\quad,\uparrow\downarrow\rangle + C^b_\pm|\uparrow\downarrow,\uparrow\quad\rangle$. Since $\rho_0 = 2\chi_a^2 + 2\chi_b^2$ for the neutral state, $\rho^a = \chi_a^2 + 2\chi_b^2$ for the cationic state $|\uparrow\quad,\uparrow\downarrow\rangle$, and $\rho^b = 2\chi_a^2 + \chi_b^2$ for the

cationic state $|\uparrow\downarrow,\uparrow\rangle$, the electron-density difference is

$$\Delta\rho_{\pm} = \rho_{\pm} - \rho_0 = \left\{(C_{\pm}^a)^2\rho^a + (C_{\pm}^b)^2\rho^b\right\} - \rho_0 = \Delta\rho_{\pm}^a\chi_a^2 + \Delta\rho_{\pm}^b\chi_b^2, \tag{7.9}$$

where $\Delta\rho_{\pm}^i$ is the electron-density difference on the site i:

$$\Delta\rho_{\pm}^a = (C_{\pm}^a)^2 + 2(C_{\pm}^b)^2 - 2, \tag{7.10}$$

$$\Delta\rho_{\pm}^b = 2(C_{\pm}^a)^2 + (C_{\pm}^b)^2 - 2. \tag{7.11}$$

From the lower eigen state of the model Hamiltonian, we obtain the electron-density difference on the fluorenyl unit as

$$\Delta\rho_{-}^b = \frac{\Delta\epsilon + \Delta U - \sqrt{(\Delta\epsilon + \Delta U)^2 + 4t^2}}{2\sqrt{(\Delta\epsilon + \Delta U)^2 + 4t^2}}, \tag{7.12}$$

where $\Delta\epsilon = \epsilon_a - \epsilon_b$ and $\Delta U = U_a - U_b$. In the case of TPF $\Delta\epsilon$ is positive (see Fig. 7.5), and we can assume ΔU positive since the hole can be delocalized on the isolated fragment b and localized on the isolated fragment a: $U_a > U_b$.

If the transfer integral and on-site Coulomb interactions are zero, $\Delta\rho_{-}$ is completely localized on the diphenylamino groups (fragment a). However, this is not the case, and t is not small compared with $\Delta\epsilon$ since we can find that the HOMO of TPF is delocalized (see Fig. 7.5). We consider the following limiting cases of $\Delta\rho_{-}^b$ for ΔU:

$$\Delta\rho_{-}^b = \begin{cases} \left(-\frac{1}{2} + \frac{\Delta\epsilon}{2\sqrt{\Delta\epsilon^2+4t^2}}\right) + \left(\frac{2t^2}{(\Delta\epsilon^2+4t^2)^{\frac{3}{2}}}\right)\Delta U + \cdots & (\Delta U \ll 1), \\ 0 \quad (\Delta U \to \infty) \end{cases} \tag{7.13}$$

Since $|\Delta\rho_{-}^b|$ is monotonously decreasing as a function of ΔU, $|\Delta\rho_{-}^b|$ decreases from $\frac{1}{2} - \frac{\Delta\epsilon}{2\sqrt{\Delta\epsilon^2+4t^2}}$ to 0. Therefore, though t is large, and the HOMO is delocalized on the fluorenyl unit, the electron-density difference on the fluorenyl group can be small if the difference of the on-site Coulomb interaction ΔU is sufficiently large.

In the cation, due to the positive ΔU, the electrons on fragment a move to fragment b to compensate negative $\Delta\rho$ on fragment b. Thus, $\Delta\rho$ on fragment b is deficient, and $\Delta\rho$ is localized on fragment a. Fragment a acts as a hole-localized unit. $\Delta\rho$ on fragment a is accommodated mainly on the nitrogen atoms. Accordingly, because of the cancellation of the VCD on the nitrogen and the deficiency of $\Delta\rho$ on fragment b, the VCCs of TPF are small. This is also the case in TPD.

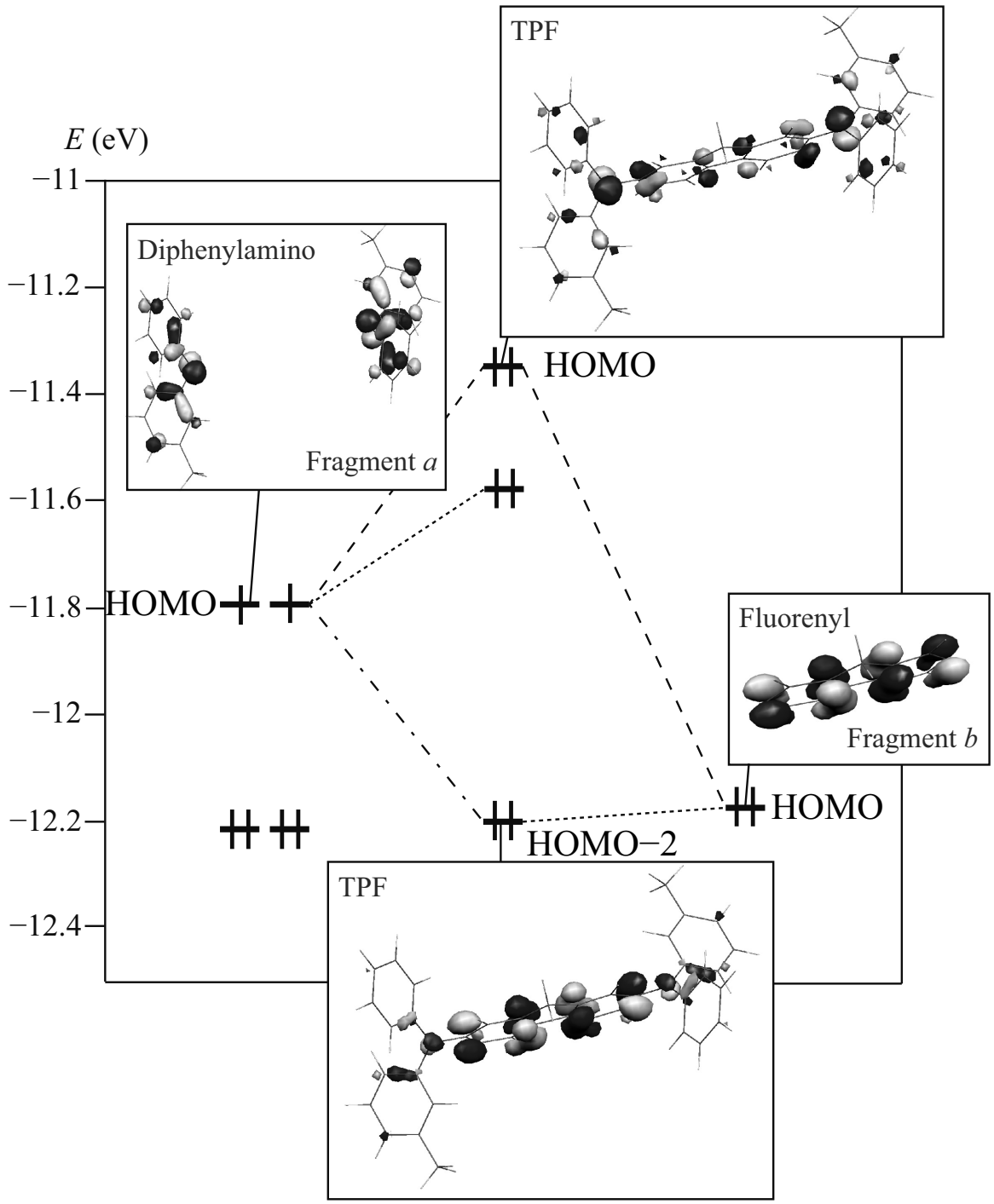

Figure 7.5: Fragment molecular orbital analysis of TPF. TPF is divided at two N−C bonds into two parts: two diphenylamino groups (fragment *a*) and central fluorenyl unit (fragment *b*).

7.5 Conclusion

We have investigated the vibronic couplings in the CBP and TPF cations on the basis of the VCD analysis. In spite of the bridge in TPF, the planarity of the central fluorenyl unit has little effect on the vibronic couplings in the TPF cation, while the bridges in CBP make increases of the maximum vibronic-coupling in the CBP cation. This effect comes from the deficiency of the electron-density difference on the central fluorenyl unit. We have discussed the effect of on-site Coulomb interaction, or electron-hole interaction on the electron-density difference using the Hubbard model. It is found that the difference of the on-site Coulomb interactions gives rise to the strong localization of the electron-density difference on the diphenylamino groups and the deficiency on the fluorenyl group in the TPF cation. They are responsible for the small VCCs in TPF. These finding will open a way to control vibronic couplings in a molecule using many-body interactions.

Bibliography

[1] L.-Z. Zhang, C.-W. Chen, C.-F. Lee, C.-C. Wu, and T.-Y. Luh, Chem. Commun. 2336 (2002).

[2] P. Strohriegl and J. V. Grazulevicius, Adv. Mater. **14**, 1439 (2002).

[3] M. Thelakkat, Macromol. Mater. Eng. **287**, 442 (2002).

[4] Y. Shirota, J. Mater. Chem. **15**, 75 (2005).

[5] K. Okumoto, H. Kanno, Y. Hamada, H. Takahashi, and K. Shibata, J. Appl. Phys. **100**, 044507 (2006).

[6] T. P. I. Saragi, T. Fuhrmann-Lieker, and J. Salbeck, Adv. Funct. Mater. **16**, 966 (2006).

[7] T. P. I. Saragi, T. Spehr, A. Siebert, T. Fuhrmann-Lieker, and J. Salbeck, Chem. Rev. **107**, 1011 (2007).

[8] Y. Shirota and H. Kageyama, Chem. Rev. **107**, 953 (2007).

[9] H. Tsuji, C. Mitsui, L. Ilies, Y. Sato, and E. Nakamura, J. Am. Chem. Soc. **129**, 11902 (2007).

[10] M. Stolka, J. F. Yanus, and D. M. Pai, J. Phys. Chem. **88**, 4707 (1984).

[11] J. Kido, C. Ohtaki, K. Hongawa, K. Okuyama, and K. Nagai, Jpn. J. Appl. Phys. **32**, L917 (1993).

[12] T. Sato, K. Tokunaga, and K. Tanaka, J. Phys. Chem. A **112**, 758 (2008).

[13] T. Sato, K. Tokunaga, N. Iwahara, K. Shizu, and K. Tanaka, *Vibronic coupling constant and vibronic coupling density* in *The Jahn-Teller-Effect - Fundamentals and*

Implications for Physics and Chemistry, H. Köppel, D. R. Yarkony, and H. Barentzen (Eds) (Springer-Verlag, Berlin and Heidelberg, 2009).

[14] T. Sato, K. Shizu, T. Kuga, K. Tanaka, and H. Kaji, Chem. Phys. Lett. **458**, 152 (2008).

[15] K. Shizu, T. Sato, K. Tanaka, and H. Kaji, Chem. Phys. Lett. **486**, 130 (2010).

[16] K. Shizu, T. Sato, K. Tanaka, and H. Kaji, Org. Electron. **11**, 1277 (2010).

[17] K. Shizu, T. Sato, K. Tanaka, and H. Kaji, Appl. Phys. Lett. **97**, 142111 (2010).

[18] B. E. Koene, D. E. Loy, and M. E. Thompson, Chem. Mater. **10**, 2235 (1998).

[19] D. E. Loy, B. E. Koene, and M. E. Thompson, Adv. Funct. Mater. **12**, 245 (2002).

[20] M. A. Baldo, S. Lamansky, P. E. Burrows, M. E. Thompson, and S. R. Forrest, Appl. Phys. Lett. **75**, 4 (1999).

[21] M. A. Baldo, M. E. Thompson, and S. R. Forrest, Nature **403**, 750 (2000).

[22] P. E. Burrows, S. R. Forrest, T. X. Zhou, and L. Michalski, Appl. Phys. Lett. **76**, 2493 (2000).

[23] R. C. Kwong, S. Lamansky, and M. E. Thompson, Adv. Mater. **12**, 1134 (2000).

[24] M. Ikai, S. Tokito, Y. Sakamoto, T. Suzuki, and Y. Taga, Appl. Phys. Lett. **79**, 156 (2001).

[25] B. W. D'Andrade, M. E. Thompson, and S. R. Forrest, Adv. Mater. **14**, 147 (2002).

[26] J. P. J. Markham, S.-C. Lo, S. W. Magennis, P. L. Burn, and I. D. W. Samuel, Appl. Phys. Lett. **80**, 2645 (2002).

[27] H. Nakatsuji, K. Kanda, and T. Yonezawa, Chem. Phys. Lett. **75**, 340 (1980).

[28] R. P. Feynman, Phys. Rev. **56**, 340 (1939).

[29] M. W. Schmidt, K. K. Baldridge, J. A. Boatz, S. T. Elbert, M. S. Gordon, J. H. Jensen, S. Koseki, N. Matsunaga, K. A. Nguyen, S. J. Su, T. L. Windus, M. Dupins, and J. A. Montgomery, J. Comput. Chem. **14**, 1347 (1993).

[30] M. J. Frisch, G. W. Trucks, H. B. Schlegel, G. E. Scuseria, M. A. Robb, J. R. Cheeseman, J. A. Montgomery, Jr., T. Vreven, K. N. Kudin, J. C. Burant, J. M. Millam, S. S. Iyengar, J. Tomasi, V. Barone, B. Mennucci, M. Cossi, G. Scalmani, N. Rega, G. A. Petersson, H. Nakatsuji, M. Hada, M. Ehara, K. Toyota, R. Fukuda, J. Hasegawa, M. Ishida, T. Nakajima, Y. Honda, O. Kitao, H. Nakai, M. Klene, X. Li, J. E. Knox, H. P. Hratchian, J. B. Cross, V. Bakken, C. Adamo, J. Jaramillo, R. Gomperts, R. E. Stratmann, O. Yazyev, A. J. Austin, R. Cammi, C. Pomelli, J. W. Ochterski, P. Y. Ayala, K. Morokuma, G. A. Voth, P. Salvador, J. J. Dannenberg, V. G. Zakrzewski, S. Dapprich, A. D. Daniels, M. C. Strain, O. Farkas, D. K. Malick, A. D. Rabuck, K. Raghavachari, J. B. Foresman, J. V. Ortiz, Q. Cui, A. G. Baboul, S. Clifford, J. Cioslowski, B. B. Stefanov, G. Liu, A. Liashenko, P. Piskorz, I. Komaromi, R. L. Martin, D. J. Fox, T. Keith, M. A. Al-Laham, C. Y. Peng, A. Nanayakkara, M. Challacombe, P. M. W. Gill, B. Johnson, W. Chen, M. W. Wong, C. Gonzalez, and J. A. Pople, GAUSSIAN 03, Revision D.02, Gaussian, Inc., Wallingford, CT, 2004.

Part II

Vibronic Coupling Density Analyses of Molecular Wires

Chapter 1

Vibronic Coupling Density Analysis for α-Oligothiophene Cations: A New Insight for Polaronic Defects

1.1 Introduction

Oligothiophenes and polythiophenes are promising materials for electronic devices. α,α'-oligothiophenes (denoted α-nT, where n is the number of thiophene rings) are attracting attention because of their good charge-transport properties, high chemical stability, and synthetic flexibility.[1] α-nT (n=3, 4, 5, 6, 8) thin films have been used as semiconductors in organic field-effect transistors (FETs) and thin-film transistors (TFTs).[2–16] Halik *et al.* investigated that the effect of α-6T alkyl side-chain length on mobility and reported that the measured carrier mobility to be 1.1 $cm^2V^{-1}s^{-1}$ for α,α'-diethylsexithiophene, which has the highest hole mobility other than pentacene.[17] For non-substituted α-5T, α-6T, and α-7T, carrier mobilities increase with n.[18]

Recently there has been renewed interest in using them as single molecular wires,[19] and to this end long oligothiophenes (up to 96-mer) have been synthesized.[20–23] Electrical resistance of single oligothiophene molecular wires (up to 23-mer) linked to gold electrodes have been measured.[24] The molecular length dependence of the electrical resistance suggests that the transport mechanism changes from tunneling to hopping at around 14-mer. Such a mechanistic transition is governed by the strength of vibronic coupling.[25]

A local picture of vibronic coupling in a molecule is described in terms of its vibronic

coupling density (VCD);[26–30] space integration of the VCD gives the linear VCC (vibronic coupling constant). VCD is the product of electron-density difference $\Delta\rho$ and the derivative of the nuclear–electronic potential v. The degree of overlap between $\Delta\rho$ and v determines the magnitude of the linear VCC with respect to a normal coordinate. One of the sources of an electrical resistance is vibronic coupling. A molecule with a large/small linear VCC inhibits a charge transport greatly/slightly. In the non-equilibrium Green's function (NEGF) method,[31] the linear vibronic coupling constant plays an important role in a mechanism of the inelastic scattering. Therefore, it is important to elucidate the reason for the relative magnitudes of linear VCCs, and VCD analysis provides some insights.[27–30,32]

When a carrier transmits through a long oligothiophene, it is natural to assume that the carrier interacts with molecular vibrations. Interaction between carrier and molecular vibration, called vibronic coupling or electron–phonon coupling, deforms the molecular structure, causes an inelastic scattering, and inhibits a carrier transport. Structural modification in neutral oligothiophenes upon ionization is known to correspond to quinoid deformation, the degree of which is governed by the magnitude of the VCC.

Raman spectra of BF_4-doped polythiophene show that the polaron is a major species.[33,34] For polythiophenes, polaron size is estimated to be four thiophene rings. In other words, structural deformation occurs mainly in four thiophene rings.[35] For oligothiophenes, polaron size has been calculated, by comparison of neutral-state and oxidized-state bond lengths, to be four thiophene rings.[36,37] Theoretical study of long oligothiophene polycations shows that polaron size is about five thiophene rings.[38] As discussed in Section 1.4.3, using VCD analysis, we can explain the reason why the size is four or five rings. Polaron formation plays an important role in conducting mechanisms for organic semiconductors, and VCD analysis opens a new way for molecular design of carrier-transporting materials.

In this chapter, we calculate the VCDs for α-nT ($n = 2 - 9$) and explain relative sizes of VCCs by means of VCD analysis. In Sections 1.2 and 1.3, we describe a method for calculating the VCC and VCD. In Sections 1.4.1 and 1.4.2, we explain the relative VCC sizes for α-2T and α-3T cations using VCD analysis. In Section 1.4.3, we investigate the n dependences of VCC, VCD, and polaron size. In Section 1.4.4, we simulate a photoelectron spectrum of α-3T and compare the spectrum with the experiment.

1.2 Theory

The Hamiltonian of a molecule is given by

$$\mathcal{H}\left(\mathbf{r},\mathbf{R}\right)=\mathcal{H}_{\mathrm{e}}\left(\mathbf{r},\mathbf{R}\right)+\mathcal{T}_{\mathrm{n}}\left(\mathbf{R}\right), \tag{1.1}$$

where $\mathcal{H}_{\mathrm{e}}\left(\mathbf{r},\mathbf{R}\right)$ is an electronic Hamiltonian, $\mathcal{T}_{\mathrm{n}}\left(\mathbf{R}\right)$ is the nuclear kinetic energy, and $\mathbf{r}$ and $\mathbf{R}$ denote sets of electronic and nuclear coordinates, respectively. The linear VCC for the i^{th} totally symmetric modes is written in terms of a set of mass-weighted normal coordinates $\{Q_i\}$:

$$V_i=\left\langle \Psi^{+}\left(\mathbf{r},\mathbf{R_0}\right)\left|\left(\frac{\partial\mathcal{H}_{\mathrm{e}}\left(\mathbf{r},\mathbf{R}\right)}{\partial Q_i}\right)_{\mathbf{R_0}}\right|\Psi^{+}\left(\mathbf{r},\mathbf{R_0}\right)\right\rangle, \tag{1.2}$$

where $\mathbf{R_0}$ is the nuclear configuration of the equilibrium geometry in the neutral state and $\Psi^{+}\left(\mathbf{r},\mathbf{R_0}\right)$ is the electronic wave function of the cationic state at equilibrium geometry. $\partial/\partial Q_i$ is related to $\partial/\partial\mathbf{R}$ by the following equation,

$$\frac{\partial}{\partial Q_i}=\sum_A\frac{\mathbf{e}_A^{(i)}}{\sqrt{M_A}}\cdot\frac{\partial}{\partial\mathbf{R}}, \tag{1.3}$$

where M_A is the mass of nucleus A and $\mathbf{e}_A^{(i)}$ is the A^{th} component of a vibrational vector of the i^{th} vibrational mode in the mass-weighted coordinates $\mathbf{e}^{(i)}$. The direction $\mathbf{e}^{(i)}$ is chosen such that V_i becomes negative; that is, geometric deformation along $\mathbf{e}^{(i)}$ lowers the energy of the cationic state of the molecule.

Using Eq. (1.3), we can write Eq. (1.2) as

$$\begin{aligned} V_i &= \sum_A\frac{1}{\sqrt{M_A}}\mathbf{e}_A^{(i)}\cdot\left\langle \Psi^{+}\left(\mathbf{r},\mathbf{R_0}\right)\left|\left(\frac{\partial\mathcal{H}_{\mathrm{e}}\left(\mathbf{r},\mathbf{R}\right)}{\partial\mathbf{R}}\right)_{\mathbf{R_0}}\right|\Psi^{+}\left(\mathbf{r},\mathbf{R_0}\right)\right\rangle \\ &= \sum_A V_{i,A}, \end{aligned} \tag{1.4}$$

where $V_{i,A}$ is called the atomic vibronic coupling constant (AVCC) of the A^{th} atom. Since the sum of the AVCCs $V_{i,A}$ is equal to the VCC V_i, the AVCC represents the contribution from the A^{th} atom to the VCC V_i.

When the Hellmann–Feynman theorem[39] holds, V_i can be written in terms of the electron-density difference $\Delta\rho$ and the derivative of the nuclear–electronic potential v_i:[27–30]

$$V_i=\int\Delta\rho\left(\mathbf{x}\right)\times v_i\left(\mathbf{x}\right)d\mathbf{x}, \tag{1.5}$$

where

$$\Delta\rho\left(\mathbf{x}\right)=\rho^{+}\left(\mathbf{x}\right)-\rho\left(\mathbf{x}\right), \tag{1.6}$$

$$v_i\left(\mathbf{x}\right)=-\sum_A \frac{Z_A}{\sqrt{M_A}}\mathbf{e}_A^{(i)}\cdot\frac{\mathbf{x}-\mathbf{R}_A}{\left|\mathbf{x}-\mathbf{R}_A\right|^3}. \tag{1.7}$$

Here, $\rho^{+}\left(\mathbf{x}\right)$ and $\rho\left(\mathbf{x}\right)$ are electron densities for the cationic and neutral states, respectively. $\mathbf{x}$ and $\mathbf{R}_A$ denote a position in three-dimensional space and the position of the A^{th} atom, respectively, and Z_A is atomic number. The product $\Delta\rho\left(\mathbf{x}\right)\times v_i\left(\mathbf{x}\right)$ is called the VCD $\eta_i\left(\mathbf{x}\right)$,[27–30]

$$\eta_i\left(\mathbf{x}\right)=\Delta\rho\left(\mathbf{x}\right)\times v_i\left(\mathbf{x}\right), \tag{1.8}$$

which gives a local picture of vibronic coupling in a molecule.

Eq. (1.8) can be written as

$$\begin{aligned}\eta_i\left(\mathbf{x}\right) &= \sum_A \Delta\rho\left(\mathbf{x}\right)\times\left(-\frac{Z_A}{\sqrt{M_A}}\mathbf{e}_A^{(i)}\cdot\frac{\mathbf{x}-\mathbf{R}_A}{\left|\mathbf{x}-\mathbf{R}_A\right|^3}\right)\\ &= \sum_A \eta_{i,A}\left(\mathbf{x}\right),\end{aligned} \tag{1.9}$$

where we introduce a quantity $\eta_{i,A}$ to represent vibronic coupling density arising from displacement of the A^{th} atom. We call $\eta_{i,A}$ the atomic vibronic coupling density (AVCD) of the A^{th} atom. Space integration of the AVCD $\eta_{i,A}$ gives the AVCC $V_{i,A}$:

$$V_{i,A}=\int \eta_{i,A}\left(\mathbf{x}\right)d\mathbf{x}. \tag{1.10}$$

Let us define an effective mode for geometric deformation $\mathbf{e}_s$. The direction of deformation is defined by

$$\mathbf{e}_s=-\sum_i \frac{V_i}{\left|\mathbf{V}\right|}\mathbf{e}^{(i)}, \tag{1.11}$$

where the i^{th} component of $\mathbf{V}$ is equal to V_i and

$$\left|\mathbf{V}\right|=\sqrt{\sum_i V_i^2}. \tag{1.12}$$

The energy of the cationic state decreases most steeply when geometric deformation occurs in the $\mathbf{e}_s$ direction. If we denote a mass-weighted coordinate in the $\mathbf{e}_s$ direction as Q_s, Q_i can be expressed as

$$Q_i=-\frac{V_i}{\left|\mathbf{V}\right|}Q_s. \tag{1.13}$$

Hence,

$$\begin{aligned}\frac{\partial \mathcal{H}_{\mathrm{e}}}{\partial Q_s} &= \sum_i \frac{\partial Q_i}{\partial Q_s}\frac{\partial \mathcal{H}_{\mathrm{e}}}{\partial Q_i} \\ &= -\sum_i \frac{V_i}{|\mathbf{V}|}\frac{\partial \mathcal{H}_{\mathrm{e}}}{\partial Q_i}. \end{aligned} \tag{1.14}$$

The vibronic coupling constant V_s with respect to Q_s is obtained as

$$\begin{aligned} V_s &= \left\langle \Psi^+(\mathbf{r},\mathbf{R_0}) \middle| \left(\frac{\partial \mathcal{H}_{\mathrm{e}}(\mathbf{r},\mathbf{R})}{\partial Q_s}\right)_{\mathbf{R_0}} \middle| \Psi^+(\mathbf{r},\mathbf{R_0}) \right\rangle \\ &= -\sum_i \frac{V_i^2}{|\mathbf{V}|} \\ &= -|\mathbf{V}|. \end{aligned} \tag{1.15}$$

From Eqs. (1.5) and (1.15), V_s can be written in terms of $\Delta\rho$ and v_i:

$$\begin{aligned} V_s &= -\sum_i \frac{V_i}{|\mathbf{V}|}\int \Delta\rho(\mathbf{x}) \times v_i(\mathbf{x})\, d\mathbf{x} \\ &= \sum_i \frac{V_i}{V_s}\int \Delta\rho(\mathbf{x}) \times v_i(\mathbf{x})\, d\mathbf{x}. \end{aligned} \tag{1.16}$$

If we define new quantities $v_s(\mathbf{x})$ and $\eta_s(\mathbf{x})$ such that

$$v_s(\mathbf{x}) = \sum_i \frac{V_i}{V_s} v_i(\mathbf{x}), \tag{1.17}$$

$$\eta_s(\mathbf{x}) = \Delta\rho \times v_s(\mathbf{x}), \tag{1.18}$$

V_s can be expressed as

$$V_s = \int \Delta\rho(\mathbf{x}) \times v_s(\mathbf{x})\, d\mathbf{x}. \tag{1.19}$$

v_s and η_s are derivative of the nuclear–electronic potential and the vibronic coupling density, respectively, for the effective mode. AVCD and AVCC for the effective mode are defined respectively by

$$\eta_{s,A}(\mathbf{x}) = \Delta\rho(\mathbf{x}) \times \frac{V_i}{V_s}\left(-\frac{Z_A}{\sqrt{M_A}}\mathbf{e}_A^{(i)} \cdot \frac{\mathbf{x}-\mathbf{R}_A}{|\mathbf{x}-\mathbf{R}_A|^3}\right), \tag{1.20}$$

$$V_{s,A} = \int \eta_{s,A}(\mathbf{x})\, d\mathbf{x}. \tag{1.21}$$

Summing the AVCDs $\eta_{s,A}$ and VCCs $V_{s,A}$ yields η_s and V_s.

There is yet another definition of the VCC. In the second quantization form, the molecular Hamiltonian (Eq. (1.1)) can be written as

$$\mathcal{H} = \sum_j \epsilon_j {c_j}^\dagger c_j + \sum_i \lambda_i \left\{ {c_{\mathrm{HOMO}}}^\dagger c_{\mathrm{HOMO}} \left(b_i^\dagger + b_i \right) \right\} + \sum_i \hbar\omega_i \left({b_i}^\dagger b_i + \frac{1}{2} \right), \qquad (1.22)$$

where ϵ_j is the orbital energy of the molecule, λ_i is the electron–phonon coupling constant, ω_i is the frequency of the i^{th} mode, ${c_j}^\dagger$ and c_j are electron creation and annihilation operators in the j^{th} molecular orbital, and ${b_i}^\dagger$ and b_i are phonon creation and annihilation operators of mode i. ${c_{\mathrm{HOMO}}}^\dagger$ and c_{HOMO} are electron creation and annihilation operators in the highest occupied molecular orbital (HOMO). λ_i is related to V_i through the following equation:

$$\lambda_i = \sqrt{\frac{\hbar}{2\omega_i}} V_i. \qquad (1.23)$$

1.3 Method of Calculation

We calculated VCCs for α-oligothiophene cations (α-nT, $n = 2 - 9$). To satisfy the Hellmann–Feynman theorem, the 6-31G basis set with the first derivative (denoted 6-31G+der) was used.[40] Structures of neutral oligothiophenes were optimized at the RHF/6-31G+der level assuming C_2 ($n = 2, 4, 6, 8$) and C_s ($n = 3, 5, 7, 9$) symmetries. Vibrational analyses were done to confirm the stability of the optimized geometries. Electronic structures of α-nT cations were calculated at the ROHF/6-31G+der level using the optimized geometries of the neutral states. All *ab initio* calculations were performed with the GAMESS computational chemistry software program.[41] A scaling factor of 0.8929[42] was used for RHF/6-31G+der theoretical frequencies.

1.4 Results and Discussion

1.4.1 VCD analysis for α-2T

Figure 1.1 shows the 6-31G+der optimized geometry with atomic numbering scheme, bond lengths, and bond angles for neutral α-2T. The sulfur atoms are located in opposite positions (transoid). In the gas phase, α-2T prefers a transoid structure.[43] Theoretical studies using different methods and different basis sets also show a twisted anti-conformation structure to be most stable.[43–49] The twist angle between the two thiophene rings is calculated to be 31.9°, in good agreement with the experimental values of 34°[50] and 32°[43] obtained by the electron diffraction in the gas phase. This nonplanarity is due to steric repulsion between the sulfur and hydrogen atoms.

Experimental values for the C1−C1', C1−S1, and C4−S1 bond lengths are 1.456, 1.733, and 1.719 Å,[43] respectively, which are close to our results. Calculated values for the C1−C2, C2−C3, and C3−C4 bond lengths are 0.02Å longer than experimental values.[43] The C1−C2 and C3−C4 bonds have double-bond character, while the C1−C1', C2−C3, C1−S1, and C4−S1 bonds have single-bond character. Hence, the thiophene rings in the optimized geometry of neutral α-2T exhibits an aromatic-type structure with six π electrons, and the bond angles are in good agreement with experimental data.[43]

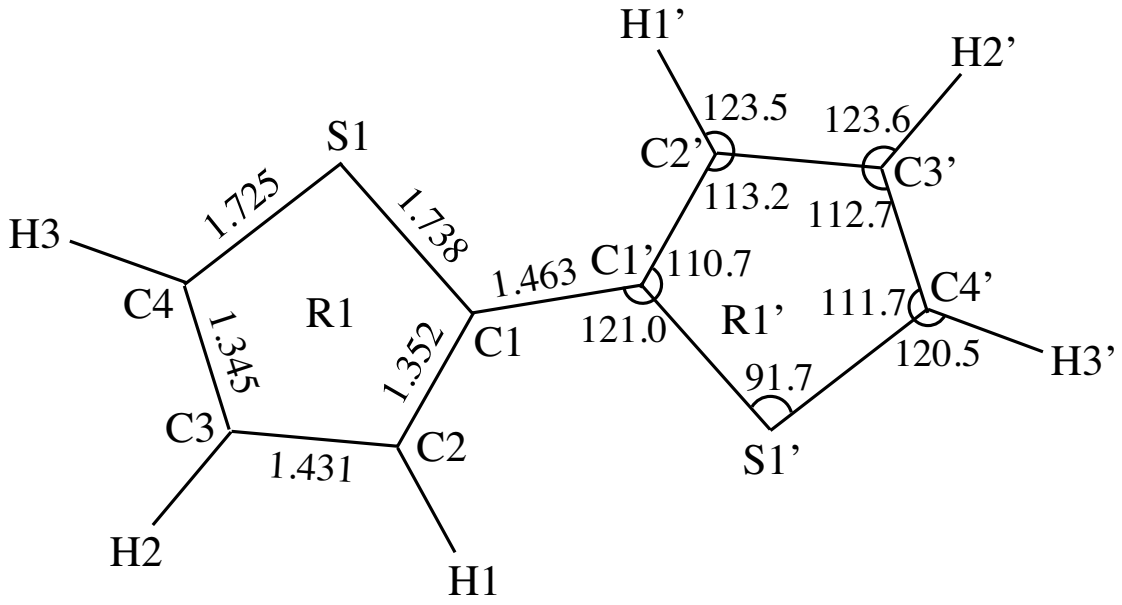

Figure 1.1: α-2T: 6-31G+der optimized geometry with atomic numbering scheme, bond lengths, and bond angles. Bond lengths are in Å; bond angles are in degrees.

Figure 1.2(a) shows calculated VCCs for α-2T. Figure 1.3 shows several totally symmetric modes. The arrows in Fig. 1.3 represent the A^{th} component of the vibrational vector $\mathbf{e}_A^{(i)}$. The largest two VCCs correspond to C=C stretching modes ($a(18)$ and $a(19)$ modes). Note that these modes involve an inter-ring C−C stretching vibration, but differ in the phases of their C3−C4 stretching vibrations. In the $a(18)$ mode, the C1−C2 and C3−C4 bonds lengthen/shorten simultaneously; in the $a(19)$ mode, the C3−C4 bond shortens/lengthens when the C1−C2 bond lengthens/shortens. Thus, VCC is smaller for the $a(19)$ mode than for the $a(18)$ mode (see also Fig. 1.4).

VCCs for the $a(10)$ and $a(13)$ modes are moderately large. The $a(10)$ mode is an in-plane bending mode, which involves C4−S1 stretching vibration. The $a(13)$ mode is an inner-ring C−C stretching mode. VCCs are small for out-of-plane bending and C−H stretching modes. The $a(4)$ and $a(21)$ modes are examples of out-of-plane bending and C−H stretching modes, respectively.

Significantly, deformation in the direction of the $a(18)$ and $a(19)$ modes lengthens the C1−C2 bond (C=C double bond) and shortens the C1−C1' bond (inter-ring C−C bond). Deformation in the direction of the $a(18)$ mode also lengthens the C3−C4 bond (C=C double bond), and deformation in the directions of the $a(13)$ mode or $a(18)$ mode shortens the C2−C3 bond (inner-ring C−C bond). These deformations convert the geometry from aromatic to quinoid. Since we chose the direction of the vibrational mode such that the VCC is negative, distortion toward a quinoid-type structure lowers the energy of the cationic state. Thus, vibronic coupling with modes that have large VCCs converts geometry from aromatic to quinoid and lowers the energy of the cationic state.

Figure 1.2(b) shows electron–phonon coupling constants λ calculated using Eq. (1.23). The relative order of λ is identical to that of $|V|$ except for the $a(1)$ mode. The moderately large λ for that mode is due to its low frequency. λ for a low-frequency mode tends to be large, per Eq. (1.23).

Figure 1.4 shows AVCCs for the $a(4)$, $a(10)$, $a(13)$, $a(18)$, $a(19)$, and $a(21)$ modes. Black/white circles represent negative/positive AVCC values, and the size of a circle is proportional to the relative magnitude of the AVCC. The sum of the AVCCs gives the VCC. AVCCs are large for the carbon atoms and small for the sulfur and hydrogen atoms, suggesting that vibronic coupling occurs mainly in the carbon backbone. The large VCCs for the $a(18)$ and $a(19)$ modes result from the large negative AVCCs for the carbon atoms.

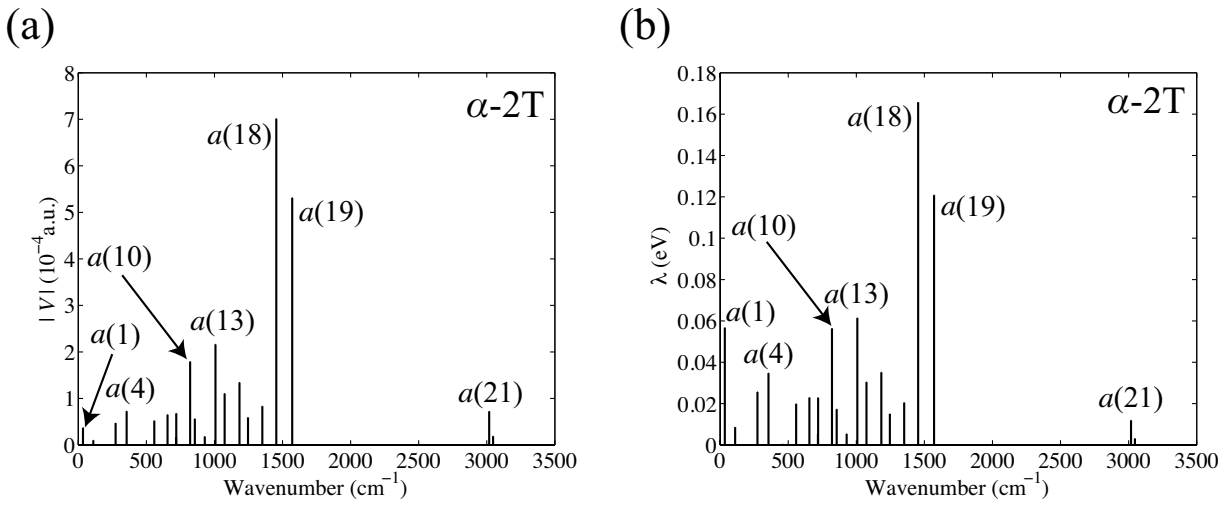

Figure 1.2: α-2T cation: (a) Absolute value of vibronic coupling constants $|V|$. (b) Corresponding electron–phonon coupling constants λ.

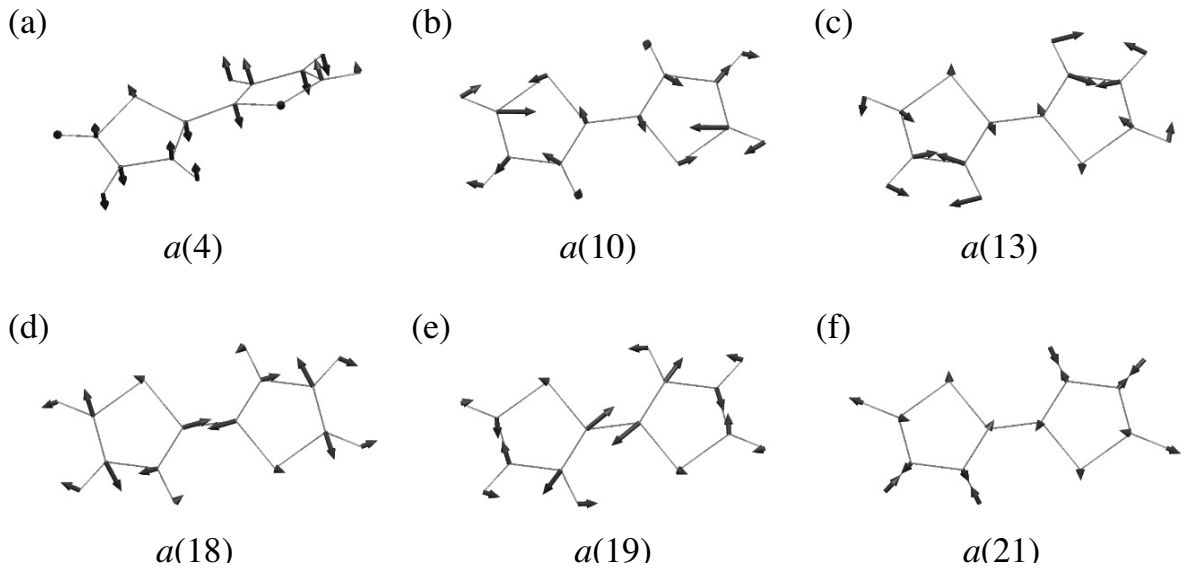

Figure 1.3: Neutral α-2T totally symmetric modes obtained at the RHF/6-31G+der level: (a) Out-of-plane bending; (b) In-plane bending; (c) Inner-ring C−C stretching; (d) C=C stretching; (e) C=C stretching; (f) C−H stretching.

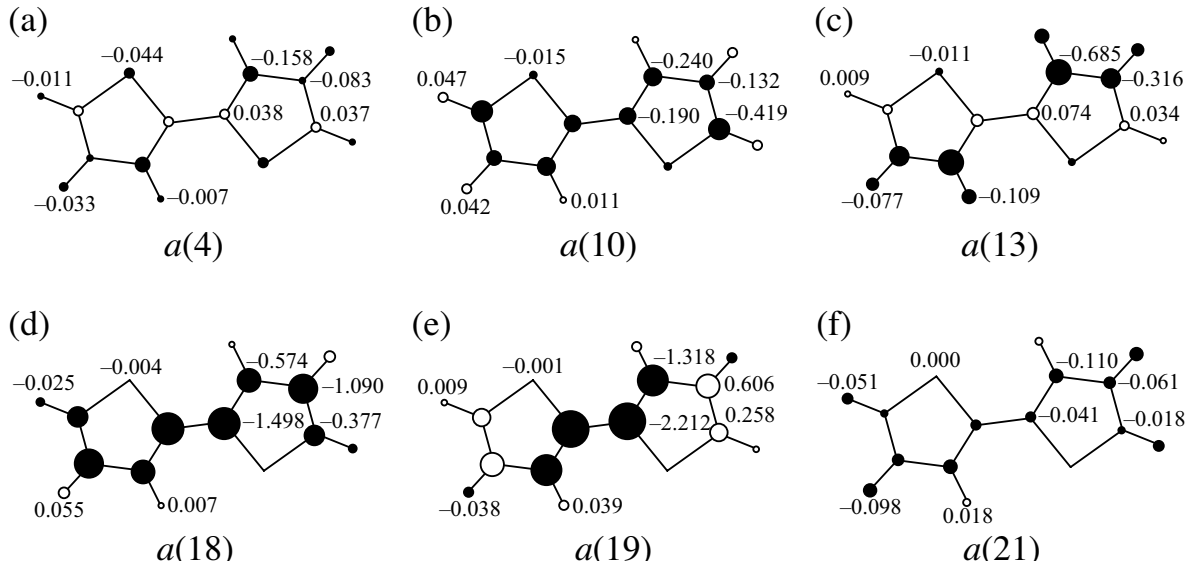

Figure 1.4: Atomic vibronic coupling constants for the following modes ($\times 10^{-4}$ a.u.): (a) $a(4)$; (b) $a(10)$; (c) $a(13)$; (d) $a(18)$; (e) $a(19)$; (f) $a(21)$.

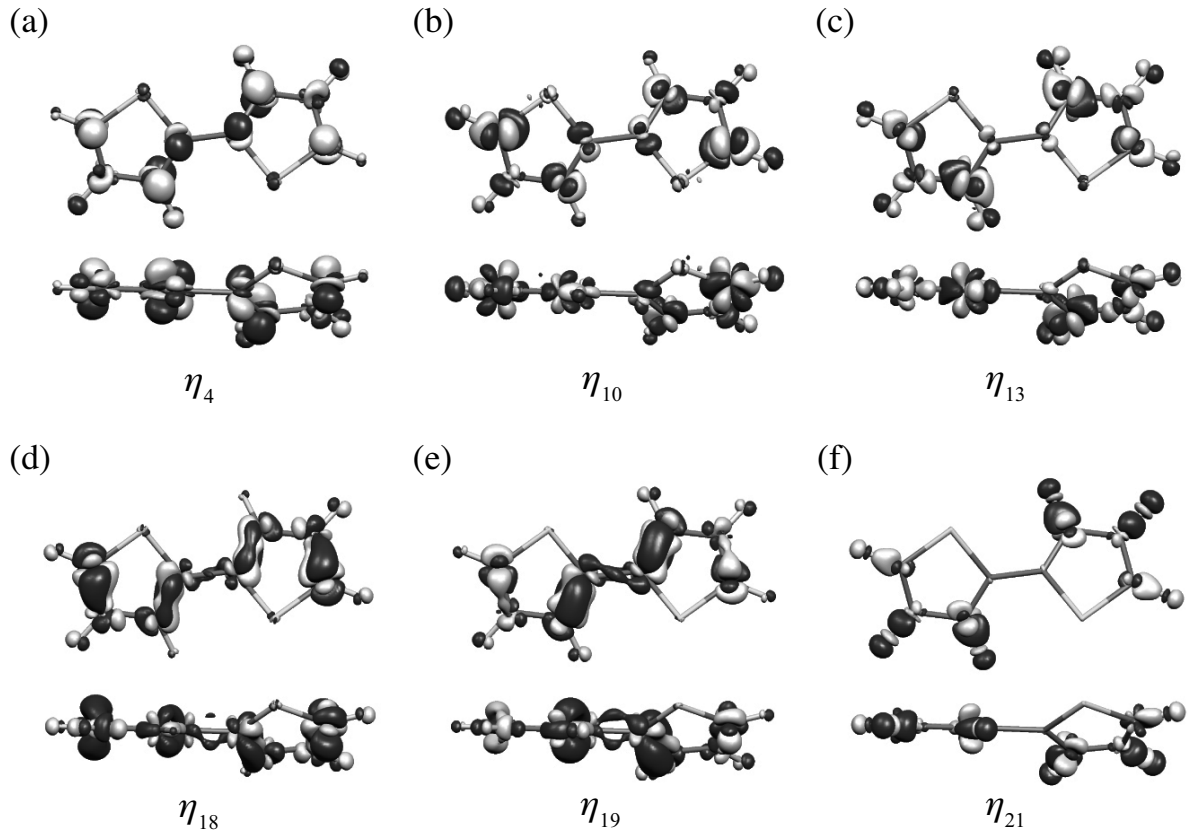

Figure 1.5: Vibronic coupling density η of the following modes at an isosurface value of 2.5×10^{-5} a.u.: (a) $a(4)$; (b) $a(10)$; (c) $a(13)$; (d) $a(18)$; (e) $a(19)$; (f) $a(21)$. Dark gray shows where values are negative; light gray shows where values are positive.

For the $a(18)$ mode, all carbon atoms have negative AVCCs; for the $a(19)$ mode, the C1 and C2 atoms have negative AVCCs and the C3 and C4 atoms have positive AVCCs. This is why the absolute value of the VCC for the $a(19)$ mode is smaller than that for the $a(18)$ mode. For the $a(10)$ mode, the carbon atoms have moderately large AVCCs. For the $a(13)$ mode, the C2 and C3 atoms have large AVCCs. Hence, the $a(10)$ and $a(13)$ modes have moderately large VCCs. For the $a(4)$ and $a(21)$ modes, all atoms have small AVCCs, leading to the small VCCs for the $a(4)$ and $a(21)$ modes.

Space integration of an AVCD $\eta_{i,A}$ gives the AVCC $V_{i,A}$. Figure 1.5 shows VCDs for the $a(4)$, $a(10)$, $a(13)$, $a(18)$, $a(19)$, and $a(21)$ modes. The VCD η_i is the product of $\Delta\rho$ and v_i. Figure 1.6(a) shows the electron-density difference $\Delta\rho$ originating from ionization. $\Delta\rho$ has large negative values (dark-gray regions) on the C1−C2 and C3−C4 bonds, but small values on the sulfur and hydrogen atoms. Figure 1.6(b) shows that the distribution pattern for regions of negative $\Delta\rho$ is similar to that for the electron density of the HOMO of neutral α-2T, which has a π-bond-like shape, suggesting that an electron is removed mainly from the HOMO. Some regions in Fig. 1.6(a) where $\Delta\rho$ is positive (light-gray regions) have σ-bond-like shape. Contribution to the positive regions comes from occupied orbitals other than the HOMO. The positive regions tend to be located between the negative regions, and appear to reduce repulsions between them. $\Delta\rho$ is distributed almost symmetrically with respect to the thiophene ring planes.

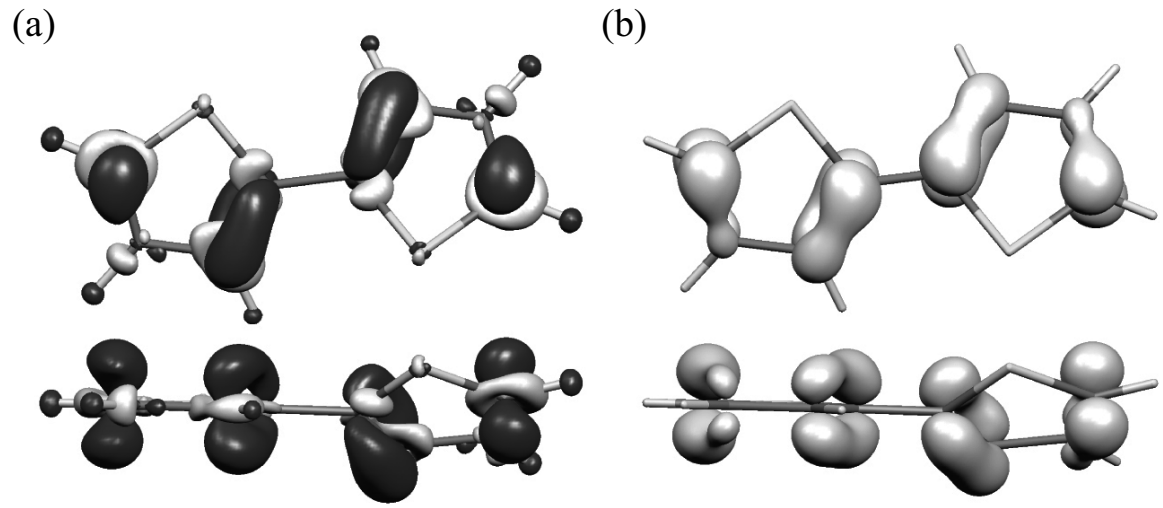

Figure 1.6: Neutral α-2T at an isosurface value of 0.005 a.u.: (a) Electron-density difference $\Delta\rho$; (b) Electron density of HOMO. Dark gray shows where values are negative; light gray shows where values are positive.

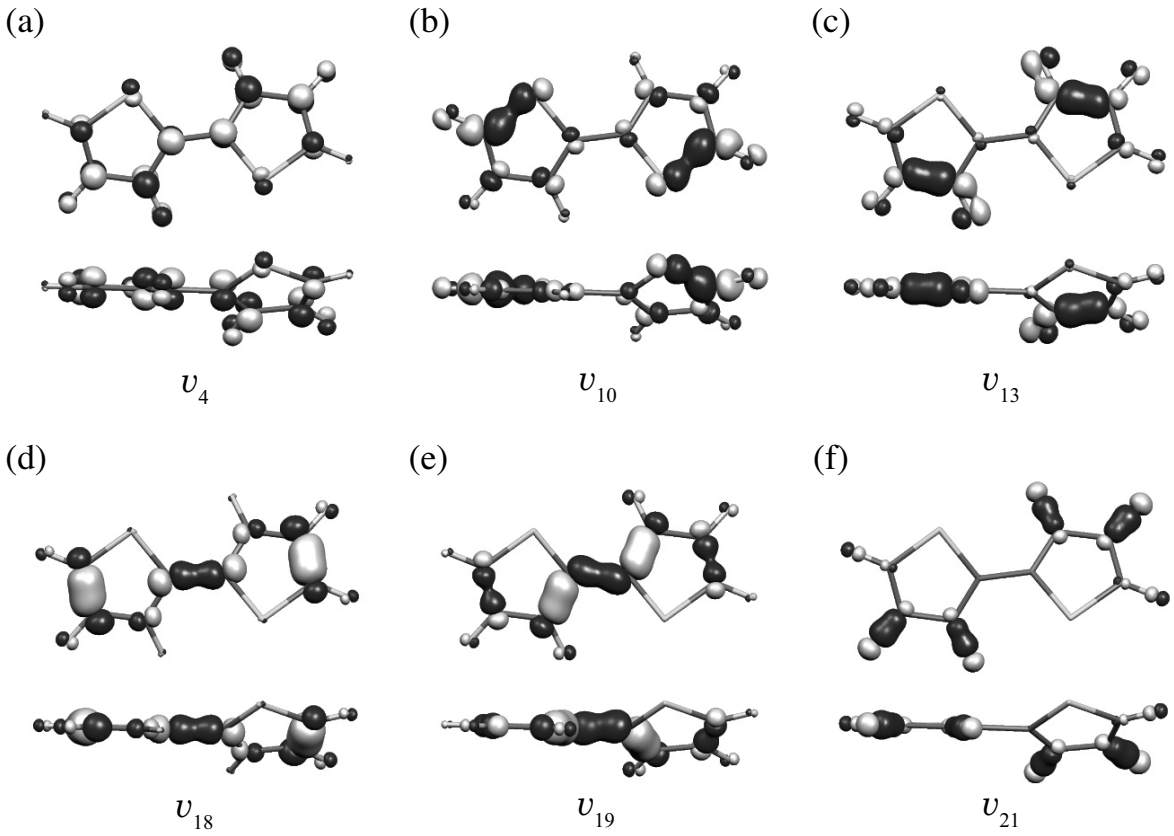

Figure 1.7: Derivatives of nuclear–electronic potential v of the following modes at an isosurface value of 0.01 a.u.: (a) $a(4)$; (b) $a(10)$; (c) $a(13)$; (d) $a(18)$; (e) $a(19)$; (f) $a(21)$. Dark gray shows where values are negative; light gray shows where values are positive.

Figure 1.7 shows derivatives of nuclear–electronic potentials for the $a(4)$, $a(10)$, $a(13)$, $a(18)$, $a(19)$, and $a(21)$ modes. By comparing Fig. 1.7 with Fig. 1.3, we find that v_i reflects the corresponding vibrational mode $a(i)$: arrow heads and tails in Fig. 1.3 correspond to dark-gray and light-gray regions in Fig. 1.7. v_i has a large value around atoms for which $\mathbf{e}_A^{(i)}$ is large and M_A is small, per Eq. (1.7).

The $a(4)$ mode is an out-of-plane bending mode, and v_4 is distributed almost vertically to and anti-symmetrically with respect to the thiophene ring planes (Fig. 1.7(a)). Since $\Delta\rho$ is almost symmetric with respect to the thiophene ring planes, the distribution of η_6 ($= \Delta\rho \times v_6$) is anti-symmetric (Fig. 1.5(a)). Hence, the VCC that is the space integration of the VCD becomes small. This is also the case for the other out-of-plane bending modes.

The AVCCs for the $a(21)$ mode are also small, but for a different reason. Since the $a(21)$ mode is a C−H stretching mode, v_{21} has a value on the C−H bonds (Fig. 1.7(f)) where $\Delta\rho$ has a small value. Hence, $\Delta\rho$ and v_{21} overlap only on the C−H bonds. The distribution of η_{21} around the C2, C3, C4, H1, H2, and H3 atoms shows the AVCDs

of these atoms, which exhibit non-symmetrical distributions (Fig. 1.5(f)). Hence, space integration of the AVCDs gives a nonzero value. However, the distribution ranges of the AVCDs are limited, and the AVCCs become quite small. Thus, a vibrational mode for which v does not overlap significantly with $\Delta\rho$ has a small VCC.

The $a(10)$ mode is an in-plane bending mode, and involves the C4−S1 stretching vibration. v_{10} is distributed largely around the S1 and C4 atoms, and has a small value around the other atoms (Fig. 1.7(b)). Since $\Delta\rho$ has a small value on the S1 atom, $\Delta\rho$ and v_{10} do not overlap there. Hence, η_{10} has a large value only around the C4 atom (Fig. 1.5(b)). This is why the S1 atom has a small AVCC despite its large displacement. The small distribution of $\Delta\rho$ around the S1 atom is responsible for the shorter change in bond length for the C−S than for the C=C bond.[37]

The $a(13)$ mode is an inner-ring C−C stretching mode, and v_{13} has a large value on the C2−C3 bond (Fig. 1.7(c)). $\Delta\rho$ and v_{13} overlap around the C2 and C3 atoms. However, since $\Delta\rho$ is not distributed in the middle of the C2−C3 bond, η_{13} has a small value in that region, and its distribution is limited around the C2 and C3 atoms (Fig. 1.5(c)). Hence, the sum of the AVCCs for the C2 and C3 atoms (-1.001×10^{-4} a.u.) is smaller than the sums of the AVCCs for the C1 and C2 atoms for the $a(18)$ and $a(19)$ modes (-2.072×10^{-4} and -3.530×10^{-4} a.u.).

The $a(18)$ and $a(19)$ modes are C=C stretching modes associated with the inter-ring C−C stretching vibration. v_{18} (Fig. 1.7(d)) and v_{19} (Fig. 1.7(e)) are distributed on the C1−C2, C3−C4, and C1−C1' bonds. v_{18} is larger on the C3−C4 bond than on the C1−C2 bond, while v_{19} is larger on the C1−C2 bond than on the C3−C4 bond. Since the distribution of $\Delta\rho$ is larger on the C1−C2 bond than the C3−C4 bond, $\Delta\rho$ overlaps significantly with v_{19} on the C1−C2 bond. This is why the absolute values of the AVCCs for the C1 and C2 atoms for the $a(19)$ mode are quite large. However, the VCC is smaller for the $a(19)$ mode than for the $a(18)$ mode because the signs of the AVCCs for the C3 and C4 atoms are opposite to those for the C1 and C2 atoms. This is because the phases of v_{19} on the C1−C2 and C3−C4 bonds are opposite.

On the C1−C2 bond, v_{19} has a positive value. Consequently, the main portion of η_{19} on that bond is negative (a negative times a positive yields a negative), which results in negative AVCCs for the C1 and C2 atoms. In contrast, since v_{19} is negative on the C3−C4 bond, η_{19} on that bond is positive (a negative times a negative yields a positive).

Hence, the AVCCs for the C3 and C4 atoms are positive. For the $a(18)$ mode, the phases of v_{18} on the C1−C2 and C3−C4 bonds are the same. This is why the AVCCs for all the carbons atoms are negative, and VCC is larger for the $a(18)$ mode than for the $a(19)$ mode.

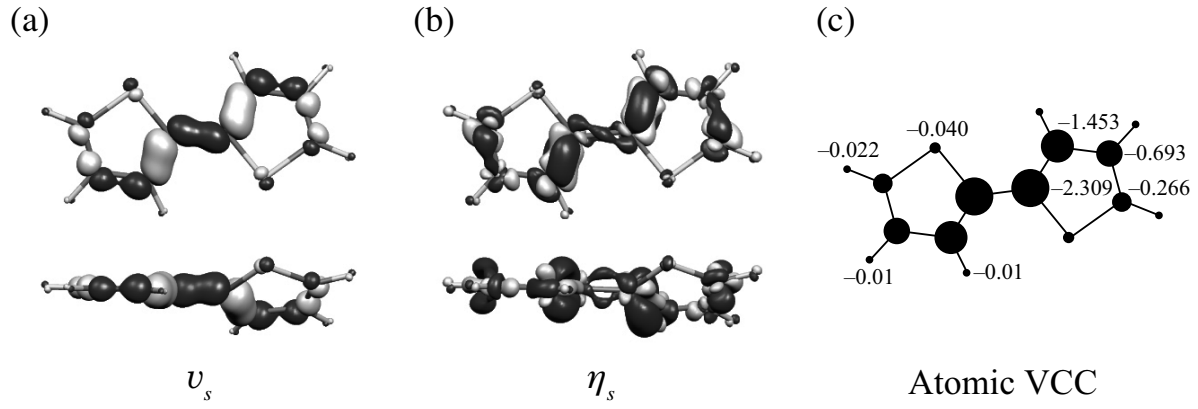

Figure 1.8: α-2T effective mode: (a) Derivative of nuclear–electronic potential v_s ($|v_s| = 0.01$ a.u.); (b) Vibronic coupling density η_s ($|\eta_s| = 2.5 \times 10^{-5}$ a.u.); (c) Atomic vibronic coupling constants ($\times 10^{-4}$ a.u.). Dark gray shows where values are negative; light gray shows where values are positive.

We now turn to vibronic coupling with the effective mode. Figure 1.8(a) shows v_s for α-2T. The $a(18)$ and $a(19)$ modes contribute significantly to v_s: V_{18}/V_s and V_{19}/V_s are 0.73 and 0.55, respectively. The wide distributions of v_s on the C1−C2 and C1−C1' bonds are due to overlap of v_{18} and v_{19}. The phases of v_{18} and v_{19} on the C3−C4 bond are opposite, and hence cancel each other, so the distribution range of v_s is smaller on the C3−C4 bond than on the C1−C2 bond. A net positive value is observed on the C3−C4 bond. The moderately large distribution on the C2−C3 bond comes from v_{13}. Since C−H stretching modes have small VCCs, v_s has only a small value around the hydrogen atoms. As stated above, the derivative of the nuclear–electronic potential reflects the corresponding vibrational mode. The distribution pattern for v_s shows that the C2−C3 and C3−C4 bonds (C=C double bonds) lengthen, when the C1−C1' and C2−C3 bonds (C−C single bonds) shorten; that is, a geometric deformation in the direction of the effective mode corresponds to conversion from an aromatic-type to a quinoid-like structure.

η_s has a large negative value on the C1−C2 and C3−C4 bonds (Fig. 1.8(b)). Hence, all the carbon atoms have negative AVCCs (Fig. 1.8(c)). V_s is calculated to be -9.608×10^{-4} a.u. The sum of the AVCCs for the carbon atoms is -9.442×10^{-4} a.u., which is 98.3%

of V_s. This result shows that vibronic coupling occurs mainly on the carbon backbone.

1.4.2 VCD analysis for α-3T

Figure 1.9 shows the 6-31G+der optimized geometry, bond lengths, and bond angles for neutral α-3T. The C1−C2, C3−C4, and C5−C6 bond lengths are 1.351, 1.352, and 1.345 Å, respectively; the C1−C1', C2−C3, and C4−C5 bonds lengths are 1.428, 1.462, 1.431 Å, respectively. Thiophene rings in the optimized geometry of neutral α-3T are aromatic-type structures. The torsion angle between adjacent thiophene rings is 30.5°, close to that of α-2T (31.9°). A torsion angle of 32° has been reported at the 6-31G* level.[51] There is no gas-phase data on geometrical parameters for α-3T.

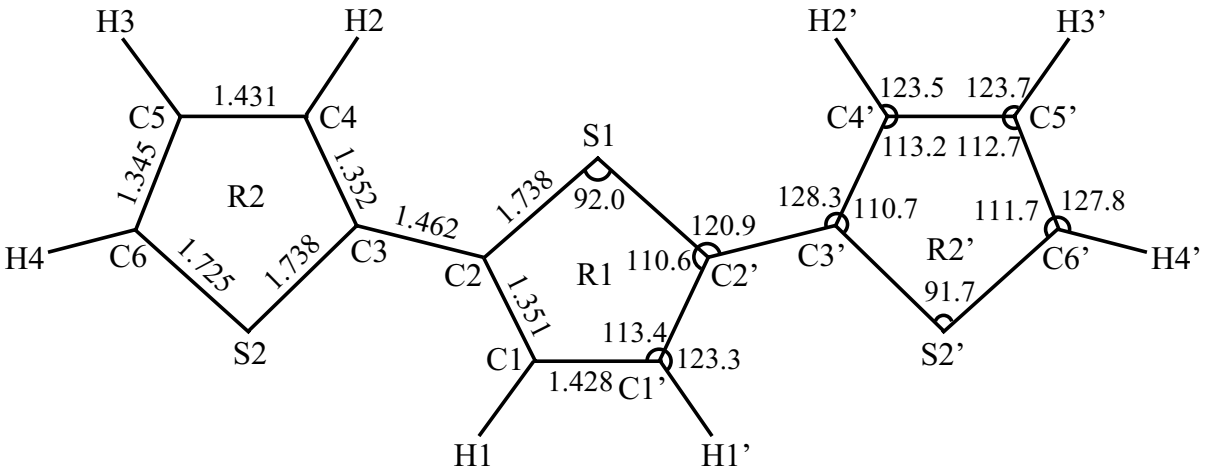

Figure 1.9: α-3T: 6-31G+der optimized geometry with atomic numbering scheme, bond lengths, and bond angles. Bond lengths are in Å; bond angles are in degrees.

Figure 1.10(a) shows VCC absolute values for the α-3T cation. The largest VCC peak corresponds to a C=C stretching mode ($a^{'}(27)$ mode; Fig. 1.11(b)), in which all C=C bonds (C1−C2, C3−C4, and C5−C6 bonds) lengthen simultaneously. The second largest VCC peak also corresponds to a C=C stretching mode ($a^{'}(28)$ mode; Fig. 1.11(c)). However, for the $a^{'}(28)$ mode, the C5−C6 bond shortens when the C1−C2 and C3−C4 bonds lengthen. Another C=C stretching mode ($a^{'}(26)$ mode; Fig. 1.11(a)) shows a weak VCC peak. For the $a^{'}(26)$ mode, the C3−C4 and C5−C6 bonds shorten when the C1−C2 bond lengthens; this opposite direction of the C=C stretching vibrations reduces the strength of vibronic coupling.

Two moderately intense VCC peaks in the range $800 - 1200$ cm^{-1} correspond to the $a^{'}(20)$ and $a^{'}(22)$ modes. The former is an inner-ring C−C (C1−C1') stretching mode; the latter is an inter-ring C−C (C2−C3) stretching mode that involves a C1−C1' stretching vibration. We discuss below the relative VCC sizes for the three C=C stretching modes. Figure 1.10(b) shows electron–phonon coupling constants λ calculated using Eq. (1.23). Constants for the low-frequency (< 500 cm^{-1}) modes are estimated to be moderately large. However, the trend in relative λ sizes is similar to the trend in relative VCC sizes.

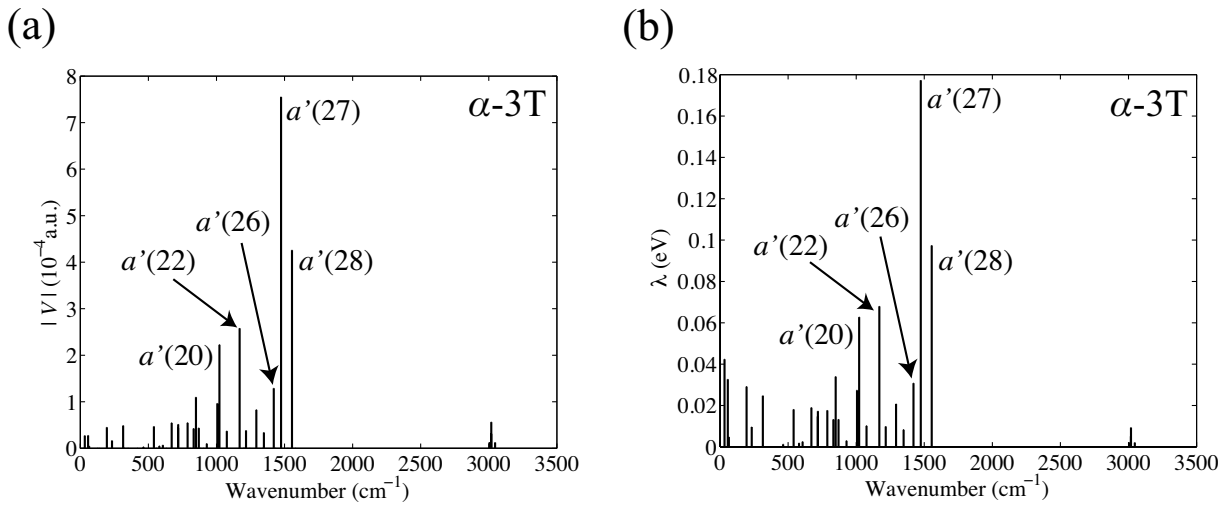

Figure 1.10: α-3T cation: (a) Absolute value of vibronic coupling constants $|V|$; (b) Corresponding electron–phonon coupling constants λ.

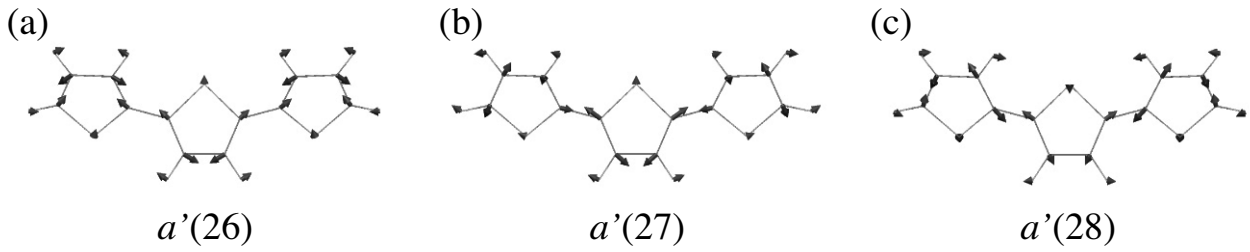

Figure 1.11: Neutral α-3T: Three totally symmetric C=C stretching modes obtained at the RHF/6-31G+der level.

Figures 1.12(a1) and (a2) show the electron-density difference $\Delta\rho$ and the electron density of the HOMO. The distribution pattern for regions where $\Delta\rho$ is negative (dark-gray regions) coincides with the pattern for the electron density of the HOMO. The main contribution to $\Delta\rho$ comes from the HOMO. $\Delta\rho$ is mainly distributed on the C1−C2

bond, is nonzero on the C3, C4, and C6 atoms, and is almost symmetric with respect to thiophene ring planes. Positive regions, which have a σ-bond-like shape, play a role in reducing repulsions between the negative regions.

Figures 1.12(b)–(d) show derivatives of the nuclear–electronic potentials v, VCD η, and AVCCs for the three C=C stretching modes. For the three modes, v has a positive value on the C1−C2 bond. Since v_{27} is largely distributed on that bond, η_{27} has a large value in that region. The large AVCCs for the C1 and C2 atoms for the $a^{'}(27)$ mode reflect this fact. Distribution ranges on the C1−C2 bond are smaller for v_{26} and v_{28} than for v_{27}. Hence, η_{26} and η_{28} have smaller values than does η_{27} in this region. This is why the AVCCs for the C1 and C2 atoms are smaller for the $a^{'}(26)$ and $a^{'}(28)$ modes than for the $a^{'}(27)$ mode. For the $a^{'}(28)$ mode, the phase of v_{28} on the C5−C6 bond is opposite to the phases on the C1−C2 and C3−C4 bonds, so that AVCCs are positive for the C5 and C6 atoms and hence, the VCC is smaller for the $a^{'}(28)$ mode than for the $a^{'}(27)$ mode. For the $a^{'}(26)$ mode, the AVCCs are positive for not just the C5 and C6 atoms but also the C3 and C4 atoms, because v_{26} has a negative value on the C3−C4 and C5−C6 bonds. Hence, the $a^{'}(26)$ mode has a smaller negative VCC than does the $a^{'}(28)$ mode. This cancellation of AVCCs is responsible for the quite weak vibronic coupling with the $a^{'}(26)$ mode. Thus, v of opposite phase on C=C double bonds reduces the vibronic coupling constant.

Figure 1.13(a) shows the derivative of the nuclear–electronic potential for effective mode v_s for α-3T. V_{26}/V_s, V_{27}/V_s, and V_{28}/V_s are calculated to be 0.13, 0.78, and 0.44, respectively. The large positive distribution of V_s on the C1−C2 bond comes mainly from v_{27}. Cancellation of v_{26} and v_{28} on the C3−C4 bond is responsible for the small positive distribution of v_s in that region. The small positive region on the C5−C6 bond originates from negative contributions from v_{26} and v_{28}; cancellation is larger on the C5−C6 bond than on the C3−C4 bond. v_{20} and v_{22} (C−C stretching modes) as well as the three C=C stretching modes contribute significantly to negative regions on the C1−C1' and C2−C3 bonds. The distribution pattern of v_s shows that quinoid deformation occurs when α-3T is ionized, as has been observed experimentally for the α-3T derivative 3′,4′-dibutyl-2,5″-diphenyl-2,2′:5′,2″-terthiophene (Bu_2Ph_2TTh).[52]

v_s overlaps significantly with $\Delta\rho$ on the C1−C2, C2−C3, C3−C4, and C5−C6 bonds. Figures 1.13(b) and (c) show η_s and AVCCs. In particular, η_s has a large negative value

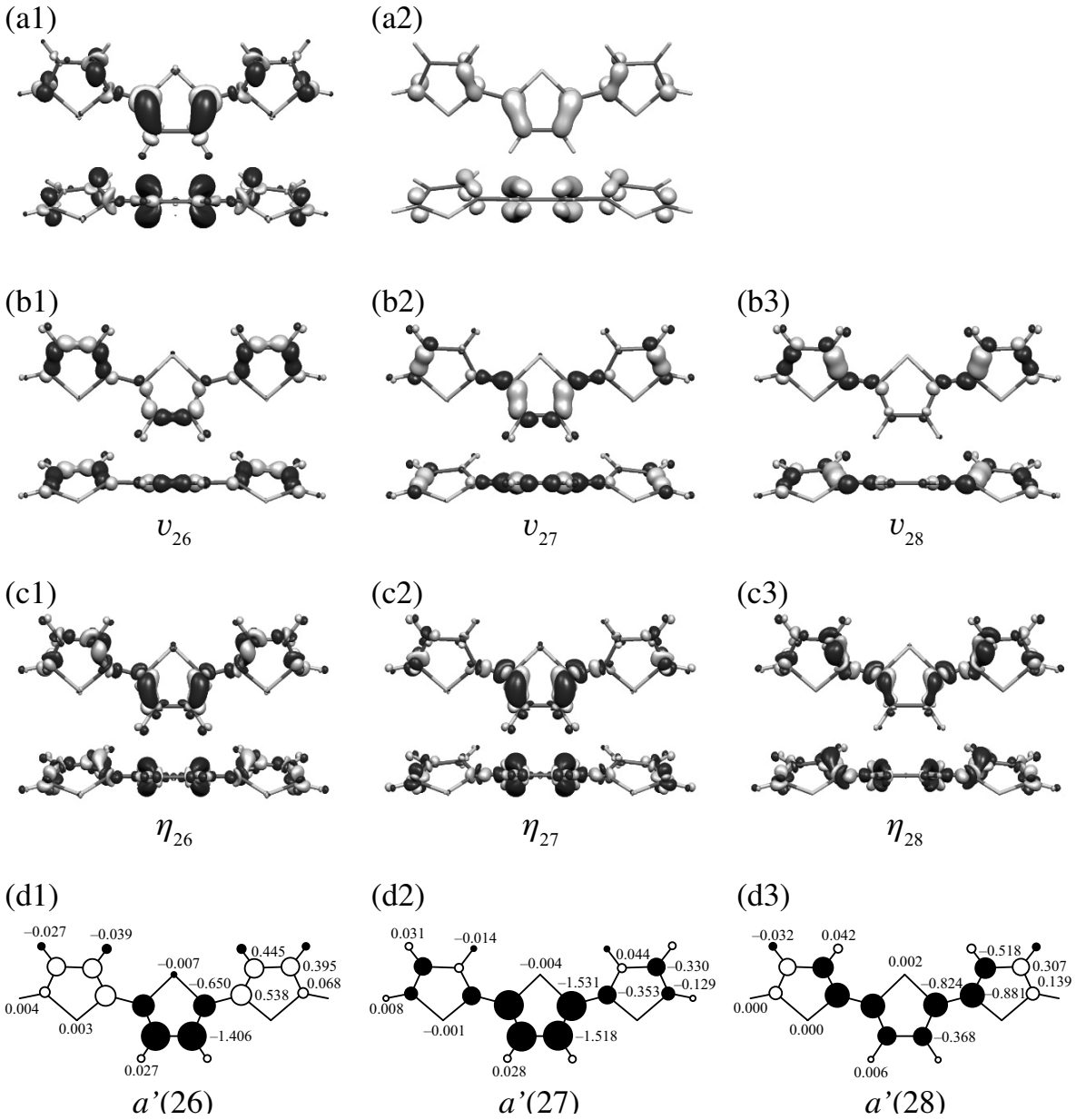

Figure 1.12: Neutral α-3T: (a1,2) Electron-density difference $\Delta\rho$ and electron density of the HOMO at an isosurface value of 0.005 a.u.; (b1–3) Derivatives of nuclear–electronic potential v for the $a^{'}(26)$, $a^{'}(27)$, and $a^{'}(28)$ modes at an isosurface value of 0.01 a.u.; (c1–3) Corresponding vibronic coupling densities ($|\eta_s| = 2.5 \times 10^{-5}$ a.u.); (d1–3) Atomic vibronic coupling constants ($\times 10^{-4}$ a.u.). Dark gray shows where values are negative; light gray shows where values are positive.

on the C1−C2 bond, so AVCCs are large for the C1 and C2 atoms. V_s is -9.715×10^{-4} a.u., 98.6% of which comes from the carbon atoms. Hence, vibronic coupling takes place mainly on the carbon backbone. The sum of the AVCCs for the central thiophene ring is -7.569×10^{-4} a.u. (77.9% of V_s); that for the terminal ring is -1.073×10^{-4} a.u. (11.0% of V_s). This result shows that vibronic coupling and quinoid deformation occur mainly on the central thiophene ring.

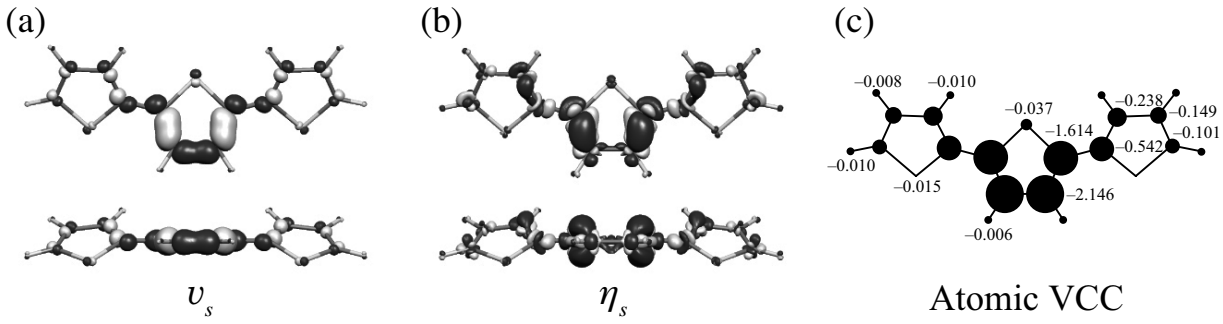

Figure 1.13: α-3T effective mode: (a) Derivative of nuclear–electronic potential v_s ($|v_s| = 0.01$ a.u.); (b) Vibronic coupling density η_s ($|\eta_s| = 2.5 \times 10^{-5}$ a.u.); (c) Atomic vibronic coupling constants ($\times 10^{-4}$ a.u.). Dark gray shows where values are negative; light gray shows where values are positive.

1.4.3 n dependence of VCC and VCD for effective mode

n dependence of VCC

Figure 1.14 shows VCCs for longer α-nT ($n = 4 - 9$) cations. Several common tendencies are evident. n peaks are observed that correspond to C=C stretching modes. The most intense VCC peak ($\approx -7 \times 10^{-4}$ a.u.) corresponds to a C=C stretching mode in which all C=C double bonds lengthen simultaneously. The second largest VCC peak ($\approx -4 \times 10^{-4}$ a.u.) also corresponds to a C=C stretching mode, but the phases of some of the C=C stretching vibrations are opposite. Two moderately intense VCC peaks ($\approx -2 \times 10^{-4}$ a.u.) appear in the range $800 - 1200$ cm^{-1}. That with the larger wavenumber and VCC corresponds to an inner-ring C−C stretching mode; the other corresponds to an inter-ring C−C stretching mode associated with an inner-ring C−C stretching vibration. Out-of-plane bending and C−H stretching modes have small VCCs, and VCCs become gradually smaller as n increases.

Figure 1.15 shows electron–phonon coupling constants λ. As is seen for α-3T, the constants for low-frequency (especially $< 500\,\mathrm{cm}^{-1}$) modes are estimated to be moderately large.

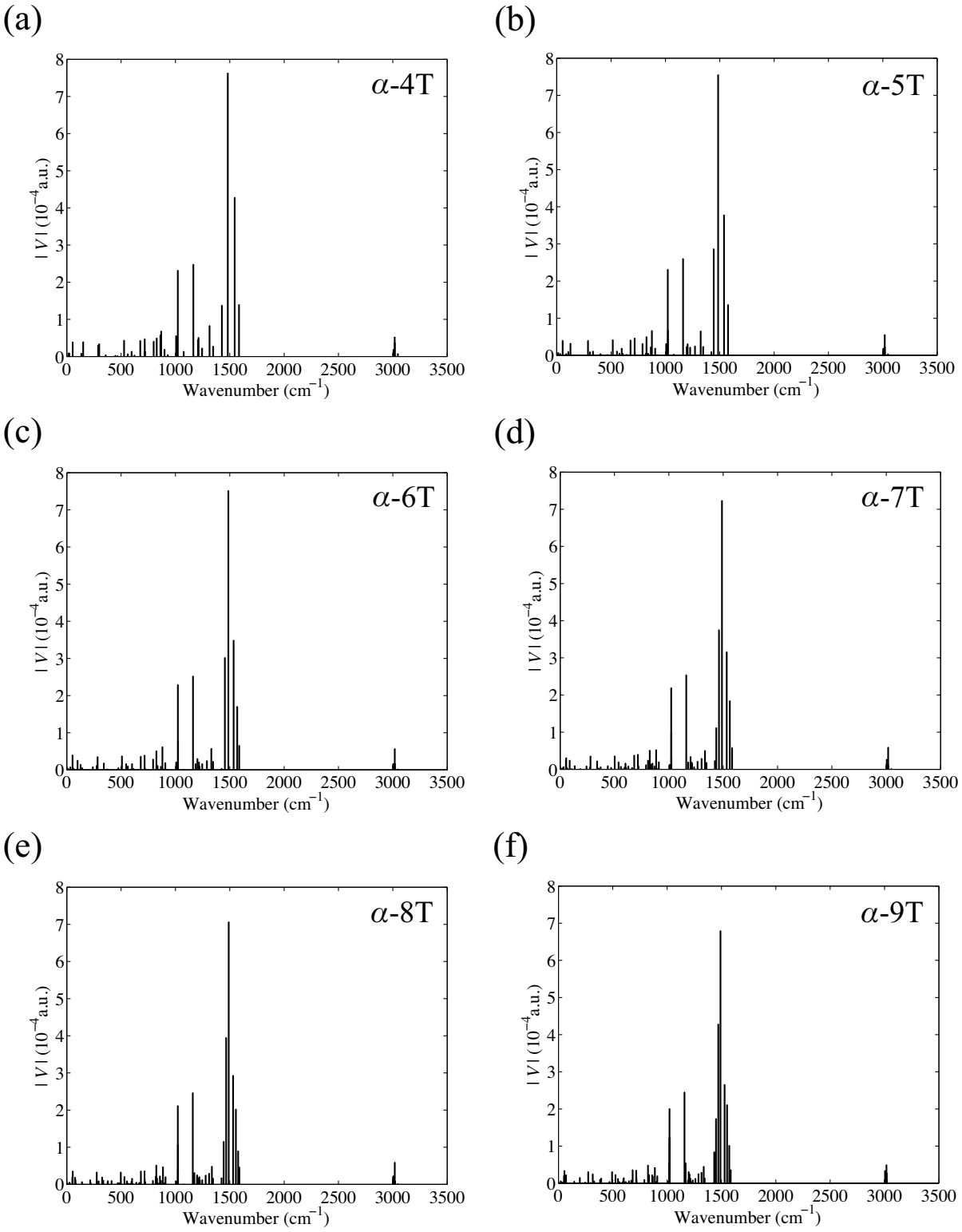

Figure 1.14: α-nT ($n = 4 - 9$): Absolute values of vibronic coupling constants $|V|$.

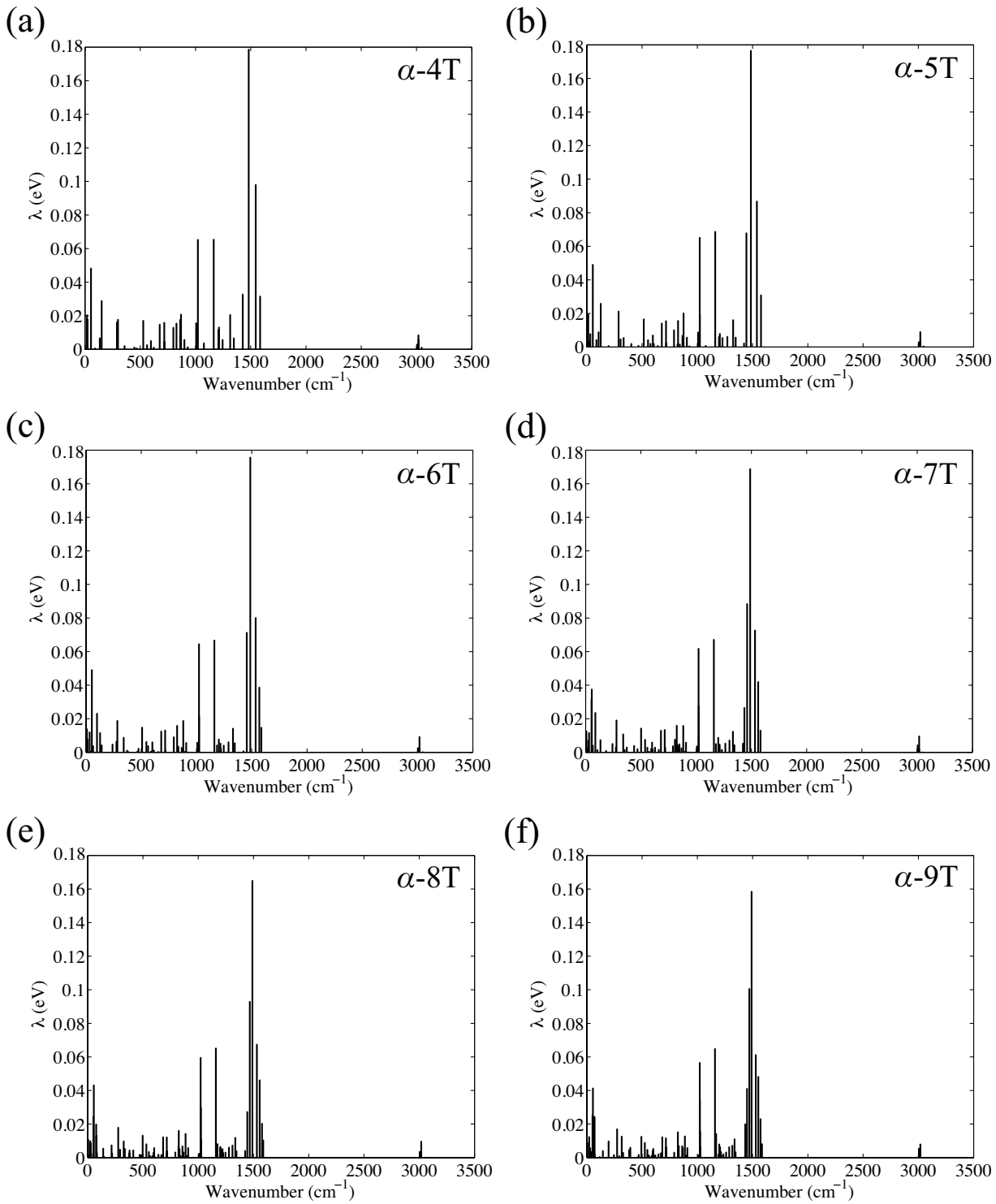

Figure 1.15: α-nT ($n = 4 - 9$): Electron–phonon coupling constants λ.

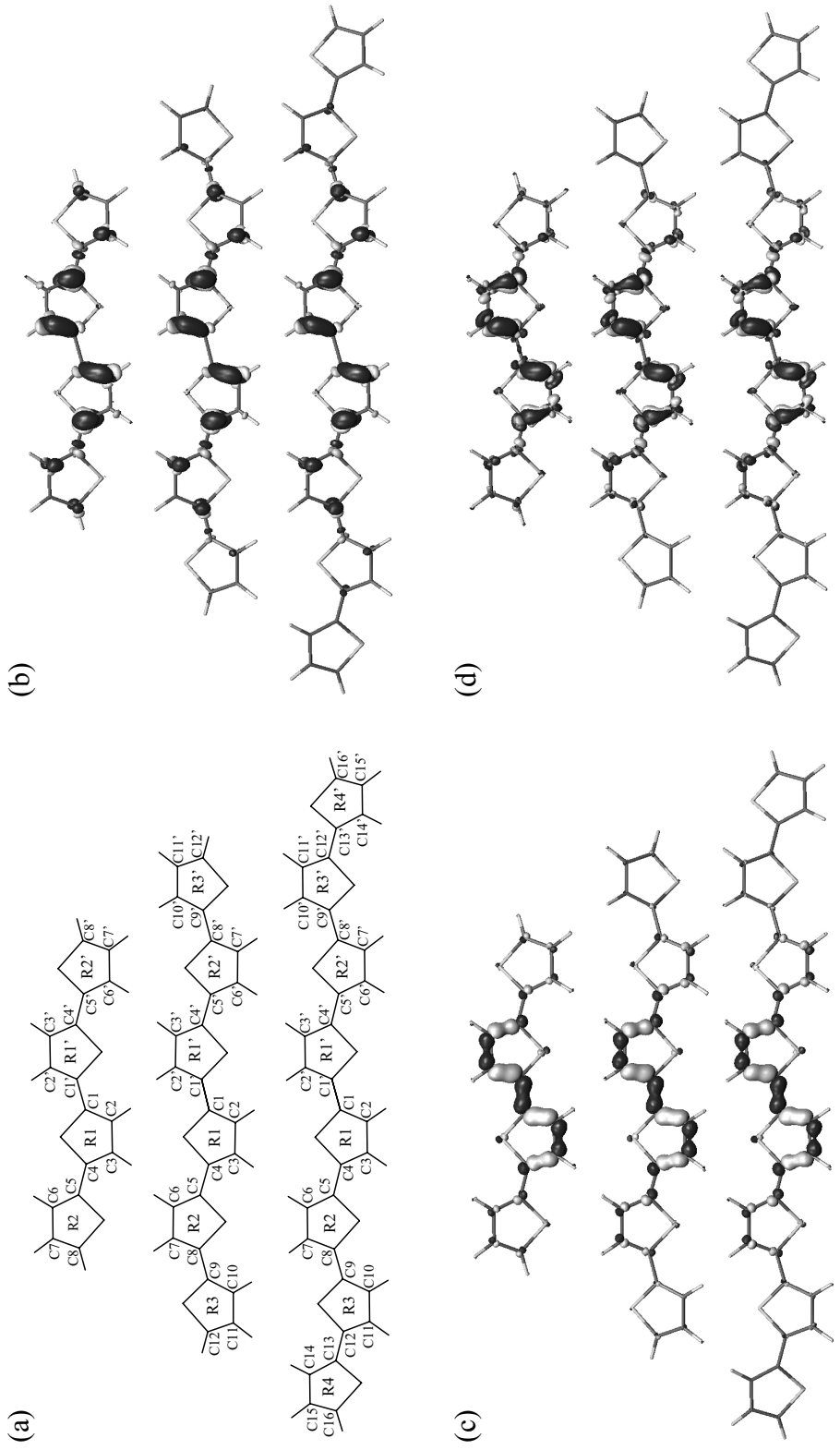

Figure 1.16: α-nT ($n = 4, 6, 8$) effective mode: (a) Atomic numbering scheme; (b) Electron-density difference $\Delta\rho$ ($|\Delta\rho| = 0.01$ a.u.); (c) Derivative of nuclear–electronic potential v_s ($|v_s| = 0.01$ a.u.); (d) Vibronic coupling density η_s ($|\eta_s| = 2.5 \times 10^{-5}$ a.u.). Dark gray shows where values are negative; light gray shows where values are positive.

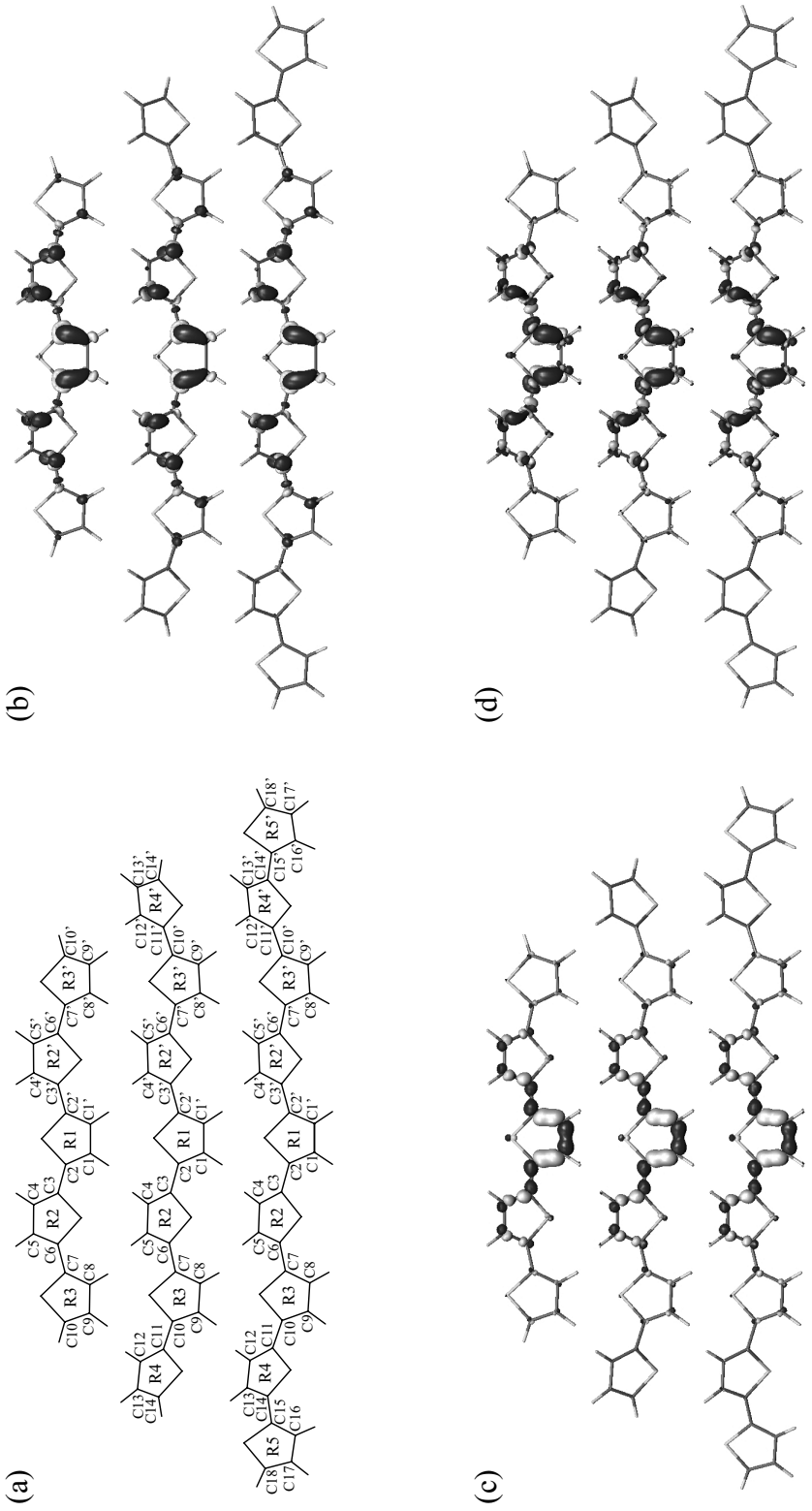

Figure 1.17: α-nT ($n = 5, 7, 9$) effective mode: (a) Atomic numbering scheme; (b) Electron-density difference $\Delta\rho$ ($|\Delta\rho| = 0.01$ a.u.); (c) Derivative of nuclear–electronic potential v_s ($|v_s| = 0.01$ a.u.); (d) Vibronic coupling density η_s ($|\eta_s| = 2.5 \times 10^5$ a.u.). Dark gray shows where values are negative; light gray shows where values are positive.

Figures 1.16(a) and (b) show atomic numbering schemes and $\Delta\rho$ for $n = 4, 6, 8$. $\Delta\rho$ is highly localized in the central four thiophene rings (R1, R1', R2, and R2' rings); as n increases, it becomes smaller in the R1, R1', R2, and R2' rings and larger in the R3 and R3' rings. In the R4 and R4' rings, distribution of $\Delta\rho$ is negligibly small. Figures 1.17(a) and (b) show atomic numbering schemes and $\Delta\rho$ for $n = 5, 7, 9$. $\Delta\rho$ is localized in the central five thiophene rings (R1, R2, R2', R3, and R3' rings). In particular, it shows a large distribution in the R1, R2, and R2' rings; as n increases it becomes smaller in the R1, R2, and R2' rings and larger in the R3 and R3' rings, and it is quite small in the R4, R4', R5, and R5' rings.

n dependence of VCC for the effective mode

Figure 1.18 shows VCCs for effective modes as a function of n. $|V_s|$ displays even-odd behavior. For even n (open squares), $|V_s|$ is smallest at $n = 2$, increases with n for $n < 4$, is largest at $n = 4$, and decreases gradually to 9.766×10^{-4} a.u. for $n > 6$. Similarly, for odd n (open triangles), $|V_s|$ is smallest at $n = 3$, increases with n for $n < 5$, is largest at $n = 5$, and decreases gradually to 9.798×10^{-4} a.u. for $n > 7$.

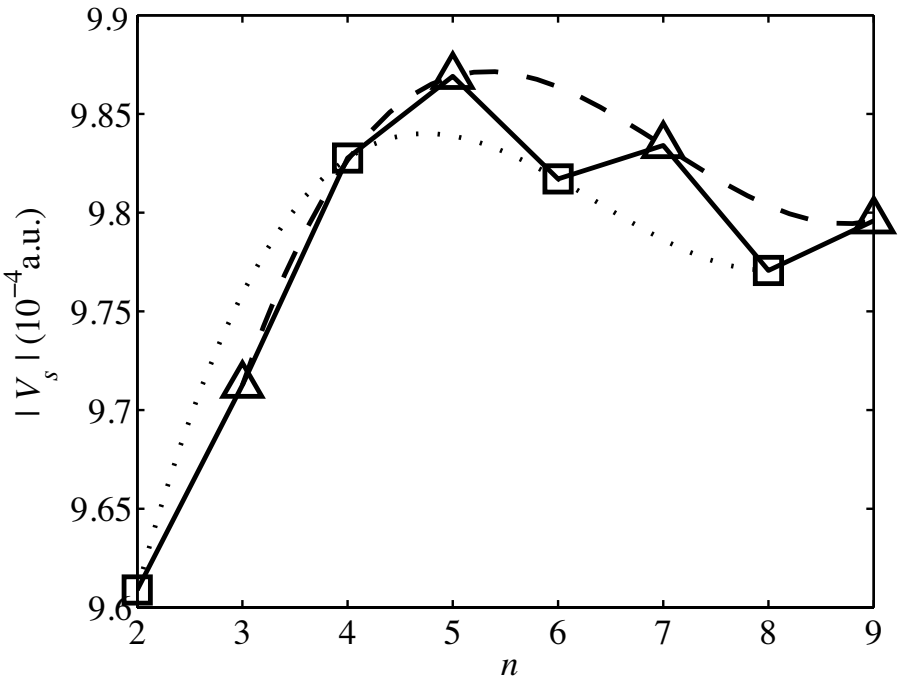

Figure 1.18: α-nT ($n = 2 - 9$): n dependence of $|V_s|$ (solid lines). Dotted lines and open squares show values for even n; dashed lines and open triangles show values for odd n.

Table 1.1: Atomic vibronic coupling constants in 10^{-4} a.u. for the effective modes of independent carbon atoms. Atom numbers are shown in Figs. 1.1, 1.9, 1.16, and 1.17.

Atom	α-2T	α-4T	α-6T	α-8T	α-3T	α-5T	α-7T	α-9T
C1	−2.309	−1.825	−1.553	−1.520	−2.146	−1.653	−1.492	−1.443
C2	−1.453	−1.238	−1.097	−1.065	−1.614	−1.488	−1.401	−1.373
C3	−0.693	−0.931	−0.910	−0.897	−0.542	−0.786	−0.810	−0.813
C4	−0.266	−0.550	−0.652	−0.650	−0.238	−0.381	−0.412	−0.418
C5		−0.148	−0.283	−0.289	−0.149	−0.316	−0.362	−0.371
C6		−0.065	−0.127	−0.133	−0.101	−0.172	−0.219	−0.230
C7		−0.053	−0.131	−0.142		−0.032	−0.065	−0.074
C8		−0.044	−0.070	−0.080		−0.014	−0.028	−0.032
C9			−0.010	−0.018		−0.017	−0.041	−0.048
C10			−0.005	−0.008		−0.019	−0.021	−0.025
C11			−0.007	−0.016			−0.003	−0.004
C12			−0.009	−0.008			−0.001	−0.002
C13				−0.001			−0.003	−0.006
C14				0.000			−0.005	−0.003
C15				−0.001				−0.001
C16				−0.002				0.000
C17								−0.001
C18								−0.001

AVCCs for carbon atoms for the effective modes of $n = 2 - 9$ are listed in Table 1.1. For even n, as n increases, AVCCs for the C1 and C2 atoms decrease while those for the C5–C8 atoms increase. This is because $\Delta\rho$ and v_s in the R2 and R2' rings increase with n.

Figure 1.16(c) shows v_s. The C=C and C−C stretching modes have large VCCs (Fig. 1.14) and contribute significantly to v_s. v_s is mainly distributed on C=C double bonds and single bonds in the R1 (R1') ring, and is nonzero around the C5–C8 atoms. At $n = 6$ and $n = 8$, the distribution of v_s in the R3, R3', R4, and R4' rings is negligible.

Figure 1.16(d) shows η_s. Since $\Delta\rho$ and v_s are distributed mainly in the central four thiophene rings, η_s has a large value in the same region. As n increases, η_s in the R2 and R2' rings increases.

The sums of AVCCs per thiophene ring are listed in Table 1.2. The VCC for the R1 ring decreases, while those for the R2 and R3 rings increase. In other words, vibronic coupling becomes weaker in the R1 ring and stronger in the R2 and R3 rings. This is because η_s extends more widely as n increases. In comparing ring VCCs for α-4T and α-2T, we find that the VCC for the α-4T R2 ring (-0.331 eV) exceeds the difference between VCCs for the R1 ring of α-4T and α-2T (0.222 eV) and, consequently, α-4T has a larger V_s than does α-2T. In contrast, for $n \geq 6$, the difference between VCCs for the R1 ring of α-nT and α-4T is larger than the increase in VCCs for the other rings and, consequently, V_s decreases with n.

Values in parentheses in Table 1.2 are obtained by dividing the VCC per thiophene ring by V_s. At $n = 6$ and $n = 8$, the sums of the VCCs for the R1, R1', R2, and R2' rings correspond to 99.2% and 98.7%, respectively, of V_s. Hence, vibronic coupling occurs mainly in the R1, R1', R2, and R2' rings. The size of the polaron is thus four thiophene rings, in agreement with several previous papers,[35–37] although why this should be is still not understood. Moro *et al.* showed that a polaronic defect occurs in the four innermost thiophene rings by comparing the bond lengths of neutral α-10T and α-10T cation at the HF/3-21* level.[37] Stafström *et al.* concluded that polaron size for α-6T is about four rings using MNDO molecular orbital calculations.[36] Polaron size has been estimated for polythiophene, using the SSH model, to be also four thiophene rings.[35]

For odd n, as n increases, AVCCs for the C1 and C2 atoms decrease, while those for the C3–C10 atoms increase (Table 1.1). At $n = 7$ and $n = 9$, AVCCs for carbon atoms in

Table 1.2: Vibronic coupling constants for the effective mode per thiophene ring in 10^{-4} a.u. Values in parentheses are the relative contributions (%) to V_s. Thiophene ring numbers are shown in Figs. 1.1, 1.9, 1.16, and 1.17.

Ring	α-2T	α-4T	α-6T	α-8T
R1	−4.804 (50.0)	−4.582 (46.6)	−4.243 (43.2)	−4.163 (42.6)
R2		−0.331(3.4)	−0.628 (6.4)	−0.660 (6.76)
R3			−0.036 (0.4)	−0.055 (0.56)
R4				−0.005 (0.05)
V_s	−9.608	−9.826	−9.814	−9.766
	α-3T	α-5T	α-7T	α-9T
R1	−7.569 (77.9)	−6.320 (64.0)	−5.819 (59.2)	−5.664 (57.8)
R2	−1.073 (11.0)	−1.683 (17.1)	−1.828 (18.6)	−1.857 (19.0)
R3		−0.092(0.9)	−0.164 (1.7)	−0.188 (1.9)
R4			−0.015 (0.2)	−0.018 (0.2)
R5				−0.004 (0.0)
V_s	−9.715	−9.870	−9.833	−9.798

the R4 and R5 rings are quite small. Figure 1.17(c) shows v_s. As in the case for even n, the C=C and C−C stretching modes contribute significantly to v_s. v_s has a large value on the C=C and C−C bonds in the central three thiophene rings, so η_s also shows a large distribution in those rings. The distribution of η_s in the other thiophene rings is quite small. The sums of VCCs per thiophene ring are listed in Table 1.2. The VCC for the R1 ring decreases, while those for the R2 and R3 rings increase, indicating that the region where vibronic coupling occurs extends more widely as molecular size increases. At $n = 7$ and $n = 9$, the sums of the VCCs for the R1, R2, and R2' rings correspond to 96.4% and 95.8%, respectively, of V_s. Hence, vibronic coupling occurs mainly in the R1, R2, and R2' rings. The contribution to V_s from the R3 and R3' rings is 3.8%, indicating that weak structural modification also occurs in those rings. We can say that polaron size is at most five thiophene rings, in good agreement with the theoretical results for α-9T obtained by AM1-level molecular orbital calculations.[53]

Interestingly, V_s is larger for odd n (Fig. 1.18, dashed line) than for even n (dotted line). The shapes of the two curves are similar, but the dashed line is shifted by about 0.03×10^{-4} a.u. The sum of the VCCs for the central six rings of α-8T is -9.756×10^{-4} a.u., very close to the sum of the VCCs for the central five rings of α-9T (-9.754×10^{-4} a.u.). Hence, the difference in V_s comes from the R4, R4', R5, and R5' rings. Actually, the sum of the VCCs for the R4 and R4' rings of α-8T is -0.010×10^{-4} a.u., and the sum for the R4, R4', R5, and R5' rings of α-9T is -0.044×10^{-4} a.u. The difference between these two sums is 0.034×10^{-4} a.u., nearly identical to the difference between the dashed and dotted lines in Fig. 1.18. Thus, η_s is more delocalized for odd n.

1.4.4 Simulation of photoelectron spectrum of $\alpha - 3$T

Relative VCC sizes of a molecular wire is measured directly employing the inelastic electron tunneling (IET) spectroscopy. However, experimental IET spectra for α-nT ($n = 2 - 8$) molecular wires have not been obtained yet. To confirm our theoretical results, we simulate a photoelectron spectrum of $\alpha - 3$T and compare the spectrum with the experiment,[54] which provides information on intramolecular vibronic coupling in the cationic state. We assume that only the effective mode contributes to the spectrum and only transitions from vibrational ground state occur. The frequency of the effective mode[55] is given by $\omega_s = \sum_i \omega_i^2 V_i^2 / V_s$ and calculated to be 1433.82 cm^{-1} ($\hbar\omega_s = 0.178$

eV). Since the C=C stretching modes contribute significantly to the effective mode, ω_s is close to the frequencies of those modes. The Franck–Condon factor for the transition from vibrational ground state in the neutral electronic state to the m^{th} vibrational state in the cationic state is expressed as $S^m \exp(-S)/m!$, where S is the Huang–Rhys factor given by $V_s^2/2\hbar\omega_s^3$.[26]

Figure 1.19 shows the comparison of the calculated photoelectron spectra with the experiment of $\alpha - 3$T. The curve was fitted using a Gaussian function of full width at half maximum of 0.14 eV. By setting the position of the $0 - 0$ transition to be 7.21 eV, the calculated spectrum is in reasonable agreement with the experiment. The peaks corresponding to $1-0$, $2-0$, $3-0$, and $4-0$ transitions are observed in the experimental spectrum, which supports our conclusion that the C=C stretching modes couple strongly to the electronic state.

1.5 Concluding Remarks

The relative VCC sizes for α-2T and α-3T was investigated in detail using VCD analysis. VCD analysis reveals that the large distribution of the electron-density difference on the C=C double bonds leads to the strong vibronic coupling of C=C stretching modes. The experimental photoelectron spectrum of α-3T supports our conclusion that the C=C stretching modes have the large VCCs.

For $\alpha - 8$T, the electron-density difference is distributed mainly in the central four thiophene rings, suggesting that the polaronic defect occurs in the four rings; for $\alpha - 9$T, the electron-density difference is distributed at most five thiophene rings, and hence, the polaron size is about five rings. Thus, vibronic coupling density analysis provides us a new insight into the reason for polaron size, and is a powerful tool for understanding transport properties of organic semiconductors and molecular wires.

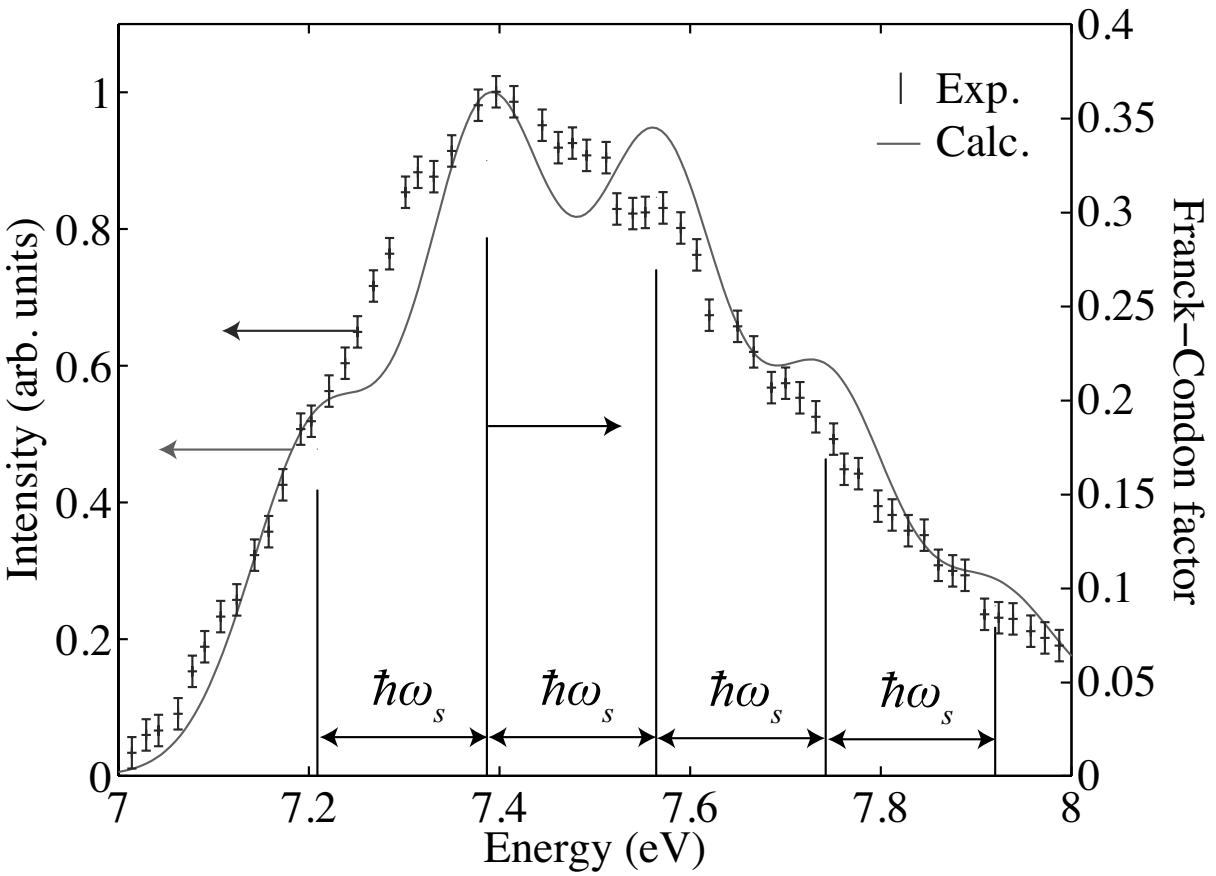

Figure 1.19: α-3T photoelectron spectrum. Solid curve shows calculated photoelectron spectrum; short vertical lines show the experimental photoelectron spectrum;[54] long vertical lines show the Franck–Condon factor.

Bibliography

[1] D. Fichou, J. Mater. Chem. **10**, 571 (2000).

[2] G. Horowitz, D. Fichou, and F. Garnier, Solid State Commun. **70**, 385 (1989).

[3] X. Peng, G. Horowitz, D. Fichou, and F. Garnier, Appl. Phys. Lett. **57**, 2013 (1990).

[4] H. Akimichi, K. Waragai, S. Hotta, H. Kano, and H. Sakaki, Appl. Phys. Lett. **58**, 1500 (1991).

[5] F. Garnier, A. Yassar, R. Hajlaoui, G. Horowitz, F. Deloffre, B. Servet, S. Ries, and P. Alnot, J. Am. Chem. Soc. **115**, 8716 (1993).

[6] B. Servet, G. Horowitz, S. Ries, O. Lagorsse, P. Alnot, A. Yassar, F. Deloffre, P. Srivastava, R. Hajlaoui, P. Lang, and F. Garnier, Chem. Mater. **6**, 1809 (1994).

[7] G. Horowitz, F. Garnier, A. Yassar, R. Hajlaoui, and F. Kouki, Adv. Mater. **8**, 52 (1996).

[8] R. Hajlaoui, G. Horowitz, F. Garnier, A. Arce-Brouchet, L. Laigre, A. E. Kassmi, F. Demanze, and F. Kouki, Adv. Mater. **9**, 387 (1997).

[9] R. Hajlaoui, D. Fichou, G. Horowitz, B. Nessakh, M. Constant, and F. Garnier, Adv. Mater. **9**, 557 (1997).

[10] Z. Bao, Y. Feng, A. Dodabalapur, V. R. Raju, and A. J. Lovinger, Chem. Mater. **9**, 1299 (1997).

[11] H. E. Katz, J. Mater. Chem. **7**, 369 (1997).

[12] F. Garnier, G. Horowitz, D. Fichou, and A. Yassar, Supramol. Sci. **4**, 155 (1997).

[13] H. E. Katz, A. J. Lovinger, and J. G. Laquindanum, Chem. Mater. **10**, 457 (1998).

[14] G. Horowitz, R. Hajlaoui, and F. Kouki, Eur. Phys. J. Appl. Phys. **1**, 361 (1998).

[15] G. Horowitz and M. E. Hajlaoui, Adv. Mater. **12**, 1046 (2000).

[16] G. Horowitz, D. Fichou, X. Peng, Z. Xu, and F. Garnier, Solid State Commun. **72**, 381 (1989).

[17] O. D. Jurchescu, J. Baas, and T. T. M. Palstra, Appl. Phys. Lett. **84**, 3061 (2004).

[18] S. Nagamatsu, K. Kaneto, R. Azumi, M. Matsumoto, Y. Yoshida, and K. Yase, J. Phys. Chem. B **109**, 9374 (2005).

[19] Y. X. Zhou, F. Jiang, H. Chen, R. Note, H. Mizuseki, and Y. Kawazoe, Phys. Rev. B **75**, 245407 (2007).

[20] T. Otsubo, Y. Aso, and K. Takimiya, Bull. Chem. Soc. Jpn. **74**, 1789 (2001).

[21] N. Sumi, H. Nakanishi, S. Ueno, K. Takimiya, Y. Aso, and T. Otsubo, Bull. Chem. Soc. Jpn. **74**, 979 (2001).

[22] T. Izumi, S. Kobashi, K. Takimiya, Y. Aso, and T. Otsubo, J. Am. Chem. Soc. **125**, 5286 (2003).

[23] F. Nishiyama, K. Ogawa, S. Tanaka, and T. Yokoyama, J. Phys. Chem. B **112**, 5272 (2008).

[24] R. Yamada, H. Kumazawa, S. Tanaka, and H. Tada, Appl. Phys. Express **2**, 025002 (2009).

[25] C. Joachim and M. A. Ratner, Proc. Natl. Acad. Sci. USA **102**, 8801 (2005).

[26] T. Sato, K. Tokunaga, N. Iwahara, K. Shizu, and K. Tanaka, *Vibronic coupling constant and vibronic coupling density* in *The Jahn-Teller-Effect - Fundamentals and Implications for Physics and Chemistry,* H. Köppel, D. R. Yarkony, and H. Barentzen (Eds) (Springer-Verlag, Berlin and Heidelberg, 2009).

[27] T. Sato, K. Tokunaga, and K. Tanaka, J. Phys. Chem. A **112**, 758 (2008).

[28] K. Tokunaga, T. Sato, and K. Tanaka, J. Mol. Struct. **838**, 116 (2007).

[29] K. Tokunaga, T. Sato, and K. Tanaka, J. Chem. Phys. **124**, 154303 (2006).

[30] T. Sato, K. Tokunaga, and K. Tanaka, J. Chem. Phys. **124**, 024314 (2006).

[31] S. Datta, *Quantum Transport: Atom to Transistor* (Cambridge University Press, Cambridge, 2005).

[32] T. Sato, K. Shizu, T. Kuga, K. Tanaka, and H. Kaji, Chem. Phys. Lett. **458**, 152 (2008).

[33] N. Yokonuma, Y. Furukawa, M. Tasumi, M. Kuroda, and J. Nakayama, Chem. Phys. Lett. **255**, 431 (1996).

[34] Y. Furukawa, J. Phys. Chem. **100**, 15644 (1996).

[35] J.-L. Brédas, F. Wudl, and A. J. Heeger, Solid State Commun. **63**, 577 (1987).

[36] S. Stafström and J.-L. Brédas, Phys. Rev. B **38**, 4180 (1988).

[37] G. Moro, G. Scalmani, U. Cosentino, and D. Pitea, Synth. Met. **108**, 165 (2000).

[38] S. S. Zade and M. Bendikov, J. Phys. Chem. C **111**, 10662 (2007).

[39] R. P. Feynman, Phys. Rev. **56**, 340 (1939).

[40] H. Nakatsuji, K. Kanda, and T. Yonezawa, Chem. Phys. Lett. **75**, 340 (1980).

[41] M. W. Schmidt, K. K. Baldridge, J. A. Boatz, S. T. Elbert, M. S. Gordon, J. H. Jensen, S. Koseki, N. Matsunaga, K. A. Nguyen, S. J. Su, T. L. Windus, M. Dupins, and J. A. Montgomery, J. Comput. Chem. **14**, 1347 (1993).

[42] J. A. Pople, M. Head-Gordon, D. J. Fox, K. Raghavachari, and L. A. Curtiss, J. Chem. Phys. **90**, 5622 (1989).

[43] S. Samdal, E. J. Samuelsen, and H. V. Volden, Synth. Met. **59**, 259 (1993).

[44] E. Fabiano and F. D. Sala, Chem. Phys. Lett. **418**, 496 (2006).

[45] J. C. Sancho-García, J. Phys. Chem. A **109**, 3470 (2005).

[46] J. C. Sancho-García and J. Cornil, J. Chem. Phys. **121**, 3096 (2004).

[47] R. Viruela, P. Viruela, R. Pou-Améigo, and E. Ortí, Synth. Met. **103**, 1991 (1999).

[48] V. Hernandez and J. T. L. Navarrete, J. Chem. Phys. **101**, 1369 (1994).

[49] C. Quattrocchi, R. Lazzaroni, and J.-L. Brédas, Chem. Phys. Lett. **208**, 120 (1993).

[50] A. Almenningen, O. Bastiansen, and P. Svendsås, Acta Chem. Scand. **12**, 1103 (1958).

[51] M. Ciofalo and G. L. Manna, Chem. Phys. Lett. **263**, 73 (1996).

[52] D. D. Graf, R. G. Duan, J. P. Campbell, L. L. Miller, and K. R. Mann, J. Am. Chem. Soc. **119**, 5888 (1997).

[53] J. Cornil, D. Beljonne, and J.-L. Brédas, J. Chem. Phys. **103**, 842 (1995).

[54] D. A. da Silva Filho, V. Coropceanu, D. Fichou, N. E. Gruhn, T. G. Bill, J. Gierschner, J. Cornil, and J.-L. Brédas, Philos. Trans. R. Soc. London, A **365**, 1435 (2007).

[55] K. Shizu, T. Sato, K. Tanaka, and H. Kaji, Chem. Phys. Lett. **486**, 130 (2010).

Chapter 2

Inelastic Electron Tunneling Spectra and Vibronic Coupling Density Analysis of 2,5-Dimercapto-1,3,4-thiadiazole and Tetrathiafulvalene Dithiol

2.1 Introduction

Inelastic electron tunneling (IET) spectra for metal-molecule-metal junctions have been studied extensively in recent years.[1–6] Peak positions of an IET spectrum correspond to vibrational energies of a molecule that interacts with a carrier, and the peak heights reflect relative strength of electron-molecular vibration interaction, or vibronic coupling.[7] Thus, IET spectra contain information about vibronic coupling between the carrier and the molecular vibrations. IET spectra are characteristic for molecules and IET spectroscopy can serve as an identification method for molecular species adsorbed on an electrode. IET spectra are also useful for choosing a molecule when we construct a molecular wire junction, and therefore, a fundamental understanding of IET spectra is needed for development of future nanoelectronics.

Selection rules for IET spectra are yet controversial. For oligo (phenylene ethynylene) (OPE), the ring mode and C≡C stretching mode show intense peaks; for oligo (viny-

lene ethynylene) (OPV), the ring mode and C=C stretching mode show intense peaks.[4] This result shows that the carrier is scattered by IR and Raman active modes. In contrast, the systematic experimental observation of the IET spectra for semifluorinated alkanethiol junctions has made it clear that the relative intensity of the spectra is not necessarily proportional to the calculated IR nor Raman intensities of the isolated semifluorinated alkanethiols.[5] Using a scanning tunneling microscope (STM), Okabayashi *et al.* have measured high-resolution STM IET spectra of alkanethiol self-assembled monolayers (SAMs)[8,9] and reported that inelastic intermolecular scattering is important in electron tunneling in the SAMs. Troisi *et al.* have estimated peak intensities in IET spectra by calculating the first derivative of the Green's function with respect to the normal mode coordinates, and concluded that only the totally symmetric modes show peak when a single tunneling channel is available.[10]

Our purpose is to provide an understanding of relative intensities in IET spectra based on vibronic coupling density (VCD) analysis.[11–14] The VCD analysis tells us the reason for relative order of strength of vibronic coupling, and hence, gives a new insight into the shape of an IET spectrum. We have applied the VCD analysis to various molecules, revealed a local picture of vibronic coupling in molecules, and shown that we can tune vibronic couplings by controlling electron-density difference $\Delta\rho$.[11–19] This guiding principle provides an effective way to design functional materials such as molecular wires as well as to interpret IET spectra.

In this chapter, using the VCD analysis, we investigate vibronic coupling in 2,5-dimercapto-1,3,4-thiadiazole (DMcT) and tetrathiafulvalene dithiol (TTF-DT) sandwiched between two gold electrodes. We calculate IET spectra for the Au/DMcT/Au and Au/TTF-DT/Au junctions employing the non-equilibrium Green's function (NEGF) formalism[20] and compare the spectra with the experimental results obtained using nanofabricated mechanically-controllable break junctions (MCBJs).[6,21] Tetrathiafulvalene (TTF) and its derivatives have been studied as electron donors for molecular conductors and superconductors;[22–24] DMcT has been known as a cathode-active material for lithium rechargeable batteries[25] and an understanding of charge transfer between DMcT and metal electrodes is quite important. These molecules are promising building blocks for molecular wires and conducting properties of them sandwiched between gold electrodes have been investigated intensively.[21,26,27]

We also calculate an IET spectrum for an Au/thiophene dithiol (Th-DT)/Au junction and compare it with that for the Au/DMcT/Au junction. The VCD analysis reveals the reason for the difference between the spectra of the two junctions. This analysis provides a new insight for IET spectra and guiding principle of design for molecular wire junctions.

2.2 Theory

2.2.1 Vibronic coupling constant and vibronic coupling density

A molecular Hamiltonian can be written as

$$\mathcal{H}\left(\mathbf{r},\mathbf{R}\right)=\mathcal{H}_{\mathrm{e}}\left(\mathbf{r},\mathbf{R}\right)+\mathcal{T}_{\mathrm{n}}\left(\mathbf{R}\right), \tag{2.1}$$

where $\mathbf{r}$ and $\mathbf{R}$ denote sets of electronic and nuclear coordinates, respectively, and $\mathcal{H}_{\mathrm{e}}\left(\mathbf{r},\mathbf{R}\right)$ and $\mathcal{T}_{\mathrm{n}}\left(\mathbf{R}\right)$ are an electronic Hamiltonian and the nuclear kinetic energy, respectively. We assume that the molecular wire is in a neutral state at first, and vibronic coupling occurs when the molecule is ionized by a carrier.

Once an equilibrium nuclear configuration $\mathbf{R}_0$ and vibrational frequencies of the molecule are obtained, we can calculate vibronic coupling constant (VCC) V_{ij}^{α} for the α^{th} mode:

$$V_{ij}^{\alpha}=\left\langle \Psi_i^{+}\left(\mathbf{r},\mathbf{R_0}\right)\left|\left(\frac{\partial\mathcal{H}\left(\mathbf{r},\mathbf{R}\right)}{\partial Q_{\alpha}}\right)_{\mathbf{R}=\mathbf{R}_0}\right|\Psi_j^{+}\left(\mathbf{r},\mathbf{R_0}\right)\right\rangle, \tag{2.2}$$

where $\Psi_i^{+}\left(\mathbf{r},\mathbf{R_0}\right)$ is an electronic wave function of the cation state in which an electron is removed from the i^{th} molecular orbital and $\{Q_{\alpha}\}$ is a set of mass-weighted normal coordinates.

For $i=j$, V_i^{α} $(\equiv V_{ii}^{\alpha})$ can be expressed as the space integration of the VCD η_i^{α}:[11–14]

$$V_i^{\alpha}=\int\eta_i^{\alpha}\left(\mathbf{x}\right)d\mathbf{x}, \tag{2.3}$$

where $\mathbf{x}$ is a position in the three-dimensional space and η_i^{α} is defined by

$$\eta_i^{\alpha}=\Delta\rho_i\left(\mathbf{x}\right)\times v_{\alpha}\left(\mathbf{x}\right), \tag{2.4}$$

where $\Delta\rho_i$ is an electron-density difference and v_{α} is the one-electron operator of the derivative of nuclear–electronic potential with respect to Q_{α}. $\Delta\rho_i$ and v_{α} are defined by

$$\Delta\rho_i\left(\mathbf{x}\right)=\rho_i^{+}\left(\mathbf{x}\right)-\rho_0\left(\mathbf{x}\right), \tag{2.5}$$

$$
\begin{aligned}
v_\alpha(\mathbf{x}) &= -\sum_A \frac{Z_A}{\sqrt{M_A}} \mathbf{e}_A^{(\alpha)} \cdot \frac{\mathbf{x}-\mathbf{R}_A}{|\mathbf{x}-\mathbf{R}_A|^3} \\
&= -\sum_A v_{\alpha,A}(\mathbf{x}),
\end{aligned} \tag{2.6}
$$

where ρ_i^+ is the electron density of the cation state in which an electron is removed from the i^{th} molecular orbital; ρ_0 is the electron density of the neutral state. M_A and $\mathbf{R}_A$ are the mass and the nuclear coordinate of the nucleus A, respectively. $\mathbf{e}_A^{(\alpha)}$ is the A^{th} component of a vibrational vector in mass-weighted coordinates $\mathbf{e}^{(\alpha)}$.

The contribution to η_i^α from the A^{th} atom is given by

$$
\eta_{i,A}^\alpha(\mathbf{x}) = \Delta\rho(\mathbf{x}) \times v_{\alpha,A}(\mathbf{x}). \tag{2.7}
$$

The space integration of $\eta_{i,A}^\alpha$ gives the contribution to V_i^α from the A^{th} atom:

$$
V_{i,A}^\alpha = \int \eta_{i,A}^\alpha(\mathbf{x}) d\mathbf{x}, \tag{2.8}
$$

where $V_{i,A}^\alpha$ is called the atomic VCC (AVCC) and

$$
\sum_A V_{i,A}^\alpha = V_i^\alpha. \tag{2.9}
$$

2.2.2 Inelastic electron tunneling spectrum

Within the framework of the Holstein–Peierls model, we can write the molecular Hamiltonian $\mathcal{H}$ in the second quantization form as

$$
\mathcal{H} = \sum_i \epsilon_i c_i^\dagger c_i + \sum_\alpha \hbar\omega_\alpha \left(b_\alpha^\dagger b_\alpha + \frac{1}{2} \right) + \sum_{ij,\alpha} \lambda_{ij}^\alpha c_i^\dagger c_j \left(b_\alpha + b_\alpha^\dagger \right) \tag{2.10}
$$

where $c_i^\dagger$ and c_i are electron creation and annihilation operators in the i^{th} molecular orbital, respectively, and $b_\alpha^\dagger$ and b_α denote phonon creation and annihilation operators of the mode α, respectively. ϵ_i is the orbital energy of the i^{th} molecular orbital. λ_{ij}^α and ω_α are electron-phonon coupling constant and frequency of the mode α, respectively. λ_{ij}^α is related to the VCC V_{ij}^α:

$$
\lambda_{ij}^\alpha = \sqrt{\frac{\hbar}{2\omega_\alpha}} V_{ij}^\alpha. \tag{2.11}
$$

ϵ_i, ω_α, and V_{HOMO}^α are calculated using DFT method, and $V_{\text{HOMO}-1}^\alpha$ is calculated using CASSCF method.

A Green's function of the molecular wire junction is given by

$$
\mathbf{G}(E) = \left[E\mathbf{I} - \mathbf{H}_{\text{e}} - \mathbf{\Sigma}(E) \right]^{-1}, \tag{2.12}
$$

where E is an energy of an electron, $\mathbf{I}$ is the identity matrix, $\mathbf{H}_{\mathrm{e}}$ is a matrix representation of $\mathcal{H}_{\mathrm{e}}$, and $\mathbf{\Sigma}(E)$ is a total self-energy,[20] which is defined later by Eq. (2.27). $\mathbf{H}_{\mathrm{e}}$ is a diagonal matrix and $(\mathbf{H}_{\mathrm{e}})_{ii} = \epsilon_i$.

Inscattering and outscattering functions for the left/right electrode is given by

$$\mathbf{\Sigma}^{\mathrm{in}}_{\mathrm{L/R}}(E) = f_{\mathrm{L/R}}(E)\,\mathbf{\Gamma}_{\mathrm{L/R}}(E), \tag{2.13}$$

$$\mathbf{\Sigma}^{\mathrm{out}}_{\mathrm{L/R}}(E) = \left(1 - f_{\mathrm{L/R}}(E)\right)\mathbf{\Gamma}_{\mathrm{L/R}}(E), \tag{2.14}$$

where

$$f_{\mathrm{L/R}}(E) = \frac{1}{1+\exp\left(\frac{E-\mu_{\mathrm{L/R}}}{k_{\mathrm{B}}T}\right)}, \tag{2.15}$$

$$\mathbf{\Gamma}_{\mathrm{L/R}}(E) = i\left\{\mathbf{\Sigma}_{\mathrm{L/R}}(E) - \mathbf{\Sigma}^{\dagger}_{\mathrm{L/R}}(E)\right\}. \tag{2.16}$$

Here, $\mu_{\mathrm{L/R}}$ and $\mathbf{\Sigma}_{\mathrm{L/R}}$ are an electrochemical potential and contact self-energy for the left/right electrode, respectively, k_{B} is the Boltzmann constant, and T is the temperature of the composite system. $\mathbf{\Sigma}_{\mathrm{L/R}}$ incorporates an effect of an interaction between the left/right electrode and the molecule and given by

$$\mathbf{\Sigma}_{\mathrm{L/R}}(E) = \tau^{\dagger}_{\mathrm{L/R}}\mathbf{g}(E)\,\tau_{\mathrm{L/R}}, \tag{2.17}$$

where $\tau_{\mathrm{L/R}}$ is an electronic coupling between the left/right electrode and the molecule and $\mathbf{g}$ is a surface Green's function.

We calculate inscattering and outscattering functions for the vibronic coupling within the first Born approximation:[28]

$$\mathbf{\Sigma}^{\mathrm{in}}_{\mathrm{S}}(E) = \sum_{\alpha}\lambda^{\alpha}\left\{(N_\alpha+1)\,\mathbf{G}^{\mathrm{n}}(E+\hbar\omega_\alpha) + N_\alpha\mathbf{G}^{\mathrm{n}}(E-\hbar\omega_\alpha)\right\}\lambda^{\alpha}, \tag{2.18}$$

$$\mathbf{\Sigma}^{\mathrm{out}}_{\mathrm{S}}(E) = \sum_{\alpha}\lambda^{\alpha}\left\{N_\alpha\mathbf{G}^{\mathrm{p}}(E+\hbar\omega_\alpha) + (N_\alpha+1)\,\mathbf{G}^{\mathrm{p}}(E-\hbar\omega_\alpha)\right\}\lambda^{\alpha}, \tag{2.19}$$

where

$$(\lambda^{\alpha})_{ij} = \lambda^{\alpha}_{ij}, \tag{2.20}$$

$$N_\alpha = \frac{1}{\exp\left(\frac{\hbar\omega_\alpha}{k_{\mathrm{B}}T}\right)-1}. \tag{2.21}$$

Here, N_α is an occupation number of phonons with energy $\hbar\omega_\alpha$. $\mathbf{G}^{\mathrm{n}}$ and $\mathbf{G}^{\mathrm{p}}$ are electron and hole correlation functions that are given by

$$\mathbf{G}^{\mathrm{n}}(E) = \mathbf{G}(E)\mathbf{\Sigma}^{\mathrm{in}}(E)\mathbf{G}^{\dagger}(E), \tag{2.22}$$

$$\mathbf{G}^{\mathrm{p}}(E) = \mathbf{G}(E)\mathbf{\Sigma}^{\mathrm{out}}(E)\mathbf{G}^{\dagger}(E), \tag{2.23}$$

where

$$\mathbf{\Sigma}^{\mathrm{in}}(E) = \mathbf{\Sigma}^{\mathrm{in}}_{\mathrm{L}}(E) + \mathbf{\Sigma}^{\mathrm{in}}_{\mathrm{R}}(E) + \mathbf{\Sigma}^{\mathrm{in}}_{\mathrm{S}}(E), \tag{2.24}$$

$$\mathbf{\Sigma}^{\mathrm{out}}(E) = \mathbf{\Sigma}^{\mathrm{out}}_{\mathrm{L}}(E) + \mathbf{\Sigma}^{\mathrm{out}}_{\mathrm{R}}(E) + \mathbf{\Sigma}^{\mathrm{out}}_{\mathrm{S}}(E). \tag{2.25}$$

A self-energy for vibronic coupling $\mathbf{\Sigma}_{\mathrm{S}}$ is a function of the energy E of the incoming electron and is related to $\mathbf{\Sigma}^{\mathrm{in}}_{\mathrm{S}}$ and $\mathbf{\Sigma}^{\mathrm{out}}_{\mathrm{S}}$ through the following equation:

$$i\left\{\mathbf{\Sigma}_{\mathrm{S}}(E) - \mathbf{\Sigma}^{\dagger}_{\mathrm{S}}(E)\right\} = \mathbf{\Sigma}^{\mathrm{in}}_{\mathrm{S}}(E) + \mathbf{\Sigma}^{\mathrm{out}}_{\mathrm{S}}(E). \tag{2.26}$$

$\mathbf{\Sigma}(E)$ is a sum of the self-energies:

$$\mathbf{\Sigma}(E) = \mathbf{\Sigma}_{\mathrm{L}}(E) + \mathbf{\Sigma}_{\mathrm{R}}(E) + \mathbf{\Sigma}_{\mathrm{S}}(E). \tag{2.27}$$

$\mathbf{G}^{\mathrm{n}}$ and $\mathbf{G}^{\mathrm{p}}$ are calculated self-consistently using Eqs. (2.12), (2.18), (2.19), and (2.22)–(2.27).

The electric current through the molecular wire junction is given by

$$I = -\frac{2e}{h}\int_{-\infty}^{+\infty} dE \mathrm{Tr}\left\{\mathbf{\Sigma}^{\mathrm{in}}_{\mathrm{L/R}}(E)\,\mathbf{G}^{\mathrm{p}}(E) - \mathbf{\Sigma}^{\mathrm{out}}_{\mathrm{L/R}}(E)\,\mathbf{G}^{\mathrm{n}}(E)\right\}, \tag{2.28}$$

where e is the elementary charge. The first and second derivative of I with respect to bias voltage V_{b} yield the conductance (dI/dV_{b}) and IET spectrum (d^2I/dV_{b}^2 vs V_{b}), respectively.

2.3 Method of calculation

All the DFT calculations were done using Gaussian 03 software.[29] For carbon, hydrogen, nitrogen, and sulfur atoms, 6-311+G* basis set was used; for gold atom, LANL2DZ basis set was used. We considered intramolecular vibronic coupling in the molecules containing gold atoms: terminal hydrogen atoms of DMcT, TTF-DT, and Th-DT are replaced by gold atoms. We denote them as Au_2DMcT, Au_2TTF-DT, and Au_2Th-DT, respectively.

Geometry optimization and vibrational analysis of neutral Au_2DMcT, Au_2TTF-DT, and Au_2Th-DT were done using B3LYP method. We assumed C_{2v} symmetry for Au_2DMcT, C_i symmetry for Au_2TTF-DT, and C_2 symmetry for Au_2Th-DT. We calculated wavefunctions of the cationic states in which the electron is removed from the HOMO (denoted as $\left|\Psi^{+}_{\mathrm{HOMO}}\right\rangle$) using the UB3LYP method and that in which the electron is removed from

the next HOMO (denoted as $\left|\Psi^{+}_{\mathrm{HOMO}-1}\right\rangle$) using the CASSCF method. The active space of our CASSCF calculation includes three electrons and three molecular orbitals (LUMO, HOMO, and next HOMO).

We calculated conductances and IET spectra for Au_2DMcT, Au_2TTF-DT, and Au_2Th-DT sandwiched between two gold electrodes (denoted as Au/DMcT/Au, Au/TTF-DT/Au, and Au/Th-DT/Au, respectively). We adopt the Green's function for a semi-infinite one-dimensional gold chain as $\mathbf{g}$.[20] The coupling between a molecule and electrode $\tau_{\mathrm{L/R}}$ depends on device geometry and molecular orientation. However, since the junction geometry is unclear, we consider $\tau_{\mathrm{L/R}}$ as a parameter.

We adopt the opposite sign of the work function of a gold surface (5.53 eV)[30] as the Fermi energy of the electrode surface E_{F}. The electrochemical potential $\mu_{\mathrm{L/R}}$ at an applied bias voltage V_{b} is set to be $\mu_{\mathrm{L/R}} = E_{\mathrm{F}} \pm eV_{\mathrm{b}}/2$.

2.4 Results and discussion

2.4.1 Vibronic coupling density analysis

Figure 2.1 shows the optimized geometries of neutral Au_2DMcT and Au_2TTF-DT with atomic numbering schemes. The optimized geometry of Au_2DMcT is planar. The optimized bond angles and lengths of Au_2DMcT are in good agreement with the experimental values of 2-amino-5-phenyl-1,3,4-thiadiazole;[31] the optimized bond angles and lengths of Au_2TTF-DT are in agreement with the experimental data for TTF obtained by Cooper *et al.*[32] The dihedral angles S1−C1−C1′−S2′, S2−C1−C1′−S1, C1′−C1−S1−C2, and C1′−C1−S2−C3 are 0.5°,179.5°, 179.4°, and 178.7°, respectively, suggesting that the central TTF moiety is almost planar. Au_2DMcT and Au_2TTF-DT have eight and 21 totally symmetric modes, respectively, that couple to the electronic state.

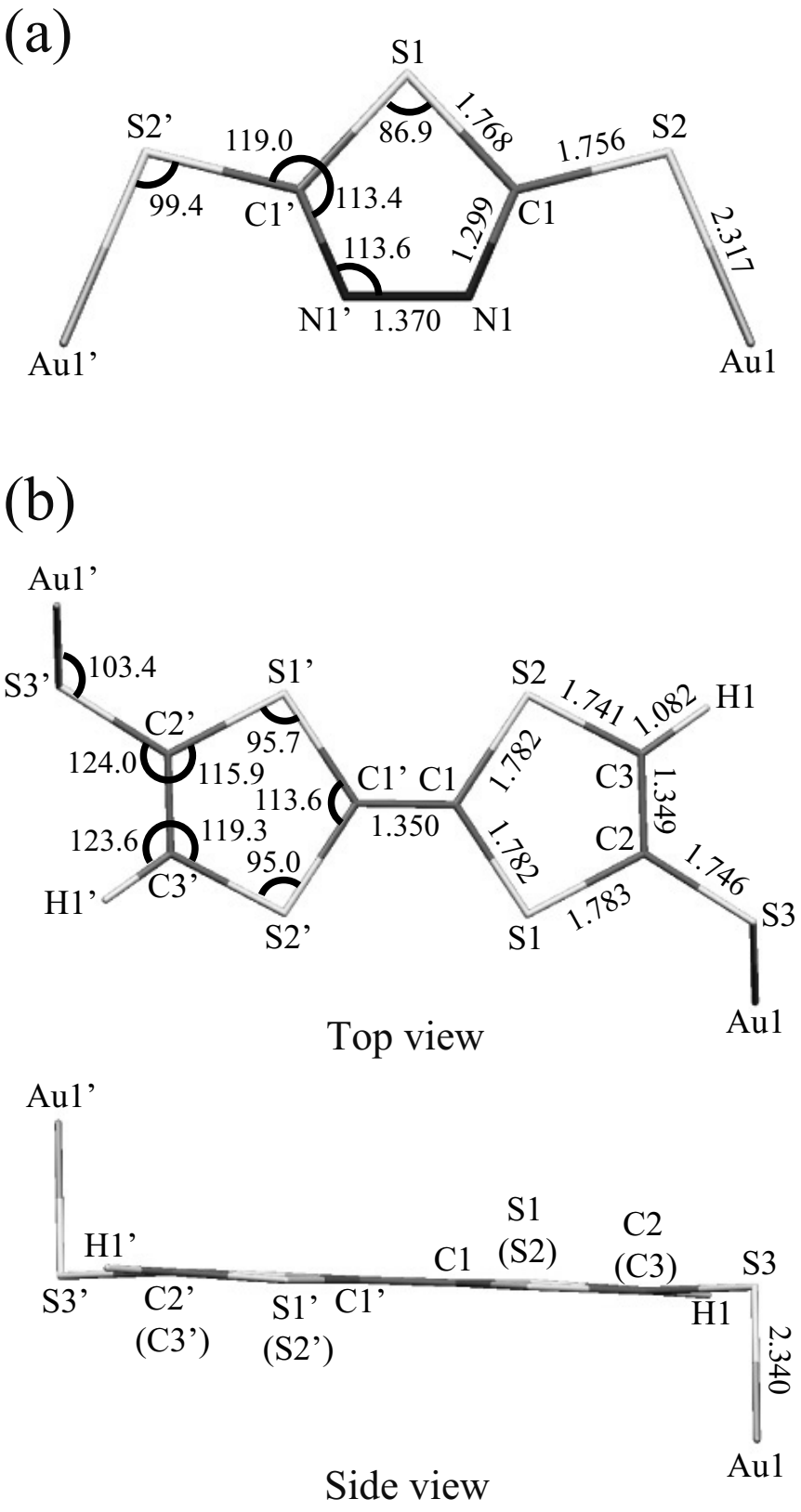

Figure 2.1: Optimized geometries with atomic numbering schemes: (a) Au_2DMcT; (b) Au_2TTF-DT. Bond lengths are in Å and bond angles in degree.

Calculated VCCs and peak positions in IET spectra for Au_2DMcT and Au_2TTF-DT together with the experimental data[6,21] are listed in Tables 2.1 and 2.2, respectively. $a(\alpha)$ denotes the α^{th} totally symmetric mode. $V^{\alpha}_{\text{HOMO/HOMO}-1}$ is the VCC for the cation state in which the electron is removed from the HOMO/next HOMO:

$$V^{\alpha}_{\text{HOMO}} = \left\langle \Psi^{+}_{\text{HOMO}} \left| \left(\frac{\partial \mathcal{H}}{\partial Q_\alpha} \right)_{\mathbf{R_0}} \right| \Psi^{+}_{\text{HOMO}} \right\rangle, \tag{2.29}$$

$$V^{\alpha}_{\text{HOMO}-1} = \left\langle \Psi^{+}_{\text{HOMO}-1} \left| \left(\frac{\partial \mathcal{H}}{\partial Q_\alpha} \right)_{\mathbf{R_0}} \right| \Psi^{+}_{\text{HOMO}-1} \right\rangle. \tag{2.30}$$

A scaling factor of 0.963[33] was used for theoretical frequencies.

Figure 2.2 shows vibrational modes with the three largest V^{α}_{HOMO}: the $a(4)$, $a(7)$, and $a(8)$ modes of Au_2DMcT; the $a(10)$, $a(19)$, and $a(20)$ modes of Au_2TTF-DT. The direction of the vibrational modes is chosen such that V^{α}_{HOMO} is negative.

First, we discuss V^{α}_{HOMO} using the vibronic coupling density analysis. For Au_2DMcT, the C=N stretching mode (the $a(8)$ mode) has quite a large VCC. The N−N stretching (the $a(7)$ mode) and S−Au stretching modes (the $a(4)$ mode) have moderately large VCCs. The C−S−C bending and N−N stretching modes (the $a(5)$ and $a(6)$ modes) have small VCCs.

For Au_2TTF-DT, the C=C stretching modes (the $a(19)$ and $a(20)$ modes) have the large VCCs, and the C−S stretching mode (the $a(10)$ mode) has the moderately large VCC. For the $a(19)$ mode, the phase of the stretching vibration of the central C=C double bond is the same as that of terminal C=C double bonds, that is, the three C=C double bonds lengthen/shorten simultaneously; for the $a(20)$ mode, the phases are opposite, that is, when the central double bond lengthens/shortens, the terminal double bonds shorten/lengthen.

Table 2.1: Vibrational modes and vibronic coupling constants (10^{-4} a.u.) for Au_2DMcT cation together with the experimental peak positions of the IET spectrum.[6]

Mode		Peak position			$V^{\alpha}_{\mathrm{HOMO}}$	$V^{\alpha}_{\mathrm{HOMO-1}}$
		Calc.		Exp.		
		cm^{-1}	mV	mV		
$a(1)$	C−S−Au bending	26.91	3		−0.02	−0.07
$a(2)$	S−Au stretching	131.17	16		−0.08	−0.17
$a(3)$	S−Au stretching	351.23	44		−0.13	−1.05
$a(4)$	S−Au stretching	361.13	45	26	−1.01	−0.52
$a(5)$	C−S−C bending	615.64	76	80	−0.77	−1.44
$a(6)$	S−C−N stretching	977.45	121		−0.12	−1.42
$a(7)$	N−N stretching	1026.19	127	128	−1.63	−0.18
$a(8)$	C=N stretching	1373.01	170	168	−5.34	−4.74

Table 2.2: Vibrational modes and vibronic coupling constants (10^{-4} a.u.) for Au_2TTF-DT cation together with the experimental peak positions of the IET spectrum.[21]

Mode		Peak position			$V^{\alpha}_{\mathrm{HOMO}}$
		Calc.		Exp.	
		cm^{-1}	mV	mV	
$a(10)$	C−S stretching	452.55	56	82	−1.09
$a(13)$	C−S stretching	609.31	76		−0.31
$a(15)$	C−S stretching	790.62	98	105	−0.37
$a(18)$	in-plane C−C−H bending	1181.96	147	142	−0.17
$a(19)$	C=C stretching	1458.59	181		−2.70
$a(20)$	C=C stretching	1521.81	189	165	−3.16

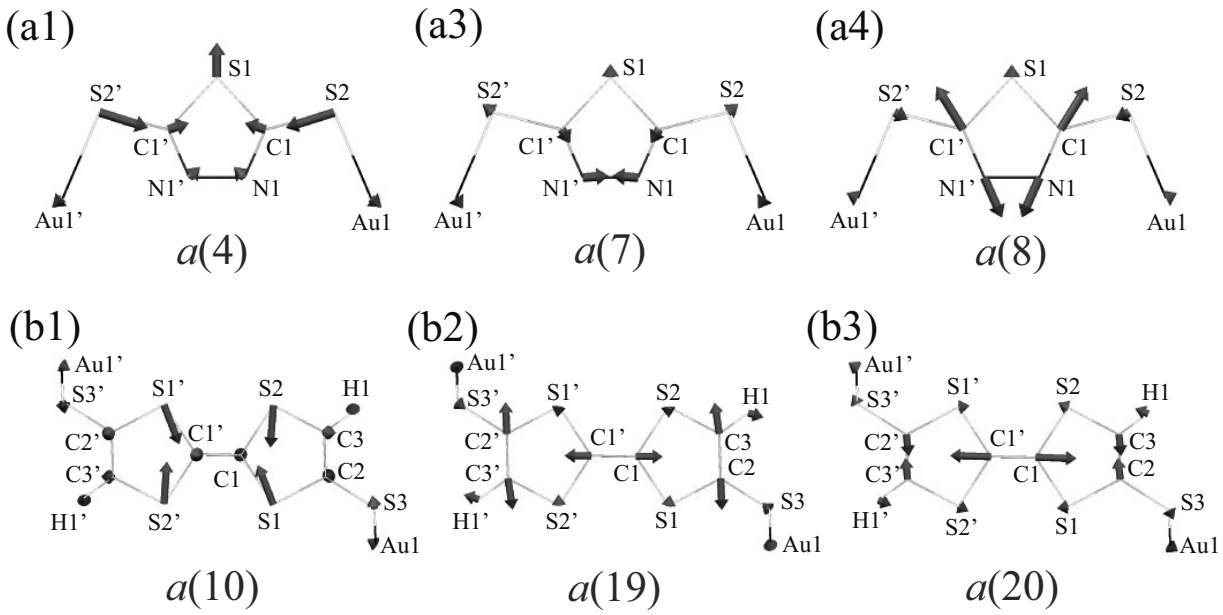

Figure 2.2: Vibrational modes with the large $V^{\alpha}_{\mathrm{HOMO}}$: (a1) $a(4)$, (a2) $a(7)$, and (a3) $a(8)$ modes of Au_2DMcT; (b1) $a(10)$, (b2) $a(19)$, and (b3) $a(20)$ modes of Au_2TTF-DT.

Figure 2.3(a) shows $\Delta\rho_{\mathrm{HOMO}}$ for Au_2DMcT. $\Delta\rho_{\mathrm{HOMO}}$ is large on the C1−N1 bond, while it is small on the S1 and Au1 atoms. $\Delta\rho_{\mathrm{HOMO}}$ has also a large value on the S2 atom bonded to the terminal Au atom. On the N1−N1$'$ bond, $\Delta\rho_{\mathrm{HOMO}}$ is large only near the N atoms, and is not distributed in the middle of the bond. Positive regions have a σ-character and originate from the occupied molecular orbitals other than the HOMO. The positive regions weaken the repulsion between negative regions.

Figure 2.3(b) shows $\Delta\rho_{\mathrm{HOMO}}$ for Au_2TTF-DT. $\Delta\rho_{\mathrm{HOMO}}$ is more spread out for Au_2TTF-DT than for Au_2DMcT, because Au_2TTF-DT is a larger π-conjugated system than is Au_2DMcT. $\Delta\rho_{\mathrm{HOMO}}$ is distributed mainly on the S1 and S2 atoms and C1−C1$'$ bond. Positive regions around the C1 and C1$'$ atoms weaken the repulsion between the negative regions above and below the C1−C1$'$ bond. $\Delta\rho_{\mathrm{HOMO}}$ is small around the C2, C3, H1, S3, and Au1 atoms.

Figure 2.4(a1–3) shows derivative of the nuclear–electronic potential v_α for the $a(4)$, $a(7)$, and $a(8)$ modes of Au_2DMcT. A head and tail of an arrow in Fig. 2.2 correspond to dark-gray and light-gray regions in Fig. 2.4. Numbers in Fig. 2.4 are AVCCs in 10^{-4} a.u.

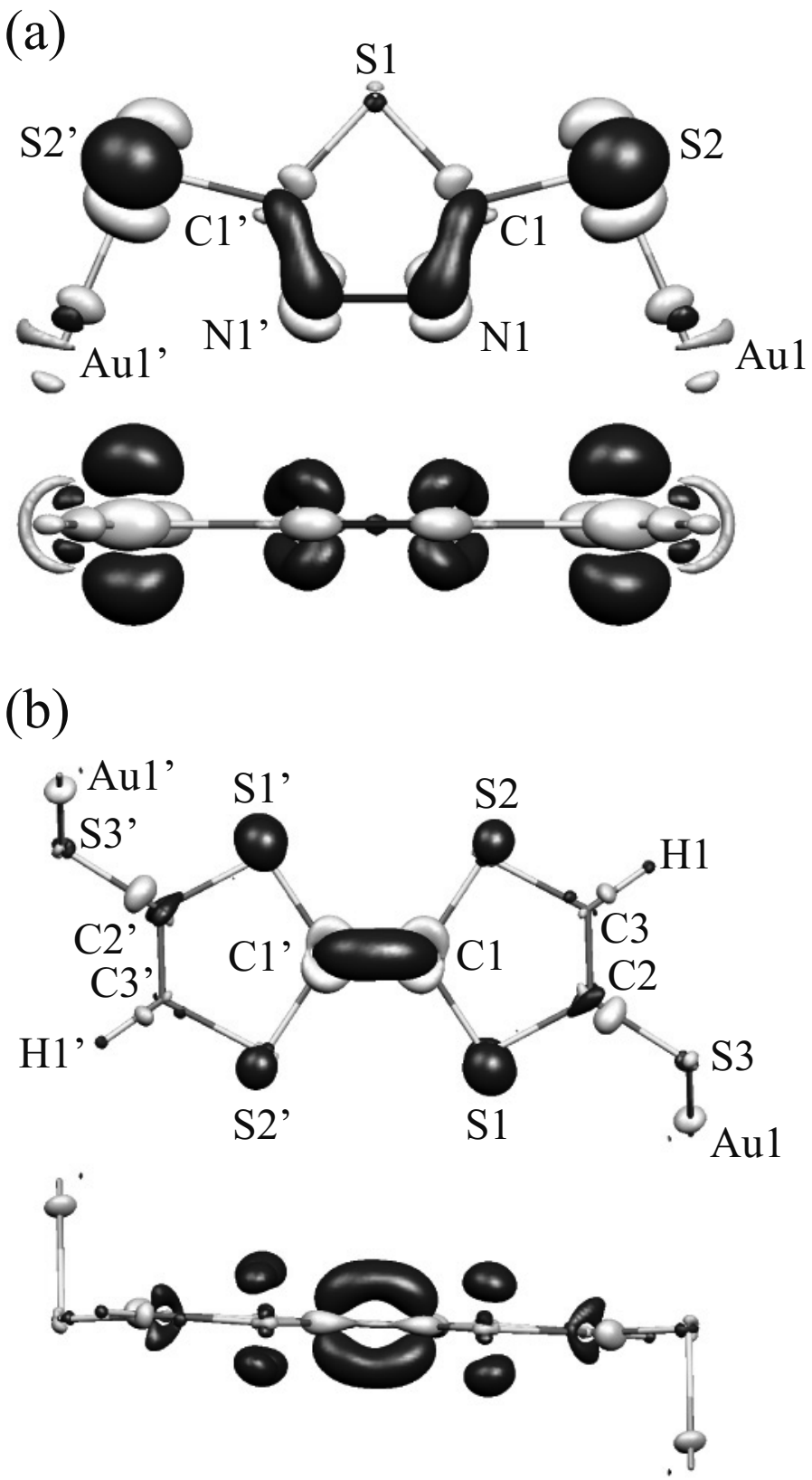

Figure 2.3: Electron-density difference $\Delta\rho_{\mathrm{HOMO}}$: (a) Au_2DMcT at an isosurface value of 0.005 a.u.; (b) Au_2TTF-DT at an isosurface value of 0.004 a.u. Dark gray shows where values are negative; light gray shows where values are positive.

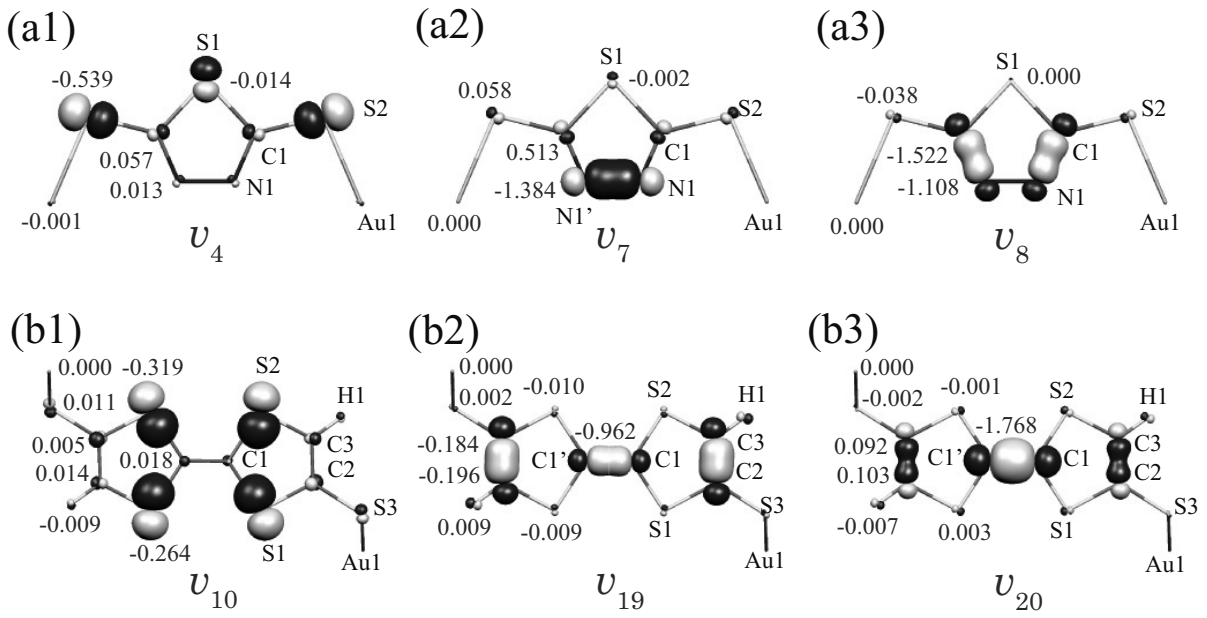

Figure 2.4: Derivative of nuclear–electronic potential v_α: (a1) $a(4)$, (a2) $a(7)$, and (a3) $a(8)$ modes of Au_2DMcT at an isosurface value of 0.02 a.u.; (b1) $a(10)$, (b2) $a(19)$, and (b3) $a(20)$ modes of Au_2TTF-DT at an isosurface value of 0.01 a.u. Dark gray shows where values are negative; light gray shows where values are positive. Numbers are atomic vibronic coupling constants $V^{\alpha}_{\mathrm{HOMO},A}$ (10^{-4} a.u.).

The $a(8)$ mode is the C=N stretching mode and v_8 is large on the C1−N1 bond (Fig. 2.4(a3)). Since $\Delta\rho_{\mathrm{HOMO}}$ is also large on the C1−N1 bond (Fig. 2.3(a)), v_8 and $\Delta\rho_{\mathrm{HOMO}}$ overlap significantly on the bond. Hence, η_8 has a large value on the C=N double bonds, and the C and N atoms have large AVCCs (-1.522 and -1.108×10^{-4} a.u., respectively).

The $a(7)$ mode is the N−N stretching mode and v_7 is largely distributed on the N1−N1′ bond (Fig. 2.4(a2)). However, since $\Delta\rho_{\mathrm{HOMO}}$ is small in the middle of the N1−N1′ bond, the region in which η_7 is large is localized around the N atoms. Hence, only the N atoms have large AVCCs (-1.384×10^{-4} a.u.), and V^{7}_{HOMO} is smaller than V^{8}_{HOMO}.

The $a(4)$ mode is the S−Au stretching mode, and v_4 is large around the S2 atom (Fig. 2.4(a1)). v_4 and $\Delta\rho_{\mathrm{HOMO}}$ overlap on the S2 atom, however, since the extent of the overlap is small, the AVCC of the S2 atom (-0.539×10^{-4} a.u.) is smaller than that of the N1 atom for the $a(7)$ mode (-1.384×10^{-4} a.u.). Hence, V^{4}_{HOMO} is smaller than V^{7}_{HOMO}. Thus, we can understand the reason for the relative order of the VCCs by analyzing the VCD distributions.

Figure 2.4(b1–3) shows v_α for the $a(10)$, $a(19)$, and $a(20)$ modes of Au_2TTF-DT. The $a(19)$ and $a(20)$ modes are C=C stretching modes, and hence, v_{19} and v_{20} are large on the C=C double bonds. Since v_{19} and v_{20} overlap significantly with $\Delta\rho_{\mathrm{HOMO}}$ on the C1−C1$'$ bond, η_{19} and η_{20} are large on the bond, which leads to the large AVCCs of the C1 and C1$'$ atoms: -0.962×10^{-4} a.u. for the $a(19)$ mode; -1.768×10^{-4} a.u. for the $a(20)$ mode.

The $a(10)$ mode includes C1−S1 and C1−S2 stretching vibrations and v_{10} is large around the S1 and S2 atoms. v_{10} and $\Delta\rho_{\mathrm{HOMO}}$ are distributed around the S1 and S2 atoms. However, the overlap between them is small compared with those for the $a(19)$ and $a(20)$ modes. Hence, the AVCCs of S1 and S2 atoms for the $a(10)$ mode are smaller than that of the C1 atom for the $a(19)$ and $a(20)$ modes. This is the reason why V^{10}_{HOMO} ($=-1.09\times10^{-4}$ a.u.) is smaller than those of V^{19}_{HOMO} ($=-2.70\times10^{-4}$ a.u.) and V^{20}_{HOMO} ($=-3.16\times10^{-4}$ a.u.).

For the $a(19)$ and $a(20)$ modes, the AVCCs of the atoms other than the carbon atoms are quite small. The sums of the AVCCs of the carbon atoms for the $a(19)$ and $a(20)$ modes are -2.684×10^{-4} and -3.146×10^{-4} a.u., respectively, which correspond to 99.4% of V^{19}_{HOMO} and 99.6% of V^{20}_{HOMO}, suggesting that vibronic coupling occurs mainly on the carbon atoms. V^{20}_{HOMO} is larger than V^{19}_{HOMO}, because for the $a(20)$ mode, the AVCC of the C1 atom is much larger than that for the $a(19)$ mode, which originates from the fact that v^{20}_{HOMO} is larger than v^{19}_{HOMO} on the C1−C1$'$ bond.

Second, we discuss the relative $V^{\alpha}_{\mathrm{HOMO}-1}$ ordering for Au_2DMcT. The $a(8)$ mode has quite a large $V^{\alpha}_{\mathrm{HOMO}-1}$ and the $a(3)$, $a(5)$, and $a(6)$ modes have moderately large $V^{\alpha}_{\mathrm{HOMO}-1}$ values (Table 2.1). The difference between the order of $V^{\alpha}_{\mathrm{HOMO}-1}$ and $V^{\alpha}_{\mathrm{HOMO}}$ reflects the difference between the distribution pattern of $\Delta\rho_{\mathrm{HOMO}-1}$ and $\Delta\rho_{\mathrm{HOMO}}$.

Figure 2.5(a) shows $\Delta\rho_{\mathrm{HOMO}-1}$ for Au_2DMcT. In contrast to $\Delta\rho_{\mathrm{HOMO}}$ (Fig. 2.3(a)), $\Delta\rho_{\mathrm{HOMO}-1}$ is largely distributed on the S1 and Au1 atoms and is not largely distributed on the middle of the C1−N1 bond. Moreover, $\Delta\rho_{\mathrm{HOMO}-1}$ is larger on the C1 atom than on the N1 atom. Hence, vibronic coupling in the sate $\left|\Psi^{+}_{\mathrm{HOMO}-1}\right\rangle$ is strong around the S1, C1, and Au1 atoms compared with that in the sate $\left|\Psi^{+}_{\mathrm{HOMO}}\right\rangle$.

Figure 2.5(b–d) shows v_3 (S−Au stretching), v_5 (C−S−C bending), and v_6 (S−C−N bending) for Au_2DMcT. v_3 overlaps with $\Delta\rho_{\mathrm{HOMO}-1}$ on the S1 and S2 atoms, which leads to the large AVCCs of the S1 and S2 atoms; v_5 overlaps with $\Delta\rho_{\mathrm{HOMO}-1}$ on the S1 and N1 atoms, which leads to the large AVCCs of the S1 and N1 atoms; v_6 overlaps with

$\Delta\rho_{\mathrm{HOMO}-1}$ on the C1 atom, which leads to the large AVCC of the C1 atom. The large $V^{\alpha}_{\mathrm{HOMO}-1}$ of the $a(8)$ mode is due to the significant overlap between $\Delta\rho_{\mathrm{HOMO}-1}$ and v_8 on the C1 and N1 atoms.

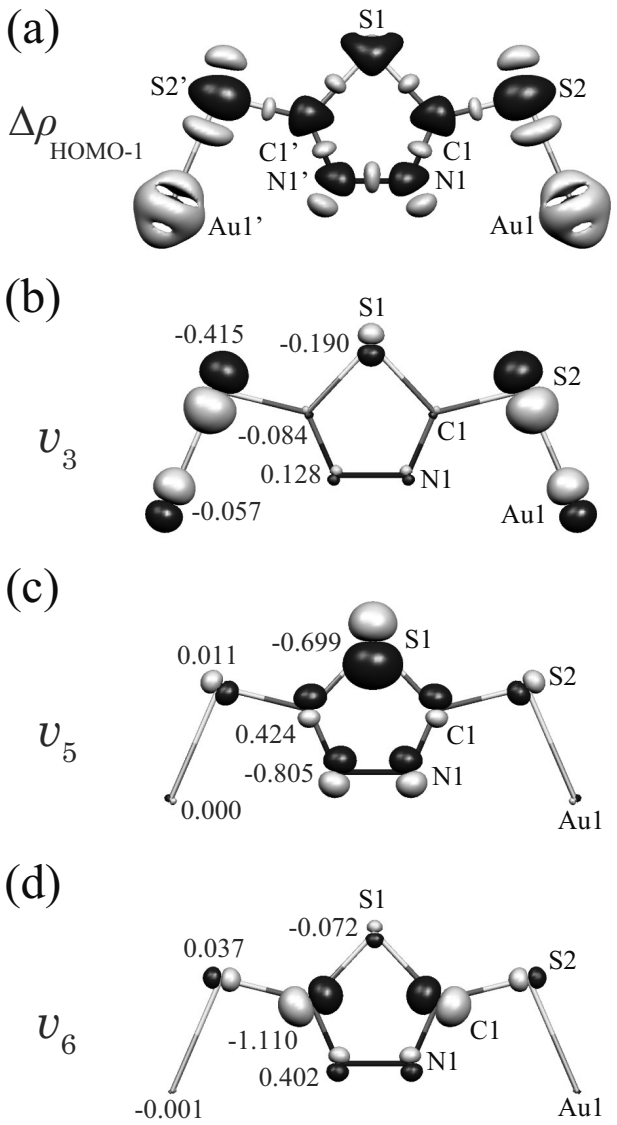

Figure 2.5: (a) Electron-density difference $\Delta\rho_{\mathrm{HOMO}-1}$ for Au_2DMcT at an isosurface value of 0.01 a.u.; (b) v_3, (c) v_5, and (d) v_6 of Au_2DMcT at an isosurface value of 0.02 a.u. Dark gray shows where values are negative; light gray shows where values are positive. Numbers in (b–d) are atomic vibronic coupling constants $V^{\alpha}_{\mathrm{HOMO}-1,A}$ (10^{-4} a.u.).

2.4.2 Inelastic electron tunneling spectra

The energy levels of HOMO of Au_2DMcT and Au_2TTF-DT are -6.08 and -5.16 eV, respectively, and the HOMO is the closest to the Fermi level of the electrode (-5.53 eV). An energy gap between the Fermi level of the electrode and the HOMO is small for the Au/TTF-DT/Au junction, suggesting that a carrier transport occurs more efficiently through the Au/TTF-DT/Au junction than through the Au/DMcT/Au junction.

For the Au/DMcT/Au junction, $\tau_{\mathrm{L/R}}$ was scaled to produce the experimental conductance[6] ($0.008G_0$ at $V_{\mathrm{b}} = 0.2$ V) and for the Au/TTF-DT/Au and Au/Th-DT/Au junctions, the same $\tau_{\mathrm{L/R}}$ value was used. We calculate the IET spectra for the Au/DMcT/Au junction assuming that an electron tunneling occurs through the HOMO and next HOMO. The two molecular orbitals belong to different irreducible representations: the HOMO and next HOMO are the a_2 and b_1 orbitals, respectively. Therefore the off-diagonal VCCs vanish:

$$\left\langle \Psi^+_{\mathrm{HOMO}} \left| \left(\frac{\partial \mathcal{H}}{\partial Q_\alpha} \right)_{\mathbf{R_0}} \right| \Psi^+_{\mathrm{HOMO}-1} \right\rangle = \left\langle \Psi^+_{\mathrm{HOMO}-1} \left| \left(\frac{\partial \mathcal{H}}{\partial Q_\alpha} \right)_{\mathbf{R_0}} \right| \Psi^+_{\mathrm{HOMO}} \right\rangle = 0 \qquad (2.31)$$

Hence, λ^α is a diagonal matrix.

Figure 2.6(a) shows calculated IET spectra for the Au/DMcT/Au junction at $T = 4.2$, 10, and 20 K. At $T = 4.2$ K, the $a(4)$, $a(5)$, $a(7)$, and $a(8)$ modes show peaks. At $T = 10$ and 20 K, the peak due to the $a(5)$ mode is not seen clearly because of the thermal broadening of the peak, that is, the broadening of the Fermi distribution function $f_{\mathrm{L/R}}$.

Calculated full-width at half-maximum (FWHM) of the peak of the N$-$N stretching mode (the $a(7)$ mode) is 8, 11, and 23 mV, respectively, at $T = 4.2$, 10, and 20 K. These values are small compared with the experimental data (25, 30, 38 mV, respectively).[6] In our calculation, only the thermal broadening influences the peak widths. The difference between the theoretical and experimental peak widths may originate primarily from instrumental broadening.

Figure 2.6(b) shows comparison of the calculated and experimental IET spectra for the Au/DMcT/Au junction at $T = 4.2$ K. The experimental d^2I/dV_{b}^2 values are scaled to fit the calculated spectrum at $V_{\mathrm{b}} = 127$ mV (the peak position of the N$-$N stretching mode). Peaks corresponding to the $a(4)$, $a(5)$, $a(7)$, and $a(8)$ modes were observed experimentally.[6] In the experimental spectrum, d^2I/dV_{b}^2 has a large value near the zero-bias region, which is called the zero-bias anomaly.[5] The zero-bias anomaly may originate from

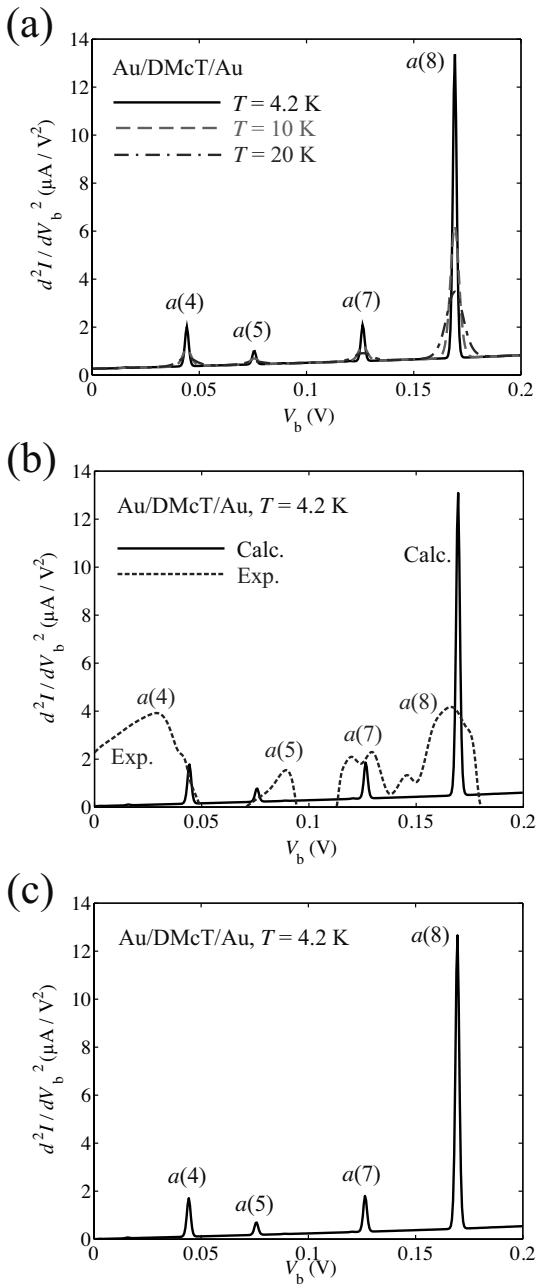

Figure 2.6: (a) Calculated inelastic electron tunneling spectra for Au/DMcT/Au junction at various temperatures. Solid line shows the spectrum at $T = 4.2$ K; dashed line shows the spectrum at $T = 10$ K; dot-dashed line shows the spectrum at $T = 20$ K. (b) Comparison of calculated and experimental inelastic electron tunneling spectra for Au/DMcT/Au junction at $T = 4.2$ K. Solid line shows the calculated spectrum; dotted line shows the experimental spectrum.[6] (c) Calculated inelastic electron tunneling spectra for Au/DMcT/Au junction at $T = 4.2$ K assuming that the electron tunneling occurs through only the HOMO.

phonon scattering in the electrodes. For $V_b > 0.05$ V, the order of the relative intensity of the spectra agrees well. The relative intensity increases in the order: $a(5) < a(7) < a(8)$. By comparing the spectra, the intensity for the $a(5)$ mode (C1−S2 stretching) is underestimated, while that for the $a(8)$ mode (C1−N1 stretching) is overestimated.

Figure 2.6(c) shows the calculated IET spectrum for the Au/DMcT/Au junction at $T = 4.2$ K assuming that the electron tunneling occurs through only the HOMO. Comparing Fig. 2.6(c) with Fig. 2.6(b), the two calculated IET spectra are almost identical. This is because the difference between the orbital energy of the next HOMO (−7.07eV) and the Fermi energy of the electrode (−5.53 eV) is large and the vibronic couplings in the state $\left|\Psi^{+}_{\mathrm{HOMO}-1}\right\rangle$ make little contribution to the IET spectrum. This result suggests that an inelastic electron tunneling occurs mainly through the HOMO. For the Au/TTF-DT/Au and Au/Th-DT/Au junctions, we consider the inelastic electron tunneling via only the HOMO.

Figure 2.7 shows calculated IET spectrum for the Au/TTF-DT/Au junction at 4.2 K. The $a(10)$, $a(19)$, and $a(20)$ modes show strong peaks. Peaks due to the $a(10)$, $a(15)$, and $a(20)$ modes were observed experimentally for Au/TTF/Au junction.[21] Although the $a(19)$ mode has the large VCC, since the peak position of the mode is close to that of the $a(20)$ mode, the peak of the $a(19)$ mode would be superimposed with the peak of the $a(20)$ mode and would not be observed in the experimental IET spectrum.

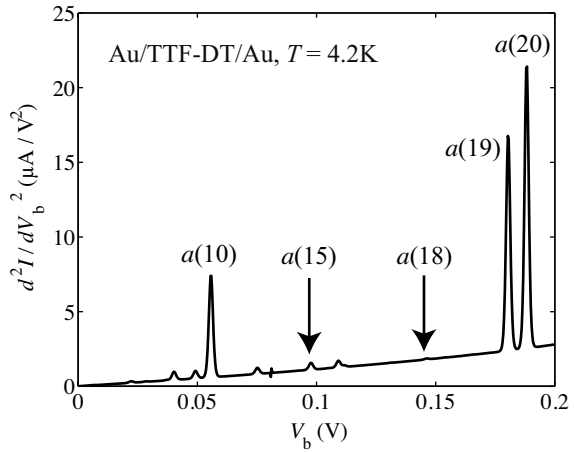

Figure 2.7: Calculated inelastic electron tunneling spectrum for Au/TTF-DT/Au junction at $T = 4.2$ K.

2.4.3 Comparison of IET spectra for the Au/Th-DT/Au and Au/DMcT/Au junctions

Molecular structure of Th-DT is similar to that of DMcT (nitrogen atoms in DMcT are replaced by −CH− groups in thiophene). Although there is no experimental assignment of IET spectra for Au/Th-DT/Au junction, it is meaningful to compare the spectra for the Au/Th-DT/Au junction with that for the Au/DMcT/Au junction.

Figure 2.8 shows calculated IET spectra for Au/Th-DT/Au junction at $T = 4.2$ K. The major difference between the IET spectra for the Au/Th-DT/Au and Au/DMcT/Au junctions is the presence of the peak due to the $a(13)$ mode (169 mV, Fig. 2.9(a)). The $a(13)$ mode contains C2−C2′ stretching and C1−C2−H1 in-plane bending vibrations. For the Au/Th-DT/Au junction, two peaks are observed around 160 mV. In contrast, for the Au/DMcT/Au junction, only one peak is observed. Hence, thiophene and DMcT can be distinguished by the peak of the $a(13)$ mode.

The $a(13)$ mode contains displacements of the C1, C2 and H1 atoms, and v_{13} is large on the C2−C2′ bond and around the C1 and H1 atoms (Fig. 2.9(b)). $\Delta\rho_{\mathrm{HOMO}}$ is also large around the C1 and C2 atoms (Fig. 2.9(c)). Hence, $\Delta\rho_{\mathrm{HOMO}}$ overlaps significantly with v_{13} on the C1 and C2 atoms. This is why the $a(13)$ mode has a large VCC and shows the strong peak in the IET spectrum.

The IET spectrum for Au/Th-DT/Au junction is similar to that for Au/DMcT/Au junction (Fig. 2.6(a)). This similarity originates from the similarity in the molecular structures and $\Delta\rho_{\mathrm{HOMO}}$ distributions. Since $\Delta\rho_{\mathrm{HOMO}}$ for Au_2Th-DT is distributed on the C1, C2, and S2 atoms, vibrational modes in which these atoms are displaced show intense peaks; S−Au stretching mode (the $a(5)$ mode, 44 mV), C−C stretching mode (the $a(11)$ mode, 133 mV), and C=C stretching mode (the $\mathbf{a}(\mathbf{12})$ mode, 155 mV).

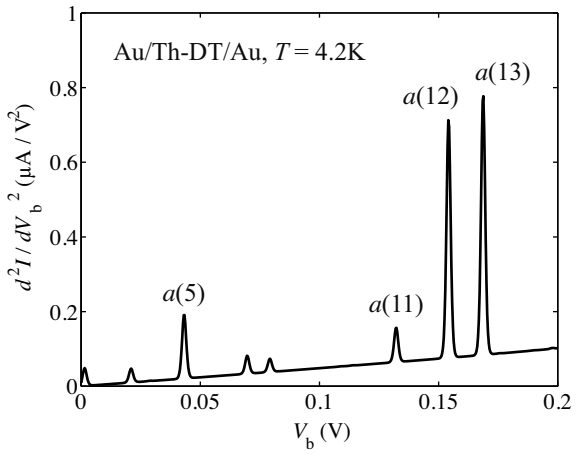

Figure 2.8: Calculated inelastic electron tunneling spectrum for Au/Th-DT/Au junction at $T = 4.2$ K.

2.5 Conclusions

We calculated the VCDs for Au_2DMcT and Au_2TTF-DT cations. The VCD analysis enables us to understand the relative order of the VCCs. For Au_2DMcT, since $\Delta\rho_{\mathrm{HOMO}}$ is large on the C−N bond, the C−N stretching mode couples strongly to the electronic state; for Au_2TTF-DT, since $\Delta\rho_{\mathrm{HOMO}}$ is large on the central C=C bond, the C=C stretching modes couple strongly to the electronic state.

We calculated the IET spectra for Au/DMcT/Au and Au/TTF-DT/Au junctions using the NEGF theory. We calculated the IET spectrum for the Au/Th-DT/Au junction and compared it with that for the Au/DMcT/Au junction. Th-DT and DMcT can be distinguished using the IET spectroscopy by the peak of the C−C stretching mode. The VCD analysis can be an effective way to understand relative intensities in IET spectra.

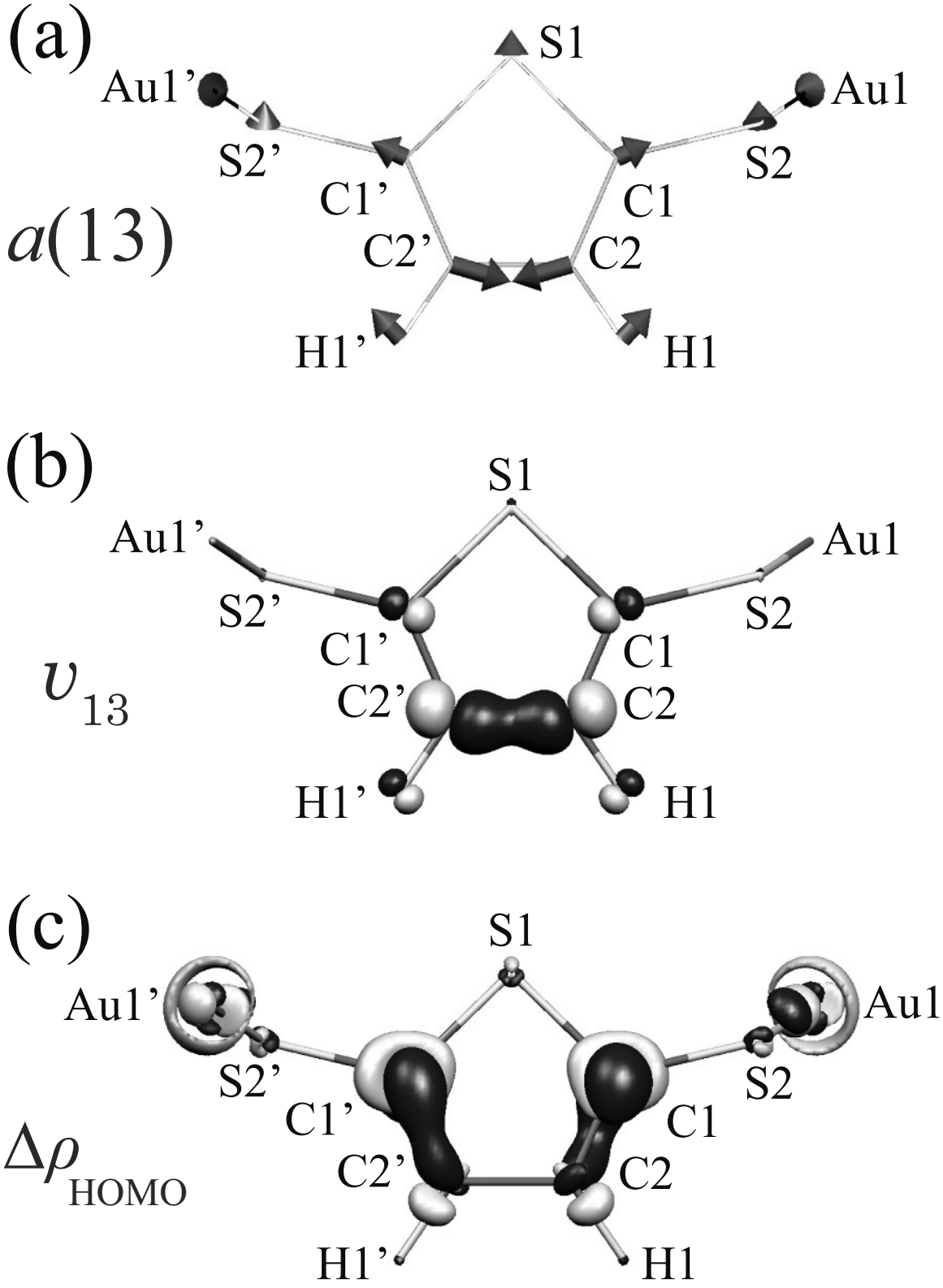

Figure 2.9: (a) The $a(13)$ mode of Au_2Th-DT; (b) derivative of nuclear–electronic potential v_{13} (= 0.02 a.u.); (c) electron-density difference $\Delta\rho_{\mathrm{HOMO}}$ (= 0.005 a.u.) of Au_2Th-DT. Dark gray shows where values are negative; light gray shows where values are positive.

Bibliography

[1] S. Gregory, Phys. Rev. Lett. **64**, 689 (1990).

[2] W. Ho, J. Chem. Phys. **117**, 11033 (2002).

[3] W. Wang, T. Lee, I. Kretzschmar, and M. A. Reed, Nano Lett. **4**, 643 (2004).

[4] J. G. Kushmerick, J. Lazorcik, C. H. Patterson, R. Shashidhar, D. S. Seferos, and G. C. Bazan, Nano Lett. **4**, 639 (2004).

[5] J. M. Beebe, H. J. Moore, T. R. Lee, and J. G. Kushmerick, Nano Lett. **7**, 1364 (2007).

[6] M. Tsutsui, M. Taniguchi, K. Shoji, K. Yokota, and T. Kawai, Nanoscale **1**, 164 (2009).

[7] M. Galperin, M. A. Ratner, and A. Nitzan, J. Phys.: Condensed Matter **19**, 103201 (2007).

[8] N. Okabayashi, Y. Konda, and T. Komeda, Phys. Rev. Lett. **100**, 217801 (2008).

[9] N. Okabayashi, M. Paulsson, H. Ueba, Y. Konda, and T. Komeda, Phys. Rev. Lett. **104**, 077801 (2010).

[10] A. Troisi and M. A. Ratner, Nano Lett. **6**, 1784 (2006).

[11] T. Sato, K. Tokunaga, and K. Tanaka, J. Chem. Phys. **124**, 024314 (2006).

[12] K. Tokunaga, T. Sato, and K. Tanaka, J. Chem. Phys. **124**, 154303 (2006).

[13] K. Tokunaga, T. Sato, and K. Tanaka, J. Mol. Struct. **838**, 116 (2007).

[14] T. Sato, K. Tokunaga, N. Iwahara, K. Shizu, and K. Tanaka, *Vibronic coupling constant and vibronic coupling density* in *The Jahn-Teller-Effect - Fundamentals and Implications for Physics and Chemistry,* H. Köppel, D. R. Yarkony, and H. Barentzen (Eds) (Springer-Verlag, Berlin and Heidelberg, 2009).

[15] T. Sato, K. Tokunaga, and K. Tanaka, J. Phys. Chem. A **112**, 758 (2008).

[16] T. Sato, K. Shizu, T. Kuga, K. Tanaka, and H. Kaji, Chem. Phys. Lett. **458**, 152 (2008).

[17] K. Shizu, T. Sato, K. Tanaka, and H. Kaji, Chem. Phys. Lett. **486**, 130 (2010).

[18] K. Shizu, T. Sato, and K. Tanaka, Chem. Phys. **369**, 108 (2010).

[19] K. Shizu, T. Sato, K. Tanaka, and H. Kaji, Org. Electron. **11**, 1277 (2010).

[20] S. Datta, *Quantum Transport: Atom to Transistor* (Cambridge University Press, Cambridge, 2005).

[21] K. Shoji, K. Morimoto, M. Tsutsui, M. Taniguchi, H. Fujiwara, T. Sugimoto, and T. Kawai, proceedings of the 2nd Annual Meeting of Japan Society for Molecular Science, Fukuoka, 2008 (unpublished).

[22] J. Yamada and T. Sugimoto, *TTF Chemistry-Fundamental and Applications of Tetrathiafulvalene* (Springer, Berlin, Germany, 2004).

[23] T. Ishiguro, K. Yamaji, and G. Saito, *Organic Superconductors* (Second edition) (Springer-Verlag, Berlin, 1997).

[24] H. Wang, K. Carlson, U. Geiser, A. Kini, A. Schultz, J. Williams, L. Montgomery, W. Kwok, U. Welp, K. Vandervoort, S. Boryschuk, A. Crouch, J. Kommers, D. Watkins, J. Schriber, D. Overmyer, D. Jung, J. Novoa, and M.-H. Whangbo, Synth. Met. **42**, 1983 (1991).

[25] N. Oyama, T. Tatsuma, T. Sato, and T. Sotomura, Nature **373**, 598 (1995).

[26] F. Giacalone, M. Á. Herranz, L. Grüter, M. T. González, M. Calame, C. Schönenberger, C. R. Arroyo, G. Rubio-Bollinger, M. Vélez, N. Agraït, and N. Martín, Chem. Commun. 4854 (2007).

[27] M. Taniguchi, M. Tsutsui, K. Shoji, H. Fujiwara, and T. Kawai, J. Am. Chem. Soc. **131**, 14146 (2009).

[28] I. S. Kristensen, M. Paulsson, K. S. Thygesen, and K. W. Jacobsen, Phys. Rev. B **79**, 235411 (2009).

[29] M. J. Frisch, G. W. Trucks, H. B. Schlegel, G. E. Scuseria, M. A. Robb, J. R. Cheeseman, J. A. Montgomery, Jr., T. Vreven, K. N. Kudin, J. C. Burant, J. M. Millam, S. S. Iyengar, J. Tomasi, V. Barone, B. Mennucci, M. Cossi, G. Scalmani, N. Rega, G. A. Petersson, H. Nakatsuji, M. Hada, M. Ehara, K. Toyota, R. Fukuda, J. Hasegawa, M. Ishida, T. Nakajima, Y. Honda, O. Kitao, H. Nakai, M. Klene, X. Li, J. E. Knox, H. P. Hratchian, J. B. Cross, V. Bakken, C. Adamo, J. Jaramillo, R. Gomperts, R. E. Stratmann, O. Yazyev, A. J. Austin, R. Cammi, C. Pomelli, J. W. Ochterski, P. Y. Ayala, K. Morokuma, G. A. Voth, P. Salvador, J. J. Dannenberg, V. G. Zakrzewski, S. Dapprich, A. D. Daniels, M. C. Strain, O. Farkas, D. K. Malick, A. D. Rabuck, K. Raghavachari, J. B. Foresman, J. V. Ortiz, Q. Cui, A. G. Baboul, S. Clifford, J. Cioslowski, B. B. Stefanov, G. Liu, A. Liashenko, P. Piskorz, I. Komaromi, R. L. Martin, D. J. Fox, T. Keith, M. A. Al-Laham, C. Y. Peng, A. Nanayakkara, M. Challacombe, P. M. W. Gill, B. Johnson, W. Chen, M. W. Wong, C. Gonzalez, and J. A. Pople, GAUSSIAN 03, Revision D.02, Gaussian, Inc., Wallingford, CT, 2004.

[30] N. W. Ashcroft and N. B. Mermin, *Solid State Physics* (Thomson Learning, New York, 1976).

[31] S. Öztürk, M. Akkurt, A. Cansız, M. Koparır, M. Şekerci, and F. W. Heinemann, Acta Crystallogr. **E60**, o820 (2004).

[32] W. F. Cooper, N. C. Kenny, J. W. Edmonds, A. Nagel, F. Wudl, and P. Coppens, J. Chem. Soc. D 889 (1971).

[33] J. A. Pople, M. Head-Gordon, D. J. Fox, K. Raghavachari, and L. A. Curtiss, J. Chem. Phys. **90**, 5622 (1989).

Part III

Miscellaneous Applications of Vibronic Coupling Density Analysis

Chapter 1

Reduced Vibronic Coupling Density and Its Application to Bis(ethylenedithio)tetrathiafulvalene (BEDT-TTF)

1.1 Introduction

Vibronic (electron-vibration) coupling plays an important role in electronic properties such as superconductivity, transport property, and so on. The vibronic coupling is governed by the magnitude of vibronic coupling constant (VCC). Thus, a clear understanding of the origin of the magnitude of the VCC is necessary for designing new materials. Sato *et al.* introduced a quantity called the vibronic coupling density (VCD)[1–4] to explain the origin of the VCC magnitude. Because an integral over space of the VCD gives the VCC, the VCD distribution provides a local picture of vibronic coupling in a molecule. Using VCD analysis, vibronic coupling in cyclopentadienyl radical,[1] benzene ions,[2] deuterated cyclopentadienyl radical and benzene cation,[3] naphthalene anion,[5] and N, N'-bis(3-methylphenyl)-N, N'-diphenyl-[1,1′-biphenyl]-4,4′-diamine (TPD) cation[6] have been investigated. Molecules with small VCCs or electron-phonon coupling constants are favorable for charge-transporting materials. The VCD analysis reveals that strong localization of VCDs on N atoms is responsible for the small VCCs of the TPD cation.[6] Weak vibronic coupling is an origin of the high hole mobility of TPD. We can design new functional

molecules through controlling VCD distributions and VCC magnitudes.

The VCD analysis has succeeded in explaining the relative strength of the VCC, but sometimes causes a misunderstanding of the local picture of the vibronic coupling. This is because the VCD contains components of which the integral over space vanishes. Those vanishing components are not essential to vibronic coupling and should be eliminated.

In this chapter, we introduce a new quantity called reduced VCD (RVCD) to eliminate the non-essential contributions in the VCD. The RVCD is obtained by subtracting terms of which the integration over space vanishes from the VCD. We also introduce reduced atomic vibronic coupling density (RAVCD) to describe the contribution of each atom to the RVCD. The RAVCD gives a local picture of the vibronic coupling near the corresponding atom more clearly than the AVCD.

To illustrate the technique, we calculate the RAVCDs for a C=C stretching mode of bis(ethylenedithio)tetrathiafulvalene (BEDT-TTF) cation, which is widely known as a donor for organic superconductors.[7,8] Various types of TTF derivatives have been synthesized, and their conducting properties have been investigated.[9,10] Since intramolecular vibronic coupling plays an important role in mechanisms of the superconductivity, there has been significant interest in determining the VCCs for TTF derivatives,[11–14] but little attention has been given to the physical reason behind the magnitudes of the VCCs. We report our analysis based on the spatial distribution of RAVCDs that allows us to easily understand the local picture of vibronic coupling and the physical origin of the magnitude of the VCC.

1.2 Theory

1.2.1 Coupling Constants and Coupling Densities

The molecular Hamiltonian is given by

$$\mathcal{H}(\mathbf{r},\mathbf{R}) = \mathcal{H}_{\mathrm{e}}(\mathbf{r},\mathbf{R}) + \mathcal{T}_{\mathrm{n}}(\mathbf{R}), \tag{1.1}$$

where $\mathcal{H}_{\mathrm{e}}(\mathbf{r},\mathbf{R})$ is an electronic Hamiltonian, $\mathcal{T}_{\mathrm{n}}(\mathbf{R})$ is the nuclear kinetic energy, and $\mathbf{r}$ and $\mathbf{R}$ are sets of electronic and nuclear coordinates, respectively. The electronic Hamiltonian $\mathcal{H}_{\mathrm{e}}(\mathbf{r},\mathbf{R})$ is the sum of the electronic kinetic energy, the electronic-electronic, the electronic–nuclear, and the nuclear–nuclear operators. Employing the Herzberg–Teller

expansion, $\mathcal{H}_{\mathrm{e}}(\mathbf{r},\mathbf{R})$ is expressed as

$$\mathcal{H}_{\mathrm{e}}(\mathbf{r},\mathbf{R}) = \mathcal{H}_{\mathrm{e}}(\mathbf{r},\mathbf{R_0}) + \sum_i \left(\frac{\partial \mathcal{H}_{\mathrm{e}}(\mathbf{r},\mathbf{R})}{\partial Q_i}\right)_{\mathbf{R_0}} Q_i + \cdots, \tag{1.2}$$

where $\{Q_i\}$ is a set of mass-weighted normal coordinates for the i^{th} vibrational mode and $\mathbf{R_0}$ is the nuclear configuration of the equilibrium geometry for an N electron state. The VCC for $N \pm 1$ electron systems for the i^{th} vibrational mode V_i is defined by

$$V_i = \left\langle \Psi_{N\pm1}(\mathbf{r},\mathbf{R_0}) \left| \left(\frac{\partial \mathcal{H}_{\mathrm{e}}(\mathbf{r},\mathbf{R})}{\partial Q_i}\right)_{\mathbf{R_0}} \right| \Psi_{N\pm1}(\mathbf{r},\mathbf{R_0}) \right\rangle, \tag{1.3}$$

where $\Psi_{N\pm1}(\mathbf{r},\mathbf{R_0})$ is the electronic wave function of the $N \pm 1$ electron systems at the equilibrium geometry of the N electron system. The corresponding electron–phonon coupling constant g_i is given by

$$g_i = \sqrt{\frac{\hbar}{2\omega_i}} V_i, \tag{1.4}$$

where ω_i is the frequency of the i^{th} mode.

$\partial/\partial Q_i$ can be written as

$$\frac{\partial}{\partial Q_i} = \sum_A \frac{\mathbf{e}_A^{(i)}}{\sqrt{M_A}} \cdot \frac{\partial}{\partial \mathbf{R}}, \tag{1.5}$$

where M_A is the mass of nucleus A, and $\mathbf{e}_A^{(i)}$ is the A^{th} component of a vibrational vector of the i^{th} vibrational mode in the mass-weighted coordinates Q_i. $\mathbf{e}_A^{(i)}$ is a 3D vector and represents the relative displacement of nucleus A for the i^{th} mode. The three components of $\mathbf{e}_A^{(i)}$ represent displacements of nucleus A along the x, y, and z axes, and are denoted as

$$\mathbf{e}_A^{(i)} = \left(e_{A,1}^{(i)}, e_{A,2}^{(i)}, e_{A,3}^{(i)}\right). \tag{1.6}$$

The $\mathbf{e}^{(i)}$ direction is chosen such that V_i is negative.

Substituting Eq. 1.5 into Eq. 1.3, we obtain

$$\begin{aligned} V_i &= \sum_A \frac{1}{\sqrt{M_A}} \mathbf{e}_A^{(i)} \cdot \left\langle \Psi_{N\pm1}(\mathbf{r},\mathbf{R_0}) \left| \left(\frac{\partial \mathcal{H}_{\mathrm{e}}(\mathbf{r},\mathbf{R})}{\partial \mathbf{R}}\right)_{\mathbf{R_0}} \right| \Psi_{N\pm1}(\mathbf{r},\mathbf{R_0}) \right\rangle \\ &= \sum_A V_{i,A}, \end{aligned} \tag{1.7}$$

where $V_{i,A}$ is the atomic vibronic coupling constant (AVCC) for atom A, and represents the contribution to the VCC V_i from atom A.

If the Hellmann–Feynman theorem[15] is satisfied, V_i can be written in terms of the electron-density difference $\Delta\rho$ and the derivative of the nuclear–electronic potential v_i:[1–4]

$$V_i = \int \Delta\rho\left(\mathbf{x}\right) \times v_i\left(\mathbf{x}\right) d\mathbf{x}, \tag{1.8}$$

where

$$\Delta\rho\left(\mathbf{x}\right) = \rho_{N\pm1}\left(\mathbf{x}\right) - \rho_N\left(\mathbf{x}\right), \tag{1.9}$$

$$v_i\left(\mathbf{x}\right) = -\sum_A \frac{Z_A}{\sqrt{M_A}} \mathbf{e}_A^{(i)} \cdot \frac{\mathbf{x} - \mathbf{R}_A}{\left|\mathbf{x} - \mathbf{R}_A\right|^3}, \tag{1.10}$$

and $\rho_{N\pm1}\left(\mathbf{x}\right)$ and $\rho_N\left(\mathbf{x}\right)$ represent the electron densities for the $N \pm 1$ and N electron systems, respectively. $\mathbf{x}$ denotes a position of electron in three-dimensional space, and Z_A is the atomic number of nucleus A. The product $\Delta\rho\left(\mathbf{x}\right) \times v_i\left(\mathbf{x}\right)$ is called the VCD[1–4] and is expressed as

$$\eta_i\left(\mathbf{x}\right) = \Delta\rho\left(\mathbf{x}\right) \times v_i\left(\mathbf{x}\right). \tag{1.11}$$

The VCD provides a local picture of vibronic coupling in a molecule.

The contribution from atom A to $\eta_i\left(\mathbf{x}\right)$ is described by the atomic vibronic coupling density (AVCD) $\eta_{i,A}\left(\mathbf{x}\right)$, which is given by

$$\begin{aligned} \eta_{i,A}\left(\mathbf{x}\right) &= \Delta\rho\left(\mathbf{x}\right) \times \left(-\frac{Z_A}{\sqrt{M_A}} \mathbf{e}_A^{(i)} \cdot \frac{\mathbf{x} - \mathbf{R}_A}{\left|\mathbf{x} - \mathbf{R}_A\right|^3} \right) \\ &= \Delta\rho\left(\mathbf{x}\right) \times v_{i,A}\left(\mathbf{x}\right). \end{aligned} \tag{1.12}$$

Integration over space of the AVCD yields the AVCC $V_{i,A}$:

$$V_{i,A} = \int \eta_{i,A}\left(\mathbf{x}\right) d\mathbf{x}. \tag{1.13}$$

1.2.2 Reduced Vibronic Coupling Density and Reduced Atomic Vibronic Coupling Density

A basis function $\phi_{\mu B}\left(\mathbf{x}\right)$ at the center of which is atom B ($\mathbf{R}_B$) can be expressed in terms of contracted Gaussian functions at the same center:

$$\phi_{\mu B}\left(\mathbf{x}\right) = \sum_p^{L_{\mu B}} d_{p\mu B} g_{p\mu B}\left(\alpha_{p\mu B}, \mathbf{x} - \mathbf{R}_B\right), \tag{1.14}$$

$$g_{p\mu B}\left(\alpha_{p\mu B},\mathbf{x}-\mathbf{R}_B\right) = \sqrt{N_{p\mu B}}\left(x_1-X_{B,1}\right)^{l_{\mu B}}\left(x_2-X_{B,2}\right)^{m_{\mu B}}\left(x_3-X_{B,3}\right)^{n_{\mu B}} \times\exp\left(-\alpha_{p\mu B}|\mathbf{x}-\mathbf{R}_B|^2\right)\left(l_{\mu B},m_{\mu B},n_{\mu B}=0,1,2,\cdots\right), \quad (1.15)$$

where $L_{\mu B}$ is a contraction length, $d_{p\mu B}$ is a contraction coefficient, $\alpha_{p\mu B}$ is a contraction exponent, $g_{p\mu B}$ is a normalized Gaussian primitive function, and $\sqrt{N_{p\mu B}}$ is a normalization factor. x_1, x_2, and x_3 are the x, y, and z components of $\mathbf{x}$, respectively, and $X_{B,1}$, $X_{B,2}$, and $X_{B,3}$ are the x, y, and z components of $\mathbf{R}_B$, respectively.

The electron-density difference $\Delta\rho\left(\mathbf{x}\right)$ can be written as

$$\begin{aligned}\Delta\rho\left(\mathbf{x}\right) &= \sum_a^{N\pm1}\left(\sum_B^M\sum_\mu^{K_B}C_{\mu Ba}^{N\pm1}\phi_{\mu B}\left(\mathbf{x}\right)\right)^2-\sum_a^N\left(\sum_B^M\sum_\mu^{K_B}C_{\mu Ba}^{N}\phi_{\mu B}\left(\mathbf{x}\right)\right)^2\\ &= \sum_{B,C}^M\sum_\mu^{K_B}\sum_\nu^{K_C}\left(\sum_a^{N\pm1}C_{\mu Ba}^{N\pm1}C_{\nu Ca}^{N\pm1}-\sum_a^N C_{\mu Ba}^N C_{\nu Ca}^N\right)\phi_{\mu B}\left(\mathbf{x}\right)\phi_{\nu C}\left(\mathbf{x}\right), \quad (1.16)\end{aligned}$$

where $\left\{C_{\mu Ba}^{N\pm1}\right\}$ and $\left\{C_{\mu Ba}^{N}\right\}$ are sets of coefficients of the a^{th} spatial orbitals for the $N\pm1$ and N electron systems, respectively; M and K_B (K_C) denote the total number of atoms and the number of Cartesian Gaussian basis functions of atom B (C), respectively. Using eqs. 1.14 and 1.15, $\Delta\rho\left(\mathbf{x}\right)$ can be expressed as

$$\begin{aligned}\Delta\rho\left(\mathbf{x}\right) &= \sum_{B,C}^M\sum_\mu^{K_B}\sum_\nu^{K_C}\sum_p^{L_{\mu B}}\sum_q^{L_{\nu C}}\left(\sum_a^{N\pm1}C_{\mu Ba}^{N\pm1}C_{\nu Ca}^{N\pm1}-\sum_a^N C_{\mu Ba}^N C_{\nu Ca}^N\right)d_{p\mu B}d_{q\nu C}\\ &\quad\times g_{p\mu B}\left(\alpha_{p\mu B},\mathbf{x}-\mathbf{R}_B\right)g_{q\nu C}\left(\alpha_{q\nu C},\mathbf{x}-\mathbf{R}_C\right)\\ &= \sum_{B,C}^M\sum_\mu^{K_B}\sum_\nu^{K_C}\sum_p^{L_{\mu B}}\sum_q^{L_{\nu C}}D_{\mu B\nu C}d_{p\mu B}d_{q\nu C}\sqrt{N_{p\mu B}N_{q\nu C}}\\ &\quad\times\left(x_1-X_{B,1}\right)^{l_{\mu B}}\left(x_2-X_{B,2}\right)^{m_{\mu B}}\left(x_3-X_{B,3}\right)^{n_{\mu B}}\\ &\quad\times\left(x_1-X_{C,1}\right)^{l_{\nu C}}\left(x_2-X_{C,2}\right)^{m_{\nu C}}\left(x_3-X_{C,3}\right)^{n_{\nu C}}\\ &\quad\times\exp\left(-\alpha_{p\mu B}|\mathbf{x}-\mathbf{R}_B|^2\right)\exp\left(-\alpha_{q\nu C}|\mathbf{x}-\mathbf{R}_C|^2\right), \quad (1.17)\end{aligned}$$

where

$$D_{\mu B\nu C}=\sum_a^{N\pm1}C_{\mu Ba}^{N\pm1}C_{\nu Ca}^{N\pm1}-\sum_a^N C_{\mu Ba}^N C_{\nu Ca}^N \quad (1.18)$$

Substituting Eq. 1.17 into Eq. 1.12, we obtain

$$\eta_{i,A}\left(\mathbf{x}\right) = -\frac{Z_A}{\sqrt{M_A}}\sum_j^3\sum_{B,C}^M\sum_\mu^{K_B}\sum_\nu^{K_C}D_{\mu B\nu C}e_{A,j}^{(i)}G_{\mu B\nu C,A,j}\left(\mathbf{x}\right), \quad (1.19)$$

where

$$
\begin{aligned}
G_{\mu B\nu C,A,j}\left(\mathbf{x}\right) &= \sum_{p}^{L_{\mu B}}\sum_{q}^{L_{\nu C}} d_{p\mu B}d_{q\nu C}\sqrt{N_{p\mu B}N_{q\nu C}}\left(x_j - X_{A,j}\right) \\
&\quad \times \left(x_1 - X_{B,1}\right)^{l_{\mu B}}\left(x_2 - X_{B,2}\right)^{m_{\mu B}}\left(x_3 - X_{B,3}\right)^{n_{\mu B}} \\
&\quad \times \left(x_1 - X_{C,1}\right)^{l_{\nu C}}\left(x_2 - X_{C,2}\right)^{m_{\nu C}}\left(x_3 - X_{C,3}\right)^{n_{\nu C}} \\
&\quad \times \frac{\exp\left(-\alpha_{p\mu B}|\mathbf{x}-\mathbf{R}_B|^2\right)\exp\left(-\alpha_{q\nu C}|\mathbf{x}-\mathbf{R}_C|^2\right)}{|\mathbf{x}-\mathbf{R}_A|^3}. \qquad (1.20)
\end{aligned}
$$

Thus, we can express $V_{i,A}$ in terms of spatial integrals of Gaussian functions:

$$
\begin{aligned}
V_{i,A} &= \int \eta_{i,A}\left(\mathbf{x}\right)d\mathbf{x} \\
&= -\frac{Z_A}{\sqrt{M_A}}\sum_{j}^{3}\sum_{B,C}^{M}\sum_{\mu}^{K_B}\sum_{\nu}^{K_C} D_{\mu B\nu C}e^{(i)}_{A,j}\int G_{\mu B\nu C,A,j}\left(\mathbf{x}\right)d\mathbf{x}. \qquad (1.21)
\end{aligned}
$$

When $B \neq A$ nor $C \neq A$, the spatial integral of $G_{\mu B\nu C,A,j}\left(\mathbf{x}\right)$ generally gives a nonzero value. When $B = A$ and $C = A$, $G_{\mu B\nu C,A,j}\left(\mathbf{x}\right)$ takes the form,

$$
\begin{aligned}
G_{\mu A\nu A,A,j}\left(\mathbf{x}\right) &= \sum_{p}^{L_{\mu A}}\sum_{q}^{L_{\nu A}} d_{p\mu A}d_{q\nu A}\sqrt{N_{p\mu A}N_{q\nu A}} \\
&\quad \times \left(x_1 - X_{A,1}\right)^{l_{\mu\nu,j}}\left(x_2 - X_{A,2}\right)^{m_{\mu\nu,j}}\left(x_3 - X_{A,3}\right)^{n_{\mu\nu,j}} \\
&\quad \times \frac{\exp\left(-\alpha_{p\mu A}|\mathbf{x}-\mathbf{R}_A|^2\right)\exp\left(-\alpha_{q\nu A}|\mathbf{x}-\mathbf{R}_A|^2\right)}{|\mathbf{x}-\mathbf{R}_A|^3}, \qquad (1.22)
\end{aligned}
$$

where

$$
\begin{cases}
\left(l_{\mu\nu,1}, m_{\mu\nu,1}, n_{\mu\nu,1}\right) = \left(l_\mu + l_\nu + 1, m_\mu + m_\nu, n_\mu + n_\nu\right), \\
\left(l_{\mu\nu,2}, m_{\mu\nu,2}, n_{\mu\nu,2}\right) = \left(l_\mu + l_\nu, m_\mu + m_\nu + 1, n_\mu + n_\nu\right), \\
\left(l_{\mu\nu,3}, m_{\mu\nu,3}, n_{\mu\nu,3}\right) = \left(l_\mu + l_\nu, m_\mu + m_\nu, n_\mu + n_\nu + 1\right).
\end{cases} \qquad (1.23)
$$

For simplicity, in the case of $B = A$ and $C = A$, A is omitted from $l_{\mu A\nu A,j}$, $m_{\mu A\nu A,j}$, and $n_{\mu A\nu A,j}$. If one of three integers, $l_{\mu\nu,j}$, $m_{\mu\nu,j}$, or $n_{\mu\nu,j}$ is odd, the spatial integral of $G_{\mu A\nu A,j}\left(\mathbf{x}\right)$ vanishes, and thus

$$
-\int \frac{Z_A}{\sqrt{M_A}}\sum_{j}^{3}\sum_{\substack{\mu,\nu \\ l_{\mu\nu,j}:\text{odd} \\ \text{or} \\ m_{\mu\nu,j}:\text{odd} \\ \text{or} \\ n_{\mu\nu,j}:\text{odd}}}^{K_A} D_{\mu A\nu A}e^{(i)}_{A,j}G_{\mu A\nu A,A,j}\left(\mathbf{x}\right)d\mathbf{x} = \int {\eta_{i,A}}'\left(\mathbf{x}\right)d\mathbf{x} = 0, \qquad (1.24)
$$

in Eq. 1.21. Therefore $\eta_{i,A}\left(\mathbf{x}\right)$ is decomposed into vanishing component ${\eta_{i,A}}'\left(\mathbf{x}\right)$ and non-vanishing component $\bar{\eta}_{i,A}\left(\mathbf{x}\right)$. The integrand in the left-hand side of Eq. 1.24 ${\eta_{i,A}}'\left(\mathbf{x}\right)$ has no contribution to $\eta_{i,A}\left(\mathbf{x}\right)$ since the integral over space vanishes, and is not essential to

the local picture of vibronic coupling. In addition, the integrand $\eta_{i,A}{}'(\mathbf{x})$ has a large value near the nucleus A, because $\eta_{i,A}{}'(\mathbf{x})$ diverges to infinity at $\mathbf{x} = \mathbf{R}_A$ (Eq. 1.22). As we will see later, the apparent complicated distribution pattern of $\eta_{i,A}(\mathbf{x})$ near the nucleus A originates from the non-essential component $\eta_{i,A}{}'(\mathbf{x})$.

We now define the non-vanishing component $\bar{\eta}_{i,A}(\mathbf{x})$ called the RAVCD. $\bar{\eta}_{i,A}(\mathbf{x})$ is defined by subtracting the integrand from $\eta_{i,A}(\mathbf{x})$:

$$\bar{\eta}_{i,A}(\mathbf{x}) = \eta_{i,A}(\mathbf{x}) - \eta_{i,A}{}'(\mathbf{x}). \tag{1.25}$$

Because the spatial integral of the second term on the right-hand side of Eq. 1.25 vanishes,

$$\int \bar{\eta}_{i,A}(\mathbf{x})\, d\mathbf{x} = \int \eta_{i,A}(\mathbf{x})\, d\mathbf{x} = V_{i,A}. \tag{1.26}$$

Although the spatial integral of $\bar{\eta}_{i,A}(\mathbf{x})$ is the same as $\eta_{i,A}(\mathbf{x})$, $\bar{\eta}_{i,A}(\mathbf{x})$ contains only the terms which are essential to vibronic coupling. The sum of $\bar{\eta}_{i,A}(\mathbf{x})$ over A is called the RVCD $\bar{\eta}_i(\mathbf{x})$:

$$\bar{\eta}_i(\mathbf{x}) = \sum_A \bar{\eta}_{i,A}(\mathbf{x}), \tag{1.27}$$

and the spatial integration of $\bar{\eta}_i(\mathbf{x})$ yields the vibronic coupling constant:

$$\int \bar{\eta}_i(\mathbf{x})\, d\mathbf{x} = V_i. \tag{1.28}$$

$\bar{\eta}_i(\mathbf{x})$ gives a local picture of vibronic coupling with the i^{th} mode, just as $\eta_i(\mathbf{x})$, but $\bar{\eta}_i(\mathbf{x})$ contains only the contributions essential to vibronic coupling.

When the normalized Gaussian primitive functions are s, p, d, f, and g-type functions, there are 35 possible sets of the numbers l_μ, m_μ, and n_μ (Table 1.1). One hundred and fifty-two sets of Cartesian Gaussian basis functions give nonzero spatial integrals of $G_{\mu A \nu A,1}(\mathbf{x})$. Half of these sets corresponds to the case where $l_\mu + m_\mu + n_\mu < l_\nu + m_\nu + n_\nu$, and the remaining half corresponds to the case where $l_\mu + m_\mu + n_\mu > l_\nu + m_\nu + n_\nu$. In Table 1.2, we list 76 sets of (l_μ, m_μ, n_μ) and (l_ν, m_ν, n_ν) for the former case. For $j = 2$, we obtain sets of Cartesian Gaussian basis functions such that $\int G_{\mu A \nu A,2}(\mathbf{x})\, d\mathbf{x} \neq 0$ by substituting $l_{\mu/\nu}$, $m_{\mu/\nu}$, and $n_{\mu/\nu}$ in Table 1.2 into $m_{\mu/\nu}$, $n_{\mu/\nu}$, and $l_{\mu/\nu}$, respectively. In a similar way, for $j = 3$, the substitution of $l_{\mu/\nu}$, $m_{\mu/\nu}$, and $n_{\mu/\nu}$ in Table 1.2 into $n_{\mu/\nu}$, $l_{\mu/\nu}$, and $m_{\mu/\nu}$ gives sets of (l_μ, m_μ, n_μ) and (l_ν, m_ν, n_ν) such that the spatial integrals of $G_{\mu A \nu A,3}(\mathbf{x})$ do not vanish. The number of possible sets of (l_μ, m_μ, n_μ) and (l_ν, m_ν, n_ν) is 1225 $(= 35 \times 35)$.

This means that $\eta_{i,A}$ contains a number of terms that make no contribution to the AVCC $V_{i,A}$. Since $G_{\mu A \nu A,A,j}(\mathbf{x})$ is large near nuclei A, the complicated $\eta_{i,A}$ (and hence, η_i) distribution pattern around nuclei A originates from those terms. Such complexity is not present in $\bar{\eta}_{i,A}$ and $\bar{\eta}_i$.

Table 1.1: Sets of numbers l_μ, m_μ, and n_μ and orbital types.

(l_μ, m_μ, n_μ)	ϕ_μ						
(0, 0, 0)	s	(3, 0, 0)	f_{xxx}	(4, 0, 0)	g_{xxxx}	(2, 2, 0)	g_{xxyy}
(1, 0, 0)	p_x	(0, 3, 0)	f_{yyy}	(0, 4, 0)	g_{yyyy}	(2, 0, 2)	g_{xxzz}
(0, 1, 0)	p_y	(0, 0, 3)	f_{zzz}	(0, 0, 4)	g_{zzzz}	(0, 2, 2)	g_{yyzz}
(0, 0, 1)	p_z	(2, 1, 0)	f_{xxy}	(3, 1, 0)	g_{xxxy}	(2, 1, 1)	g_{xxyz}
(2, 0, 0)	d_{xx}	(2, 0, 1)	f_{xxz}	(3, 0, 1)	g_{xxxz}	(1, 2, 1)	g_{yyxz}
(0, 2, 0)	d_{yy}	(1, 2, 0)	f_{yyx}	(1, 3, 0)	g_{yyyx}	(1, 1, 2)	g_{zzxy}
(0, 0, 2)	d_{zz}	(0, 2, 1)	f_{yyz}	(0, 3, 1)	g_{yyyz}		
(1, 1, 0)	d_{xy}	(1, 0, 2)	f_{zzx}	(1, 0, 3)	g_{zzzx}		
(1, 0, 1)	d_{xz}	(0, 1, 2)	f_{zzy}	(0, 1, 3)	g_{zzzy}		
(0, 1, 1)	d_{yz}	(1, 1, 1)	f_{xyz}				

1.3 Method of Calculation

We calculated the VCCs for BEDT-TTF cation. Employing the 6-31G basis set with their first derivatives[16] (denoted 6-31G+der), we confirmed that the Hellmann-Feynman theorem[15] holds. We optimized the structure of a neutral BEDT-TTF at the B3LYP/6-31G+der level of theory assuming C_2 symmetry. Employing the vibrational analysis, we confirmed that the optimized geometry is a stationary minimum, and calculated the wavefunction of the cationic state at the ROB3LYP/6-31G+der level using the optimized geometry of the neutral state. All the *ab initio* calculations were done using Gaussian 03 software.[17]

Table 1.2: Non-vanishing sets of the numbers (l_μ, m_μ, n_μ) and (l_ν, m_ν, n_ν) for the case where $l_\mu + m_\mu + n_\mu < l_\nu + m_\nu + n_\nu$. For $j = 2$, non-vanishing sets are obtained by substituting $l_{\mu/\nu}$, $m_{\mu/\nu}$, and $n_{\mu/\nu}$ into $m_{\mu/\nu}$, $n_{\mu/\nu}$, and $l_{\mu/\nu}$, respectively. For $j = 3$, the substitution of $l_{\mu/\nu}$, $m_{\mu/\nu}$, and $n_{\mu/\nu}$ into $n_{\mu/\nu}$, $l_{\mu/\nu}$, and $m_{\mu/\nu}$ gives non-vanishing sets.

(l_μ, m_μ, n_μ)			(l_ν, m_ν, n_ν)	$(l_{\mu\nu,1}, m_{\mu\nu,1}, n_{\mu\nu,1})$
s	(0,0,0)	p_x	(1,0,0)	(2,0,0)
s	(0,0,0)	f_{xxx}	(3,0,0)	(4,0,0)
s	(0,0,0)	f_{yyx}	(1,2,0)	(2,2,0)
s	(0,0,0)	f_{zzx}	(1,0,2)	(2,0,2)
p_x	(1,0,0)	d_{xx}	(2,0,0)	(4,0,0)
p_x	(1,0,0)	d_{yy}	(0,2,0)	(2,2,0)
p_x	(1,0,0)	d_{zz}	(0,0,2)	(2,0,2)
p_x	(1,0,0)	g_{xxxx}	(4,0,0)	(6,0,0)
p_x	(1,0,0)	g_{yyyy}	(0,4,0)	(2,4,0)
p_x	(1,0,0)	g_{zzzz}	(0,0,4)	(2,0,4)
p_x	(1,0,0)	g_{xxyy}	(2,2,0)	(4,2,0)
p_x	(1,0,0)	g_{xxzz}	(2,0,2)	(4,0,2)
p_x	(1,0,0)	g_{yyzz}	(0,2,2)	(2,2,2)
p_y	(0,1,0)	d_{xy}	(1,1,0)	(2,2,0)
p_y	(0,1,0)	g_{xxxy}	(3,1,0)	(4,2,0)
p_y	(0,1,0)	g_{yyyx}	(1,3,0)	(2,4,0)
p_y	(0,1,0)	g_{zzxy}	(1,1,2)	(2,2,2)
p_z	(0,0,1)	d_{xz}	(1,0,1)	(2,0,2)
p_z	(0,0,1)	g_{xxxz}	(3,0,1)	(4,0,2)
p_z	(0,0,1)	g_{zzzx}	(1,0,3)	(2,0,4)
p_z	(0,0,1)	g_{yyxz}	(1,2,1)	(2,2,2)
d_{xx}	(2,0,0)	f_{xxx}	(3,0,0)	(6,0,0)

table continued on next page

d_{xx}	(2,0,0)	f_{yyx}	(1,2,0)	(4,2,0)
d_{xx}	(2,0,0)	f_{zzx}	(1,0,2)	(4,0,2)
d_{yy}	(0,2,0)	f_{xxx}	(3,0,0)	(4,2,0)
d_{yy}	(0,2,0)	f_{yyx}	(1,2,0)	(2,4,0)
d_{yy}	(0,2,0)	f_{zzx}	(1,0,2)	(2,2,2)
d_{zz}	(0,0,2)	f_{xxx}	(3,0,0)	(4,0,2)
d_{zz}	(0,0,2)	f_{yyx}	(1,2,0)	(2,2,2)
d_{zz}	(0,0,2)	f_{zzx}	(1,0,2)	(2,0,4)
d_{xy}	(1,1,0)	f_{yyy}	(0,3,0)	(2,4,0)
d_{xy}	(1,1,0)	f_{xxy}	(2,1,0)	(4,2,0)
d_{xy}	(1,1,0)	f_{zzy}	(0,1,2)	(2,2,2)
d_{xz}	(1,0,1)	f_{zzz}	(0,0,3)	(2,0,4)
d_{xz}	(1,0,1)	f_{xxz}	(2,0,1)	(4,0,2)
d_{xz}	(1,0,1)	f_{yyz}	(0,2,1)	(2,2,2)
d_{yz}	(0,1,1)	f_{xyz}	(1,1,1)	(2,2,2)
f_{xxx}	(3,0,0)	g_{xxxx}	(4,0,0)	(8,0,0)
f_{xxx}	(3,0,0)	g_{yyyy}	(0,4,0)	(4,4,0)
f_{xxx}	(3,0,0)	g_{zzzz}	(0,0,4)	(4,0,4)
f_{xxx}	(3,0,0)	g_{xxyy}	(2,2,0)	(6,2,0)
f_{xxx}	(3,0,0)	g_{xxzz}	(2,0,2)	(6,0,2)
f_{xxx}	(3,0,0)	g_{yyzz}	(0,2,2)	(4,2,2)
f_{yyy}	(0,3,0)	g_{xxxy}	(3,1,0)	(4,4,0)
f_{yyy}	(0,3,0)	g_{yyyx}	(1,3,0)	(2,6,0)
f_{yyy}	(0,3,0)	g_{zzxy}	(1,1,2)	(2,4,2)
f_{zzz}	(0,0,3)	g_{xxxz}	(3,0,1)	(4,0,4)
f_{zzz}	(0,0,3)	g_{zzzx}	(1,0,3)	(2,0,6)
f_{zzz}	(0,0,3)	g_{yyxz}	(1,2,1)	(2,2,4)
f_{xxy}	(2,1,0)	g_{xxxy}	(3,1,0)	(6,2,0)
f_{xxy}	(2,1,0)	g_{yyyx}	(1,3,0)	(4,4,0)
f_{xxy}	(2,1,0)	g_{zzxy}	(1,1,2)	(4,2,2)
f_{xxz}	(2,0,1)	g_{xxxz}	(3,0,1)	(6,0,2)

table continued on next page

f_{xxz}	(2,0,1)	g_{zzzx}	(1,0,3)	(4,0,4)
f_{xxz}	(2,0,1)	g_{yyxz}	(1,2,1)	(4,2,2)
f_{yyx}	(1,2,0)	g_{xxxx}	(4,0,0)	(6,2,0)
f_{yyx}	(1,2,0)	g_{yyyy}	(0,4,0)	(2,6,0)
f_{yyx}	(1,2,0)	g_{zzzz}	(0,0,4)	(2,2,4)
f_{yyx}	(1,2,0)	g_{xxyy}	(2,2,0)	(4,4,0)
f_{yyx}	(1,2,0)	g_{xxzz}	(2,0,2)	(4,2,2)
f_{yyx}	(1,2,0)	g_{yyzz}	(0,2,2)	(2,4,2)
f_{yyz}	(0,2,1)	g_{xxxz}	(3,0,1)	(4,2,2)
f_{yyz}	(0,2,1)	g_{zzzx}	(1,0,3)	(2,2,4)
f_{yyz}	(0,2,1)	g_{yyxz}	(1,2,1)	(2,4,2)
f_{zzx}	(1,0,2)	g_{xxxx}	(4,0,0)	(6,0,2)
f_{zzx}	(1,0,2)	g_{yyyy}	(0,4,0)	(2,4,2)
f_{zzx}	(1,0,2)	g_{zzzz}	(0,0,4)	(2,0,6)
f_{zzx}	(1,0,2)	g_{xxyy}	(2,2,0)	(4,2,2)
f_{zzx}	(1,0,2)	g_{xxzz}	(2,0,2)	(4,0,4)
f_{zzx}	(1,0,2)	g_{yyzz}	(0,2,2)	(2,2,4)
f_{zzy}	(0,1,2)	g_{xxxy}	(3,1,0)	(4,2,2)
f_{zzy}	(0,1,2)	g_{yyyx}	(1,3,0)	(2,4,2)
f_{zzy}	(0,1,2)	g_{zzxy}	(1,1,2)	(2,2,4)
f_{xyz}	(1,1,1)	g_{yyyz}	(0,3,1)	(2,4,2)
f_{xyz}	(1,1,1)	g_{zzzy}	(0,1,3)	(2,2,4)
f_{xyz}	(1,1,1)	g_{xxyz}	(2,1,1)	(4,2,2)

1.4 Results and discussion

The optimized geometry of neutral BEDT-TTF is a boat structure as shown in Fig. 1.1a, which is supported by X-ray crystal structure analysis.[18] The C1, S1, S2, C1′, S1′, and S2′ atoms are almost coplanar: calculated dihedral angles S1−C1−C1′−S1′ and S1−C1−S2−C1′ are 176.9 and 177.4°, respectively. Calculated C1−C1′ and C2−C3 bond lengths are 1.349 and 1.347 Å, respectively, and C1−C1′ and C2−C3 bonds have a double-bond character. There are 37 totally symmetric modes that couple to the electronic state. We denote the i^{th} totally symmetric mode as $a(i)$.

There are three totally symmetric modes that have relatively large VCCs V and electron–phonon coupling constants g: 495.83 cm^{-1} [the $a(15)$ mode, C−S stretching]; 1546.49 cm^{-1} [the $a(32)$ mode, C=C stretching]; 1596.26 cm^{-1} [the $a(33)$ mode, C=C stretching]. $a(32)$ and $a(33)$ modes differ in the directions of their C2−C3 stretching vibration: for the $a(33)$ mode, C1−C1′ (C2−C3) bonds lengthen (shorten) simultaneously (Fig. 1.1a); for the $a(33)$ mode, the C1−C1′ bond lengthens (shortens) when the C2−C3 bond shortens (lengthens).

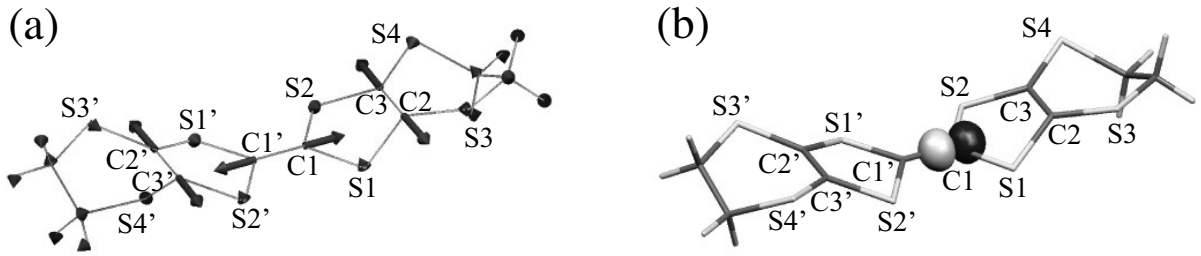

Figure 1.1: (a) $a(32)$ mode. (b) Derivative of the nuclear–electronic potential for C1 atom $v_{32,\text{C1}}$ at an isosurface value of 5×10^{-3} a.u. Dark gray shows where values are negative; light gray shows where values are positive.

Table 1.3: Frequency (cm^{-1}), vibronic coupling constant V (10^{-4} a.u.), and electron–phonon coupling constant g (meV).

	Present work			Kozlov *et al.*[a]		Faulhaber *et al.*[b]		Visentini *et al.*[c]	
	Calc., B3LYP/6-31G+der			Calc., MNDO		Calc., LDA		Exp.	
Mode	Frequency	V	g	Frequency	g	Frequency	g	Frequency	g
$a(15)$	495.83	1.29	73.9	508	30	511.0	22	513	40
$a(32)$	1546.49	4.05	131.2	1427	132	1431.0	51	1414	71
$a(33)$	1596.26	1.17	37.4	1465	30	1455.0	107	1460	43

[a]Ref 11.

[b]Ref 12.

[c]Ref 13.

Calculated frequencies, V, and g together with the values reported in the past[11–13] are listed in Table 1.3. The trend that strong vibronic coupling contains C−S stretching and C=C stretching modes is consistent with the previous theoretical[11,12] and experimental results.[13] The values of g for the $a(15)$ and $a(32)$ modes are close to those obtained using MNDO method. For the $a(33)$ mode, g is in reasonable agreement with the experimental result. By contrast, for the $a(15)$ and $a(32)$ modes, g is overestimated. In the remainder of this publication, we discuss the reason why the VCC for $a(32)$ is the largest, by analyzing the AVCD $\eta_{32,A}$ and the RAVCD $\bar{\eta}_{32,A}$ for this mode.

Figure 1.2a shows the electron-density distribution for the highest occupied molecular orbital (HOMO). The HOMO electron-density distribution is large on the central TTF moiety and has a π-orbital character. Figure 1.2b shows the electron-density difference $\Delta\rho$ upon ionization. The distribution pattern for the negative $\Delta\rho$ (dark-gray regions in Fig. 1.2b) is similar to that for the electron density of the HOMO. This comes from the fact that the electron is removed mainly from the HOMO. In addition, it should be noted that regions where $\Delta\rho$ is positive have a σ-orbital character and originate from occupied molecular orbitals other than the HOMO. The positive $\Delta\rho$ distribution relaxes Coulomb repulsion between regions where $\Delta\rho$ is negative. The main portion of $\Delta\rho$ is distributed on the TTF unit, suggesting that vibronic coupling in BEDT-TTF occurs mainly in the central TTF moiety.

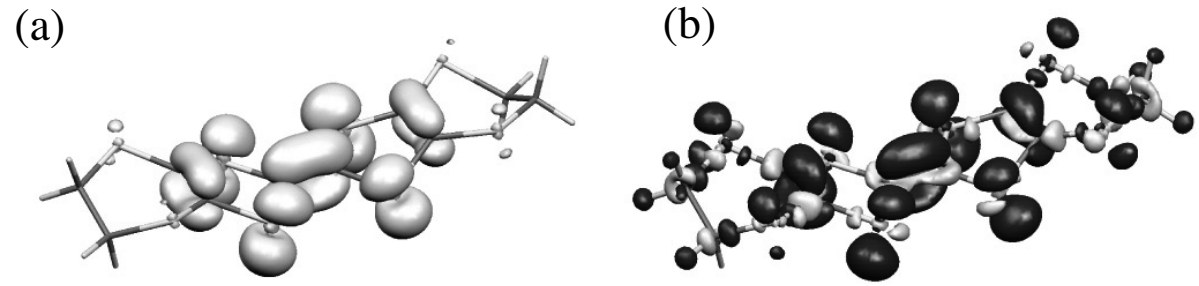

Figure 1.2: (a) Electron-density distributions of the HOMO. (b) Electron-density difference $\Delta\rho$ at an isosurface value of 2×10^{-3} a.u. Dark gray shows where values are negative; light gray shows where values are positive.

Figure 1.1b shows the derivative of the nuclear–electronic potential $v_{32,\mathrm{C1}}$ for the $a(32)$ mode. Reflecting large displacement of the C1 atom, v_{32} is large near the C1 atom. Because both $\Delta\rho$ and $v_{32,\mathrm{C1}}$ is large on the C1−C1$'$ bond, $v_{32,\mathrm{C1}}$ overlaps significantly

with $\Delta\rho$ in that region. For the same reason, $v_{32,\mathrm{C2}}$ and $v_{32,\mathrm{C3}}$ overlap significantly with $\Delta\rho$.

The extent of the overlap between $v_{32,A}$ and $\Delta\rho$ is reflected in the AVCC magnitude. The value for the C1, C2, and C3 atoms are -0.71×10^{-4}, -0.67×10^{-4}, and -0.63×10^{-4} a.u., respectively. The sum of the AVCCs of C1, C1′ C2, C2′, C3, and C3′ atoms is -4.02×10^{-4} a.u., which corresponds to 99.3% of the VCC for the $a(32)$ mode (-4.05×10^{-4} a.u.). This suggests that vibronic coupling occurs mainly on the double-bonded carbon atoms.

We calculated AVCD and RAVCD for the C1 and S1 atoms for the $a(32)$ mode to investigate a local picture of the vibronic coupling. Figures 1.3a, b, and c show the AVCD $\eta_{32,\mathrm{C1}}$, RAVCD $\bar{\eta}_{32,\mathrm{C1}}$, and the vanishing component $\eta_{32,\mathrm{C1}}{}'$, respectively. Since the plane formed by the S1, C1, and S2 atoms does not coincide with a plane of symmetry, $\eta_{32,\mathrm{C1}}$, $\bar{\eta}_{32,\mathrm{C1}}$, and $\eta_{32,\mathrm{C1}}{}'$. are not symmetric with respect to the plane. Comparing $\eta_{32,\mathrm{C1}}$ with $\bar{\eta}_{32,\mathrm{C1}}$, the distribution range of $\bar{\eta}_{32,\mathrm{C1}}$ around the C1 atom is smaller than that of $\eta_{32,\mathrm{C1}}$; negative and positive regions inside solid lines in Fig. 1.3a are not observed in Fig. 1.3b. These regions originate from $\eta_{32,\mathrm{C1}}{}'$ for which the spatial integration vanishes (Fig. 1.3c).

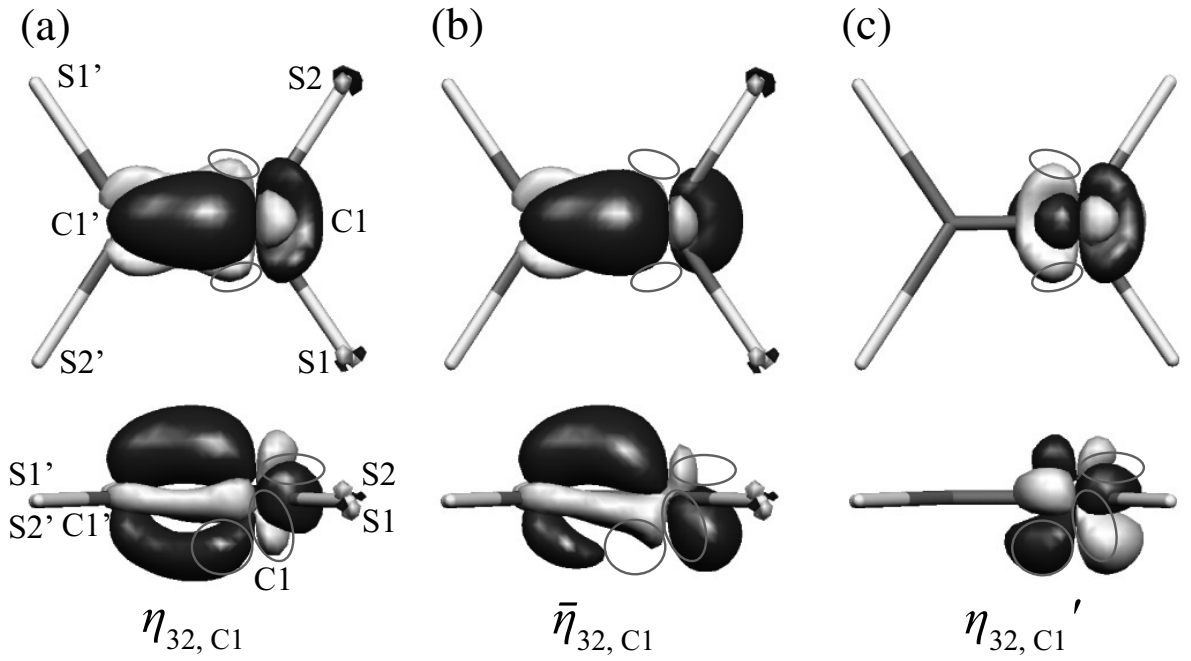

Figure 1.3: Isosurfaces for (a) AVCD $\eta_{32,\mathrm{C1}}$, (b) RAVCD $\bar{\eta}_{32,\mathrm{C1}}$, and (c) the vanishing component $\eta_{32,\mathrm{C1}}{}'$. An isosurface value is 5×10^{-6} a.u. Dark gray shows where values are negative; light gray shows where values are positive.

The distribution range of negative $\bar{\eta}_{32,\mathrm{C1}}$ is larger than that of positive $\bar{\eta}_{32,\mathrm{C1}}$. Hence, the space integral of $\bar{\eta}_{32,\mathrm{C1}}$ gives a negative value (-0.71×10^{-4} a.u.). Negative $\bar{\eta}_{32,\mathrm{C1}}$ is large on the C1$-$C1$'$ bond and below the S1-C1-S2 plane and has a π character. Positive $\bar{\eta}_{32,\mathrm{C1}}$ is mainly distributed in the plane and has a σ character. $\bar{\eta}_{32,\mathrm{C1}}$ is large around the C1 atom, because both $v_{32,\mathrm{C1}}$ and $\Delta\rho$ are large around that atom. Around the C1$'$ atom, despite $v_{32,\mathrm{C1}}$ is small, since $\Delta\rho$ is large, $\bar{\eta}_{32,\mathrm{C1}}$ has a large value. Thus, $\bar{\eta}_{32,\mathrm{C1}}$ clearly shows a local picture of vibronic coupling on the C1$-$C1$'$ bond.

We calculated contributions from p-type atomic orbitals to $\eta_{32,\mathrm{C1}}$, $\bar{\eta}_{32,\mathrm{C1}}$, and $\eta_{32,\mathrm{C1}}{}'$ denoted as $\eta^{pp}_{32,\mathrm{C1}}$, $\bar{\eta}^{pp}_{32,\mathrm{C1}}$, and $\eta^{pp}_{32,\mathrm{C1}}{}'$, respectively. $\eta^{pp}_{32,\mathrm{C1}}$ is calculated by summing up all terms in which $l_{\nu B}+m_{\nu B}+n_{\nu B} = 1$ and $l_{\nu C}+m_{\nu C}+n_{\nu C} = 1$ in Eq. 1.19; $\eta^{pp}_{32,\mathrm{C1}}{}'$ is calculated by summing up all terms in which $l_\nu + m_\nu + n_\nu = 1$ in Eq. 1.24; $\bar{\eta}^{pp}_{32,\mathrm{C1}} = \eta^{pp}_{32,\mathrm{C1}} - \eta^{pp}_{32,\mathrm{C1}}{}'$.

Figures 1.4a, b, and c show $\eta^{pp}_{32,\mathrm{C1}}$, $\bar{\eta}^{pp}_{32,\mathrm{C1}}$, and $\eta^{pp}_{32,\mathrm{C1}}{}'$, respectively. $\eta^{pp}_{32,\mathrm{C1}}$, $\bar{\eta}^{pp}_{32,\mathrm{C1}}$, and $\eta^{pp}_{32,\mathrm{C1}}{}'$ are not symmetric with respect to the S1-C1-S2 plane for the same reason for $\eta_{32,\mathrm{C1}}$, $\bar{\eta}_{32,\mathrm{C1}}$, and $\eta_{32,\mathrm{C1}}{}'$. Comparing Fig. 1.4a with Fig. 1.3a, we find that the distribution pattern of $\eta^{pp}_{32,\mathrm{C1}}$ is similar to that of $\eta_{32,\mathrm{C1}}$, suggesting that the p-type atomic orbitals make large contributions to $\eta_{32,\mathrm{C1}}$. $\bar{\eta}^{pp}_{32,\mathrm{C1}}$ is largely distributed near the C1′ atom; it is not largely distributed near the C1 atom. This is because $\eta^{pp}_{32,\mathrm{C1}}{}'$ is as large as $\eta^{pp}_{32,\mathrm{C1}}$ around the C1 atom. This result shows that the motion of the C1 atom couples strongly to the p-type atomic orbitals of the C1′ atom, whereas it does not couple strongly to those of the C1 atom. $\eta^{pp}_{32,\mathrm{C1}}$ is apparently large near the C1 atom, which leads to a misinterpretation that the motion of the C1 atom couples strongly to the p-type atomic orbitals of the C1 atom. Thus, the analysis based on the AVCD sometimes leads to a misunderstanding of the local picture of the vibronic coupling.

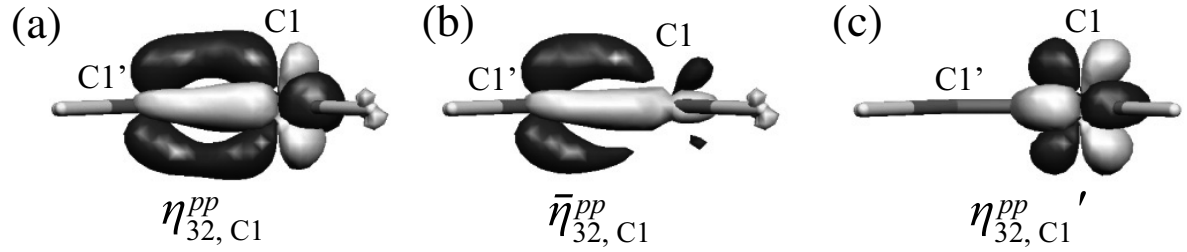

Figure 1.4: Isosurfaces for (a) $\eta^{pp}_{32,\mathrm{C1}}$, (b) $\bar{\eta}^{pp}_{32,\mathrm{C1}}$, and (c) $\eta^{pp}_{32,\mathrm{C1}}{}'$. An isosurface value is 5×10^{-6} a.u. Dark gray shows where values are negative; light gray shows where values are positive.

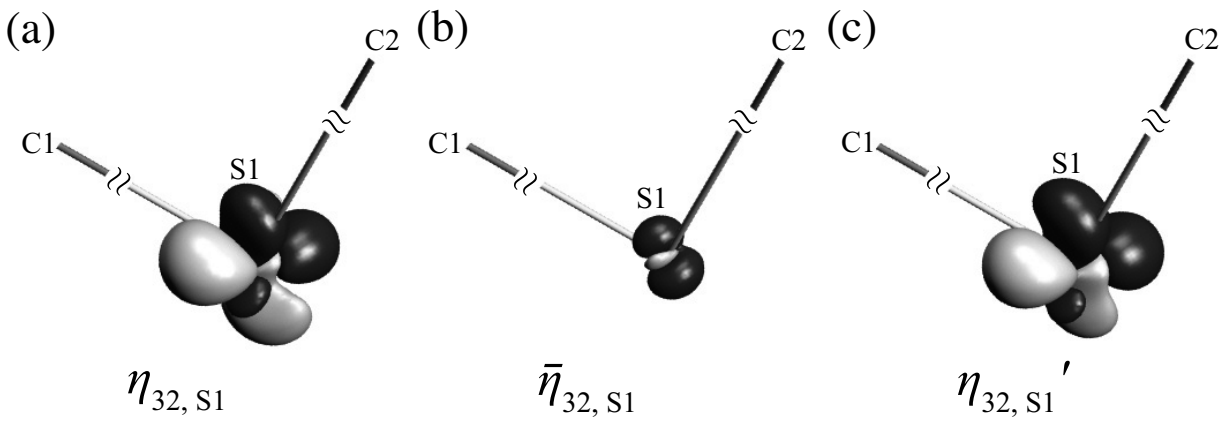

Figure 1.5: Isosurfaces for (a) $\eta_{32,S1}$, (b) $\bar{\eta}_{32,S1}$, and (c) $\eta_{32,S1}{}'$. An isosurface value is 3×10^{-4} a.u. Dark gray shows where values are negative; light gray shows where values are positive.

Figures 1.5a, b, and c show the AVCD $\eta_{32,S1}$, RAVCD $\bar{\eta}_{32,S1}$, and the vanishing component $\eta_{32,S1}{}'$, respectively. The AVCC of the S1 atom is negative (-1.13×10^{-6} a.u.). However, from $\eta_{32,S1}$, we cannot determine whether the spatial integration of $\eta_{32,S1}$ is positive or negative since positive $\eta_{32,S1}$ is distributed as largely as negative $\eta_{32,S1}$ (Fig. 1.5a). This is because values of $\eta_{32,S1}{}'$ are comparable to those of $\eta_{32,S1}$ (Fig. 1.5c). The large $\eta_{32,S1}{}'$ values make a local picture of vibronic coupling around the S1 atom difficult to be grasped. In contrast, from $\bar{\eta}_{32,S1}$, we can easily understand the reason why the AVCC of the S1 atom is negative: the region where $\bar{\eta}_{32,S1}$ are negative is larger than the region where they are positive (Fig. 1.5b). The analysis based on RAVCD is useful especially for the case where AVCD is strongly localized on an atom.

1.5 Conclusion

We introduced the RVCD and RAVCD to discuss the origin of vibronic couplings in a molecule. The RVCD and RAVCD are defined as subtractions of the components of the integrals of which yield zero from the VCD and AVCD.

As an example, we presented AVCDs and RAVCDs for the C=C stretching mode of BEDT-TTF cation. RAVCD exhibits the origin of the strongest vibronic coupling of the C=C stretching mode. The large electron density difference on the C=C bond is responsible for the strong vibronic coupling.

Using the reduced coupling densities, we can gain new physical insights more clearly than conventional VCD and AVCD. Furthermore, the RVCD analysis provides a new guiding principle of the molecular design for functional molecules, such as an organic superconductor, molecular wire, and so on.

Bibliography

[1] T. Sato, K. Tokunaga, and K. Tanaka, J. Chem. Phys. **124**, 024314 (2006).

[2] K. Tokunaga, T. Sato, and K. Tanaka, J. Chem. Phys. **124**, 154303 (2006).

[3] K. Tokunaga, T. Sato, and K. Tanaka, J. Mol. Struct. **838**, 116 (2007).

[4] T. Sato, K. Tokunaga, N. Iwahara, K. Shizu, and K. Tanaka, *Vibronic coupling constant and vibronic coupling density* in *The Jahn-Teller-Effect - Fundamentals and Implications for Physics and Chemistry,* H. Köppel, D. R. Yarkony, and H. Barentzen (Eds) (Springer-Verlag, Berlin and Heidelberg, 2009).

[5] T. Sato, K. Tokunaga, and K. Tanaka, J. Phys. Chem. A **112**, 758 (2008).

[6] T. Sato, K. Shizu, T. Kuga, K. Tanaka, and H. Kaji, Chem. Phys. Lett. **458**, 152 (2008).

[7] T. Ishiguro, K. Yamaji, and G. Saito, *Organic Superconductors* (Second edition) (Springer-Verlag, Berlin, 1997).

[8] H. Wang, K. Carlson, U. Geiser, A. Kini, A. Schultz, J. Williams, L. Montgomery, W. Kwok, U. Welp, K. Vandervoort, S. Boryschuk, A. Crouch, J. Kommers, D. Watkins, J. Schriber, D. Overmyer, D. Jung, J. Novoa, and M.-H. Whangbo, Synth. Met. **42**, 1983 (1991).

[9] M. Mas-Torrent, P. Hadley, S. T. Bromley, X. Ribas, J. Tarrés, M. Mas, E. Molins, J. Veciana, and C. Rovira, J. Am. Chem. Soc. **126**, 985 (2004).

[10] Y. Misaki, Sci. Technol. Adv. Mater. **10**, 024301 (2009).

[11] M. E. Kozlov, K. I. Pokhodnia, and A. A. Yurchenko, Spectrochim. Acta A **45**, 437 (1989).

[12] J. C. Faulhaber, D. Y. Ko, and P. R. Briddon, Synth. Met. **60**, 227 (1993).

[13] G. Visentini, M. Masino, C. Bellitto, and A. Girlando, Phys. Rev. B **58**, 9460 (1998).

[14] M. Taniguchi, Y. Misaki, and K. Tanaka, Solid State Commun. **114**, 75 (2000).

[15] R. P. Feynman, Phys. Rev. **56**, 340 (1939).

[16] H. Nakatsuji, K. Kanda, and T. Yonezawa, Chem. Phys. Lett. **75**, 340 (1980).

[17] M. J. Frisch, G. W. Trucks, H. B. Schlegel, G. E. Scuseria, M. A. Robb, J. R. Cheeseman, J. A. Montgomery, Jr., T. Vreven, K. N. Kudin, J. C. Burant, J. M. Millam, S. S. Iyengar, J. Tomasi, V. Barone, B. Mennucci, M. Cossi, G. Scalmani, N. Rega, G. A. Petersson, H. Nakatsuji, M. Hada, M. Ehara, K. Toyota, R. Fukuda, J. Hasegawa, M. Ishida, T. Nakajima, Y. Honda, O. Kitao, H. Nakai, M. Klene, X. Li, J. E. Knox, H. P. Hratchian, J. B. Cross, V. Bakken, C. Adamo, J. Jaramillo, R. Gomperts, R. E. Stratmann, O. Yazyev, A. J. Austin, R. Cammi, C. Pomelli, J. W. Ochterski, P. Y. Ayala, K. Morokuma, G. A. Voth, P. Salvador, J. J. Dannenberg, V. G. Zakrzewski, S. Dapprich, A. D. Daniels, M. C. Strain, O. Farkas, D. K. Malick, A. D. Rabuck, K. Raghavachari, J. B. Foresman, J. V. Ortiz, Q. Cui, A. G. Baboul, S. Clifford, J. Cioslowski, B. B. Stefanov, G. Liu, A. Liashenko, P. Piskorz, I. Komaromi, R. L. Martin, D. J. Fox, T. Keith, M. A. Al-Laham, C. Y. Peng, A. Nanayakkara, M. Challacombe, P. M. W. Gill, B. Johnson, W. Chen, M. W. Wong, C. Gonzalez, and J. A. Pople, GAUSSIAN 03, Revision D.02, Gaussian, Inc., Wallingford, CT, 2004.

[18] H. Kobayashi, A. Kobayashi, Y. Sasaki, G. Saito, and H. Inokuchi, Bull. Chem. Soc. Jpn. **59**, 301 (1986).

Chapter 2

Vibronic Coupling Density Analysis for Free-Base Porphin Cation

2.1 Introduction

Organic field-effect transistors (OFETs) have received considerable attention because of their potential applications in low-cost flexible electronic devices.[1–5] In the last two decades, porphyrin-based thin film transistors (TFTs) have been fabricated and their hole-mobilities have been measured.[6–18] The hole mobilities range between 10^{-6}–10^{-1} $cm^2V^{-1}s^{-1}$. To understand the hole-transport properties of porphyrin-based TFTs, ionization potentials, electron affinities, transfer integrals, reorganization energies, and crystal structures of the porphyrins have been studied.[17–19] However, vibronic (electron–vibration) coupling, which is one of the important factors that influence the hole-transport properties, has not been studied in detail. In general, inelastic scatterings of holes due to the vibronic couplings inhibit hole transport. Hence, molecules with weak vibronic couplings in their cationic states are suitable as hole-transport materials for TFTs.

The strength of a vibronic coupling is quantitatively described by a vibronic coupling constant (VCC). In general, molecules with small VCCs are potentially good charge-transporting materials. We have theoretically studied vibronic couplings in various hole-transporting materials employing vibronic coupling density (VCD) analysis.[20–22] Through these studies, we have concluded that localizations of electron-density difference $\Delta\rho$ (the difference between the electron densities of the ionic and neutral states) on atoms reduce the VCCs and, consequently, improve the hole-mobilities. For example, for well-known

hole-transporting molecules, N,N'-diphenyl-N,N'-di(m-tolyl)benzidine (TPD) and carbazole, the strong localizations of $\Delta\rho$ on the N atoms are responsible for the small VCCs of these molecules.

The VCD analysis has provided an effective guiding principle for designing charge-transporting materials as well as detailed pictures of the vibronic couplings. Using the VCD analysis, we have theoretically propose an efficient electron-transporting molecule for organic light-emitting diodes (OLEDs) with suitable highest occupied and lowest unoccupied molecular orbital energies.[23] In this chapter, we apply the VCD analysis to the vibronic couplings in the free-base porphin (FBP) cation as a starting point for understanding vibronic couplings in the hole-transport properties in porphyrins.

2.2 Theory

The intramolecular vibronic coupling between the electronic state and the ith vibrational mode of the molecule is described by the VCC V_i. V_i can be expressed as the space integral of the VCD of the ith vibrational mode η_i:[24,25]

$$V_i = \int \eta_i(\mathbf{x})\, d\mathbf{x}, \tag{2.1}$$

where $\mathbf{x}$ denotes a position in the 3D space.

For a hole-transport process, η_i can be expressed as the product of the electron-density difference between the cationic and neutral states $\Delta\rho(\mathbf{x})$ and the one-electron part of the derivative of the nuclear–electronic potential with respect to the normal coordinate of the ith mode $v_i(\mathbf{x})$:

$$\eta_i(\mathbf{x}) = \Delta\rho(\mathbf{x}) \times v_i(\mathbf{x}), \tag{2.2}$$

where

$$\Delta\rho(\mathbf{x}) = \rho^{+}(\mathbf{x}) - \rho(\mathbf{x}), \tag{2.3}$$

$$v_i(\mathbf{x}) = \sum_A v_{i,A}(\mathbf{x}) = \sum_A -\frac{Z_A}{\sqrt{M_A}}\mathbf{e}_A^{(i)} \cdot \frac{\mathbf{x}-\mathbf{R}_A}{|\mathbf{x}-\mathbf{R}_A|^3}. \tag{2.4}$$

Here, $\mathbf{x}$ denotes a position in the space, $\rho^{+}(\mathbf{x})$ and $\rho(\mathbf{x})$ are electron densities for the cationic and neutral states, respectively, at the equilibrium geometry of the neutral state.

Z_A, M_A, and $\mathbf{R}_A$ are the atomic number, mass, and position of the Ath nucleus, respectively, and $\mathbf{e}_A^{(i)}$ is the mass-weighted 3D component of the Ath atom of the ith vibrational mode $\mathbf{e}^{(i)}$. Only the totally symmetric modes have non-zero VCCs and contribute to the vibronic couplings. $v_{i,A}$ is the contribution from the Ath atom to v_i and represents a distribution of v_i around the Ath atom.

The contribution from the Ath atom to η_i is called an atomic vibronic coupling density (AVCD) $\eta_{i,A}$. $\eta_{i,A}$ is defined by

$$\eta_{i,A}(\mathbf{x}) = \Delta\rho(\mathbf{x}) \times v_{i,A}(\mathbf{x}). \tag{2.5}$$

The space integral of $\eta_{i,A}$ gives an atomic vibronic coupling constant (AVCC) $V_{i,A}$ of the Ath atom:

$$V_{i,A} = \int \eta_{i,A}(\mathbf{x})\, d\mathbf{x}. \tag{2.6}$$

$V_{i,A}$ is the contribution from the Ath atom to V_i. The sum of $V_{i,A}$ over A gives again V_i:

$$\sum_A V_{i,A} = V_i. \tag{2.7}$$

The magnitude of $V_{i,A}$ reflects the extent of overlap between $\Delta\rho$ and $v_{i,A}$. In general, $V_{i,A}$ is small for an atom around which an overlap between $\Delta\rho$ and $v_{i,A}$ is small.

η_i and $\eta_{i,A}$ contain vanishing components which make no contribution to V_i and $V_{i,A}$, respectively. A reduced vibronic coupling density (RVCD) $\bar{\eta}_i$ and a reduced atomic vibronic coupling density (RAVCD) $\bar{\eta}_{i,A}$ are defined by eliminating those vanishing components from η_i and $\eta_{i,A}$, respectively.[26] The space integral of $\bar{\eta}_i$ and $\bar{\eta}_{i,A}$ give again V_i and $V_{i,A}$, respectively:

$$\int \bar{\eta}_i(\mathbf{x})\, d\mathbf{x} = V_i, \tag{2.8}$$

$$\int \bar{\eta}_{i,A}(\mathbf{x})\, d\mathbf{x} = V_{i,A}. \tag{2.9}$$

2.3 Method of calculation

The geometry of FBP was optimized assuming D_{2h} symmetry at the B3LYP/6-311+G(d) level of theory[27–30] followed by vibrational analysis at the same level of theory. We confirmed that the optimized geometry is a stationary minimum. The cationic state of FBP was calculated at the UB3LYP/6-311+G(d) level of theory using the optimized structure of the neutral state. All the *ab initio* calculations were done employing Gaussian 03 software.[31] The calculated frequencies are uniformly scaled by 0.975 which has been suggested by Verdal *et al.* for the B3LYP/6-311G(d,p) frequencies calculated for FBP.[32]

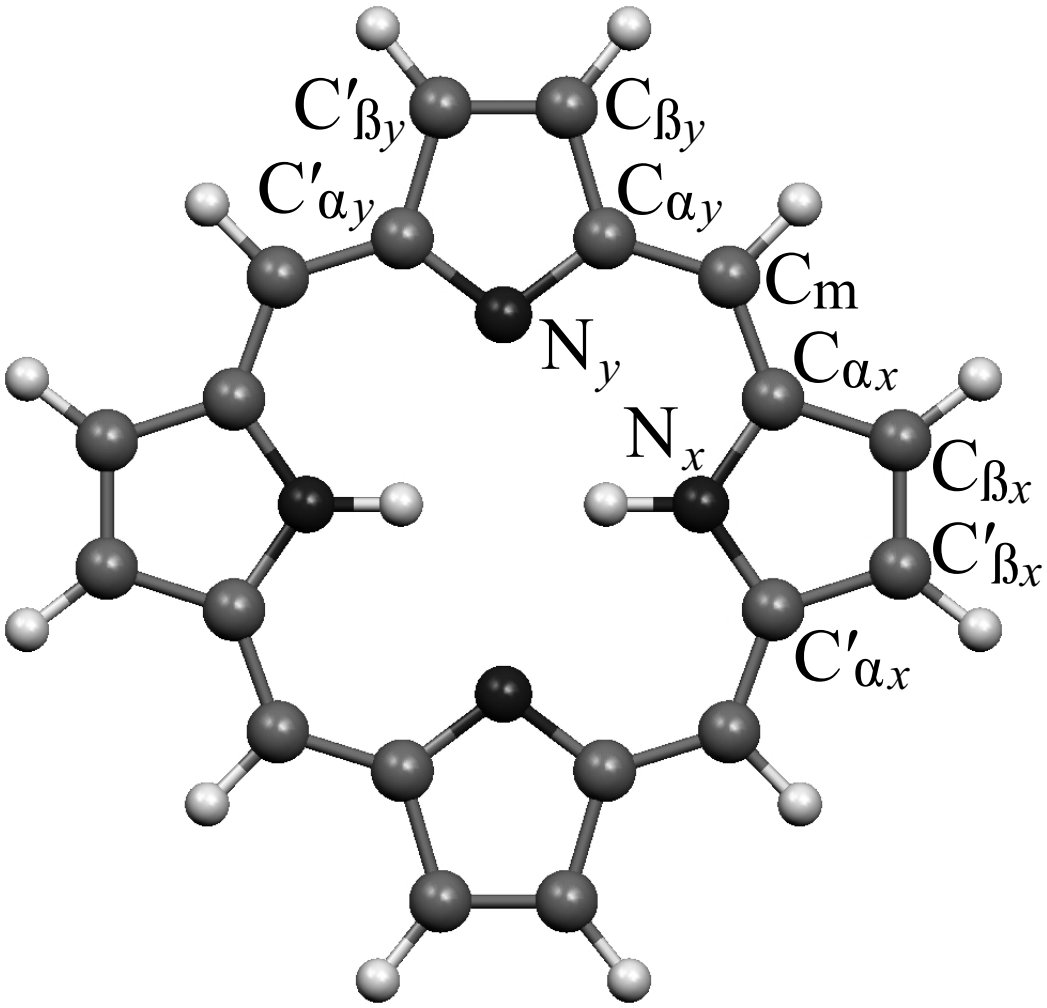

Figure 2.1: Stable structure of the neutral free-base porphin calculated at the B3LYP/6-311+G(d) level of theory with the atomic labeling.

2.4 Results and discussion

Fig. 2.1 shows the stable structure of the neutral FBP calculated at the B3LYP/6-311+G(d) level of theory. We followed the atomic labeling used in the preceding studies.[32–34] The stable structure is planar, which is supported by X-ray crystallographic data.[35]

Table 2.1: Calculated and experimental bond lengths (Å) and angles (degree) of free-base porphin (FBP).

	calc	exp[a]
$C'_{\beta_x}-C_{\beta_x}$	1.371	1.365 ± 0.006
$C_{\beta_x}-C_{\alpha_x}$	1.434	1.431 ± 0.006
$C_{\alpha_x}-C_{\rm m}$	1.392	1.387 ± 0.011
$C_{\rm m}-C_{\alpha_y}$	1.399	1.376 ± 0.006
$C_{\alpha_y}-C_{\beta_y}$	1.459	1.452 ± 0.013
$C_{\beta_y}-C'_{\beta_y}$	1.355	1.345 ± 0.001
$C_{\alpha_x}-N_x$	1.371	1.380 ± 0.003
$C_{\alpha_y}-N_y$	1.361	1.377 ± 0.014
$C'_{\alpha_x}-N_x-C_{\alpha_x}$	110.9	108.6 ± 0.8
$N_x-C_{\alpha_x}-C_{\beta_x}$	106.5	107.9 ± 1.0
$C_{\alpha_x}-C_{\beta_x}-C'_{\beta_x}$	108.0	107.9 ± 0.5
$N_x-C_{\alpha_x}-C_{\rm m}$	125.7	125.2 ± 0.6
$C_{\alpha_x}-C_{\rm m}-C_{\alpha_y}$	127.1	127.1 ± 0.6
$C'_{\alpha_y}-N_y-C_{\alpha_y}$	105.8	106.1 ± 0.2
$N_y-C_{\alpha_y}-C_{\beta_y}$	110.9	109.8 ± 0.6
$C_{\alpha_y}-C_{\beta_y}-C'_{\beta_y}$	106.2	107.2 ± 1.2
$N_y-C_{\alpha_y}-C_{\rm m}$	125.5	125.0 ± 0.9

[a]X-ray crystallographic data for FBP.[35]

Optimized geometrical parameters together with experimental values[35] are listed in Table 2.1. The calculated bond lengths are in good agreement with the experimental values. The differences between the calculated and experimental values are within the error of measurement for the $C'_{\beta_x}-C_{\beta_x}$, $C_{\beta_x}-C_{\alpha_x}$, $C_{\alpha_x}-C_{\rm m}$, and $C_{\alpha_y}-C_{\beta_y}$ bond lengths,

and the $C_{\alpha_x}-C_{\beta_x}-C'_{\beta_x}$, $N_x-C_{\alpha_x}-C_m$, $C_{\alpha_x}-C_m-C_{\alpha_y}$, $C_{\alpha_y}-C_{\beta_y}-C'_{\beta_y}$, and $N_y-C_{\alpha_y}-C_m$ bond angles. For the remaining geometrical parameters, although the difference between the calculated and experimental values is outside the error of measurement, the deviation is small: for the $C_m-C_{\alpha_y}$ and $C_{\beta_y}-C'_{\beta_y}$ bond lengths, the calculated values are longer by 0.023 and 0.010 Å than the experimental values, respectively; for the $C_{\alpha_x}-N_x$ and $C_{\alpha_y}-N_y$ bond lengths, the calculated values are shorter by 0.009 and 0.016 Å than the experimental values, respectively; for the $C'_{\alpha_x}-N_x-C_{\alpha_x}$ and $N_y-C_{\alpha_y}-C_{\beta_y}$ bond angles, the calculated values are large by 2.3 and 1.1°, respectively; for the $N_x-C_{\alpha_x}-C_{\beta_x}$ and $C'_{\alpha_y}-N_y-C_{\alpha_y}$ bond angles, the calculated values are small by 1.4 and 0.3°, respectively. The X-ray crystallographic data supports the accuracy of our method for calculating the structure of FBP.

The calculated frequencies and experimental ones[34,36,37] determined from Raman spectra for FBP are listed in Table 2.2. The differences between the calculated and experimental frequencies are within 10 cm^{-1} except for the $a_g(4)$ mode. Hence, the scaling factor of 0.975 is also appropriate for the B3LYP/6-311+G(d) calculated frequencies. We followed the modes description used by Li *et al.*.[33]

The calculated VCCs for the totally symmetric modes of the FBP cation are listed in Table 2.2. The direction of the vibrational modes is defined such that V_i is negative. The calculated VCCs are less than 2.0×10^{-4} a.u., which is small as a π-conjugated molecule. The $a_g(10)$ mode (the pyrrole half-ring stretching mode, Fig. 2.2a) has the largest VCC. The $a_g(10)$ mode involves the $C_{\alpha_x}-C_{\beta_x}$ and $C_{\alpha_y}-C_{\beta_y}$ stretching vibrations. The displacement of the α-carbon atoms (C_{α_x} and C_{α_y}) and nitrogen atoms (N_x and N_y) are large. The second largest VCC corresponds to the $a_g(13)$ mode (the $C_\beta-C_\beta$ stretching mode), in which the $C_{\beta_x}-C'_{\beta_x}$ and $C_{\beta_y}-C'_{\beta_y}$ stretching vibrations are out of phase. The other totally symmetric $C_\beta-C_\beta$ stretching mode (the $a_g(14)$ mode) has the smaller VCC than the $a_g(13)$ mode. The $a_g(14)$ mode is different in the phase of the two $C_\beta-C_\beta$ stretching vibrations. In the $a_g(14)$ mode, the $C_{\beta_x}-C'_{\beta_x}$ and $C_{\beta_y}-C'_{\beta_y}$ stretching vibrations are in phase. The $a_g(15)$ mode (the $C_\alpha-C_m$ stretching mode, Fig. 2.2b) has the third largest VCC. In the $a_g(15)$ mode, the α-carbon and meso-carbon atoms (the C_m atoms) are displaced largely. The VCCs of the other totally symmetric modes are of the order of 10^{-5} a.u. and hence, quite small.

Table 2.2: Calculated vibronic coupling constants V_i (10^{-4} a.u.) and frequencies (cm^{-1}) of totally symmetric modes for free-base porphin (FBP). The direction of the vibrational modes is defined such that V_i is negative. Experimental frequencies determined from Raman spectra for FBP are also listed. Pyr, trans, deform, breath, bend, and str mean pyrrole, translational, deformation, breathing, bending, and stretching, respectively.

mode	description	frequency		V_i
		calc	exp	
$a_g(1)$	pyr trans	152.00	155[a], 157[b]	−0.068
$a_g(2)$	pyr trans	301.98	309[a,b]	−0.093
$a_g(3)$	pyr deform	713.72	723[a,b]	−0.502
$a_g(4)$	pyr deform	720.78	736[b]	−0.178
$a_g(5)$	pyr breath	947.35	952[a,b]	−0.218
$a_g(6)$	pyr breath	983.78	987[a], 988[b]	−0.035
$a_g(7)$	C_β−H bend	1054.22	1063[b]	−0.191
$a_g(8)$	C_β−H bend	1061.03	1064[a], 1063[b]	−0.121
$a_g(9)$	C_m−H bend	1174.10	1177[a], 1182[b]	−0.378
$a_g(10)$	pyr half-ring str	1345.92	1352[a], 1353[b]	−1.730
$a_g(11)$	pyr half-ring str	1394.78	1384[a]	−0.029
$a_g(12)$	C_α−C_m str	1424.93	1424[a], 1425[b]	−0.227
$a_g(13)$	C_β−C_β str	1494.63	1492[a], 1493[b]	−1.315
$a_g(14)$	C_β−C_β str	1547.02	1544[a], 1546[b]	−1.001
$a_g(15)$	C_α−C_m str	1599.60	1609[a], 1610[b]	−1.173
$a_g(16)$	C_m−H str	3098.33		−0.167
$a_g(17)$	C_β−H str	3148.43		−0.236
$a_g(18)$	C_β−H str	3163.10		−0.175
$a_g(19)$	N−H str	3509.87		−0.016

[a]Normal Raman spectra.[34]

[b]Resonance Raman spectra.[36,37]

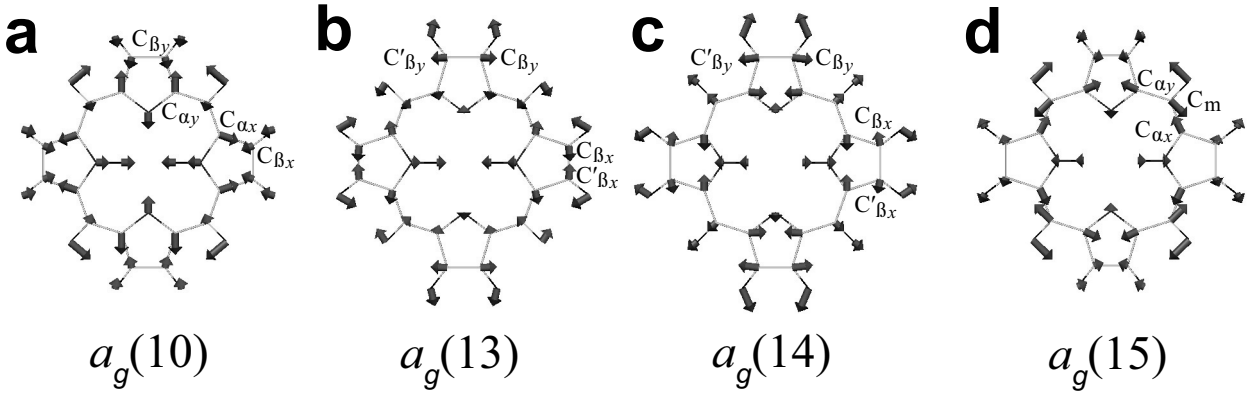

Figure 2.2: Vibrational modes with vibronic coupling constants larger than 1.0×10^{-4} a.u.: (a) $a_g(10)$; (b) $a_g(13)$; (c) $a_g(14)$; (d) $a_g(15)$.

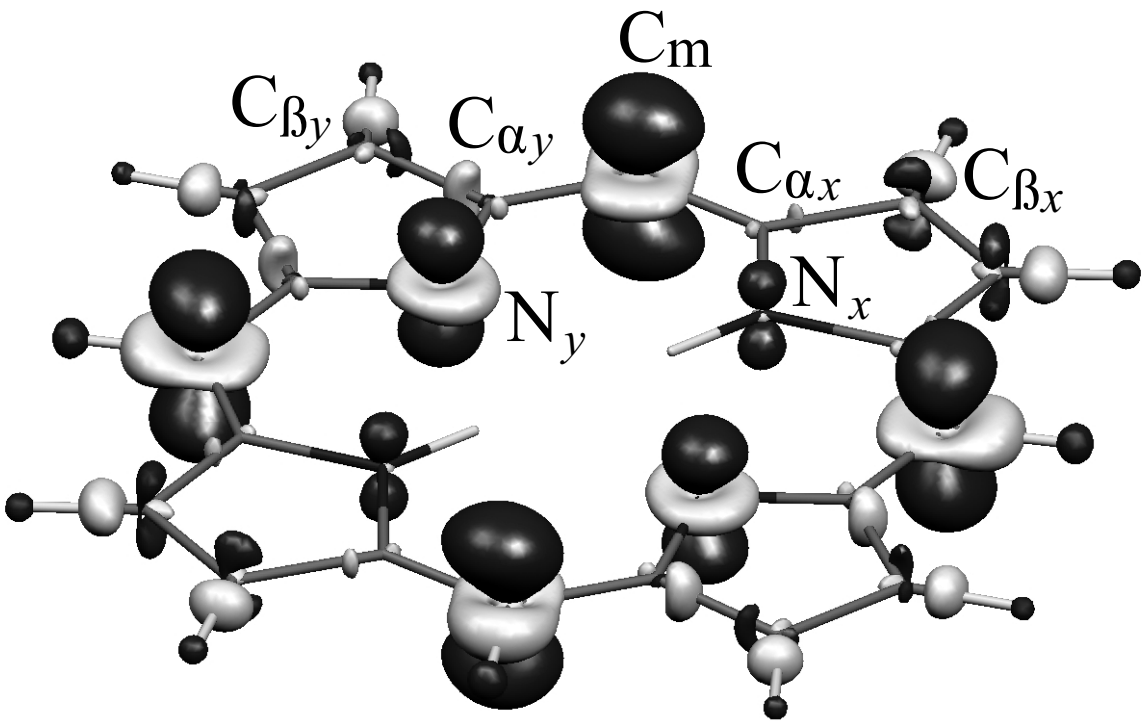

Figure 2.3: Electron-density difference $\Delta\rho$ at the isosurface value of 0.03 a.u. Dark gray shows where values are negative; light gray shows where values are positive.

In the following, we investigate the reason for the small VCCs of the FBP cation. Fig. 2.3 shows the electron-density difference $\Delta\rho$ of the FBP cation. $\Delta\rho$ is large on the C_m and N_y atoms and small on the C_{α_x}, C_{β_x}, C_{α_y}, C_{β_y}, N_x, and H atoms. It should be noted that $\Delta\rho$ is quite small on the bonds. The large negative $\Delta\rho$ on the meso carbon and nitrogen atoms has a π-orbital-like shape, which reflects a π-orbital-like shape of the highest occupied molecular orbital (HOMO) of the neutral FBP, since an electron is removed from the HOMO. By contrast,the large positive $\Delta\rho$ on the meso carbon and nitrogen atoms has a σ-orbital-like shape. The positive $\Delta\rho$ originates from orbital relaxations of the doubly occupied molecular orbitals other than the HOMO due to electron-hole interactions. The positive regions have a role of relaxing Coulomb repulsions between the negative regions over the molecular plane. The polarization in $\Delta\rho$ plays a crucial role in the VCD.[20,24]

$\Delta\rho$ has a great influence on the strength of vibronic couplings. According to Eqs. (2.1) and (2.2), V_i increases as the overlap between $\Delta\rho$ and v_i increases. We have shown that molecules whose $\Delta\rho$ is largely distributed on bonds give rise to large V_i values. By contrast, molecules whose $\Delta\rho$ is not largely distributed on bonds but strongly localized on atoms have small V_i values. Examples of the former case are biphenyl, fluorene, and α-oligothiophenes cations;[22,38] those of the latter case are TPA, TPD, and carbazole cations,[20–22] in which $\Delta\rho$ is strongly localized on the N atoms. For FBP, all the vibronically active modes are in-plane modes and v_i is distributed largely on bonds. Hence, the strong localization of $\Delta\rho$ on the meso-carbon atoms (Fig. 2.3) decreases the overlap between $\Delta\rho$ and v_i on the bonds, and give the small V_i.

The $a_g(10)$ and $a_g(15)$ modes illustrates the effect of the localization of $\Delta\rho$ on the meso-carbon atoms on V_i of the FBP cation. Figs. 2.4a and b show the one-electron part of the derivative of the nuclear–electronic potential v_{10} and RVCD $\bar{\eta}_{10}$, respectively. v_{10} is large on the pyrrole rings while it is small on the C_m and H atoms. In general, $\bar{\eta}_i$ is small in a region in which the overlap between $\Delta\rho$ and v_{10} is small. For the $a(10)$ mode, since the distribution patterns of $\Delta\rho$ and v_{10} are different, the overlap between $\Delta\rho$ and v_{10} is small over the whole region. For example, around the C_m atom, $\Delta\rho$ is large while v_{10} is small; around the C_{α_x}, C_{β_x}, C_{α_y}, C_{β_y} atoms, v_{10} is large while $\Delta\rho$ is small; around the N_x and N_y atoms, $\Delta\rho$ and v_{10} are not so large. In addition, around the H atoms, $\Delta\rho$ and v_{10} are small. For these reasons, $\bar{\eta}_{10}$ is small over the whole region, which leads to the small V_{10} value.

The AVCCs provide a quantitative discussion of the local vibronic couplings. Comparing the AVCCs in Fig. 2.4, the C_{α_x}, C_{α_y}, and N_y atoms have large AVCCs. By contrast, the values for the other atoms are quite small. The sum of the AVCCs of the C_{α_x}, C_{α_y}, and N_y atoms is -1.694×10^{-4} a.u., which corresponds to 97.9% of V_{10} ($= -1.730 \times 10^{-4}$ a.u.). It should be emphasized that the strong localization of $\Delta\rho$ on the meso-carbon atoms is the major reason for the small AVCCs and consequently, the small V_{10} value. The small displacement of the meso-carbon atoms, around which $\Delta\rho$ is quite large, is responsible for the weak vibronic coupling of the $a_g(10)$ mode. In a similar way, we can explain the small VCCs of the $a_g(13)$ and $a_g(14)$ modes, in which the meso-carbon atoms are not displaced largely.

Figs. 2.5a and b show v_{15} and $\bar{\eta}_{15}$, respectively. In contrast to the $a_g(10)$, $a_g(13)$, and $a_g(14)$ modes, since the $a_g(15)$ mode involves the $C_\alpha - C_m$ stretching vibrations, the meso-carbon atoms are displaced largely. Hence, v_{15} is large on the $C_{\alpha_x} - C_m$ and $C_{\alpha_y} - C_m$ bonds. However, around the $C_m - H$ bond, v_{15} is approximately antisymmetric with respect to the bond, while $\Delta\rho$ is approximately symmetric. Consequently, $\bar{\eta}_{15}$ cancels around the meso-carbon atoms and hence, their AVCCs are small. In addition, the antisymmetric distribution of v_{15} causes the sign of the AVCCs of the β-carbon atoms (the positive AVCC values) to be opposite to those of the α-carbon atoms (the negative AVCC values). These AVCCs are canceled out each other, and V_{15} is reduced. In summary, for the $a_g(15)$ mode, although $\Delta\rho$ overlaps significantly with v_{15} around the meso-carbon atoms, the cancellation of $\bar{\eta}_{15}$ occurs and V_{15} is small since v_{15} is approximately antisymmetric with respect to the $C_m - H$ bonds. For the totally symmetric modes other than the $a_g(10)$, $a_g(13)$, $a_g(14)$, and $a_g(15)$ modes, small AVCCs of the meso-carbon atoms are responsible for the small VCCs of those modes. The strong localization of $\Delta\rho$ on the meso-carbon atoms weakens the vibronic couplings on the pyrrole rings.

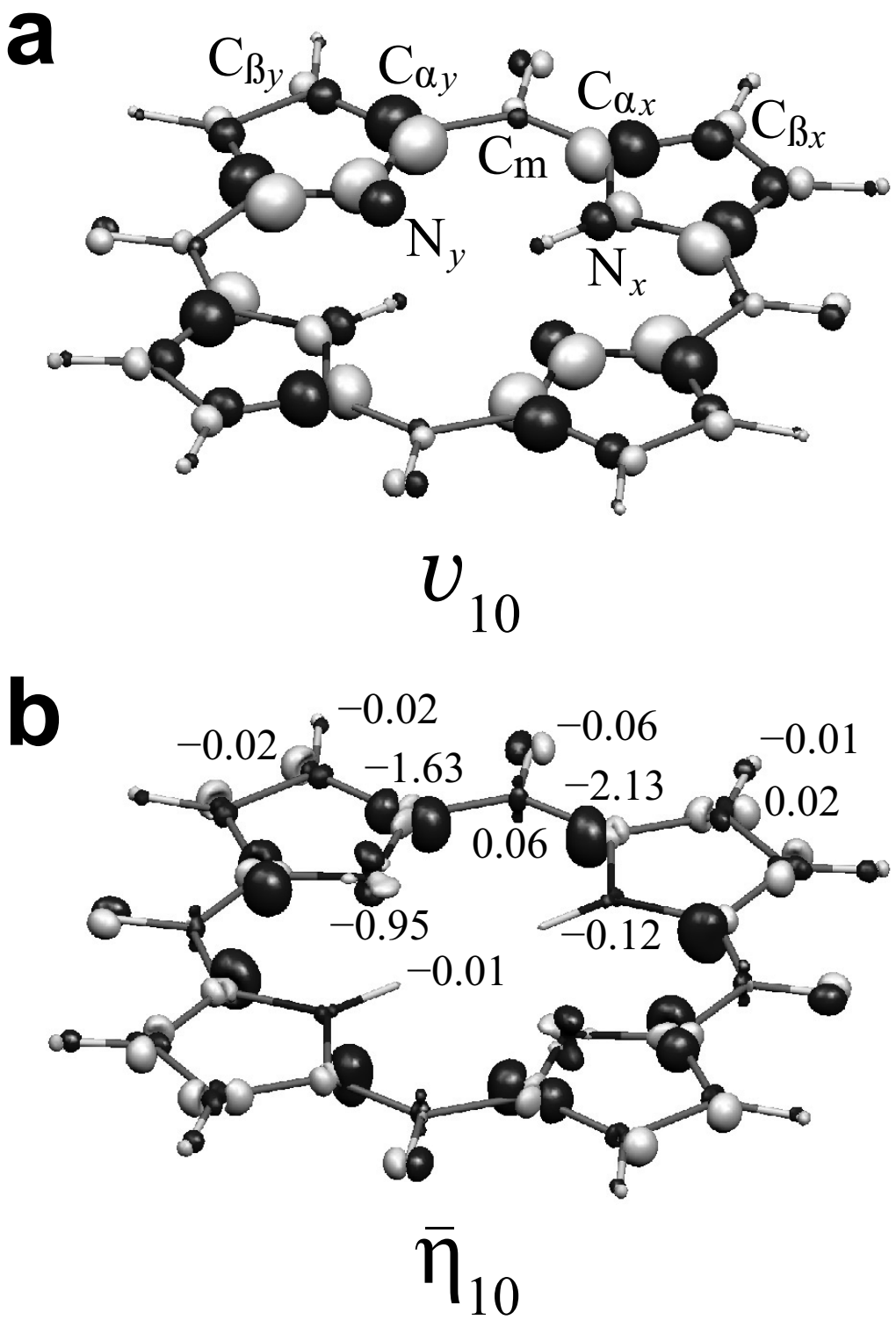

Figure 2.4: (a) One-electron part of the derivative of the nuclear–electronic potential v_{10} at the isosurface value of 0.01 a.u. (b) Reduced vibronic coupling density $\bar{\eta}_{10}$ at the isosurface value of 2.0×10^{-5} a.u. Dark gray shows where values are negative; light gray shows where values are positive. Numbers denote the atomic vibronic coupling constants (10^{-5} a.u.).

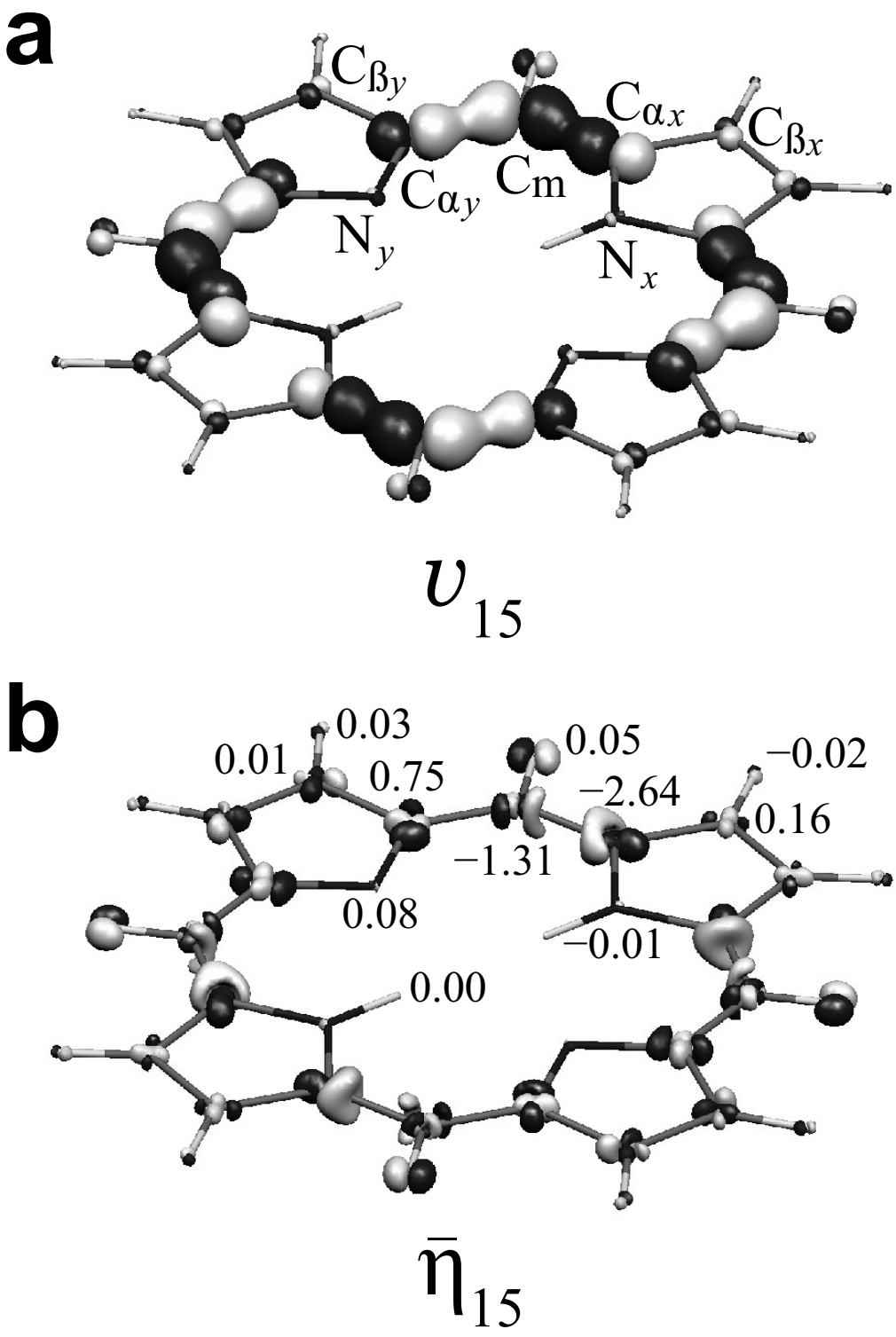

Figure 2.5: (a) One-electron part of the derivative of the nuclear–electronic potential v_{15} at the isosurface value of 0.01 a.u. (b) Reduced vibronic coupling density $\bar{\eta}_{15}$ at the isosurface value of 2.0×10^{-5} a.u. Dark gray shows where values are negative; light gray shows where values are positive. Numbers denote the atomic vibronic coupling constants (10^{-5} a.u.).

2.5 Concluding remarks

We calculated the VCCs and RVCDs of the FBP cation at the UB3LYP/6-311+G(d) level of theory. FBP has the small VCCs as a π-conjugated molecule. VCD analysis reveals that the strong localization of the electron-density difference on the meso-carbon atoms leads to the small VCCs of the FBP cation. We can reduce the VCCs and improve the hole-transporting properties by controlling the electron-density difference. Following this guiding principle, we have already succeeded in theoretically designing an efficient electron-transporting molecule for OLEDs.[23] Employing the VCD analysis, it is possible to design a porphyrin-based hole-transporting molecule by controlling its vibronic coupling.

Bibliography

[1] A. Tsumura, H. Koezuka, and T. Ando, Appl. Phys. Lett. **49**, 1210 (1986).

[2] L. Torsi, A. Dodabalapur, L. J. Rothberg, A. W. P. Fung, and H. E. Katz, Science **272**, 1462 (1996).

[3] A. Brown, C. Jarrett, D. de Leeuw, and M. Matters, Synth. Met. **88**, 37 (1997).

[4] G. Horowitz, Adv. Mater. **10**, 365 (1998).

[5] M. Muccini, Nat. Mater. **5**, 605 (2006).

[6] P. G. Schouten, J. M. Warman, M. P. de Haas, M. A. Fox, and H. L. Pan, Nature **353**, 736 (1991).

[7] Y.-Y. Noh, J.-J. Kim, Y. Yoshida, and K. Yase, Adv. Mater. **15**, 699 (2003).

[8] P. Checcoli, G. Conte, S. Salvatori, R. Paolesse, A. Bolognesi, M. Berliocchi, F. Brunetti, A. D'Amico, A. D. Carlo, and P. Lugli, Synth. Met. **138**, 261 (2003).

[9] S. Aramaki, Y. Sakai, and N. Ono, Appl. Phys. Lett. **84**, 2085 (2004).

[10] P. B. Shea, J. Kanicki, and N. Ono, J. Appl. Phys. **98**, 014503 (2005).

[11] P. B. Shea, A. R. Johnson, N. Ono, and J. Kanicki, IEEE Trans. Electron Dev. **52**, 1497 (2005).

[12] P. B. Shea, J. Kanicki, L. R. Pattison, P. Petroff, M. Kawano, H. Yamada, and N. Ono, J. Appl. Phys. **100**, 034502 (2006).

[13] P. B. Shea, C. Chen, J. Kanicki, L. R. Pattison, P. Petroff, H. Yamada, and N. Ono, Appl. Phys. Lett. **90**, 233107 (2007).

[14] P. B. Shea, L. R. Pattison, M. Kawano, C. Chen, J. Chen, P. Petroff, D. C. Martin, H. Yamada, N. Ono, and J. Kanicki, Synth. Met. **157**, 190 (2007).

[15] T. Minari, M. Seto, T. Nemoto, S. Isoda, K. Tsukagoshi, and Y. Aoyagi, Appl. Phys. Lett. **91**, 123501 (2007).

[16] A. S. Dhoot, S. Aramaki, D. Moses, and A. J. Heeger, Adv. Mater. **19**, 2914 (2007).

[17] C.-M. Che, H.-F. Xiang, S. S.-Y. Chui, Z.-X. Xu, V. A. L. Roy, J. J. Yan, W.-F. Fu, P. T. Lai, and I. D. Williams, Chem. Asian J. **3**, 1092 (2008).

[18] P. Ma, Y. Chen, X. Cai, H. Wang, Y. Zhang, Y. Gao, and J. Jiang, Synth. Met. **160**, 510 (2010).

[19] H. Ishii and K. Seki, IEEE Trans. Electron Dev. **44**, 1295 (1997).

[20] T. Sato, K. Shizu, T. Kuga, K. Tanaka, and H. Kaji, Chem. Phys. Lett. **458**, 152 (2008).

[21] K. Shizu, T. Sato, K. Tanaka, and H. Kaji, Chem. Phys. Lett. **486**, 130 (2010).

[22] K. Shizu, T. Sato, K. Tanaka, and H. Kaji, Org. Electron. **11**, 1277 (2010).

[23] K. Shizu, T. Sato, K. Tanaka, and H. Kaji, Appl. Phys. Lett. **97**, 142111 (2010).

[24] T. Sato, K. Tokunaga, and K. Tanaka, J. Phys. Chem. A **112**, 758 (2008).

[25] T. Sato, K. Tokunaga, N. Iwahara, K. Shizu, and K. Tanaka, *Vibronic coupling constant and vibronic coupling density* in *The Jahn-Teller-Effect - Fundamentals and Implications for Physics and Chemistry,* H. Köppel, D. R. Yarkony, and H. Barentzen (Eds) (Springer-Verlag, Berlin and Heidelberg, 2009).

[26] K. Shizu, T. Sato, and K. Tanaka, Chem. Phys. Lett. **491**, 65 (2010).

[27] A. D. Becke, J. Chem. Phys. **98**, 5648 (1993).

[28] C. Lee, W. Yang, and R. G. Parr, Phys. Rev. B **37**, 785 (1988).

[29] R. Krishnan, J. S. Binkley, R. Seeger, and J. A. Pople, J. Chem. Phys. **72**, 650 (1980).

[30] T. Clark, J. Chandrasekha, G. W. Spitznagel, and P. von Ragué Schleyer, J. Comput. Chem. **4**, 294 (1983).

[31] M. J. Frisch, G. W. Trucks, H. B. Schlegel, G. E. Scuseria, M. A. Robb, J. R. Cheeseman, J. A. Montgomery, Jr., T. Vreven, K. N. Kudin, J. C. Burant, J. M. Millam, S. S. Iyengar, J. Tomasi, V. Barone, B. Mennucci, M. Cossi, G. Scalmani, N. Rega, G. A. Petersson, H. Nakatsuji, M. Hada, M. Ehara, K. Toyota, R. Fukuda, J. Hasegawa, M. Ishida, T. Nakajima, Y. Honda, O. Kitao, H. Nakai, M. Klene, X. Li, J. E. Knox, H. P. Hratchian, J. B. Cross, V. Bakken, C. Adamo, J. Jaramillo, R. Gomperts, R. E. Stratmann, O. Yazyev, A. J. Austin, R. Cammi, C. Pomelli, J. W. Ochterski, P. Y. Ayala, K. Morokuma, G. A. Voth, P. Salvador, J. J. Dannenberg, V. G. Zakrzewski, S. Dapprich, A. D. Daniels, M. C. Strain, O. Farkas, D. K. Malick, A. D. Rabuck, K. Raghavachari, J. B. Foresman, J. V. Ortiz, Q. Cui, A. G. Baboul, S. Clifford, J. Cioslowski, B. B. Stefanov, G. Liu, A. Liashenko, P. Piskorz, I. Komaromi, R. L. Martin, D. J. Fox, T. Keith, M. A. Al-Laham, C. Y. Peng, A. Nanayakkara, M. Challacombe, P. M. W. Gill, B. Johnson, W. Chen, M. W. Wong, C. Gonzalez, and J. A. Pople, GAUSSIAN 03, Revision D.02, Gaussian, Inc., Wallingford, CT, 2004.

[32] N. Verdal, P. M. Kozlowski, and B. S. Hudson, J. Phys. Chem. A **109**, 5724 (2005).

[33] X. Y. Li and M. Z. Zgierski, J. Phys. Chem. **95**, 4268 (1991).

[34] P. M. Kozlowski, A. A. Jarzçki, P. Pulay, X.-Y. Li, and M. Z. Zgierski, J. Phys. Chem. **100**, 13985 (1996).

[35] B. M. L. Chen and A. Tulinsky, J. Am. Chem. Soc. **94**, 4144 (1972).

[36] A. L. Verma and H. J. Bernstein, Biochem. Biophys. Res. Commun. **57**, 255 (1974).

[37] K. Solovyov, L. Gladkov, A. Gradyushko, N. Ksenofontova, A. Shulga, and A. Starukhin, J. Mol. Struct. **45**, 267 (1978).

[38] K. Shizu, T. Sato, and K. Tanaka, Chem. Phys. **369**, 108 (2010).

General Conclusion

In this thesis, we investigated the vibronic couplings in the charge-transporting molecules for organic light-emitting diodes (OLEDs), organic field-effect transistors (OFETs), and electrode-single molecule-electrode junctions employing the vibronic coupling density (VCD) analyses. We succeeded in theoretically designing novel hole- and electron-transporting molecules exhibiting efficient single molecule transport-properties compared with those of existing hole- and electron-transporting molecules. The main results are summarized as follows.

Part I deals with design of novel charge-transporting materials for OLEDs. In Chapter 1, we calculated the VCCs in the TPD cation from the evaluation of vibronic coupling integrals. The calculated constants were very small compared with other π conjugated systems. The calculated constants were analyzed on the basis of the VCD. The VCD analysis clearly reveals that large contributions originate from the phenyl group and the tolyl group. The excess carrier density is accommodated on the nitrogen atoms. However, the density difference on the nitrogen atoms cannot contribute to the vibronic coupling, since the symmetric density distribution around the atoms are canceled. In addition, the hole transport property of the electrode-TPD molecule-electrode system was investigated using the non-equilibrium Green's function (NEGF) theory. Reflecting the small coupling, the current suppression and power loss are less than 1/2 compared with other π conjugated systems such as oligothiophenes.

In Chapter 2, we calculated the VCCs of TPA in the cation state and discussed their relative ordering by means of the VCD analysis. The small overlap between the electron-density difference $\Delta\rho$ and the derivative of the nuclear–electronic potential v_i in the phenyl groups is responsible for the weak vibronic couplings in the TPA cation. The VCCs of the TPA cation are small. We calculated the reorganization energies ΔE_s for the effective modes for TPA cations and compared them with those for the TPD and biphenyl cations.

The tolyl and phenyl groups as well as the central biphenyl unit contribute to ΔE_s for the TPD cation. This is because $\Delta\rho$ of the TPD cation localizes on the N atoms, and the vibronic couplings in the biphenyl moiety is weak. The localization of $\Delta\rho$ on the N atoms leads to a small reorganization energy for TPD cation.

In Chapter 3, we calculated the VCDs of the biphenyl, fluorene, and carbazole cations. The VCD analysis reveals that strong localization of $\Delta\rho$ on the N atom leads to the small VCCs of carbazole. In general, localized $\Delta\rho$ on an atom decreases the vibronic coupling and enhance the hole mobility. Substituting the biphenyl or fluorenyl moieties in the molecule with the carbazolyl moiety can weaken the vibronic couplings in the molecule and improve the hole mobility. This guiding principle opens a new way for the molecular design of carrier-transporting materials based on the VCD analysis. Though the HF method gives qualitatively good results, it sometimes yields overestimated VCCs. This is because $\Delta\rho$ calculated by the HF method is highly delocalized over bonds, compared with the DFT method. Therefore, for carbazole, the HF method yields quantitatively good result, since $\Delta\rho$ in carbazole does not largely delocalized over the bonds.

In Chapter 4, we investigated the relation between the strength of vibronic coupling and the extent of $\Delta\rho$ distribution by choosing ethylene dimer as an example. We calculated and compared the VCCs of the state in which $\Delta\rho$ is delocalized over the two ethylene molecules and those in which it is strongly localized on one of the ethylene molecules. Our major finding is that the VCCs for the delocalized $\Delta\rho$ case are $1/\sqrt{2}$ of those for the localized $\Delta\rho$ case. In other words, the size of the vibronic coupling constants is inversely proportional to the square root of the number of the atoms over which $\Delta\rho$ is distributed. This finding may open the way to tuning vibronic coupling through controlling $\Delta\rho$ distribution and enable us to design functional materials such as charge-transporting molecules.

In Chapter 5, we theoretically designed a hole-transporting molecule, hexaaza[1_6]para-biphenylophane (HAPBP). HAPBP exhibits the weaker vibronic coupling and higher hole-transporting properties than the well-known hole-transporting materials, TPD, TAD, and α-NPD. HAPBP has the smaller number of vibronically active mode than TPD, TAD, and α-NPD because of its high symmetric structure. Furthermore, the VCCs of the HAPBP cation are smaller than those of the TPD, TAD, and α-NPD cations because the electron-density difference of the HAPBP cation is localized on six N atoms equivalently and quite

small. The weak vibronic coupling of the HAPBP cation is due to the small number of vibronically active mode resulting from the selection rule for the vibronic coupling and the small VCCs originating from the symmetrically delocalized distributions of VCDs. In addition, HAPBP has the higher HOMO and LUMO energy levels than TPD, TAD, and α-NPD, suggesting that HAPBP exhibits superior hole-injecting and electron-blocking properties to TPD, TAD, and α-NPD. For these reasons, HAPBP is expected to be a candidate for a hole-transporting material.

In Chapter 6, we designed a boron-containing molecule with high-symmetry, hexaboracyclophane (HBCP). The theoretically designed HBCP exhibits weaker vibronic coupling and higher electron-transporting property than *mer*-Alq_3 and 3TPYMB. Furthermore, since the HOMO/LUMO energy level of HBCP is lower than that of 3TPYMB, HBCP can be a superior electron-injecting and hole-blocking material to 3TPYMB when *mer*-Alq_3 is used as an emitting layer. Usually, amorphous materials have been used in OLEDs. HBCP might be highly crystalline in nature because of its high symmetry. Amorphous HBCP-based materials would be obtained, for example, by introducing bulky substituents into HBCP.

In Chapter 7, we investigated the vibronic couplings in the CBP and TPF cations on the basis of the VCD analysis. In spite of the bridge in TPF, the planarity of the central fluorenyl unit has little effect on the vibronic couplings in the TPF cation, while the bridges in CBP make increases of the maximum vibronic-coupling in the CBP cation. This effect comes from the deficiency of the electron-density difference on the central fluorenyl unit. We have discussed the effect of on-site Coulomb interactions, or electron-hole interactions on the electron-density difference using the Hubbard model. It is found that the difference of the on-site Coulomb interactions gives rise to the strong localization of the electron-density difference on the diphenylamino groups and the deficiency on the fluorenyl group in the TPF cation. They are responsible for the small VCCs in TPF. These finding will open a way to control vibronic couplings in a molecule using many-body interactions.

Part II deals with the VCD analyses of the molecular wires. In Chapter 1, we calculated the VCDs for α-nT ($n = 2 - 9$) and explained relative sizes of VCCs by means of the VCD analysis. The relative VCC sizes for α-2T and α-3T was investigated in detail using the VCD analysis. The VCD analysis reveals that the large distribution of the electron-

density difference on the C=C double bonds leads to the strong vibronic couplings of the C=C stretching modes. The experimental photoelectron spectrum of α-3T supports our conclusion that the C=C stretching modes have the large VCCs. For α-8T, the electron-density difference is distributed mainly in the central four thiophene rings, suggesting that the polaronic defect occurs in the four rings; for α-9T, the electron-density difference is distributed at most five thiophene rings, and hence, the polaron size is about five rings. Thus, the VCD analysis provides us a new insight into the reason for polaron size, and is a powerful tool for understanding transport properties of organic semiconductors and molecular wires.

In Chapter 2, we calculated the VCDs for Au_2DMcT and Au_2TTF-DT cations. The VCD analysis enables us to understand the relative order of the VCCs. For Au_2DMcT, since $\Delta\rho_{\mathrm{HOMO}}$ is large on the C−N bond, the C−N stretching mode couples strongly to the electronic state; for Au_2TTF-DT, since $\Delta\rho_{\mathrm{HOMO}}$ is large on the central C=C bond, the C=C stretching modes couple strongly to the electronic state. We calculated the IET spectra for Au/DMcT/Au and Au/TTF-DT/Au junctions using the NEGF theory. We calculated the IET spectrum for the Au/Th-DT/Au junction and compared it with that for the Au/DMcT/Au junction. Th-DT and DMcT can be distinguished using the IET spectroscopy by the peak of the C−C stretching mode. The VCD analysis can be an effective way to understand relative intensities in IET spectra.

Part III deals with miscellaneous applications of the VCD analysis. In Chapter 1, we introduced the reduced vibronic coupling density (RVCD) and the reduced atomic vibronic coupling density (RAVCD) to discuss the origin of vibronic couplings in a molecule. The RVCD and RAVCD are defined as subtractions of the components of the integrals of which yield zero from the VCD and AVCD. As an example, we presented AVCDs and RAVCDs for the C=C stretching mode of the BEDT-TTF cation. RAVCD exhibits the origin of the strongest vibronic coupling of the C=C stretching mode. The large $\Delta\rho$ on the C=C bond is responsible for the strong vibronic coupling. Using the reduced coupling densities, we can gain new physical insights more clearly than conventional VCD and AVCD. Furthermore, the RVCD analysis provides a new guiding principle of the molecular design for functional molecules, such as an organic superconductor, molecular wire, and so on.

In Chapter 2, we calculated the VCCs and RVCDs of the free-base porphin (FBP)

cation. FBP has the small VCCs as a π-conjugated molecule. VCD analysis reveals that the strong localization of $\Delta\rho$ on the meso-carbon atoms leads to the small VCCs of the FBP cation. We can reduce the VCCs and improve the hole-transporting properties by controlling $\Delta\rho$. Following this guiding principle, we have already succeeded in theoretically designing an efficient electron-transporting molecule for OLEDs in Chapters 5 and 6 of Part I. Employing the VCD analysis, it is possible to design a porphyrin-based hole-transporting molecule by controlling its vibronic coupling.

The aim of this thesis is to analyze vibronic couplings in a charge-transport process, derive guiding principles for designing effective charge-transporting molecules, and theoretically design novel charge-transporting molecules by controlling their vibronic couplings. We hope that findings in this thesis could give effective guiding principles for designing charge-transporting molecules and molecular wires, and form the basis for the *vibronics*.